An Efficient Numerical Framework for Capturing Localised 3D Stress Fields in Laminated Composites

By

MAYANK PATNI

Department of Aerospace Engineering
UNIVERSITY OF BRISTOL

A dissertation submitted to the University of Bristol in accordance with the requirements of the degree of DOCTOR OF PHILOSOPHY in the Faculty of Engineering.

AUGUST 2019

Word count: 65,622

Abstract

Composite materials offer considerable advantages in the impetus towards lightweighting and therefore the exploitation of fibre-reinforced composites in engineering structures has been steadily diversifying from e.g. sports equipment and racing cars, to helicopters and commercial aeroplanes. Furthermore, recent advancements in composite manufacturing technology have facilitated the use of complex configurations in industrial design applications. For reliable design of multilayered structures, accurate stress analysis tools are required. However, with an increasing structural complexity, predicting structure's response can be non-intuitive and often can not be modelled adequately using classical lamination theory. High-fidelity finite element methods (FEM) are often employed to obtain reliable three-dimensional (3D) stress analyses with the desired level of accuracy. However, these models are computationally expensive and are prohibitive for iterative design studies. Consequently, over the years, several one-dimensional (1D) and two-dimensional (2D) models based on higher-order theories have been proposed for the analysis of multilayered composite structures with the aim of predicting accurate 3D stress fields in a computationally efficient manner. The majority of these numerical models either lack kinematic fidelity or accuracy in capturing localised regions of the structure, or have limited capabilities to model complex structures.

The work presented here uses the Unified Formulation (UF) that supersedes classical theories by exploiting a compact, hierarchical notation that allows most classic and recent theories to be retrieved from one, hence *unified*, model. Importantly, and unlike many classic theories, the UF applies to the partial differential equations governing three-dimensional elasticity. Full stress and strain fields are, therefore, recovered by its implementation. Although current implementations are found wanting in this respect, in a UF setting, complex geometries could easily be analysed. This is because the displacement field is expressed by means of classic 1D (beam-like case) and 2D (plate- and shell-like cases) finite element elements that need not be prismatic. Additional expansion functions are employed to approximate 3D kinematics over cross-sections (beam-like case) and through-thickness (plate- and shell-like cases). In the present work, the 1D UF is adopted and developed further by introducing a hierarchical, Serendipity Lagrange polynomials-based, cross-sectional expansion model. The 3D stress predicting capabilities of the proposed model is verified against high-fidelity finite element models and other numerical and experimental results available in the literature by means of static analyses of isotropic, constant- and variable-stiffness laminated composite, beam-like and stiffened structures. Special attention is given to the accuracy of the model in capturing 3D stress response in the localised regions, such as near geometric or constitutive discontinuities, constraints and point of load application, and using these further for predicting the structure's failure response. Finally, to showcase a possible application, the model is applied to analyse non-prismatic and curved structures. The general formulation presented herein is well-suited for accurate and computationally efficient stress analysis for industrial design applications.

To my beloved daughter NAISHA,
without whom this work would have finished six months earlier!

Acknowledgements

The completion of this thesis would not have been possible without the support from a number of key people. First and foremost, I would like to extend my sincere gratitude to my advisors, Prof. Paul M. Weaver and Dr Alberto Pirrera, for their guidance, support and for being incredible mentors. I am very grateful to them for imparting scientific advice and knowledge which led to many insightful discussions in these years. Prof. Weaver is one of the smartest Professor I have known. He is full of energy and enthusiasm. His passion and dedication for scientific research always inspire me. Dr Pirrera provided constant support at every step of the way. I am very thankful to him for fixing up the secondment postings which has helped me in growing my network and in taking the research to the next level. I always admire Dr. Pirrera for his writing skills and the way he scrutinises the technical content to make it clear and impactful.

I have been fortunate to be a part of the Bristol Composites Institute (ACCIS) and surrounded by passionate and intellectual individuals, from whom I have learnt so much. In particular, I would like to thank Dr Rainer Groh for the limitless time he has provided to me for technical discussions. My kind regards to Prof. Stephen Halett for providing constructive feedback on my progress each year during the internal review meeting. Special acknowledgments are due to my colleagues, Sergio Minera and Aewis Hii, for the endless and insightful technical discussions during these years. I would like to express my gratitude to Prof. Erasmo Carrera, Dr Alfonso Pagani and Dr Enrico Zappino, who have shared their extensive knowledge on the numerical formulation during my stay at Politecnico di Torino. Furthermore, I would take this opportunity to thank Prof. Chiara Bisagni for allowing me to conduct research activity at the Delft University of Technology and for sharing her valuable time and expertise. I would also like to thank Dr. Tomas Vronsky for hosting me at Vestas Technology Ltd., Southampton.

This research has been developed in the framework of the FULLCOMP project funded by the H2020 Marie Skłodowska-Curie European Training Network (Grant number 642121) and is greatly acknowledged. Special thank goes to my FULLCOMP colleagues and friends: Alberto, Luke, Ibrahim, Margarita, Sander, Yanchuan, Gabriele, Lorenzo, Pietro and Giorgios.

Finally, my regards to most important people of my life, my entire family, without their support this thesis would not have been possible. Specially, my parents and my sister for their blessings and encouragement which inspired me at every step of the way. My parents-in-law for rejoicing over every achievement of mine. My beloved wife, Sakshi, who always stood by my side. I can't thank her enough for all her support and understanding, specially when I had to work late nights and during the weekends. My beautiful and lovely daughter, Naisha, who came into this world a year ago to be my stress-buster. No matter how much anxious I was, my baby girl always cherished me with her adorable smile.

Bristol, August 2019

Mayank Patni

Author's Declaration

I declare that the work in this dissertation was carried out in accordance with the requirements of the University's Regulations and Code of Practice for Research Degree Programmes and that it has not been submitted for any other academic award. Except where indicated by specific reference in the text, the work is the candidate's own work. Work done in collaboration with, or with the assistance of, others, is indicated as such. Any views expressed in the dissertation are those of the author.

SIGNED: ..... DATE: .....

Mayank Patni

Some of the topics outlined in this thesis have been published in peer-reviewed journals and/or presented at international conferences.

Journal Articles

1. S. Minera[†], **M. Patni**[†], E. Carrera, M. Petrolo, P.M. Weaver, A. Pirrera (2018). Three-dimensional stress analysis for beam-like structures using Serendipity Lagrange shape functions, *International Journal of Solids and Structures*, 141, 279-296. [†] **Equal Contributions**.

2. **M. Patni**, S. Minera, R.M.J. Groh, A. Pirrera, P.M. Weaver (2018). Three-dimensional stress analysis for laminated composite and sandwich structures, *Composites Part B: Engineering*, 155, 299-328.

3. **M. Patni**, S. Minera, R.M.J. Groh, A. Pirrera, P.M. Weaver (2019). On the accuracy of localised 3D stress fields in tow-steered laminated composite structures, *Composite Structures*, 225, 111034.

4. **M. Patni**, S. Minera, R.M.J. Groh, A. Pirrera, P.M. Weaver (2019). Efficient 3D Stress Capture of Variable Stiffness and Sandwich Beam Structures, *AIAA Journal*, 57(9), 4042-4056.

5. **M. Patni**, S. Minera, C. Bisagni, P.M. Weaver, A. Pirrera (2019). Geometrically nonlinear finite element model for predicting failure in composite structures, *Composite Structures*, 225, 111068.

6. S.O. Ojo, **M. Patni**, P.M. Weaver (2019). Comparison of Weak and Strong Formulations for the 3D stress predictions of composite beam structures, *International Journal of Solids and Structures*, 178-179, 145-166.

7. **M. Patni**, S. Minera, P.M. Weaver, A. Pirrera. Efficient modelling of beam-like structures with general non-prismatic, curved geometry, *In Preparation*.

Conference Papers / Presentations

8. **M. Patni**, S. Minera, P.M. Weaver, A. Pirrera (2017). 3D stress analysis for complex cross-section beams using unified formulation based on Serendipity Lagrange polynomial expansion, *Proceedings of the* 3^{rd} *International Conference on Mechanics of Composites*, Bologna, Italy, July 2017.

9. **M. Patni**, S. Minera, E. Carrera, P.M. Weaver, A. Pirrera (2017). On the accuracy of the displacement-based Unified Formulation for modelling laminated composite beam structures, *Proceedings of the* 20^{th} *International Conference on Composite Structures (ICCS20)*, Paris, France, September 2017.

10. **M. Patni**, S. Minera, A. Pirrera, P.M. Weaver (2017). A computationally efficient model for three-dimensional stress analysis of stiffened curved panels, *Proceedings of the International Conference on Composite Materials and Structures (ICCMS)*, Hyderabad, India, December 2017.

11. **M. Patni**, S. Minera, A. Pirrera, P.M. Weaver (2018). Three-dimensional Stress Distribution in Tow-Steered Composite Structures, *Proceedings of the* 1^{st} *International Conference on Mechanics of Advanced Materials and Structures*, Turin, Italy, June 2018.

12. S.A.M. Rebulla, **M. Patni**, P.M. Weaver, A. Pirrera, M.P. O'Donnell (2019). Comparing the effect of geometry and stiffness on the effective load paths in non-symmetric laminates, *Proceedings of the American Institute of Aeronautics and Astronautics (AIAA) Science and Technology Forum and Exposition*, San Diego, California, USA, January 2019.

13. **M. Patni**, S. Minera, C. Bisagni, A. Pirrera, P.M. Weaver (2019). Geometrically nonlinear Unified Formulation model for capturing failure in composite stiffened structures, *Proceedings of the* 5^{th} *International Conference on Mechanics of Composites*, Lisbon, Portugal, July 2019.

Use of published work in this thesis

The literature reviews of references [1-7] above have served as a foundation for Chapter 2. Chapters 3 and 4 are based on the work published in [1] and [10]. Chapters 5, 6, 7, 8 and 9 are drawn from the work in [2], [3], [4], [5] and [7], respectively.

TABLE OF CONTENTS

List of Tables

List of Figures

Figure **Page**

List of common abbreviations

1D, 2D, 3D	One-, Two- and Three-Dimensional, respectively
CLT	Classical Laminate Analysis
CS	Constant-Stiffness
DOF	Degree of Freedom
DQM	Differential Quadrature Method
EB	Euler-Bernoulli Beam
ESL	Equivalent Single Layer
FEM	Finite Element Method
FSDT	First-order Shear Deformation Theory
GBT	Generalized Beam Theory
GDQ	Generalized Differential Quadrature
GUF	Generalised Unified Formulation
HR	Hellinger-Reissner
HSDT	Higher-order Shear Deformation Theory
IC	Interlaminar Continuity
LE	Lagrange Expansion
LW	Layer-Wise
MZZF	Murakami Zig-Zag Function
PVD	Principle of virtual displacements
RMVT	Reissner Mixed-Variational Theory
RZT	Refined Zig-Zag Theory
SLE	Serendipity Lagrange Expansion
TB	Timoshenko Beam
TE	Taylor Expansion
TOT	Third Order Theory
UF	Unified Formulation
VABS	Variational Asymptotic Beam Section
VAM	Variational Asymptotic Method
VAT	Variable Angle Tow

VS	Variable-Stiffness
ZZ	Zig-Zag

Roman Symbols

A	Area of cross-section
$\boldsymbol{C}$	Material stiffness matrix
$\bar{\boldsymbol{C}}$	Transformed material stiffness matrix
C_{ijkl}	Components of fourth-order stiffness tensor
$\bar{C}_{ij}$	Transformed elastic coefficients
$\mathscr{D}$	Kinematic partial differential operator
$\boldsymbol{E}$	Young's modulus
E_{ii}	Young's moduli in normal ii-direction
$\boldsymbol{E}$	Green-Lagrange strain vector
f	Generalised load vector
F_τ, F_s	Cross-section expansion shape functions
$\boldsymbol{F}$	Deformation gradient
G	Shear modulus
G_i	Effective transverse shear rigidity of the entire layup
G_{ij}	Shear moduli in ij-direction
h	Laminate total thickness
h^k	Thickness of layer k
I	Second moment of area
$\boldsymbol{J}^{\text{2D}}$	2D Jacobian matrix
$\boldsymbol{J}^{\text{2D}}$	3D Jacobian matrix
$\boldsymbol{K}$	Global stiffness matrix
$\boldsymbol{K}_{\text{s}}$	Secant stiffness matrix
$\boldsymbol{K}_{\text{T}}$	Tangent stiffness matrix
$\boldsymbol{K}^{\tau sij}$	Fundamental Nucleus of the stiffness matrix
L	Length of the beam
M	Number of terms in the cross-sectional expansion
N_i, N_j	1D Lagrange shape functions
N_{l}	Total number of layers
N_{e}	Number of Lagrange nodes within each beam element
N^{2D}	2D Lagrange shape functions
N^{3D}	3D Lagrange shape functions
$\mathscr{O}$	Complexity of an algorithm
$\boldsymbol{R}$	Rotation tensor
$\boldsymbol{S}$	Second Piola-Kirchhoff stress tensor

T_0	Local fibre angle at the centre of a variable stiffness laminate
T_1	Local fibre angle at the ends of a variable stiffness laminate
$\boldsymbol{T}$	Transformation matrix
$\boldsymbol{U}$	Displacement vector
$\boldsymbol{u}_i$, $\boldsymbol{u}_j$	Generalised nodal displacement vectors
$\boldsymbol{u}_{i\tau}$, $\boldsymbol{u}_{js}$	Generalized displacement vectors
u,v,w	Displacement components in x, y and z directions, respectively
V	Volume of elastic continuum
W	Work done by internal and external forces
x,y,z	Cartesian global coordinates

Greek Symbols

γ_{xz},γ_{yz}	Transverse shear strains
γ_{xy}	In-plane shear strain
δ	Virtual variation
$\boldsymbol{\varepsilon}$	Linear Green-Lagrangian strain vector
$\varepsilon_{xx},\varepsilon_{yy}$	In-plane normal strains
ε_{zz}	Transverse normal strain
θ	Fibre orientation angle
ν	Poisson's ratio
$\boldsymbol{\sigma}$	Cauchy stress tensor
$\hat{\boldsymbol{\sigma}}$	Corotational Cauchy stress tensor
σ_{xx},σ_{yy}	In-plane normal stresses
σ_{zz}	Transverse normal stress
τ_{xz},τ_{yz}	Transverse shear stresses
τ_{xy}	In-plane shear stress
ϕ^M	Murakami's zig-zag function
ϕ_x^R,ϕ_y^R	Refined zig-zag theory functions
ψ_x,ψ_y	Zig-Zag rotations about x and y axis

Superscripts

i, j	Indices related to the beam nodes
k	Quantities corresponding to the k^{th} layer
τ, s	Indices related to the cross-section expansion terms
(e)	Quantity defined at the elemental level

Subscripts

i, j	Indices related to the beam nodes
k	Quantity corresponding to the interface between the k and $k+1$ layers
τ, s	Indices related to the cross-section expansion terms
(e)	Quantity defined at the elemental level

CHAPTER 1

INTRODUCTION

Composite structures are widely exploited in many engineering fields. For instance, the state-of-the-art civil aircraft (B787 and A350) are mostly (by volume) made of composite materials, due to their excellent specific strength and stiffness properties. The design of composites leads to challenging tasks since those competences that stemmed from the adoption of metallic materials are often inadequate for composites. Insights on many different disciplines and tight academic/industrial cooperation are required to fully exploit composite structure capabilities.

The present research is done in the framework of the H2020 Marie Skłodowska-Curie European Training Network project **FULLCOMP** - FULLy integrated analysis, design, manufacturing and health-monitoring of COMPosite structures. The full spectrum of the design of composite structures is dealt with - manufacturing, health-monitoring, failure, modelling, multi-scale approaches, testing, prognosis and prognostic. The FULLCOMP consortium is composed of 7 Universities, 1 research institute and 1 industry, where 12 PhD students worked in an international framework with an aim to develop integrated analysis tools for improving the design and production of composites.

1.1 Research Motivation and Objectives

As environmental concerns and governmental regulations push towards a more efficient use of materials and resources, engineering structures are progressively being developed and optimised to increase their performance and/or to reduce their mass and carbon footprint. Composite materials offer considerable advantages in the impetus towards lightweighting, due to their high specific stiffness and strength. In combination, these more stringent design drivers and the availability of advanced materials promote the employment of increasingly slender and

thin-walled, monocoque and semi-monocoque structures. The aerospace, automotive and wind energy industries provide prime examples of structures that gain efficiency through increased slenderness. See, for instance, the A350 and 787 wings or recent multi-MW wind turbine blades. However, as slenderness increases, structures become more susceptible to complex nonlinear deformations. Engineers must, therefore, be aware of the limits of both elastic stability and material strength to produce efficient, reliable designs

In engineering design, long slender structures are typically analysed using axiomatic beam models. These models are valid under the premise that the longitudinal dimension of a structure is at least one order of magnitude larger than representative cross-sectional dimensions. This geometric feature allows the governing elasticity equations to be reduced from three to one dimension, (with the reference axis coinciding with the beam axis), and in so doing, brings about significant physical insight and computational benefits. However, their accuracy is limited by Saint-Venant's principle, *i.e.* to regions remote from the boundary constraints, discontinuities and points of load application. To account for effects that are not captured by classical axiomatic theories, several refined finite element (FE) models have been developed. However, geometric complexities and accurate approximations of the displacement field can lead to computationally expensive models, where a large number of unknown variables is required. Such models can become computationally prohibitive when employed for nonlinear problems that require iterative solution techniques.

Moreover, the increasing use of laminated composites as load-bearing structures in novel applications require advanced numerical models to accurately predict their structural response. For instance, in laminated safety glass, layers of stiff and brittle glass are joined by soft and ductile interlayers of polyvinyl butyral or ethylene-vinyl acetate. As the material properties of glass and interlayer differ by multiple orders of magnitude, its structural response to external stimuli is non-intuitive and cannot be captured accurately using classical lamination theory [11]. Another example is using laminated composites in wind turbine blade roots, where the thicker aspect ratio induces significant transverse shearing and transverse normal deformations, which cannot be predicted by classical lamination theory. Furthermore, recent advancements in composite manufacturing technology have facilitated the production of laminates with curvilinear fibres, so-called variable-stiffness (VS) composites (or Variable Angle Tow composites). This technological advance removes the constraint on fibres to be rectilinear within each lamina and provides scope for an enlarged design space. However, both types of composite laminate—with unidirectional and curvilinear fibres—lack reinforcement through the thickness and are prone to delamination failure, which adversely affects their structural integrity. Demanding levels of performance, especially in the aerospace industry, call for efficient modeling tools to predict the initiation of failure. To this end, models for accurate full-field stress prediction are an important prerequisite.

Providing a robust and efficient tool, with advanced modelling techniques, is one of the major challenges in the field of computational mechanics due to the four major non-classical effects

relevant to multilayered composite structures,

- Severe transverse shear deformations due to low orthotropy ratio (G_{13}/E_{11}), which increases the channelling of axial stresses towards the surfaces [12], a phenomenon not captured by models with simple kinematic assumptions.
- Transverse normal deformation results in changes in laminate thickness, which is particularly pernicious for sandwich laminates with soft cores.
- The zig-zag effect due to transverse anisotropy, whereby differences in layer-wise transverse shear and normal moduli lead to a sudden change in the slope of the three displacement fields at layer interfaces, and results in non-intuitive internal load redistributions.
- Localised boundary layers towards singularities, which exacerbate all of the three previously mentioned effects and lead to stress gradients that are drivers of failure initiation.

It is because of the aforementioned complexities, amongst others, that high-fidelity finite element methods (FEM) are often employed to obtain reliable three-dimensional (3D) stress analyses with the desired level of accuracy. However, these models are computationally expensive and require a vast amount of computer storage space. Thus, with the aim of developing computationally efficient, yet robust, design tools for the practicing engineer, there remains a need for efficient modelling techniques for accurate stress predictions that account for these non-classical effects.

Over the years, several models based on higher-order theories have been proposed for the analysis of multi-layered composite beams with the aim of predicting accurate 3D stress fields in a computationally efficient manner. The present research follows along the same line with particular focus on developing a robust modelling framework for industrial design applications. The overall aims of the research are summarised as follows:

1. To develop a robust higher-order modelling framework that predicts variationally consistent 3D stress fields, including around local features such as geometric, kinematic or constitutive boundaries. The model should be applicable to isotropic, anisotropic and laminated beams with 3D heterogeneity (*i.e.* laminates comprised of layers with material properties that may differ by multiple orders of magnitude and that also vary continuously in the plane of the beam).
2. To develop an efficient higher-order modelling framework that predicts complex nonlinear deformations and accurately captures 3D stress fields for failure and damage prediction in composite structures.
3. To extend the modelling technique to analyse structures of arbitrary shapes in order to maximise the model's potential use in industrial design applications.

4. To implement the higher-order model numerically via a computer code that allows localised 3D stress fields and stress gradients towards boundaries and singularities to be captured in a computationally efficient manner.

1.2 Thesis Outline

The thesis is structured as follows:

- Chapter 2 begins with an overview on the fundamental principles of mechanics and leads to a detailed review of the literature on refined structural theories. Research on higher-order structural theories has received considerable attention throughout the last century. All of these works has led to an extensive corpus of work. Therefore, it is not possible to mention all papers and different theories that have been published. Rather the author has given special attention to those models that are relevant to the present work and have most aided the author's understanding of the field. The chapter further provides the literature review on numerical tools available for modelling laminated composite structures with straight- and curvilinear-reinforced fibres. Furthermore, various methods developed, for predicting failure in laminated composites, are discussed. The chapter concludes with a review of the literature on available numerical tools for modelling non-prismatic and curved structures.

- Chapter 3 presents refined beam models based on the Unified Formulation for capturing 3D displacement and stress fields. A hierarchical, cross-sectional expansion model, based on the Serendipity Lagrange functions, is proposed together with several mapping techniques for modelling complex cross-section beam structures. To capture localised regions accurately without increasing the computational expense, methods such as variable kinematics and biased-node distributions are proposed.

- In Chapter 4, the Serendipity Lagrange expansion-based Unified Formulation (UF-SLE) model, derived in Chapter 3, is used to analyse beam-like structures made of isotropic material. The benefits offered by the proposed model over existing expansion models in the Unified Formulation framework are discussed. To highlight the ability of the UF-SLE model in capturing localised regions, various structures such as T-section beam, C-section beam, flat and curved stiffened panels, are considered. For all cases, the accuracy of the model is verified against 3D finite element solutions and analytical solutions, where applicable.

- In Chapter 5, the UF-SLE model is used to analyse a comprehensive set of straight-fibre composite and sandwich beams in bending. The model is verified against 3D elasticity and 3D finite element solutions, and also compared against a mixed-variational formulation available in the literature. The model is then used to predict high-order effects on the structural behaviour such as stress gradients towards clamped edges. Finally, the computational efficiency gain over 3D finite element model is highlighted.

- Chapter 6 extends the analysis of Chapter 5 to tow-steered, variable-stiffness beams. The results of the present formulation are again compared against 3D finite element solutions. The correlation of the stress fields with the benchmark solution demonstrate the successful application of the model to layered structures with material properties that vary continuously or discretely in all three dimensions. Furthermore, the ability of the proposed approach in predicting accurate 3D stress fields efficiently including around local features such as geometric, kinematic or constitutive boundaries, is assessed.

- Chapter 7 proposes an equivalent single layer approach of the UF-SLE model in contrast to its layer-wise form presented in Chapters 5 and 6. To account for through-thickness transverse anisotropy in laminated composites, various zig-zag functions are incorporated. The proposed model is used to analyse constant- and variable-stiffness laminates and its accuracy is verified against 3D elasticity and 3D finite element solutions. Finally, the computational expense incurred by the layer-wise and the equivalent single layer approach is highlighted.

- Chapter 8 presents theory and implementation of the UF-SLE model applied to non-linear problems in structural mechanics. Geometric nonlinearities are considered and static responses for isotropic and laminated composite structures are studied. In addition, to assess the enhanced capabilities of the proposed model, the postbuckling response of a composite stiffened panel is compared with experimental results from the literature. Furthermore, the 3D stress fields evaluated in the postbuckling regime are used to detect failure of the stiffened panel.

- Chapter 9 extends the modelling approach based on the Unified Formulation, described in Chapter 3, to account for non-prismatic and curved beam-like structures. The proposed model is benchmarked against 3D finite element model, analytical models and experimental results available in the literature, by means of static analyses of tapered isotropic, sandwich and corrugated structures.

- Chapter 10 summarises the contributions of this thesis along with future perspectives.

Chapters 3, 4 and 9 are the outcomes of the collaborative work done with my colleague Sergio Minera. More specifically, Sections 3.4, 3.5, 4.2, 4.3.2 and 9.2.3 are shared across our PhD theses.

CHAPTER 2

LITERATURE REVIEW

Consider a structure, referred to a Cartesian coordinate system (x,y,z), subjected to certain load and displacement boundary conditions. It can be defined by 15 unknown quantities, *i.e.* three displacement components (u_x, u_y, u_z), six strain components (ε_{xx}, ε_{yy}, ε_{zz}, ε_{yz}, ε_{xz}, ε_{xy}) and six stress components (σ_{xx}, σ_{yy}, σ_{zz}, σ_{yz}, σ_{xz}, σ_{xy}). There exists a unique equilibrium state, for a proper set of boundary condition, that can be determined by solving the six kinematic, six constitutive and three equilibrium equations of elasticity given as follows, for a structure deforming isothermally, linearly and statically,

$$\begin{aligned} &\text{Kinematics:} && \varepsilon_{ij} = \frac{1}{2}(u_{i,j} + u_{j,i}), \quad i,j = x,y,z, \\ &\text{Constitutive:} && \sigma_{ij} = C_{ijkl}\varepsilon_{kl}, \quad i,j,k,l = x,y,z, \\ &\text{Equilibrium:} && \sigma_{ij_{,j}} = 0, \quad i,j = x,y,z, \end{aligned} \tag{2.1}$$

where C_{ijkl} are the components of the fourth-order stiffness matrix and a subscript preceded by a comma denotes differentiation with respect to the corresponding spatial coordinate. Furthermore, the Einstein summation convention is implied over repeated indices. These governing field of equations, combined with the boundary conditions of essential or natural type, can be solved using three distinct approaches, namely displacement-based approach, stress-based approach and mixed approach, which are briefly described as follows.

In a displacement-based method, the governing equations are written in terms of the displacement field by eliminating stresses using kinematics and constitutive equation (2.1). Conversely, in a stress-based method, the governing equations are expressed in terms of stresses by taking the constitutive equation in terms of compliance matrix and substituting it in the kinematic equation. In a mixed formulation, the displacement and stress fields are solved simultaneously. Finding an exact solution to linear elasticity problems using any of the above method is difficult. There-

fore, the governing equations are solved using the variational principles of solid mechanics, *e.g.* Principle of Virtual Displacements (PVD), which is a powerful technique for finding approximate solutions to elasticity problems. Using this principle, some of the governing field equations are solved exactly, whereas other equations produce a residual. For instance, the commonly used displacement-based FEM, derived from the PVD, provides accurate displacement field predictions, but the stress computations are less reliable. This is due to the fact that the equilibrium and natural boundary conditions are only satisfied globally in an average sense. The accuracy of the solution is then improved by refining the kinematics (*i.e.* by increasing the mesh density in FEM). In contrast, when the stress-based method is employed, *i.e.* the stress computations are exact and the displacement fields obtained lacks accuracy. The mixed stress/displacement-based method overcomes these limitations and is widely adopted in the solid mechanics research community. In the present work, a displacement-based method is adopted, whose governing equations are solved using the PVD, and developed further for solving a wide range of structural mechanics problems.

The remainder of this chapter aims to provide a detailed review of the literature on displacement-based, classical and refined, structural theories that have received considerable attention throughout the last century and have led to an extensive corpus of work. The objective here is not to mention all papers and theories that have been published, rather it is to classify different formulations into groups and to discuss their merits and limitations. Furthermore, various numerical formulations developed for analysing straight-fibre and tow-steered composite laminates are reviewed. The chapter concludes with a review of the recent literature on nonlinear refined structural models and numerical tools for modelling curved and non-prismatic structures.

2.1 Refined Structural Theories

Analysis of the structural behaviour of slender bodies such as columns, blades, aircraft wings and bridges have been simplified by the development of beam models by reducing the three-dimensional problem to a set of variables dependent on the coordinate of the beam axis. This approach permits the use of one-dimensional (1D) structural elements that are simpler and computationally more efficient than two-dimensional (2D) (plate/shell) or three-dimensional (3D) (solid) elements. Structural theories that are fundamentally used to approximate 3D problems are either classified as asymptotic or axiomatic approaches [3] in which the 3D problem is sufficiently reduced to a 2D or 1D problem.

Classical axiomatic theories are sufficiently accurate for relatively slender beam structures (length to thickness ratio $L/t > 20$) but their accuracy is limited by Saint-Venant's principle, *i.e.* to regions remote from the boundary constraints, discontinuities and points of load application. Traditionally, the most popular axiomatic postulations use a purely displacement-based approach. These include, for instance, the classical theory of beams developed by Euler-Bernoulli [13] and Timoshenko [14, 15]—a comprehensive comparison of which can be found in [16]. The Euler-

Bernoulli beam model assumes a plane section remains plane after deformation, *i.e.* there is no distortion of the cross-section, and thus, it does not account for transverse shear deformations. The Timoshenko's beam model (TB) enhances the Euler-Bernoulli's beam (EB) model by applying the First Order Shear Deformation Theory (FSDT). In FSDT, the effect of shear deformation on the cross-section is captured in an average sense. It improves the global structural response predictions such as deflection, buckling and vibrational modes, but cannot predict non-classical effects such as warping, out-of-plane deformations, localised strains and stresses. Furthermore, FSDT is limited by its uniform transverse shear strain assumption, and therefore, shear correction factors are needed to adjust the constant through-thickness strain profile [17–19].

A considerable amount of work has been done by researchers to improve the global response of classical beam theories by introducing appropriate shear correction factors [20–22]. An extensive effort was made by Gruttmann and co-workers to compute shear correction factors for several structural cases [23–25]: torsional and flexural shearing stresses in prismatic beams; arbitrary shaped cross-sections; wide, thin-walled, and bridge-like structures. Determining the magnitude of these shear correction factors is not a straightforward task and various methods addressing such concerns have been published in the literature [18, 26, 27]. In this regard, an asymptotic power series expansion method for highly-orthotropic single-layers is proposed by Groh and Weaver [28].

In order to account for higher-order through-thickness distribution of transverse shear stresses, and to guarantee traction-free boundary conditions along the beam's longitudinal surface, several researchers introduced Higher-Order Shear Deformation Theory (HSDT). A pictorial represntation of the deformed geometries of an edge before and after deformation in various beam theories are shown in Figure 2.1. Some considerations of higher-order beam theories were made by Washizu [29]. Levinson [30] proposed a third-order displacement field for the axial deformation of a beam with a constant transverse displacement. Reddy [31] extended Levinson's theory to 2D problems and derived the governing equations using the Principle of Virtual Displacement. Both, Levinson [30] and Reddy [31], enforced the physical boundary conditions of vanishing transverse shear strains at the top and bottom surfaces. In doing so, the number of variable are reduced but the Euler-Bernoulli rotation (for 1D) or the Kirchhoff rotation (for 2D) was introduced into the in-plane displacement field approximation. This condition leads to a static inconsistency at clamped edges [28]. This method has been adopted by many researchers and a large number of shear shape functions, that approximates the parabolic distribution of the transverse shear strains, have been published ranging from polynomial and trigonometric, to hyperbolic and exponential.

The Saint-Venant solution [32] has been the theoretical base of many advanced beam models. An approach developed by Ladevèze and co-workers [33] reduces a three-dimensional (3D) model to a beam-like structure thereby simplifying the 3D elasticity equations. Using this method a beam model can be constructed as the sum of a Saint-Venant part and a residual, higher-order

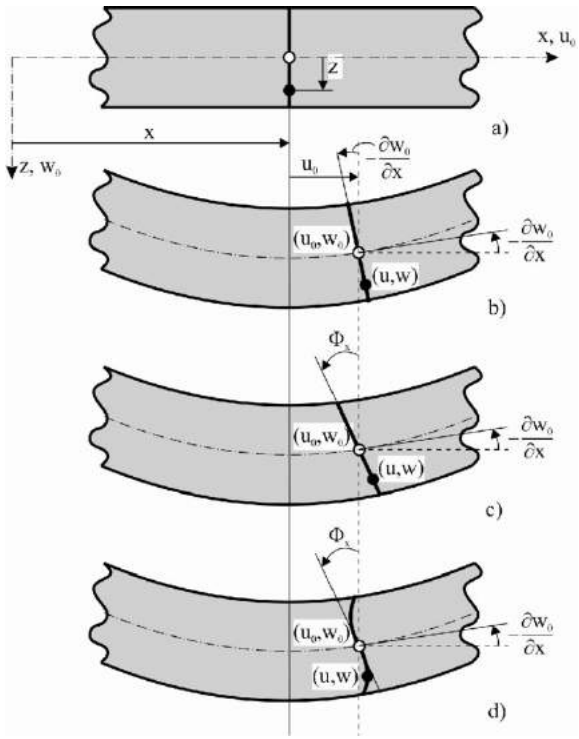

Figure 2.1: Undeformed and deformed geometries of an edge before and after deformation in the beam theories [2]: (a) undeformed; (b) Euler-Bernoulli; (c) Timoshenko (or FSDT); (d) HSDT.

part. In a following work, Ladevèze [34] used linear shape functions on beams with general cross-section and developed an exact beam theory for calculating 3D displacements and stresses. However, the theory is only applicable if one neglects localised effects that occur at extremities and geometric discontinuities. Other beam theories have been based on the displacement field proposed by Iesan [35] and solved by means of a semi-analytical finite element by Dong and co-workers [36, 37].

Another powerful tool to develop structural models is the asymptotic method. As for asymptotic approaches, approximation of the 3D problem is achieved through a perturbation parameter δ (thickness to length ratio) for which the solution of the equilibrium equations converges to the 3D solution in the limiting case, $\delta \to 0$. Applications to beam models have been exploited by Berdichevsky *et al.* [38, 39] in the framework of the Variational Asymptotic Method (VAM). Furthermore, Yu *et al.* [40, 41] recently developed the Variational Asymptotic Beam Sectional Analysis (VABS) by using VAM to separate the 3D elastic problem into a 2D linear problem in the cross-section and a 1D beam problem in the longitudinal direction. This strategy has the advantage of controlling the number of unknowns in the beam problem, leading to a computationally efficient solution. Despite this advantage, the general asymptotic approach suffers from a relatively poor convergence rate as the thickness increases [42]. Besides, extension of the general asymptotic method to multi-layered structures presents further difficulties due to the anisotropic

properties of multi-layered composites that can make through-thickness considerations important in otherwise geometrically thin structures.

Classical approaches have also been enhanced by the Generalized Beam Theory (GBT) for thin-walled structures, as given by Silvestre and Camotim [43], where transverse cross-sectional displacements are obtained from the axial ones. In GBT, in order to obtain a displacement representation compatible with classical beam theories, each component of displacement is expressed as a product of two single-variable functions—one depending on the longitudinal position along the reference axis and the other on cross-sectional coordinates. However, since thin plate assumptions are adopted [43], through-thickness strains are set to be zero and full 3D stress fields cannot be captured. Following on from early implementations of the GBT, many other high-order theories, based on enriched cross-section displacement fields, have been developed in order to describe effects that classical models cannot capture.

Of relevance to the present work, one of the most recent contributions to the development of refined beam theories is the Unified Formulation by Carrera and co-workers [44]. The Unified Formulation relies on the displacement-based version of the finite element method, which can handle arbitrary geometries as well as loading conditions. The formulation provides one-dimensional (beam) [45] and two-dimensional (plate and shell) [46] models that extend the classical approximations by exploiting a compact, hierarchical notation that allows most classic and recent formulations to be retrieved from one, hence *unified*, model. The governing field equations are formulated based on a generalised axiomatic expansion. Different order theories are easily implemented without the need for separately deriving new field equations. The displacement field is expressed over the cross-section (beam case) and through the thickness (plate and shell cases) by employing various expansion functions including Taylor polynomials [45], Lagrange polynomials [44], exponential and trigonometric functions [47], Chebyshev [48] and Legendre polynomials [49]. Amongst these, Taylor (TE) and Lagrange expansion (LE) models are most widely adopted. TE models are hierarchical and the degree of accuracy with which kinematic variables are captured is enriched by increasing the order of the cross-sectional expansion. On the other hand, LE models are based on cross-sectional discretisations using Lagrange elements of given kinematic order and refinement is obtained by increasing the mesh density, *i.e.* by increasing the number of Lagrange elements in the cross-section. This formulation accounts for classical and non-classical effects by increasing the order of the assumed fields without the need for further ad-hoc formulations. An extension of Carrera's Unified Formulation is the Generalized Unified Formulation (GUF) by Demasi [50, 51]. In GUF, each displacement variable is independently expanded along the thickness leading to a wide variety of new theories. Both the Unified Formulation models have been exploited majorly in the last decade for analysing a wide range of structures.

The available literature on the Unified Formulations shows the advanced capabilities of the model in solving a wide range of structural mechanics problems in a computationally efficient

manner[3, 44, 45, 49, 52, 53]. However, there are some key limitations associated with this model which are highlighted as follows. Taylor expansion based-Unified formulation models incur numerical instabilities when enriched to capture stresses near geometric discontinuities, such as corners, whilst Lagrange expansion models can have slow mesh convergence rates. Another known limitation of Carrera's Unified Formulation (CUF) is the oscillation of shear stresses along the beam axis that appears if the mesh along the beam length is not sufficiently fine. Furthermore, current implementations of the Unified Formulation model can account for prismatic structures only. Varying cross-section along the beam's longitudinal axis or modelling curved beam structures is not possible with its current version. In the present work, Carrera's Unified Formulation is adopted and is further developed by addressing the aforementioned limitations.

2.2 Modelling Laminated Composites

2.2.1 Straight-Fibre Composites

Multi-layered composite structures are widely used in engineering fields such as the automotive, aerospace, marine, sports and health sectors. The primary reasons are the high stiffness- and strength-to-weight ratios of these materials. Moreover, straight-fibre laminated composites allow designers to tailor properties through-thickness by varying the fibre orientation of the plies within the laminate and optimising the stacking sequence for structural performance. The increasing application of such structural members has stimulated interest in the development of tools for accurate stress predictions.

In modelling multi-layered composite and sandwich structures, major modeling challenges include: (i) predicting transverse shear and normal deformations occurring due to low orthotropy ratios (G_{13}/E_{11}) [12]; (ii) capturing the slope variation of the three displacement fields across the thickness due to transverse anisotropy, commonly known as the Zig-Zag (ZZ) effect [54]; and (iii) to account for the inter-laminar continuity (IC) of displacements and transverse stresses.

In this context, many efforts have been carried out over recent decades to accurately assess the response of laminated composites. The Euler-Bernoulli beam theory and Kirchhoff plate/shell models that support Classical Laminate Analysis (CLA) [55] are inaccurate for modelling moderately deep laminates with relatively low transverse shear modulus. The inaccuracy arising from transverse shear and normal strains across the laminate cross-section, as well as zig-zag effects in the displacement field approximation, being neglected. The FSDT [56] extends the kinematics of classical theories and captures the effect of transverse shear deformation in an average sense. However, for thick composite and sandwich laminates, FSDT is limited by its uniform transverse shear strain assumption [57]. Furthermore, piecewise-constant transverse shear stresses, predicted by FSDT, do not obey the continuity requirement at layer interfaces and do not disappear at the top and bottom surfaces. In both the theories, composite layers are

analyzed based on an equivalent single-layer description, which lacks the kinematic fidelity to accurately predict the 3D structural response of laminated composites. To overcome their deficiencies, over the years, several models based on HSDT have been proposed for the analysis of multi-layered composite beams [30, 58–60]. These models can be formally divided into two broad categories: discrete layer approximation theories based on Layer-Wise (LW) models and global approximation theories based on Equivalent Single-Layer (ESL) models.

Many researchers [46, 61, 62] have adopted LW approaches that assumes separate displacement field expansions for each material layer. This assumption allows for a correct representation of the strain field and an accurate determination of 3D stresses at the layer level. Swift and Heller [63] presented a layered Timoshenko beam theory for the general case of unsymmetrically stacked laminated beams. Seide [60] extended bending theory of laminated plates to include shearing deformation in each layer, and assumed constant shear strain in each layer of the laminate but different in each layer. Several layer-wise theories based on the piece-wise linearly varying in-plane displacements while a constant transverse displacement were developed [64–66]. Ferreira [67, 68] proposed a layerwise theory and the multiquadrics discretization method for static and vibration analysis of composite and sandwich plates. The linear displacement field assumption is adopted by most of the LW theories, which predicts constant interlaminar transverse strain and stress. To overcome this limitation, many LW higher-order theories have been proposed. Plagianakos and Saravanos [69] presented a higher-order theory by introducing quadratic and cubic interpolation functions into piece-wise linear displacement field in order to accurately predict the transverse interlaminar shear stresses in thick sandwich laminated composites. Cetkovic [70] assumed a quadratic function of transverse displacement with respect to the thickness coordinate while maintaining the linear expansion of the in-plane displacement field. Carrera's Unified Formulation with higher-order expansion functions is adopted in several studies for predicting the static and vibration behavior of doubly-curved laminated plates and shells [71, 72]. A recent overview of layer-wise theories for composite laminates and structures can be found in [73].

The LW models are able to satisfy both inter-laminar continuity and zig-zag requirements. However, the number of variables in the model scales with the number of layers in the laminate and thus, the added accuracy comes at greater computational cost. Therefore, with an aim to develop computationally efficient models for multi-layered composite structures, many researchers have proposed equivalent single-layer theory. The ESL theory condenses the laminate onto an equivalent single layer, such that the number of unknowns is independent of the number of layers. The major advantage of this theory is the significant reduction in the total number of mathematical variables and the required computational effort. Numerous theories based on the ESL concept have been proposed [60, 74, 75]. Reddy [58] proposed a third-order shear deformation theory for laminated plates, which provides a parabolic distribution of transverse shear stress through-thickness. Furthermore, to account for thickness stretching, *i.e.* transverse

normal deformation, generalized higher-order theories have been developed [59]. Kulikov and Plotnikova [76] developed four-noded curved equivalent single layer shell elements for the analysis of thin-walled composite structures. Arruda *et al.* [77] proposed Legendre polynomials as approximation functions, within Carrera's Unified Formulation using equivalent single layer model to study the deflection and strains of GFRP composite structures. For many applications, ESL theories provide an accurate description of the global laminate response. However, they are inadequate for capturing accurate three-dimensional ply-level stresses. This shortcoming is due to the displacement field approximation, which predicts continuous transverse strains across the interface of different material laminates. To overcome this deficiency, several attempts have been made to incorporate changes in the layerwise slopes of the in-plane displacements by employing ZZ functions.

Based on an historical review of the topic by Carrera [78], the ZZ theories can generally be divided into three groups:

- Lekhnitskii Multilayered Theory
- Ambartsumyan Multilayered Theory
- Reissner Multilayered Theory

Lekhnitskii [79] was the first to propose a ZZ theory formulated for multilayered beams. His work was later extended to the analysis of plates by Ren [80]. Ambartsumyan [81] developed a ZZ theory for orthotropic laminates which was later extended to symmetric laminates with off-axis plies by Whitney. The theory provided excellent results for global laminate behaviour when compared to the Pagano's 3D elasticity solutions. However, Whitney pointed out that the theory inaccurately predicts transverse shear stresses and fails to capture the large slope discontinuity at layer interfaces. Later, Reissner proposed a Mixed Variational Theorem (RMVT) for multilayered structures which led to variationally consistent equilibrium and constitutive equations. Murakami was the first to apply the RMVT and introduced two ZZ functions, called as the Murakami's Zig-Zag functions (MZZF), which is widely adopted by researchers. The MZZF is constructed by *a priori* assuming a periodic change of the displacement field slope at layer interfaces. Numerous studies [53, 82–85] available in the literature adopt the concept of enhancing the displacement field with MZZF and have shown significant improvement in the accuracy with a marginal increase in the computational cost with respect to classical ESL models. However, the MZZF fails to predict accurate ply-level stresses when employed for sandwich structures with large face-to-core stiffness ratios and thick laminates with arbitrary layup [86].

As an alternative, the Refined Zig-Zag Theory (RZT) developed by Tessler *et al*. [87, 88] can be used. The RZT accounts for layer-wise differences in transverse shear moduli, which are the properties that physically drive the ZZ effect. Here, the differences in transverse shear rigidities of each layer, and the average transverse shear rigidities of the entire layup, define the layer-wise ZZ slopes of the in-plane displacement fields. Recent works [86, 89, 90] have shown the

superiority of the RZT ZZ functions in capturing accurate ply level 3D stresses for straight-fibre laminated composites. Thus, an accurate choice of the ZZ function seems to be of paramount importance. The relative accuracies of the MZZF and the RZT ZZ function, employed with the Unified Formulation model, are compared further in Chapter 7.

Most of the LW and ESL theories available in the literature are displacement-based; meaning that the displacement components are the unknown variables, and all the strains and the stresses are derived from the displacement assumptions using the kinematic and constitutive relations, respectively. This, however, does not guarantee *a priori* the IC condition on transverse stresses. One way to overcome this limitation is to recover the transverse stresses by integration of the in-plane stresses in Cauchy's 3D stress equilibrium equations [91, 92]. Another possible solution is to use a mixed formulation, which posits a simultaneous assumption of displacement and stress fields. Many authors have proposed mixed formulations based on the Hu-Washizu (HW) principle [29], Hellinger-Reissner (HR) principle [93] and Reissner's Mixed Variational Theory (RMVT) [94, 95]. In this regard, Groh and Weaver [89] performed a detailed comparison between two mixed theories, namely HR and RMVT. The third-order refined zig-zag theory derived from the Hellinger-Reissner mixed variational statement (HR3-RZT) is shown to predict accurate 3D stresses for arbitrary straight-fibre laminates. Moreover, being an equivalent single layer theory, it is computationally efficient, as the number of unknown variables is independent of the number of layers considered. Despite the high level of accuracy and efficiency, this model cannot be used as a general analysis tool for industrial applications, due to its inability to model complex geometries and boundary conditions. In addition, the mixed displacement/stress-based models have denser stiffness matrices, unlike the commonly used displacement-based Finite Element (FE) formulations, where the stiffness matrix is sparse. While analysing large structures, the size and sparsity of the stiffness matrix are important factors that define the effort required in finding the solution. Furthermore, numerical issues may arise in a mixed formulation because the vector of unknowns contain displacements and stresses, which are of different orders of magnitude.

2.2.2 Tow-Steered Composites

The concept of steering fibres (tows) curvilinearly within individual laminae adds a further dimension to the tailoring capability of laminated composites and can improve structural performance without increasing weight. Hence, studies on so-called Variable Angle Tow (VAT) composites are gaining attention. VAT composites are also referred to as variable-stiffness composites [96], curvilinear fibre-reinforced composites [97] or variable-axial fibre-reinforced composites [98] in the literature.

The notion of tailoring the structural performance by steering the fibre paths spatially in the plane of a composite laminate was proposed in the early 1970s [99]. However, recent advancements in composite manufacturing technologies have facilitated the production of laminates with variable angle tows and this has spawned an increased interest in the topic. Compared

to constant-stiffness laminates (straight-fibre path), superior structural performance can be achieved for variable-stiffness laminates, where the in-plane stiffness varies spatially throughout the structure [100–103]. Previous works on VAT laminates have extensively demonstrated significant improvements in the stress distribution around holes [104, 105]. Hyer and Lee [102] studied variable stiffness composites with circular holes, by varying the fibre orientations on a region-by-region basis. Stress redistributions driven by tow-steering have been shown to substantially improve the compressive buckling limit of flat laminates [106, 107]. Wu *et al.* [107–109] solved the pre-buckling, buckling and initial post-buckling problems of flat VAT plates and developed a two-step optimisation framework to minimise the end-shortening strain in the post-buckling regime for a fixed compressive load. Hao *et al.* [110] proposed a bi-level optimisation framework to find the optimum design of variable-stiffness panels with multiple cutouts. On a component level, Stodieck *et al.* [111] have shown tow-steered laminates improve the aeroelastic behaviour of rectangular composite wings when compared to unidirectional laminates. Coburn *et al.* [112] proposed a semi-analytical method for the buckling analysis of blade-stiffened VAT panels and investigated the concept of using VAT to obtain greater buckling loads. Recently, Scott *et al.* [113] have shown variable stiffness blades improve the performance characteristics of wind turbine systems.

To date, most studies on VAT composites deal with global structural phenomena, *e.g.* vibration and buckling [102, 103, 114–118]. An extensive review of the literature can be found in [119]. With the increasing promise of VAT composites for structural design, there is also a need for developing accurate, yet computationally efficient, modelling techniques for predicting 3D stress fields. In general, predicting 3D stress fields accurately in composite structures is important as through-thickness damage, such as delaminations, is driven by transverse shear and transverse normal stresses. In VAT composites there are additional complexities because variations in material properties can lead to non-intutive and complex stress variations increasing the possibility of damage [120]. In addition, even though buckling is a global structural phenomenon, increases in the buckling load using variable fibre paths occur as a result of local stress redistributions. Capturing localised, three-dimensional stress fields accurately is therefore essential for safe design. However, relatively little work has been conducted in this direction. Whilst investigating VAT plates Akbarzadeh *et al.* [121] examined the effect of transverse shear deformation and embedded manufacturing defects on the structural responses. Akhavan and Ribeiro [122, 123] used a p-version finite element (FE) approach based on a Reddy-type third-order shear deformation theory to investigate the natural modes of vibration, the non-linear bending deflection, and the stresses. Díaz *et al.* [124] presented a numerical method for obtaining the interlaminar stresses in variable stiffness composite panels. Later, Groh and Weaver [28] showed that using Reddy-type models can lead to static inconsistencies at clamped boundaries. Recently, Soriano and Díaz [125] carried out three-dimensional FE analyses and introduced a continuum damage mechanics model to study their failure processes.

Most papers published on modelling VAT laminates use finely meshed FE models that can be computationally prohibitive for rapid design iterations. In this regard, several attempts have been made to develop computationally more efficient numerical models. Demasi *et al.* [126] formulated equivalent single-layer, zig-zag and layer-wise models based on the Generalised Unified Formulation (GUF) [127] and benchmarked the performance of the different approaches. However, the study mainly focused on highlighting the computational efficiency gains over 3D FE models. By validating relatively simple stacking sequences, the robustness of the approach in analysing arbitrary and complex lay-ups remains an open question. Tornabene *et al.* [128, 129] developed a structural model based on an equivalent single-layer approach for free vibration and linear static analysis of doubly-curved shells reinforced by curvilinear fibres. The Generalized Differential Quadrature (GDQ) method is employed to obtain the numerical solution. Groh and Weaver [11, 130] described a third-order zig-zag implementation within a Hellinger-Reissner mixed variational framework and use it to predict accurate 3D stresses for arbitrary VAT laminates. However, they observed discrepancies in the transverse normal stresses for some laminates when compared with 3D FE solutions. Resolving this disparity in transverse stress results is one of the motivations of the present study. Moreover, an important aspect of the present work, in contrast to published articles on VAT composites, is highlighting the effect of mathematical singularities present in the constitutive relations along the laminate. The presence of an absolute function in the fibre orientation distribution leads to discontinuities and is widely employed by many researchers. However, to the authors' knowledge, none of them discuss its implications on stress computation. Negative implications would arise if this singularity is not appropriately modelled. For instance, this could happen by employing the Differential Quadrature Method (DQM) whilst also modelling the VAT composite beam structure using a single continuous domain [131]. Furthermore, inaccuracies in transverse stress fields could arise if these stress fields are computed by employing a stress recovery technique (using Cauchy's 3D equilibrium equations) as adopted by Díaz *et al.* [124]. Overall, there is very little work in the literature regarding detailed analyses of full 3D stress fields in VAT composites and how these could be tailored to optimise structures for specific objectives. Hence, the present work (Chapters 6 and 7) aims to contribute in this field.

2.3 3D Stress Fields for Failure Prediction

Thin-walled and slender structures are extensively used in industries, where they are subjected to a variety of loads and are susceptible to complex nonlinear deformations. Reliable utilisation of such structures requires prior knowledge of their failure response. For instance, composite stiffened panels, commonly used in aerospace structures, can, in many cases, operate far beyond the buckling load and only fail deep into the postbuckling range [132]. In order to account for such failures, accurate prediction of the structural behaviour, including failure mechanisms, is

essential during, and possibly early into, the design phase. Having said that, accurate evaluation of stress fields becomes important.

In this regard, significant efforts have been made in the development of tools for predicting ply failure mechanisms under plane stress states [133–135]. However, using two-dimensional (2D) stress fields in conjunction with 2D failure theories may not result in accurate evaluation of the failure indices, and thus, three-dimensional (3D) stress states are required [136]. In general, predicting 3D stress fields accurately in composite structures is important as through-thickness damage, such as delamination, is driven by transverse shear and transverse normal stresses. Moreover, using 3D stress states in a consistent way, provides not only the prediction for the onset of ply damage, but also additional information regarding the type of failure and the orientation of the fracture plane [137, 138]. To this end, high-fidelity finite element methods (FEM) are often employed to obtain reliable 3D stresses with the desired level of accuracy [139]. However, using these models becomes prohibitively expensive, from a computational standpoint, whenever thin and/or multi-layered composite structures are to be analyzed. The problem is further exacerbated for the already costly geometrically nonlinear or transient analyses. The Unified Formulation models available in the literature are viable alternatives to 3D FEM for predicting 3D stress fields accurately in a computationally efficient manner. For instance, de Miguel *et al.* [140] performed failure evaluations using 3D stress fields determined by employing Lagrange expansions. The approach is shown to be computationally efficient compared to 3D Finite Element (FE) models and also computes accurate out-of-plane stress fields required for predicting the onset of delamination in multi-layered composites. However, their work [140] is limited to linear static analyses.

Many efforts have been carried out over recent decades with numerous numerical models being proposed to assess the nonlinear structural response of laminated composites [141–145], perhaps due to the computational cost and complexity, the reporting of fully 3D nonlinear stress analyses of laminates in the literature is rather limited. In recent works by Pagani and Carrera [146, 147], the Unified Formulation is extended to account for large deflections and postbuckling of solid and thin-walled laminated beam structures. Global/local deformations were investigated using Lagrange expansion functions in the cross-section. The model is limited to monoclinic material and is not suitable for analysing anisotropic material structures. More recently, in order to capture shear deformations and local cross-sectional warping, Hui *et al.* [148] proposed a geometrically nonlinear high-order kinematic model using hierarchical expansion functions (Taylor) in the cross-section. Although, the model predicts the displacement and stress fields accurately and efficiently, it is based on a plane-stress assumption, and therefore, cannot capture 3D stress fields. Moreover, more general limitations of using the Taylor-expansion-based Unified Formulation are highlighted in [149]. Therefore, there is a need for more efficient and accurate numerical model for which can predict full 3D stress state in the structure for subsequent failure and damage analysis.

2.4 Numerical Tools for Non-prismatic and Curved Structures

Static linear and non-linear analysis of non-prismatic and curved beams is of great importance, particularly in mechanical, civil and aerospace engineering applications. Many applications, such as aerospace and automotive, demand variable-thickness sandwich or tapered composite construction, for functional and/or aerodynamic reasons. Therefore, to design and use such structures, it is essential to accurately compute deflections and stresses. For slender and thin-walled structures, one-dimensional (1D) and two-dimensional (2D) finite element models are commonly employed due to their efficiency and accuracy. However, their accuracy may be limited to describing only the general overall behaviour, *e.g.* thin-shell formulations predicting only in-plane bending and stretching response, and recovering local features, such as through-thickness transverse stresses or displacement field gradients close to singularities, may not be possible. One way to approach the problem is to treat the structure as a three-dimensional (3D) continuum and utilise 3D equilibrium equations and associated point-wise boundary conditions to compute stresses and deflections. However, solving a 3D boundary value problem or employing a 3D finite element (FE) method is tedious and time consuming. Therefore, there is a need to develop a simplified mathematical model that is easy to use and able to capture the salient features of the displacement and stress fields in non-prismatic and curved beam structures.

Modelling of non-prismatic structural elements is a non trivial task in the design process. For instance, considering a statically-loaded non-prismatic beam behaving under the assumption of plane stress, then the most stressed cross-section generally does not coincide with the cross-section subjected to the maximal internal force [150]. Moreover, continuous variation of the beam's cross-section affects several aspects of the beam behaviour such as the cross-section stress distribution [151] and the beam's constitutive relation [152, 153]. Therefore, several attempts have been made by researchers in developing tools for investigating deflection and stresses in non-prismatic beams. Hodges *et al.* [154] proposed a variational asymptotic method (VAM) for recovering the stress, strain, and displacement fields for the linearly tapered isotropic beam. Trinh and Gan [155] presented an energy based FE method and derived new shape functions for a linearly tapered Timoshenko beam. Balduzzi *et al.* [9, 156] proposed a Timoshenko-like model for planar multilayer non-prismatic beams and solved the problem of the recovery of stress distribution within the cross-section of bi-symmetric tapered steel beams. Developing models for estimating stress distributions accurately in tapered laminated composite and sandwich structures is essential to predict failure initiation and propagation. Research on sandwich structures with a variable thickness has been conducted since the eighties [157–161]. Hoa *et al.* [162] investigated interlaminar stresses in tapered laminates using the 3D FE method. Jeon and Hong [163] investigated the bending behaviour of tapered sandwich plates constituting an orthotropic core of unidirectional linear thickness variation and two uniform anisotropic composite skins. The minimum total potential energy method was used to derive the governing equations and approximate solutions were obtained with the Ritz method. Recently, Ai and

Weaver [164] developed a nonlinear layer-wise sandwich beam model to capture the effects of a combination of geometric taper and variable stiffness of the core on the static response of a sandwich beam. In the model, the face sheets are assumed to behave as Euler beams and the core is modelled based on the first-order shear deformation theory.

Furthermore, over the last few decades, significant efforts have been made in the development of numerical tools for modelling curved beams. One of the earliest contributions was by Belytschko and Glaum [165], who extended their previous work on initially curved beams [166] and developed a nonlinear, higher-order, corotational FE formulation for analysing curved beams and arches. Surana and Sorem [167] developed a geometrically nonlinear framework for three-dimensional curved beam elements undergoing large rotations. A slightly different approach, using Reissner's beam theory, was proposed by Ibrahimbegović and Frey [168, 169], where a hierarchical three-dimensional curved beam element is used to mitigate the shear and membrane locking caused by lower-order elements. Petrov and Géradin [170] developed a finite element theory for initially curved and twisted beams based on the exact solutions for three-dimensional solids. Yu *et al.* [171] proposed a model for naturally curved anisotropic beams with thin-walled cross-sections. In their model, eigen functions are used as an expansion series to approximate the displacement field, allowing effects such as torsion and warping, to be described accurately. Recently, the differential quadrature technique [172–174] has received interest from researchers in analysis of curved beams. An extensive review on development of geometric nonlinear theory for the analysis of curved beams is well documented in a recently published review paper [175].

Despite many theories and models available for analysing tapered and curved structures, high-fidelity FE models are often employed in practices, as they offer increased freedom in modelling complex geometrical features. For instance, modelling a wind turbine blade, which involves geometrical features such as variable section, curvature, taper and twist, is straightforward with the FE method. However, the computational expense associated with the 3D FE technique makes it less attractive, and therefore, analysts end up approximating the solution by employing 1D or 2D models. As an alternative to 3D FE analysis, the Unified Formulation approach (developed by Carrera and coworkers [3, 45]) is becoming increasingly popular. In recent years, several research papers have been published on the Unified Formulation framework to study linear and non-linear deflection [44, 147–149, 176], 3D stress fields [149, 177, 178], failure and damage mechanics [140, 179], free vibration [52, 180], buckling and post-buckling behaviour [146, 181] of metallic and composite structures. However, the existing modelling capabilities are largely limited to prismatic structures, and therefore, are not appropriate for analysing complex, real-life, geometrical configurations. With the classical Unified Formulation, modelling tapered beam structures is possible if the beam's width is treated as the longitudinal axis and the tapered plane as its cross-section [182, 183]. However, this approach is clearly a workaround. Furthermore, in a recent work, curved-beam structures are analysed with the classical Unified Formulation using the Frenet-Serret description [184]. The model has a couple of limitations: (i) the cross-sectional

shape and size cannot vary along the beam direction, (ii) it requires the exact description of the curved line defining the beam's axis.

In Chapter 9, a new methodology within the Unified Formulation framework is proposed which solves above mentioned limitations.

CHAPTER 3

SERENDIPITY LAGRANGE EXPANSIONS-BASED UNIFIED FORMULATION MODEL

Simple analytical and 1D FE models are widely employed by practising engineers for the stress analysis of beam structures, because of their simplicity and acceptable levels of accuracy. However, the validity of these models is limited by assumptions of material heterogeneity, geometric dimensions and slenderness, and by Saint-Venant's Principle, *i.e.* they are only applicable to regions remote from boundary constraints, discontinuities and points of load application. To predict accurate stress fields in these locations, computationally expensive 3D FE analyses are routinely performed. Alternatively, displacement-based high-order beam models are often employed to capture localised 3D stress fields. A promising approach towards this end is the Unified Formulation (UF) by Carrera and co-workers which relies on a displacement-based formulation of the finite element method, described in Sections 3.1 and 3.2, and is able to recover complex, 3D stress fields in a computationally efficient manner. The formulation provides 1D (beam) models [45] that extend the classical approximations by exploiting a compact, hierarchical notation and allows most classic and recent formulations to be retrieved from one, hence *unified*, model. The displacement field is expressed over the cross-section by employing various expansion functions including Taylor, Lagrange, exponential, trigonometric, Chebyshev and Legendre polynomials as described in the previous chapter. Amongst these, Taylor (TE) and Lagrange expansion (LE) models are most widely adopted. TE models are hierarchical and the degree of accuracy with which kinematic variables are captured is enriched by increasing the order of the cross-sectional expansion. On the other hand, LE models are based on cross-sectional discretisations using Lagrange elements of given kinematic order and refinement is obtained by increasing the mesh density, *i.e.* by increasing the number of Lagrange elements in the cross-section. Both models are found to be accurate and computationally efficient, but

have limitations. Namely, TE models incur numerical instabilities when enriched to capture stresses near geometric discontinuities, such as corners, whilst LE models can have slow mesh convergence rates.

Another known limitation of Carrera's Unified Formulation is the oscillation of shear stresses along the beam axis that appears if the mesh along the beam length is not sufficiently fine. To this end, we propose collocating beam nodes towards the boundaries using Chebyshev biased grids, as described in Section 3.3, which reduces problematic oscillations in numerical solutions (the Runge effect) [185]. Furthermore, in this chapter, we present a new approach for the analysis of beam-like structures that overcome all of the above limitations of TE and LE models. The approach is based on the UF and, as a novelty, hierarchical Lagrange polynomials are used to define cross-sectional displacement fields. This new element class, called *Serendipity Lagrange expansion* (SLE), is based on the Trunk (or Serendipity) Space which is a polynomial space spanned by the set of monomials $\alpha^i \beta^j$, $i,j = 0,1,2,\ldots,N$, where N is the order of the polynomial [4]. SLE model combines two of the main features of TE and LE models, *i.e.* they are hierarchical and facilitate numerically stable cross-sectional refinements via remeshing. Section 3.4 provides an overview of TE and LE models and details of the derivation of the new SLE model. The cross-section modelling capabilities are further enhanced by introducing a two-dimensional mapping technique, as discussed in Section 3.5, to model beams with curved cross-sections. Furthermore, Section 3.6 introduces Node-Dependent Kinematics (NDK) within the Unified Formulation framework which allows variable kinematic description to be defined at each beam node. With this methodology, high-order expansion functions are employed at desired regions, such as near the boundaries, discontinuities and points of load application, while low-order expansion functions are used elsewhere in the structure.

3.1 Finite Element Formulation

The Unified Formulation relies on a displacement-based version of the finite element method. The advantage of a finite element discretisation is that arbitrary geometries and boundary conditions can readily be modelled. The fundamental equations are summarised here for completeness and clarity of exposition.

Let us consider an elastic continuum of volume V, embedded in $\mathbb{R}^3$. In a finite element setting, the volume is discretised into a series of N-noded subdomains (the elements), so that displacement fields of the form

$$\boldsymbol{U}(x,y,z) = \begin{bmatrix} u(x,y,z) \\ v(x,y,z) \\ w(x,y,z) \end{bmatrix}$$

can be approximated element-wise by means of local shape functions, N_i, and generalised nodal

displacements, $\boldsymbol{u}_i^\top = \{u_i, v_i, w_i\}$, such that

$$\boldsymbol{U}^{(\mathrm{e})}(x,y,z) = N_i(x,y,z)\,\boldsymbol{u}_i, \qquad \text{with} \qquad i = 1,\ldots,N. \tag{3.1}$$

In the previous expression and throughout remainder of this chapter, the Einstein summation convention is implied over repeated indices.

As per the classical theory of elasticity, the stress and strain tensors can be expressed by six-term vectors as

$$\boldsymbol{\sigma}^\top = \left\{\sigma_{xx}, \sigma_{yy}, \sigma_{zz}, \tau_{yz}, \tau_{xz}, \tau_{xy}\right\},$$
$$\boldsymbol{\varepsilon}^\top = \left\{\varepsilon_{xx}, \varepsilon_{yy}, \varepsilon_{zz}, \gamma_{yz}, \gamma_{xz}, \gamma_{xy}\right\}.$$

These tensors are related through the material's stiffness matrix $\bar{\boldsymbol{C}}$ by Hooke's law, stating that

$$\boldsymbol{\sigma} = \bar{\boldsymbol{C}}\boldsymbol{\varepsilon}. \tag{3.2}$$

For an explicit definition of the coefficients in $\bar{\boldsymbol{C}}$, the reader is referred to Appendix A.

Using equation (3.1), the strain-displacement relationship in its linear form may be recast as

$$\boldsymbol{\varepsilon} = \mathscr{B}_i \boldsymbol{u}_i, \tag{3.3}$$

where

$$\mathscr{B}_i = \begin{bmatrix} \frac{\partial N_i}{\partial x} & 0 & 0 \\ 0 & \frac{\partial N_i}{\partial y} & 0 \\ 0 & 0 & \frac{\partial N_i}{\partial z} \\ 0 & \frac{\partial N_i}{\partial z} & \frac{\partial N_i}{\partial y} \\ \frac{\partial N_i}{\partial z} & 0 & \frac{\partial N_i}{\partial x} \\ \frac{\partial N_i}{\partial y} & \frac{\partial N_i}{\partial x} & 0 \end{bmatrix}.$$

Elastic equilibrium is enforced via the Principle of Virtual Displacements, which, in a quasi-static setting, states that

$$\delta W_{\mathrm{int}} = \delta W_{\mathrm{ext}}, \tag{3.4}$$

where W_{int} and W_{ext} are the internal and external works, respectively, and δ denotes virtual variation with respect to displacements.

By definition, the internal work is the work done by stresses over corresponding virtual strains. Noting that $W_{\mathrm{int}} = \sum_{\mathrm{e}} W_{\mathrm{int}}^{(\mathrm{e})}$ and letting $V^{(\mathrm{e})}$ be the volume of the generic element

$$\delta W_{\mathrm{int}}^{(\mathrm{e})} = \int_{V^{(\mathrm{e})}} \delta\boldsymbol{\varepsilon}^\top \boldsymbol{\sigma}\, dV, \tag{3.5}$$

where[2]

$$\begin{aligned} \delta\boldsymbol{\varepsilon} &= \delta\left[\mathscr{B}_j \boldsymbol{u}_j\right] \\ &= \mathscr{B}_j \delta\boldsymbol{u}_j. \end{aligned} \tag{3.6}$$

[2]Note the change of subscript for consistent summations using Einstein notation.

Substituting equations (3.2) and (7.14) into equation (8.11),

$$\begin{aligned}\delta W_{\text{int}}^{(e)} &= \int_{V^{(e)}} \delta\boldsymbol{\varepsilon}^{\top}\boldsymbol{\sigma}\, dV \\ &= \int_{V^{(e)}} \delta\boldsymbol{\varepsilon}^{\top}\boldsymbol{C}\boldsymbol{\varepsilon}\, dV \\ &= \int_{V^{(e)}} \delta\boldsymbol{u}_j^{\top}\mathscr{B}_j^{\top}\boldsymbol{C}\mathscr{B}_i\boldsymbol{u}_i\, dV \\ &= \delta\boldsymbol{u}_j^{\top}\left(\int_{V^{(e)}} \mathscr{B}_j^{\top}\boldsymbol{C}\mathscr{B}_i\, dV\right)\boldsymbol{u}_i \\ &= \delta\boldsymbol{u}_j^{\top}\boldsymbol{K}_{ij}^{(e)}\boldsymbol{u}_i.\end{aligned} \tag{3.7}$$

If we now denote body forces per unit volume as $\boldsymbol{g}$, surface forces per unit area as $\boldsymbol{p}$, line forces per unit length as $\boldsymbol{q}$ and concentrated forces acting on Q as $\boldsymbol{P}$, the external work is

$$-\delta W_{\text{ext}}^{(e)} = \int_{V^{(e)}} \delta\boldsymbol{u}^{\top}\boldsymbol{g}\, dV + \int_S \delta\boldsymbol{u}^{\top}\boldsymbol{p}\, dS + \int_l \delta\boldsymbol{u}^{\top}\boldsymbol{q}\, dl + \delta\boldsymbol{u}^{\top}|_Q\boldsymbol{P}. \tag{3.8}$$

Recasting equation (3.8) as $-\delta W_{\text{ext}}^{(e)} = \delta\boldsymbol{u}^{\top}\boldsymbol{f}^{(e)}$ and substituting equation (8.12) into equation (7.11) we get

$$\delta\boldsymbol{u}_j^{\top}\boldsymbol{K}_{ij}^{(e)}\boldsymbol{u}_i = \delta\boldsymbol{u}_j^{\top}\boldsymbol{f}^{(e)}, \tag{3.9}$$

which is a statement of elastic equilibrium in weak form, where $\boldsymbol{K}_{ij}^{(e)}$ and $\boldsymbol{f}^{(e)}$ are, respectively, the structural stiffness matrix and the generalised load vector of the generic element.

3.2 One-dimensional Unified Formulation

A typical way to overcome the limitations of classical beam models and to refine the structural analyses that employ them is to enrich the kinematics of the approximated displacement field. The use of Taylor expansions, for instance, is common to many theories where high-order terms are included to enrich the kinematic approximation. In general, the higher the order, the higher the computational effort required. One of the advantages of the Unified Formulation is that, owing to the notation adopted, beam models of increasing kinematic refinement are readily developed.

In the UF framework, a 3D structure is discretised with a finite number of transverse planes running along the longitudinal axis of the structure as shown in Figure 3.1. For simplicity, the structure's longitudinal axis can be thought of as a beam and the transverse planes as its cross-sections. Let us consider a beam-like structure as shown in Figure 3.2, where the beam extends along the y-axis and cross-sections lie in the xz-plane. The beam is discretised with traditional 1D finite elements and the cross-sectional deformations are approximated using different expansions as explained in Section 3.4. Mathematically, this means that the displacement field and its virtual variations may be written as a product of two functions: cross-sectional expansion functions, $F(x,z)$, and 1D Lagrange shape functions, $N(y)$, along the beam axis. In principle, these functions

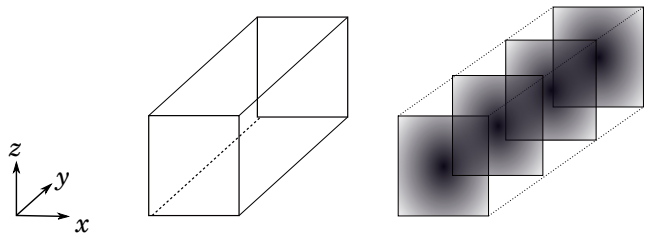

Figure 3.1: Unified Formulation framework - 3D structure discretisation.

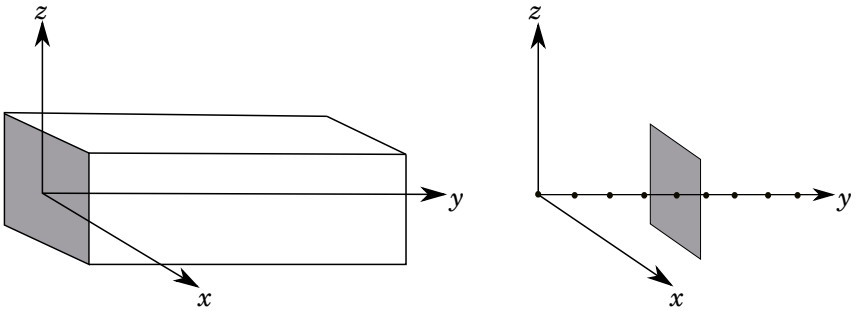

Figure 3.2: Unified Formulation reference system - Axis orientation and beam nodes.

can have as many terms as desired. The more terms there are, the richer the kinematics. With reference to equation (3.1),

$$\begin{aligned} \boldsymbol{U}^{(\mathrm{e})} &= F_\tau(x,z)N_i(y)\,\boldsymbol{u}_{i\tau}, \\ \delta\boldsymbol{U}^{(\mathrm{e})} &= F_s(x,z)N_j(y)\,\delta\boldsymbol{u}_{js}, \end{aligned} \qquad \text{with} \quad \tau,s = 1,...,M \quad \text{and} \quad i,j = 1,...,N_\mathrm{e} \tag{3.10}$$

where M is the number of terms in the cross-sectional expansion depending on the order; N_e is the number of Lagrange nodes within each element along the beam; and $\boldsymbol{u}_{i\tau}$ and $\boldsymbol{u}_{js}$ are generalized displacement vectors. For the sake of clarity, it is important to stress that the cross-sectional mesh captures the warping of the cross-section with one set of 2D shape functions, $F(x,z)$, while the axial behaviour is modelled by a separate 1D mesh with an independent set of 1D shape functions, $N(y)$. This approach differentiates the method from classic 3D FE method, where 3D shape functions are used over volumetric brick or tetrahedral elements that offer no separation of cross-sectional and axial deformations. Moreover, the current methodology overcomes the limitation on the aspect ratio of a 3D brick element in FE analysis by decoupling the shape functions along the longitudinal axis and across the transverse plane.

Substituting equation (3.10) into equation (3.5) and following the steps as shown in equation (3.7) gives

$$\begin{aligned} \delta W^{(\mathrm{e})}_{\mathrm{int}} &= \delta\boldsymbol{u}^\top_{js}\left(\int_{V^{(\mathrm{e})}} \mathfrak{B}^\top_{js}\boldsymbol{C}\mathfrak{B}_{i\tau}\,dV\right)\boldsymbol{u}_{i\tau}, \\ &= \delta\boldsymbol{u}^\top_{js}\boldsymbol{K}^{\tau sij}_{(\mathrm{e})}\boldsymbol{u}_{i\tau}, \end{aligned} \tag{3.11}$$

where

$$\mathfrak{B}_{i\tau} = \begin{bmatrix} \frac{\partial N_i F_\tau}{\partial x} & 0 & 0 \\ 0 & \frac{\partial N_i F_\tau}{\partial y} & 0 \\ 0 & 0 & \frac{\partial N_i F_\tau}{\partial z} \\ 0 & \frac{\partial N_i F_\tau}{\partial z} & \frac{\partial N_i F_\tau}{\partial y} \\ \frac{\partial N_i F_\tau}{\partial z} & 0 & \frac{\partial N_i F_\tau}{\partial x} \\ \frac{\partial N_i F_\tau}{\partial y} & \frac{\partial N_i F_\tau}{\partial x} & 0 \end{bmatrix},$$

and substituting equation (3.10) into equation (3.8) gives

$$-\delta W_{\text{ext}}^{(\text{e})} = \delta \boldsymbol{u}_{js}^{\top} \boldsymbol{f}^{(\text{e})}. \tag{3.12}$$

Finally, equating internal and external work

$$\delta \boldsymbol{u}_{js}^{\top} \boldsymbol{K}_{(\text{e})}^{\tau s i j} \boldsymbol{u}_{i\tau} = \delta \boldsymbol{u}_{js}^{\top} \boldsymbol{f}^{(\text{e})}, \tag{3.13}$$

which is a statement of elastic equilibrium in weak form in the UF notation. The term $\boldsymbol{K}_{(\text{e})}^{\tau s i j}$ is referred to as the elemental stiffness matrix. For a specific set of values of i, j, τ and s, $\int_{V^{(\text{e})}} \mathfrak{B}_{js}^{\top} \boldsymbol{C} \mathfrak{B}_{i\tau}\, dV$ becomes equal to $\boldsymbol{K}^{\tau s i j}$, which is a (3×3) matrix referred as the *Fundamental Nucleus* of the stiffness matrix. Its explicit form can be found in Appendix B.

The UF makes the assembly of the matrices a trivial operation that can be easily implemented in a computer code. Fundamental Nuclei obtained, by using four loops on indices i, j, τ and s, are assembled to build an elemental stiffness matrix [3]. The elemental stiffness matrices are further assembled in a global stiffness matrix following the standard FE procedure, as depicted in Figure 3.3. The resulting equation, $\boldsymbol{K}\boldsymbol{u} = \boldsymbol{f}$ is then solved to find the generalised displacements.

In the UF, the choice of F_τ and M is arbitrary. In the literature, different kinds of expansion functions have been used, including Taylor, Lagrange, Legendre, exponential trigonometric and Chebyshev polynomials [44, 47–49, 186]. In this work, as a novelty, we introduce and adopt Serendipity Lagrange expansions, which are described in Section 3.4, together with more traditional models for comparison.

3.3 Chebyshev-Biased Node Distribution

1D UF models can lead to inaccurate prediction of shear stresses near the boundaries. For instance, considering a cantilever beam, shear stress oscillations may be observed along the axis near the fixed support. One way to overcome this problem is to increase the number of beam elements or to use a high-order expansion in the longitudinal direction. Both choices can significantly increase the number of unknowns required for convergence. These mesh-dependent stress oscillations are of numerical nature and are detrimental to the objective we set out to achieve, *i.e.* performing detailed, yet inexpensive, stress analyses around localised features in beam-like structures. To solve this issue, we propose a simple, yet effective, approach to

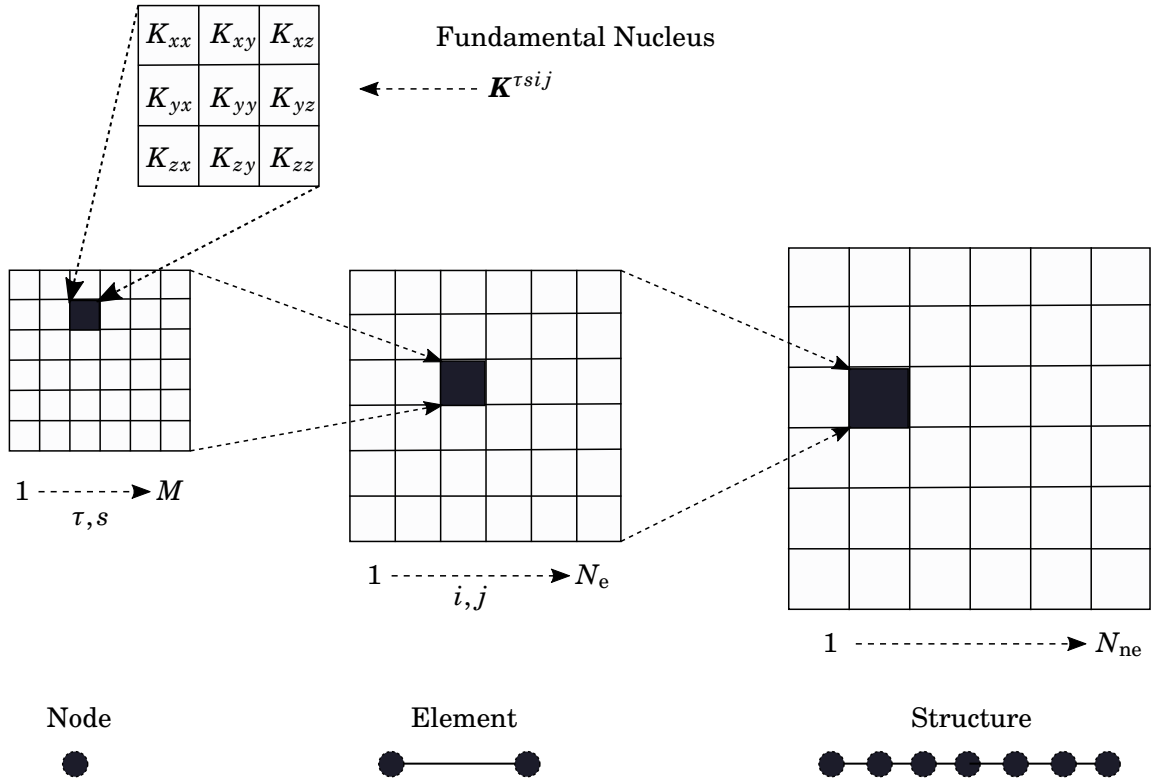

Figure 3.3: Unified Formulation: global stiffness matrix assembly procedure [3].

redistribute the nodes with a bias towards boundaries and features. Namely, the nodes are distributed using a Chebyshev biased mesh.

Chebyshev polynomials are known to give better convergence criteria and minimise Runge phenomena [187]. These polynomials of the first kind of order n, denoted as $T_n(y) \in [-1,1]$, are a set of orthogonal functions defined as the solutions to the Chebyshev differential equation. They are related to Legendre and Jacobi Polynomials [188, 189] and may be defined using a series expansion:

$$T_n(y) = \frac{n}{2} \sum_{i=0}^{\lfloor \frac{n}{2} \rfloor} \binom{n}{2i} y^{n-2i} \left(y^2 - 1\right)^i . \tag{3.14}$$

Chebyshev meshes are defined using the set of zeros of equation (3.14) in $[-1,1]$, i.e.

$$y_k = \cos\left(\frac{2k-1}{2n}\pi\right), \qquad k = 1, \ldots, n, \tag{3.15}$$

which can be mapped in $[0, L]$ as follows:

$$y_k = \frac{L}{2} - \frac{L}{2}\cos\left(\frac{2k-1}{2n}\pi\right). \tag{3.16}$$

As ahown in Figure 3.4, we use y_k to place n nodes along the length L of the beam. Consequently, the nodes are positioned more compactly towards boundaries.

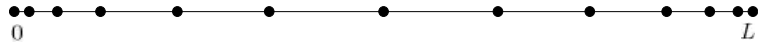

Figure 3.4: Sample Chebyshev grid in $[0, L]$.

3.4 Cross-Sectional Expansion Models

As mentioned in Section 3.2, in the Unified formulation, cross-sectional expansion functions can be chosen arbitrarily. That said, the most widely adopted expansions are based on Taylor and Lagrange polynomials. These two types of functions are used in fundamentally different ways, with profound implications on some computational and numerical aspects of the implementation.

3.4.1 Taylor Expansion Model

In Taylor expansion models, the cross-sectional displacement field at the i^{th} Lagrange beam node is expressed with complete, Taylor polynomials containing terms of the form $F_\tau = x^n z^m$. For example, a second-order expansion ($N = 2$) has constant, linear and quadratic terms as follows

$$\boldsymbol{u}_i = \{u_{x_i}, u_{y_i}, u_{z_i}\}^T = \boldsymbol{u}_{i1} + x\boldsymbol{u}_{i2} + z\boldsymbol{u}_{i3} + x^2\boldsymbol{u}_{i4} + xz\boldsymbol{u}_{i5} + z^2\boldsymbol{u}_{i6}, \tag{3.17}$$

where the terms $\boldsymbol{u}_{i\tau}^{\mathrm{T}} = \left\{u_{x_{i\tau}}, u_{y_{i\tau}}, u_{z_{i\tau}}\right\}$ on the right hand side are unknown variables to be determined. High-order models, *i.e.* models with high-order kinematics, can be obtained by enriching the polynomial expansion. The reader is referred to [3] for a more detailed treatment of TE models.

3.4.2 Lagrange Expansion Model

In Lagrange expansion models, beam elements are further discretised by dividing cross-sections into a number of local sub-domains. Two-dimensional (2D) Lagrange polynomials are used as expansion functions over the sub-domains. The order of the Lagrange polynomials spanning each sub-domain depends on the number of computational nodes therein. For instance, a 9-noded Lagrange type element (L9) is spanned by quadratic expansions so that the displacement field at the i^{th} beam node becomes

$$\boldsymbol{u}_i = F_1\boldsymbol{u}_{i1} + F_2\boldsymbol{u}_{i2} + F_3\boldsymbol{u}_{i3} + F_4\boldsymbol{u}_{i4} + F_5\boldsymbol{u}_{i5} + F_6\boldsymbol{u}_{i6} + F_7\boldsymbol{u}_{i7} + F_8\boldsymbol{u}_{i8} + F_9\boldsymbol{u}_{i9}, \tag{3.18}$$

where the expansion functions, F_τ, are 2D Lagrange polynomials and the terms $\boldsymbol{u}_{i\tau}$ on the right hand side are unknown variables. Unlike in TE models, these global unknowns are pure displacement components at the computational nodes defined across the sub-domains. Refined model accuracy is obtained by increasing the number of sub-domains or the number of nodes therein, or in other words, by increasing the cross-sectional mesh density. A more detailed description of LE models can be found in [186].

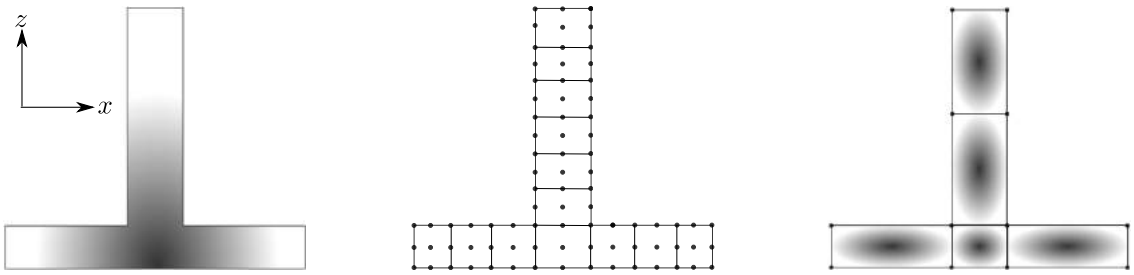

Figure 3.5: Typical cross-sectional discretisation for: (a) Taylor expansions (hierarchical); (b) Lagrange expansions (node-based); (c) Serendipity Lagrange expansions (hierarchical and node-based). Grey shading indicates hierarchical shape functions over the section or section sub-domain.

3.4.3 Numerical Integration over Unified Formulation Elements

Sections 3.4.1 and 3.4.2 highlight one of the fundamental differences between TE models and LE models. Taylor expansions are defined to span cross-sections starting from the origin of xz-planes along the y-axis. Lagrange expansions are defined on quadrilateral sub-domains. This difference is illustrated graphically in Figures 3.5(a) and 3.5(b).

In practical terms, the fact that Lagrange expansions are defined on cross-sectional sub-domains implies that an additional mapping is required for integrations over $V^{(e)}$. To clarify, like traditional beam elements, N-noded CUF elements based on Taylor expansions are obtained through integration of $\int_{V^{(e)}} \mathscr{B}_j^\top \boldsymbol{C} \mathscr{B}_i \, dV$ over a master element defined in $\eta \in [-1,1]$, which is then mapped onto $(x,y,z) \in [x_1^{(e)}, x_N^{(e)}] \times [y_1^{(e)}, y_N^{(e)}] \times [z_1^{(e)}, z_N^{(e)}]$, *i.e.* the element position in global coordinates. An identical operation is required, for elements based on Lagrange expansions, to integrate $\int_{V^{(e)}} \mathfrak{B}_{js}^\top \boldsymbol{C} \mathfrak{B}_{i\tau} \, dV$, however an additional mapping is required to link physical sub-domains in cross-sectional xz-planes to the master computational domain $(\alpha,\beta) \in [-1,1] \times [-1,1]$. A visual representation of this two-dimensional map is given in Figure 3.6.

Throughout this work, cross-sectional sub-domains defined in (x,z) are mapped and interpolated using linear Lagrange polynomials, F_k, as

$$x = F_k x_k, \quad z = F_k z_k, \qquad \text{with} \quad k = 1,\ldots,4 \tag{3.19}$$

where (x,z) is the mapped coordinate and (x_k,z_k) are the physical coordinates of the nodes of the generic quadrilateral sub-domain. As customary, by using equation (3.19) one can compute the Jacobian of the transformation, which is required for integrals oven the master domain.

3.4.4 Serendipity Lagrange Expansion Model

In TE models, it is straightforward to enrich the displacement field by choosing higher order expansions. On the other hand, in LE models, the displacement field is enriched by increasing the

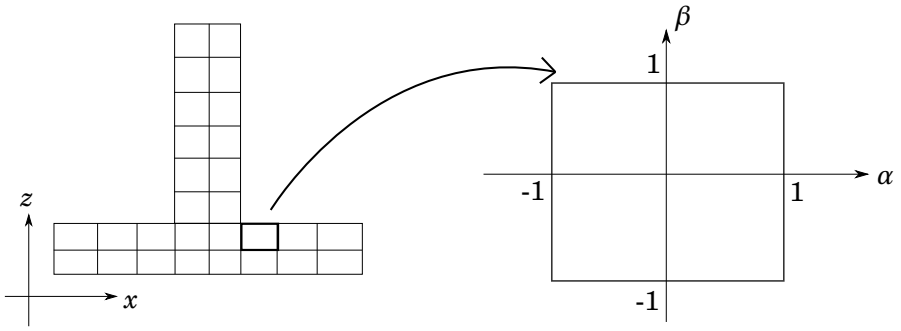

Figure 3.6: Schematic depiction of the mapping from physical cross-sectional sub-domains to computational master reference system.

number of nodes in the beam cross-section. In choosing TEs over LEs one trades-off numerical stability for ease of refinement, *i.e.* no need for remeshing. We now introduce alternative expansion functions, based on hierarchical *Serendipity Lagrange* polynomials, that eliminate this duality. Adopting this expansion model, cross-sections are discretised using four-noded Lagrange sub-domains. In addition, and as a novelty, the displacement field within sub-domains can be enriched by increasing the order of the local Serendipity Lagrange expansion as depicted in Figure 3.5(c), where the shading indicates enrichment hierarchy. The proposed expansion model is based on the hierarchical finite element shape functions as derived from Trunk (or Serendipity) polynomial spaces in [4].

In order to build the new expansion functions, a set of 1D polynomials and a set of 2D polynomials are required. These polynomials are combined and used as expansion functions for the displacement field within the computational sub-domains. Enrichment of the model kinematics can then be achieved by increasing the expansion order and/or the number of nodes in the cross-section, which will be shown to be tantamount to combining the benefits of TE and LE models, whilst also eliminating their limitations.

3.4.4.1 1D Lagrange-type Polynomials

In this section, we introduce the 1D polynomials used to build the 2D Serendipity Lagrange expansions.

Let us consider the set $\Xi^{1D} = \{\xi \in \mathbb{R} : -1 \leq \xi \leq 1\}$ and let $N \geq 2$ be the number of equally spaced points ξ_i within Ξ^{1D}.[3] Starting at $\xi = -1$,

$$\xi_i = -1 + \frac{2}{(N-1)}(i-1), \qquad \text{where} \qquad i = 1,\ldots,N. \tag{3.20}$$

[3]By construction N will also be the order of the polynomial.

An N^{th}-order polynomial, $p_N(\xi)$, can be found such that

$$\begin{aligned} p_N(-1) &= 0, \\ p_N(1) &= 0, \\ p_N(\xi_i) &= 0. \end{aligned} \tag{3.21}$$

The explicit form of this polynomial is

$$p_N(\xi) = (\xi - \xi_1)(\xi - \xi_2)\cdots(\xi - \xi_{N-1})(\xi - \xi_N), \tag{3.22}$$

such that, for instance,

$$\begin{aligned} p_2(\xi) &= (\xi + 1)(\xi - 1), \\ p_3(\xi) &= (\xi + 1)\xi(\xi - 1), \\ p_4(\xi) &= (\xi + 1)(\xi + \tfrac{1}{3})(\xi - \tfrac{1}{3})(\xi - 1), \\ p_5(\xi) &= (\xi + 1)(\xi + \tfrac{1}{2})\xi(\xi - \tfrac{1}{2})(\xi - 1), \\ p_6(\xi) &= (\xi + 1)(\xi + \tfrac{3}{5})(\xi + \tfrac{1}{5})(\xi - \tfrac{1}{5})(\xi - \tfrac{3}{5})(\xi - 1), \\ p_7(\xi) &= (\xi + 1)(\xi + \tfrac{2}{3})(\xi + \tfrac{1}{3})\xi(\xi - \tfrac{1}{3})(\xi - \tfrac{2}{3})(\xi - 1). \end{aligned} \tag{3.23}$$

Traditional Lagrange polynomials can readily be derived from (3.22), for details see [185, 189].

We note that the property of vanishing values on the boundary of Ξ^{1D} is essential to ensure continuity of the displacement field at the interfaces between cross-sectional sub-domains, which in turn allows for the formulation of hierarchical shape functions.

3.4.4.2 2D Lagrange-type Polynomials

Polynomials of the family $p_N(\xi)$ can be used to define their N^{th}-order 2D counterparts in $\Xi^{2D} = \{(\alpha, \beta) \in \mathbb{R}^2 : -1 \leq \alpha \leq 1, -1 \leq \beta \leq 1\}$. These 2D polynomials are to be employed as hierarchical Lagrange-type shape functions. With this aim in mind, we need three different sets of functions, each with specific requirements:

1. A set of four first-order Lagrange polynomials. These are bi-linear polynomials that take value 1 at each of the four nodes and 0 on the others. These are named polynomials of type I.

2. A set of N^{th}-order polynomials that vanish along three sides of Ξ^{2D} in order to satisfy the continuity of displacements across cross-sectional sub-domains. These are named polynomials of type IIA and IIB.

3. A set of N^{th}-order polynomials defined in the interior subset of Ξ^{2D} that vanish along its four sides. These are named as polynomials of type III.

Letting $r = 1,\ldots,N$, and $s = 1,2,3,4$, the Serendipity expansion functions are indicated by $F_\tau^{(\mathrm{t})}(\alpha,\beta)$, where the subscript τ is an index defined as

$$\tau = \begin{cases} s & \text{for} \quad r = 1 \\ 4(r-1)+s & \text{for} \quad r = 2,3 \\ 4(r-1)+\frac{(r-3)(r-4)}{2}+s \\ (4r+1)+\frac{(r-3)(r-4)}{2},\ldots,4r+\frac{(r-2)(r-3)}{2} \end{cases} \text{for} \quad r \geq 4 \quad , \tag{3.24}$$

and the superscript (t) denotes the polynomial type as follows

$$\mathrm{t} = \begin{cases} \mathrm{I} & \text{for} \quad r = 1 \quad \text{and} \quad \tau \in [s] \\ \mathrm{IIA} & \text{for} \quad r = 2,3 \quad \text{and} \quad \tau \in [4(r-1)+s] \\ \mathrm{IIB} & \text{for} \quad r \geq 4 \quad \text{and} \quad \tau \in \left[4(r-1)+\frac{(r-3)(r-4)}{2}+s\right] \\ \mathrm{III} & \text{for} \quad r \geq 4 \quad \text{and} \quad \tau \in \left[(4r+1)+\frac{(r-3)(r-4)}{2},\ldots,4r+\frac{(r-3)(r-4)}{2}\right] \end{cases} . \tag{3.25}$$

Following on from equations (3.24) and (6.3),

$$F_\tau^{(\mathrm{I})} = \frac{1}{4}(1+\alpha_s\alpha)(1+\beta_s\beta), \tag{3.26}$$

where (α_s,β_s) are the coordinates of the four corner nodes in $\Xi^{2\mathrm{D}}$.

$$F_\tau^{(\mathrm{IIA,IIB})} = \frac{1}{2}\begin{bmatrix}(1-\beta)\\(1+\alpha)\\(1+\beta)\\(1-\alpha)\end{bmatrix}^\top \begin{bmatrix}\delta_{1s} & 0 & 0 & 0\\ 0 & \delta_{2s} & 0 & 0\\ 0 & 0 & \delta_{3s} & 0\\ 0 & 0 & 0 & \delta_{4s}\end{bmatrix}\begin{bmatrix}p_r(\alpha)\\p_r(\beta)\\p_r(-\alpha)\\p_r(-\beta)\end{bmatrix}, \tag{3.27}$$

where δ_{ij} is the Kronecker delta and the argument of $p_r(-\alpha)$ and $p_r(-\beta)$ is negative to ensure that all $F_\tau^{(\mathrm{IIA,IIB})}$ polynomials of odd order are identical and separate by a 90 degree rotation; a property of shape functions required to ensure uniqueness and completeness. And finally,

$$F_\tau^{(\mathrm{III})} = p_n(\alpha)p_m(\beta), \tag{3.28}$$

with $n,m = 2,3,...N$, constrained by $n+m = r$ and $n+m \leq N$.

Figure 3.7 shows the first few polynomials $F_\tau^{(\mathrm{t})}$, sorted by order, type and index τ. Henceforth, N^{th}-order Serendipity Lagrange models are implicitly assumed to include all of the shape functions of orders 1 to N, as opposite to just order N. As an example, a model of order $N = 5$ contains:

1. Four bi-linear Lagrange polynomials (type I). Subscripts 1 to 4;
2. Four second-order polynomials (type II). Subscripts 5 to 8;
3. Four third-order polynomials (type II). Subscripts 9 to 12;

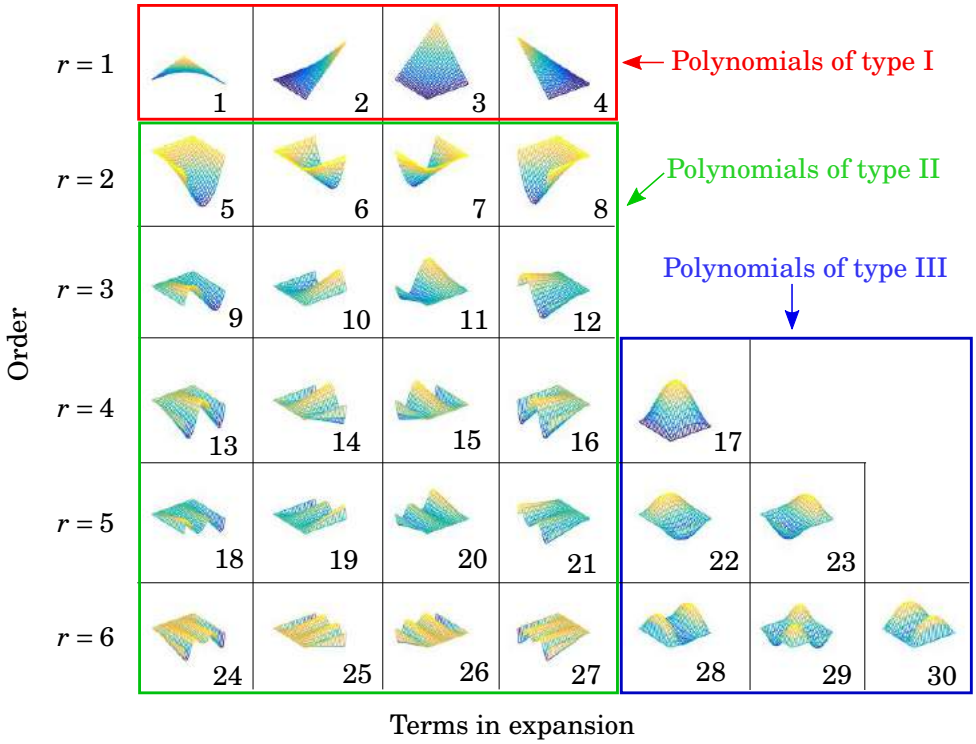

Figure 3.7: Serendipity Lagrange hierarchical shape functions (adapted from [4]).

4. Five fourth-order polynomials (4 type II, 1 type III). Subscripts 13 to 17;

5. Six fifth-order polynomials (4 type II, 2 type III). Subscripts 18 to 23.

The explicit form of the shape functions can be found in Appendix C. The cross-sectional displacements of order $N = 2$, at the i^{th} Lagrange beam node, take the form (using the notation $F_\tau = F_\tau^{(t)}$):

$$\boldsymbol{u}_i = \sum_{k=1}^{4} F_k^{(\mathrm{I})} \boldsymbol{u}_{ik} + F_5^{(\mathrm{II})} \boldsymbol{u}_{i5} + F_6^{(\mathrm{II})} \boldsymbol{u}_{i6} + F_7^{(\mathrm{II})} \boldsymbol{u}_{i7} + F_8^{(\mathrm{II})} \boldsymbol{u}_{i8}. \tag{3.29}$$

In conclusion, the SLE model is beneficial in that it has characteristics of both TE and LE models, because: (a) Serendipity polynomials have the same hierarchical nature as TEs; (b) as in LE models, they are defined on sub-domains thus enabling local refinement and enhanced numerical stability via cross-sectional discretisation. A schematic representation of the trade-offs between the three expansion models, in terms of accuracy and degrees of freedom (DOFs), is shown in Figure 3.8.

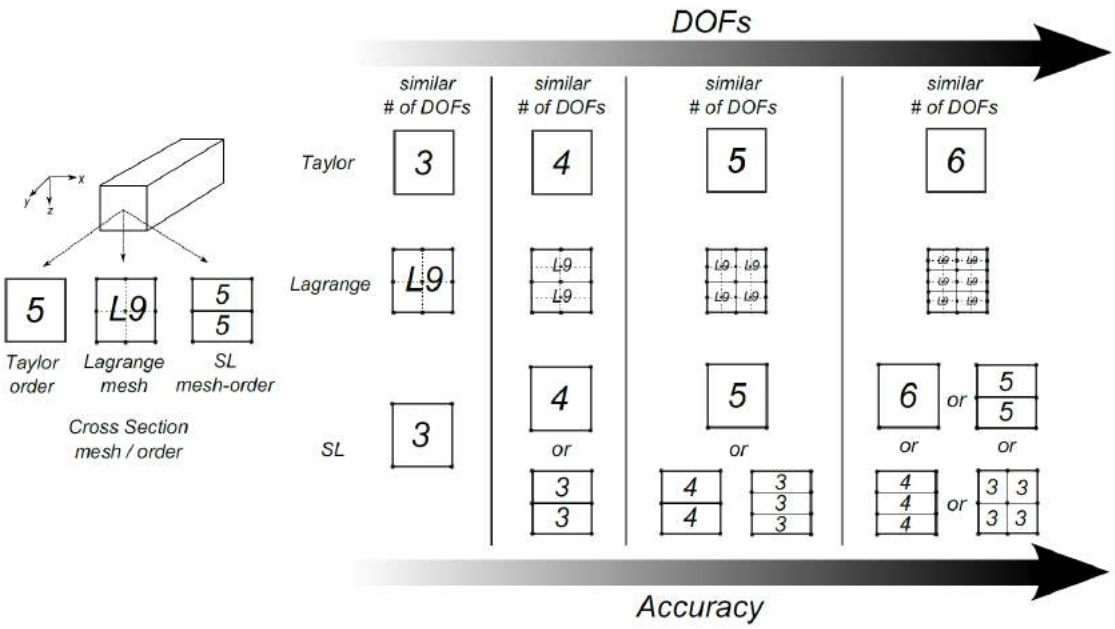

Figure 3.8: Schematic summary of possible cross-sectional discretisation strategies in Taylor, Lagrange and Serendipity Lagrange expansion models.

3.5 Curved Cross-Section Mapping

A correct geometrical description of the structure is of fundamental importance when dealing with complex, curved cross-section beams. The SLE functions, as defined in the previous section, are used to enrich the kinematics in the cross-section. These functions are integrated over the cross-section of the beam, which requires transformation of the coordinates. If the edges of a quadrilateral element are straight, the approximation of the geometry is obtained through linear mapping by using linear Lagrange polynomials as given by equation (3.19). However, if the cross-section is curved, nonlinear mapping functions must be employed. A few possible ways to describe the cross-section geometry are listed below.

1. Using the blending function method as a local mapping technique to describe the exact physical boundaries of the cross-section domain [190]
2. Using nonlinear functions for exact geometry description [4].
3. Employing CAD-basis functions for exact geometry representation.

The first method requires a polynomial description for each of the four sides of the element. The method can become cumbersome if the cross-section is complex or highly-distorted. In the second method, an exact description of the curve is required, and therefore, its use is limited to certain cross-sections. To overcome the limitations of the above two methods, CAD-basis functions can be used to describe the exact cross-section geometry, as they offer increased flexibility in

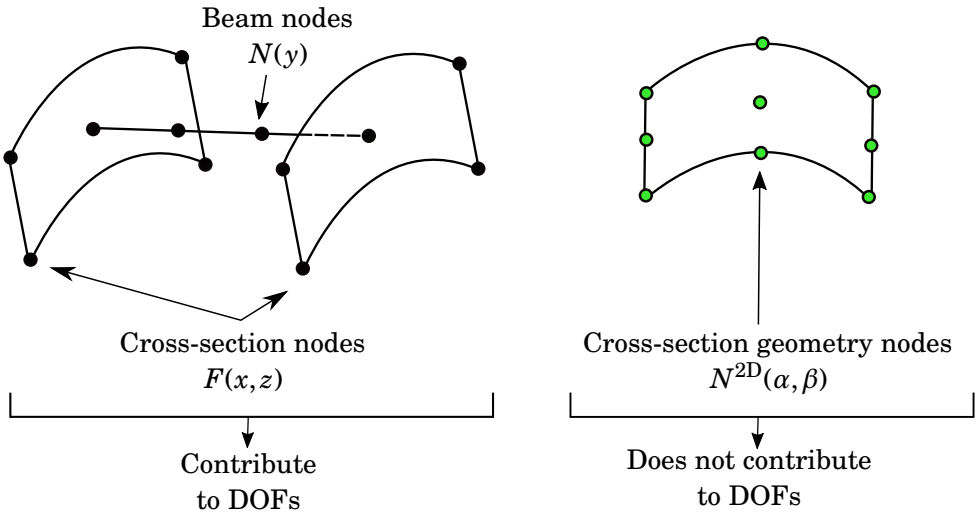

Figure 3.9: Two-dimensional mapping for modelling curved cross-section beams (a) kinematic description (b) geometry description.

modelling complex sections. Nevertheless, any of these methods can be employed, as long as the cross-section is described exactly.

In the isoparametric FE analysis, the same shape functions are used for the geometric and the kinematic description. A similar approach is followed in the Unified Formulation framework. However, if the cross-section is curved, accurate geometry description may require high-order or more elements in the cross-section. Using the same order and the number of elements for the kinematic description, increases the computational expense. Therefore, we propose to use different sets of shape functions for the geometric and the kinematic description. The proposed approach is described further below.

The displacement field is approximated by using the cross-section expansion functions, $F(x,z)$, and the beam shape functions, $N(y)$, as described in Section 3.2. For the cross-section geometry approximation, 2D higher-order Lagrange functions are used. Let $N^{2D}(\alpha,\beta)$ be a function, defined in $[-1,1]^2$, describing the geometry such that the position vector $\boldsymbol{x}$ of any given point in the structure, in the global Cartesian system, can be represented as

$$\boldsymbol{x} = N_k^{2D}(\alpha,\beta)\boldsymbol{x}_k, \tag{3.30}$$

where $\boldsymbol{x}_k \in \mathrm{IR}^2$ are the coordinates of the nodes of an element, and $k = 1,...,N_{ne}$, where N_{ne} is the number of nodes; 9-noded (quadratic) or 16-noded (cubic) Lagrange elements are used. It is to be noted that the number of nodes per element and the number of elements used to approximate the cross-section geometry are independent of the discretisation used for the analysis, and do not contribute to the DOFs, as depicted in Figure 3.9. The 2D cross-section mapping from the master computational domain to the physical domain, as described in Section 3.4.3, requires a Jacobian

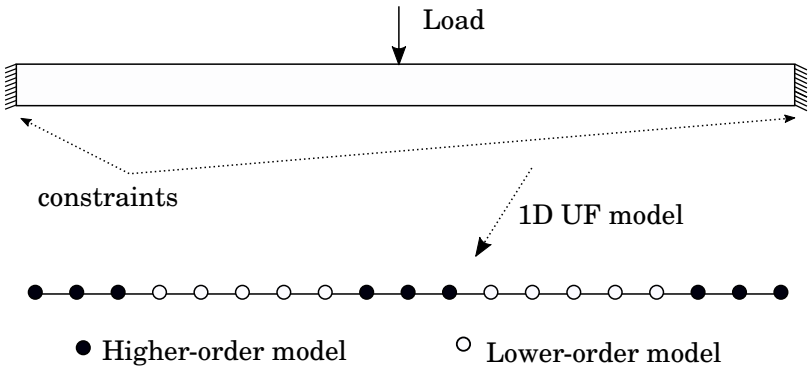

Figure 3.10: A schematic representation of a node-dependent kinematic model.

transformation, $\boldsymbol{J}^{2D}$, which is given by

$$\begin{Bmatrix} F_{,x}(x,z) \\ F_{,z}(x,z) \end{Bmatrix} = \underbrace{\begin{bmatrix} x_{,\alpha} & z_{,\alpha} \\ x_{,\beta} & z_{,\beta} \end{bmatrix}^{-1}}_{\boldsymbol{J}^{2D}} \begin{Bmatrix} F_{,\alpha}(\alpha,\beta) \\ F_{,\beta}(\alpha,\beta) \end{Bmatrix}, \tag{3.31}$$

The entries of $\boldsymbol{J}^{2D}$ are the derivatives of equation (3.30), and are interpreted as the local curvilinear basis vectors at any point in the cross-section. This method accounts for curved-section prismatic beams and is further extended in Chapter 9 to model non-prismatic and curved beams.

3.6 Node-Dependent Kinematics

In numerical analyses with finite elements, a local refinement is often necessary to improve the numerical accuracy in the area with strong local effects such as stress concentrations. Usually to save the computational costs, analysts tend to use detailed models only within those regions of interest (such as constraint ends, loaded surfaces or regions with other local effects like embedded components). In the Unified Formulation, the mechanical behavior of the beam is firstly captured by the cross-section expansion functions, $F(x,z)$, then interpolated by the nodal shape functions, $N(y)$, of the beam element. Such a feature makes it possible to adopt different types of cross-section functions at each beam node, obtaining node-dependent kinematic (NDK) finite element models, depicted in Figure 3.10. The displacement field given by equation (3.10) can be further written as

$$\boldsymbol{U}^{(e)} = F^i_\tau(x,z) N_i(y) \boldsymbol{u}_{i\tau}, \tag{3.32}$$

where $F^i_\tau(x,z)$ is the node-dependent cross-section expansion function.

Carrera *et al.* [191] proposed refined 1D models with node-dependent kinematics and employed TE and LE functions within the same beam model. However, the model requires bridging

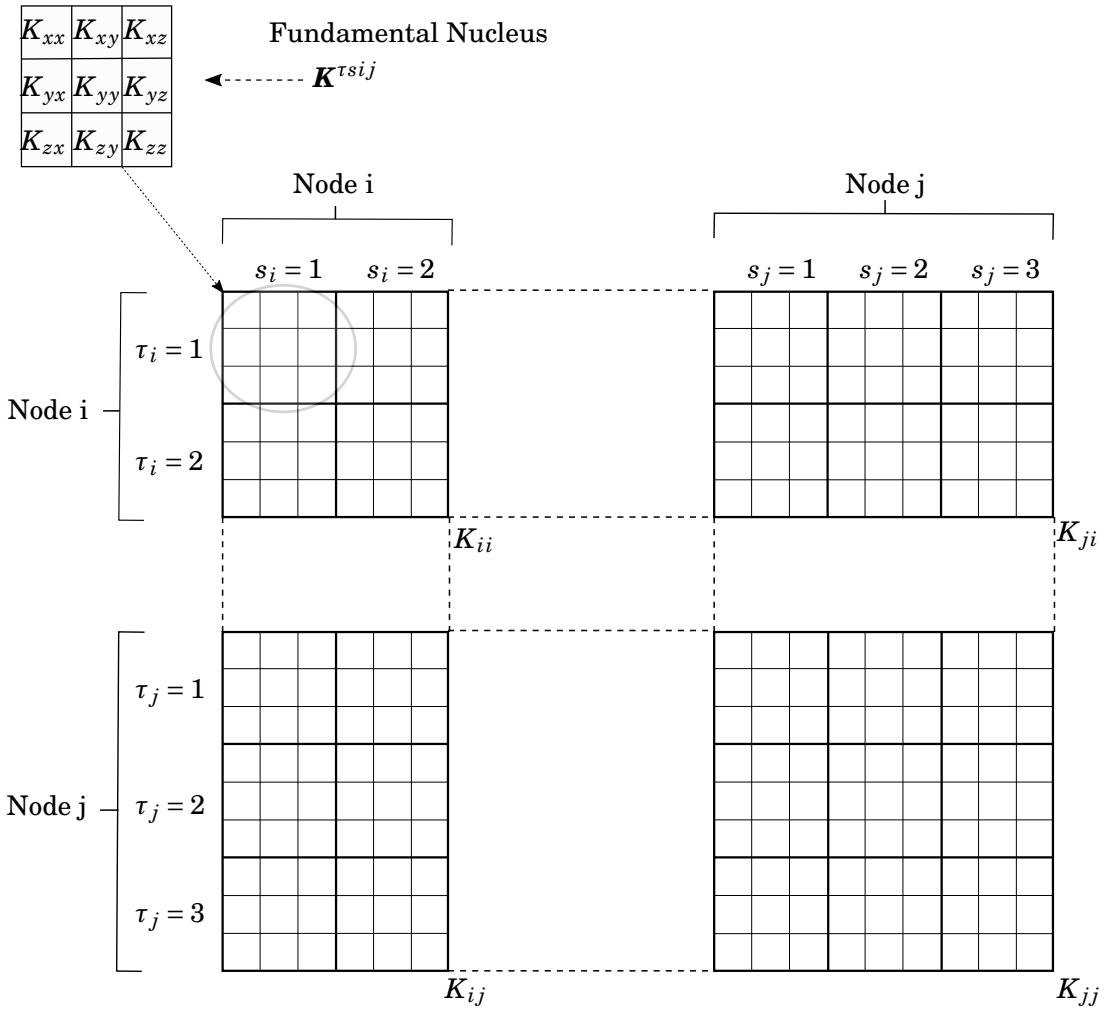

Figure 3.11: Assembly of the stiffness matrix with node-dependent kinematics.

(or transition) elements to maintain the continuity of displacement field between sections integrated with TE and LE functions. To avoid this extra model building effort, in the present work, SLE functions are employed. Cross-sections at each beam node are discretised, in the usual manner, with the same number of SLE elements and nodes. This discretisation naturally leads to a continuous displacement field. The local kinematic refinement is further achieved by increasing the order of expansion at desired beam nodes, without changing the mesh. The assembly of the stiffness matrix for a NDK model is depicted by Figure 3.11. In the figure, a general unit of stiffness matrix $\boldsymbol{K}^{ij}$ is considered, with number of expansion terms on node i is $M_i = 2$, while that on node j is, $M_j = 3$.

3.7 Conclusions

In this chapter, the one-dimensional Unified Formulation developed by Carrera and co-workers is presented. In addition to the commonly used cross-section expansion models, based on Taylor and Lagrange functions, a new class of hierarchical expansion model, referred as Serendipity Lagrange Expansion (SLE), is proposed. The SLE model combines two of the main features of Taylor and Lagrange expansion models, *i.e.* they are hierarchical and facilitate numerically stable cross-sectional refinements via remeshing. The hierarchical feature allows high-order terms to be added into the displacement field approximation while the cross-section discretisation feature allows geometric discontinuities to be modelled. The cross-section modelling capabilities are further enhanced by employing a different set of shape functions for exact geometry description to account for beams with curved cross-sections. Furthermore, a variable kinematic description at each beam node can be readily obtained by implementing the Node-Dependent Kinematics (NDK) approach. This technique improves the accuracy of the solution in the region with strong local effects without increasing the computational expense and also eliminates the need for a separate global/local analyses.

CHAPTER 4

THREE-DIMENSIONAL STRESS ANALYSIS FOR ISOTROPIC BEAM-LIKE STRUCTURES

In the previous chapter, the Serendipity Lagrange expansion-based Unified Formulation model is described for analysing beam-like structures. The Unified Formulation relies on the displacement-based version of the finite element method. Capturing 3D stress fields accurately using displacement-based weak formulations can be challenging. Since stresses and strains are obtained by differentiating the displacement field components, the stress equilibrium equations are satisfied in a weak sense and not necessarily point-wise. In this chapter, the 3D stress predicting capabilities of the UF-SLE model is verified against commonly used UF expansion models as well as high-fidelity FE model by means of static analyses of isotropic beam-like structures. Special attention is given to the accuracy of the model in capturing 3D stress response in the localised regions, such as near geometric discontinuities, constraints and point of load application. To this end, a few challenging examples are considered, for example, T-beam, flat and curved panels stiffened with transverse ribs and longitudinal stringers, C-section beam subjected to a point load. We also investigate the effect of collocating beam nodes towards the boundaries using Chebyshev biased grids, which reduce problematic oscillations in numerical solutions. Moreover, the variable kinematic model described in the previous chapter is assessed herein and is shown to offer significant computational benefits without compromising on the accuracy of the solution. In all numerical cases assessed, displacements and stresses are computed at various locations along the structure. Results obtained show the capability of the present formulation to model complex structures which otherwise could only be done with computationally expensive 3D FE analysis.

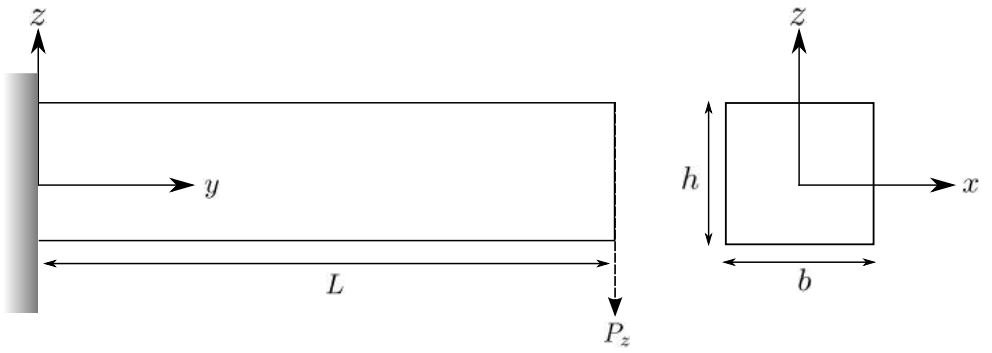

Figure 4.1: Square cross-section cantilever beam with applied tip load.

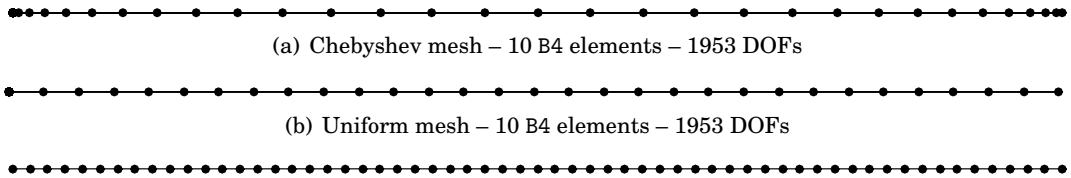

(a) Chebyshev mesh – 10 B4 elements – 1953 DOFs

(b) Uniform mesh – 10 B4 elements – 1953 DOFs

(c) Uniform mesh – 20 B4 elements – 3843 DOFs

Figure 4.2: Chebyshev and uniform node distributions along the beam length and their respective DOFs for Taylor model with $N = 5$.

4.1 Comparison of Chebyshev and Uniform Node Distribution

This section draws a comparison between the convergence behaviour of stress fields obtained using Chebyshev and uniform beam meshes. For this purpose, a clamped-free, square cross-section beam of length $L = 1\,\text{m}$, height $h = 0.1\,\text{m}$ and width $b = 0.1\,\text{m}$ is considered. A load $P_z = -10\,\text{N}$ is applied at the end ($y = L$), on the neutral axis, as shown in Figure 4.1. The constituent material is isotropic with Young's modulus $E = 75\,\text{GPa}$ and Poisson's ratio $\nu = 0.33$. A 3D FE analysis, performed with the commercial FE code, ANSYS, is used as a reference for validation, where the beam is discretised using 40000 SOLID186 (3D 20-noded) elements to yield converged results.

One-dimensional UF models, based on Taylor expansions, are used for the analyses presented in this section, as they are known to perform well with beams of square cross-section. The analyses are carried out with expansion order $N = 5$ and different meshes of 4-noded (B4) elements with uniform and Chebyshev distributions (refer to Section 3.3 for Chebyshev biased grid). Ensuing nodes and respective degrees of freedom are shown in Figure 4.2, where it can be seen that the Chebyshev and uniform meshes, with 10 B4 elements, have almost half the DOFs of the uniform mesh with 20 B4 elements.

Normal stress (σ_{yy}) values along the beam, at $x = 0$, $z = h/2$, are plotted in Figure 4.3(a), showing that results match the ANSYS model throughout the length, except for the region near the clamped end. For further clarity, Figure 4.3(b) zooms in on the deviations displaying

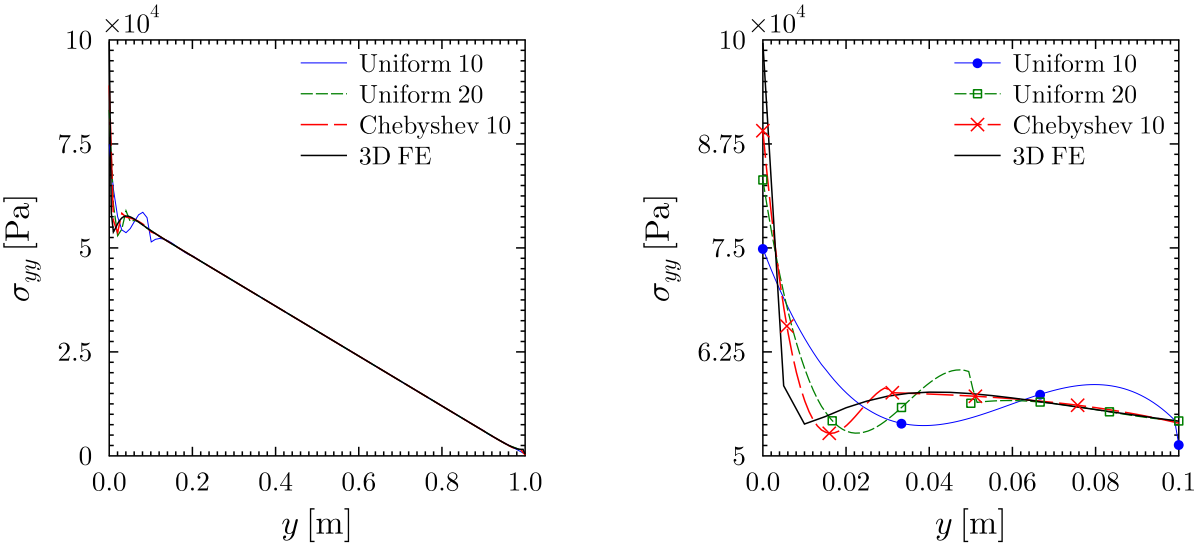

(a) σ_{yy} for $(x,z) = (0, h/2)$ and $y \in [0, L]$

(b) σ_{yy} for $(x,z) = (0, h/2)$ and $y \in [0, 0.1L]$

Figure 4.3: Variation of normal stress (σ_{yy}) along the length of the cantilever, square cross-section beam meshed with uniform and Chebyshev grids.

σ_{yy} from root up to 10% of the beam length, *i.e.* for $y \in [0, 0.1L]$. Similarly, shear stress (τ_{yz}) distributions along the beam at $x = 0$, $z = 0$, are plotted in Figures 4.4(a) and 4.4(b). Finally, through-the-thickness variations of σ_{yy} and τ_{yz} at $x = 0$, $y = 0.1L$ are plotted in Figures 4.5(a) and 4.5(b).

As expected, results show clearly that a Chebyshev grid of 10 elements provides enhanced accuracy near the boundary than uniform meshes of 10 and 20 elements. This conclusion confirms that biased UF meshes, refined towards regions of high stress gradients, can improve accuracy with no need for increasing the total number of nodes (and DOFs).

4.2 Comparison Between TE, LE and SLE Models

4.2.1 Square Cross-Section Beam

In this section, we compare the SLE model with the traditional TE and LE models. First, a cantilevered, square cross-section beam is considered, as in Section 4.1. Ten `B4` elements, with a Chebyshev-biased distribution, are employed for the mesh in the longitudinal direction. 3D FE results are used as a reference. Analytical results, obtained with classical theories such as Euler-Bernoulli (EB) and Timoshenko beam (TB), are provided for comparison. In addition, results are also compared to Timoshenko's enhanced analytical (TB-EN) solution obtained using Airy's stress function [17]. This enhanced formulation predicts accurate transverse shear stress distribution. In chapter 11 of reference [17], the formulation is termed as "exact". However, it is

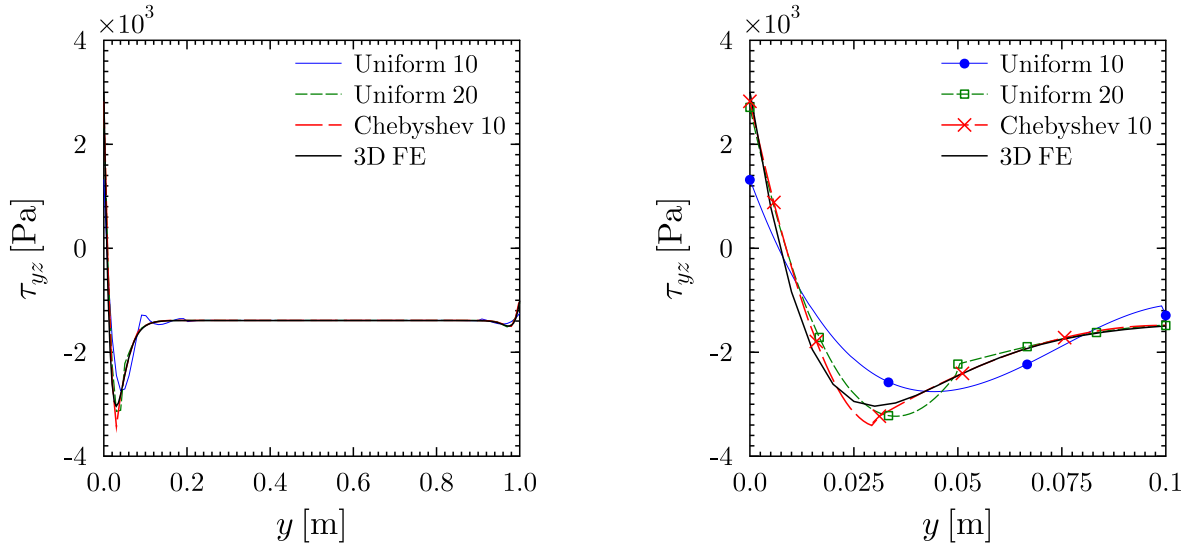

(a) τ_{yz} for $(x,z) = (0,0)$ and $y \in [0,L]$

(b) τ_{yz} for $(x,z) = (0,0)$ and $y \in [0,0.1L]$

Figure 4.4: Variation of shear stress (τ_{yz}) along the length of the cantilever, square cross-section beam meshed with uniform and Chebyshev grids.

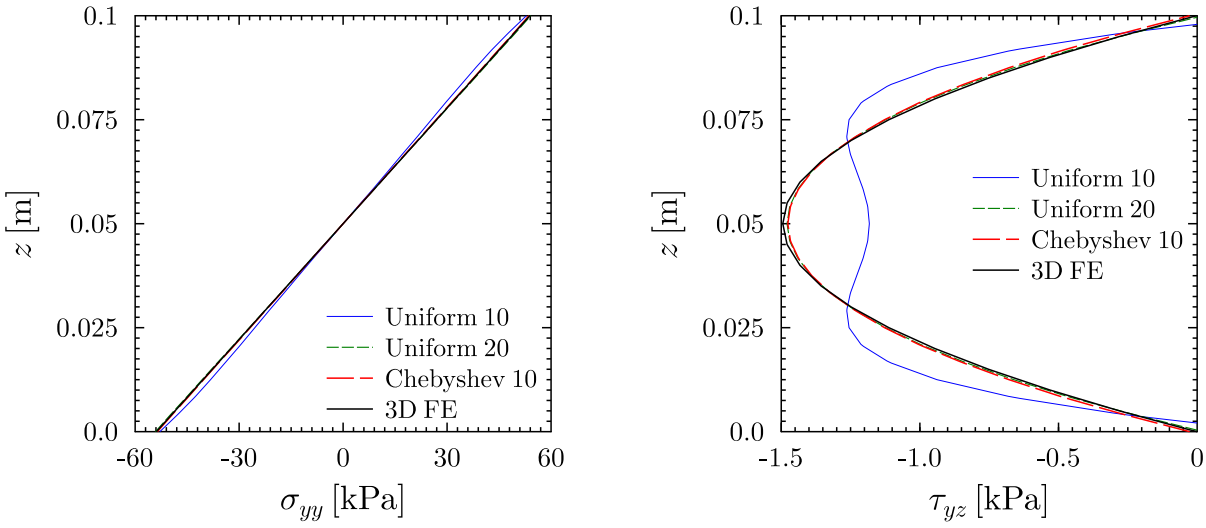

(a) Normal stress

(b) Shear stress

Figure 4.5: Through the thickness variation of normal (σ_{yy}) and shear stress (τ_{yz}) at $(x,y) = (0,0.1L)$ for the cantilever, square cross-section beam meshed with uniform and Chebyshev grids.

derived by enforcing certain stress components to be zero and assumes that the bending stress varies linearly along the thickness coordinate. As such, strictly speaking, the formulation is not exact, as these conditions hold true when measuring the stress distribution remote from boundary constraints. In contrast, the present formulation accounts for all stress components without any of the above-mentioned assumptions and is expected to predict the stress response accurately in all regions within the structure. The following analytical expressions are employed to calculate deflection and stresses [17, 48]:

$$u_z^{\text{EB}} = \frac{P_z L^3}{3EI} \tag{4.1}$$

$$u_z^{\text{TB}} = \frac{P_z L^3}{3EI} + \frac{P_z L}{AG} \tag{4.2}$$

$$\sigma_{yy}^{\text{EB,TB,TB-EN}} = \frac{P_z (L-y) z}{I} \tag{4.3}$$

$$\tau_{yz}^{\text{TB}} = -\frac{3P_z}{2A} \tag{4.4}$$

$$\tau_{yz}^{\text{TB-EN}} = \tau_{yz}^{\text{TB}} \left[\frac{-\nu}{1+\nu} \left(\frac{1}{3} + \sum_{n=1}^{\infty} \frac{4}{\pi^2} \frac{(-1)^n}{n^2 \cosh(n\pi)} \right) + 1 \right] \tag{4.5}$$

where, as is customary, G is the shear modulus, I is the second moment of area with respect to the x axis and A is the area of the cross-section.

Transverse displacement, normal and shear stresses are evaluated at various locations as shown in Table 4.1. The through-thickness variation of shear stress at the beam's midspan is plotted in Figure 4.6 for SLE ($N = 5$), TE ($N = 5$) and three LE models with different cross-sectional meshes. Plots of the percentage error of displacement, normal and shear stress (with respect to 3D FE solution) versus DOFs are shown in Figure 4.7.

Results show that the SLE model with one cross-sectional element of order $N = 1$ provides identical results to the LE model with one L4 element. This result is expected because the models have identical kinematical descriptions. The benefits of using SLE elements can be seen for expansions of order greater than one ($N > 1$). SLE, TE and LE models perform similarly in terms of convergence of displacement and normal stress. Turning our attention to shear stresses, SLE and TE models achieve convergence at around 2000 DOFs. Conversely, as shown in Figure 4.7c, LE model fails to do so. Even upon further cross-sectional discretisation and a number of DOFs in excess of 26000, Figure 4.8 indicates that τ_{yz} does not fully converge. This numerical issue is attributed to the use of low order—linear (L4) or quadratic (L9)—shape functions for the cross-sectional elements, which upon differentiation can only provide piecewise constant or linear stress variations respectively.

To demonstrate the capabilities of the proposed SLE model in predicting the local variation of 3D stresses towards the clamped edges, relevant stress components are measured at several locations along the beam. In the present example, in order to capture 3D stress fields accurately, the beam's cross-section is divided into a 2×2 mesh of SLE domains of order $N = 8$. Figure 4.9 shows the through-thickness variation of shear (τ_{yz}) and transverse normal stress (σ_{zz}) at

Table 4.1: Displacement and stress components of the square cross-section beam.

	$u_z(0,L,0)$ [m] $\times 10^{-6}$	$\sigma_{yy}(0,0.21437L,h/2)$ [Pa]	$\tau_{yz}(0,L/2,0)$ [Pa]	DOFs #
ANSYS				
SOLID186	-5.330	47138.0	-1392.4	541059
Analytical				
EB	-5.333	47137.8	-	-
TB	-5.368	47137.8	-1500	-
TB-Enhanced	-5.333	47137.8	-1388.8	-
Taylor Expansions				
T1	-5.369	47139.9	-1000.0	279
T2	-5.314	47137.6	-1000.0	558
T3	-5.322	47148.0	-1396.6	930
T4	-5.326	47137.4	-1396.6	1395
T5	-5.328	47140.8	-1387.6	1953
T6	-5.328	47123.4	-1387.6	2604
T7	-5.329	47131.1	-1389.6	3348
Lagrange Expansions				
1×1 L4	-4.462	47139.7	-1000.0	372
2×1 L4	-4.939	49928.9	-1091.4	558
2×2 L4	-5.064	49761.3	-934.3	837
1×1 L9	-5.315	47145.3	-958.6	837
2×1 L9	-5.322	47139.7	-1579.9	1116
2×2 L9	-5.325	47138.6	-1583.2	2325
3×2 L9	-5.326	47136.4	-1341.2	3255
3×3 L9	-5.327	47136.5	-1342.3	4557
Serendipity Lagrange Expansions				
SL1	-4.462	47139.7	-1000.0	372
SL2	-5.315	47146.9	-958.6	744
SL3	-5.324	47149.1	-1396.6	1116
SL4	-5.327	47136.1	-1409.2	1581
SL5	-5.328	47139.2	-1387.6	2139
SL6	-5.329	47123.5	-1387.3	2790
SL7	-5.329	47134.0	-1389.6	3534

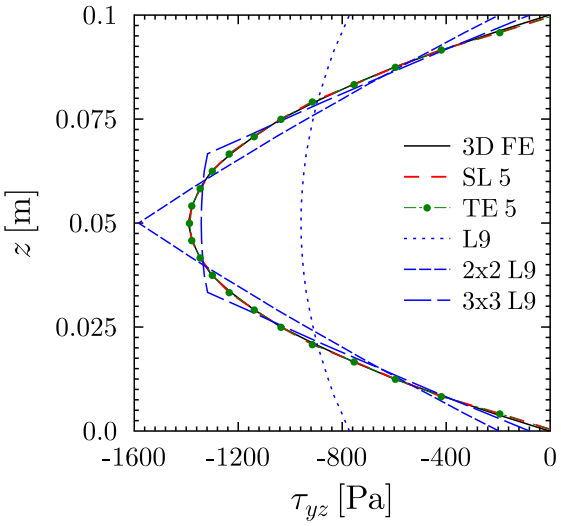

Figure 4.6: Through-thickness plot of shear stress (τ_{yz}) at the beam's mid-span, $(x, y) = (0, L/2)$.

different locations from the clamped support. In the latter region, significant localised changes in σ_{zz} occur, which can be characterized by the presence of an inflection point. Moving away from the clamped end, boundary layer effects are less evident. Our calculations are in good agreement with 3D FE results at a significantly reduced computational cost ($\approx$ 1/10 of DOFs). Similar analyses, carried out with a TE model of order $N = 8$, are found to produce similar results, with some differences. For instance, Figure 4.9b shows σ_{zz} to match the reference solution almost everywhere, except in a small region near the free surfaces, where $\partial\sigma_{zz}/\partial z$ is expected to vanish. Unlike the SLE model, the TE model fails to capture this feature. This discrepancy can be explained by the fact that SLEs allow not only the order of expansion to be increased, but also to discretise the cross-section. Owing to these capabilities, boundary effects in the stress profiles can be more readily captured.

In a TE setting, the only way to improve the prediction of transverse normal stresses along the beam's free surface is to increase the expansion order. However, this leads to numerical instabilities, which may be measured by computing the conditioning number (r_c) of the ensuing stiffness matrix [185]. Figure 4.10a is a plot of $1/r_c$, reciprocal of the conditioning number, versus, N, the expansion order of SL and TE models with one cross-sectional element. From the figure, we observe that, for increasing N, the stiffness matrix of TE models becomes ill-conditioned (i.e. r_c diverges). Conversely, the conditioning properties of SL models are almost independent from the expansion order. This is shown to be the case also for LE models, proving that cross-sectional discretisation improves numerical stability.

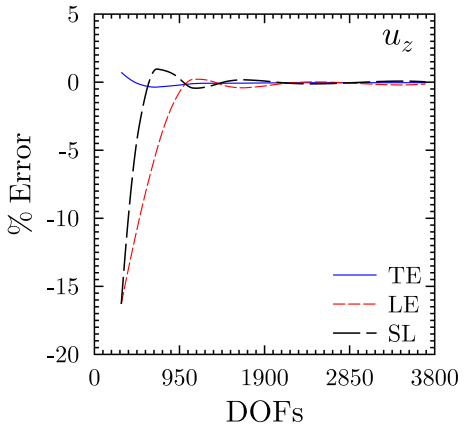

(a) Displacement (u_z) at $[0, L, 0]$

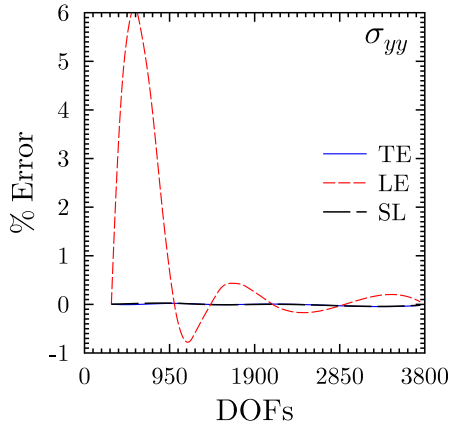

(b) Normal stress (σ_{yy}) at $[0, L/5, h/2]$

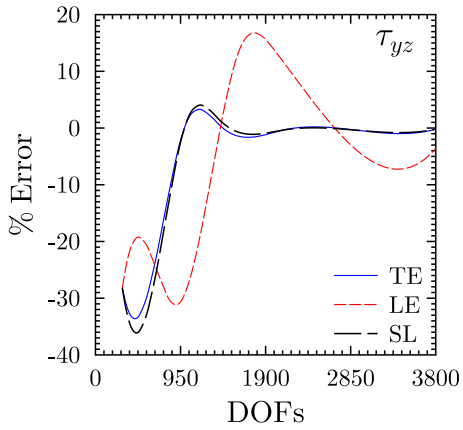

(c) Shear stress (τ_{yz}) at $[0, L/2, 0]$

Figure 4.7: Relative error with respect to reference 3D FE solution.

4.2.2 T-Section Beam

In order to show the enhanced capabilities of the SLE model, in comparison with TE and LE models, an additional beam of more complex geometry is examined. Specifically, we consider the T-section beam shown in Figure 4.11. Material properties are the same as in the previous example. The beam is clamped at one end and loaded with a concentrated force, $P_z = -10\,\mathrm{N}$, at the other end. The analysis is performed with Taylor, Lagrange and Serendipity Lagrange expansion models. Converged 3D FE results from ANSYS, computed by discretising the structure with 554,036 `SOLID186` elements, are taken as a reference for comparison. Displacement fields, as well as, normal and shear stresses are evaluated at several locations and a convergence analysis is performed by varying the order of TE and SLE models and by refining the cross-sectional mesh for the LE model. For an accurate estimation of the stress field at the intersection between flange

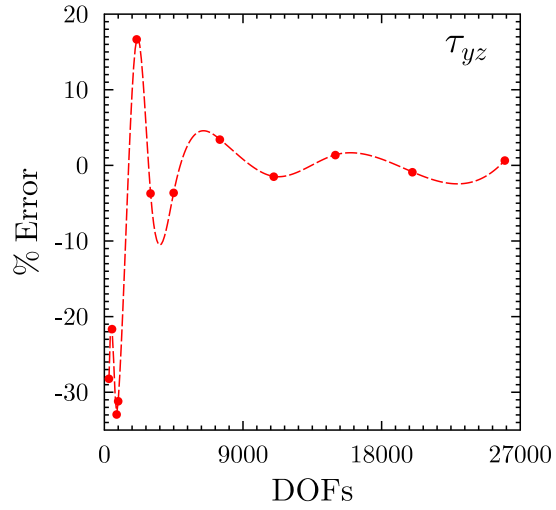

Figure 4.8: Relative error of shear stress (τ_{yz}) at $[0, L/2, 0]$ with respect to reference 3D FE solution for refined Lagrange expansion models.

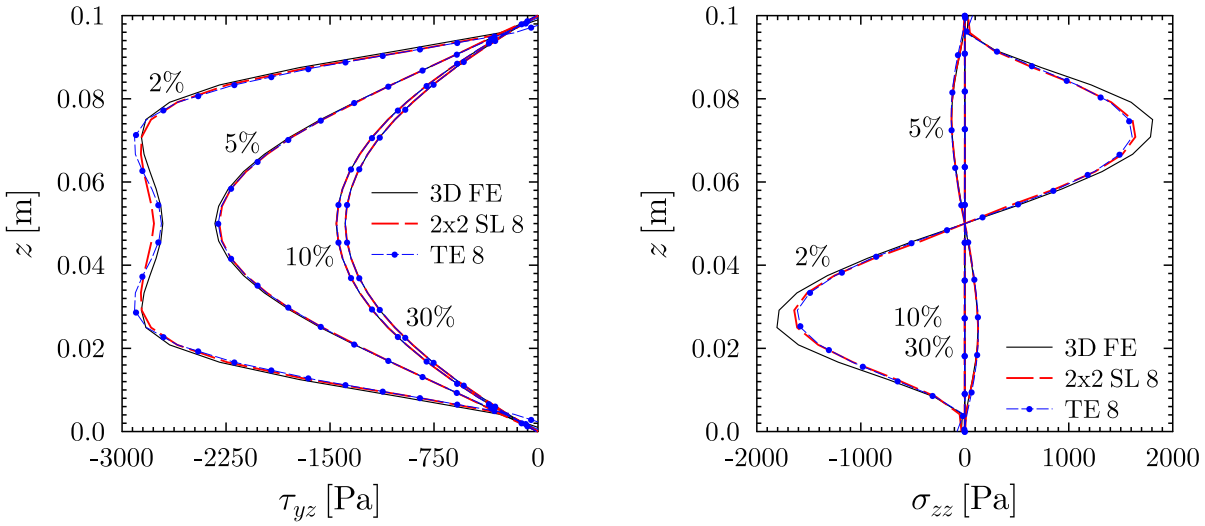

(a) Transverse shear stress

(b) Transverse normal stress

Figure 4.9: Through-thickness plot of shear and transverse normal stresses (τ_{yz} and σ_{zz}) at 2%, 5%, 10% and 30% of the beam length from the clamped end and $x = 0$.

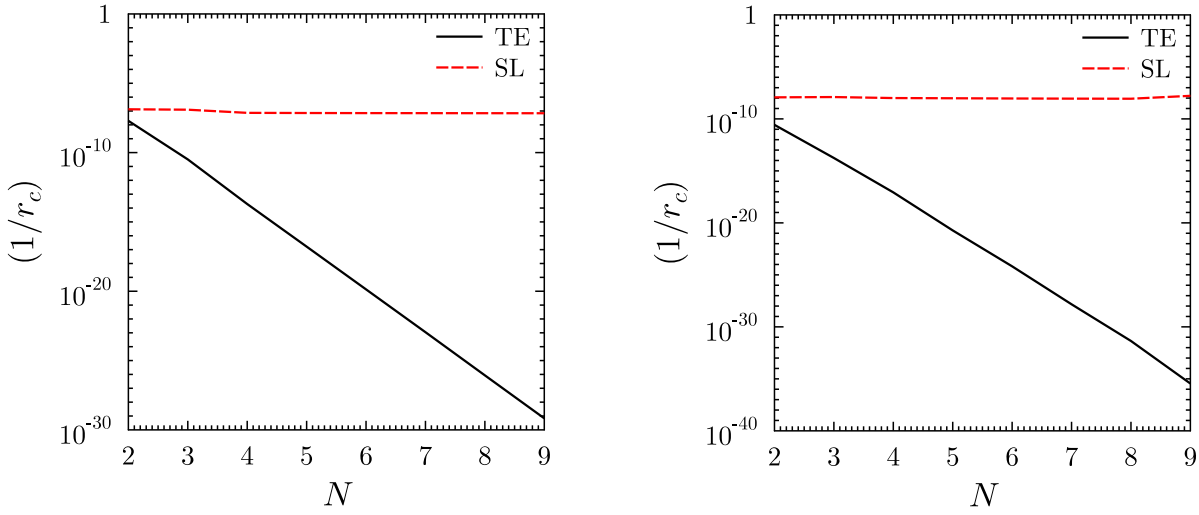

(a) Square cross-section

(b) T-section

Figure 4.10: Conditioning number of the system's stiffness matrix versus expansion order for Taylor and Serendipity Lagrange models.

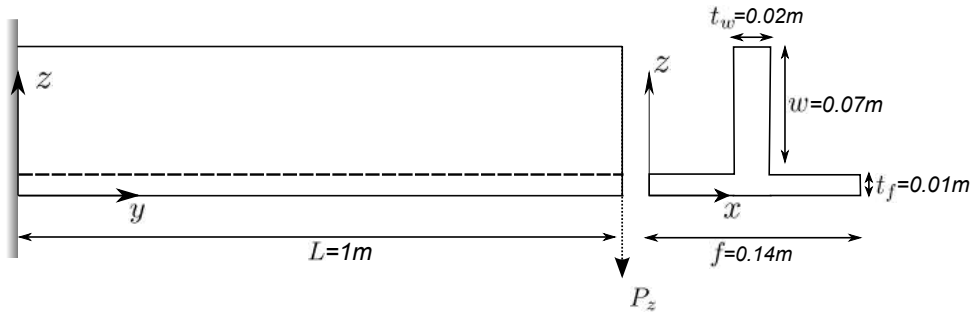

Figure 4.11: T-section cantilever beam with applied tip load.

and web, several cross-sectional LE and SLE meshes have been trialled. Resulting discretisations are shown in Figure 4.12, where it can be seen that local refinement is required in the regions with high stress gradients. For the LE mesh, convergence is achieved with 488 `L9` elements; In comparison, the SLE model necessitates some 66 `SL8` elements. Figure 4.10b confirms that, also in this case, TE model lose numerical stability for increasing N, which limits our analyses to order 9. In contrast, LE and SLE models are found to be numerically stable again.

Elastic field results are reported in Table 4.2. As expected, TE models produce accurate and converged displacement and normal stress values, but fail to represent shear stresses to an acceptable degree of precision. LE and SLE models are numerically stable, as such they are able to capture the response of the structure better than TEs, particularly localised stresses concen-

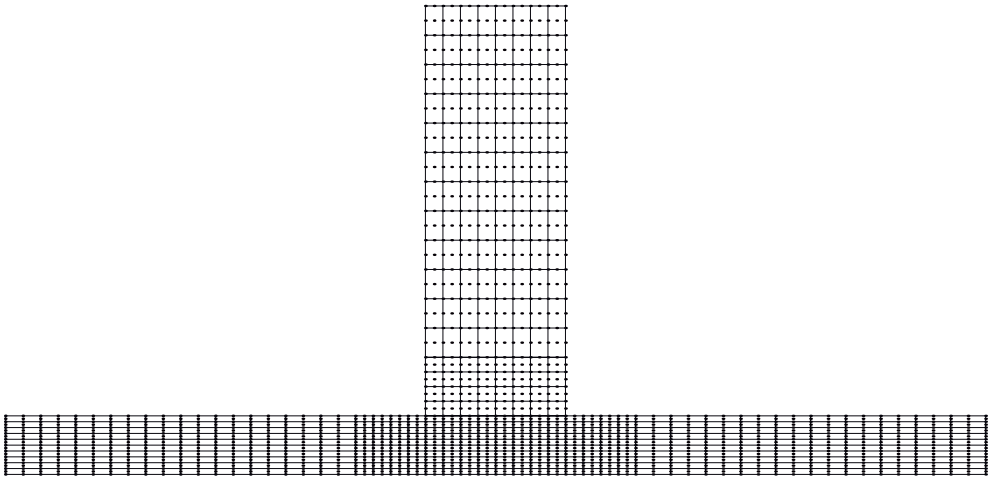

(a) Lagrange Expansion model mesh

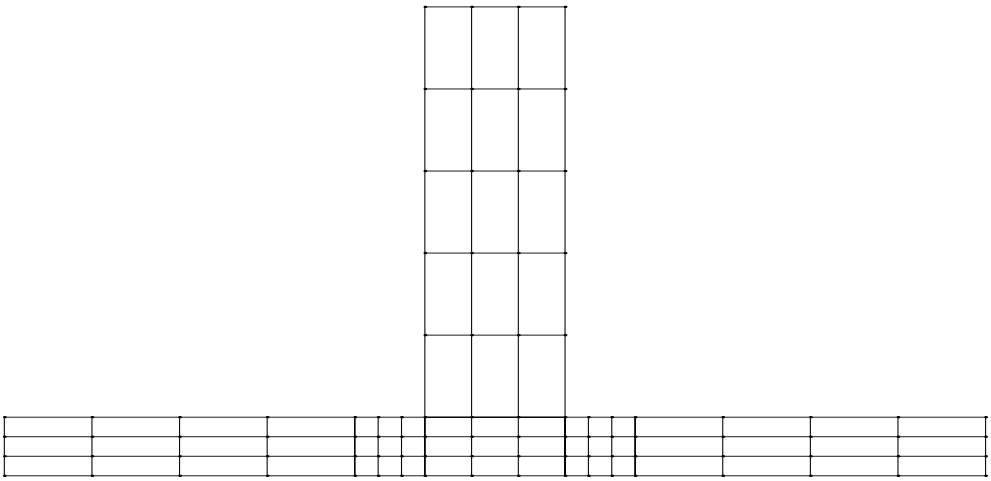

(b) Serendipity Lagrange model mesh

Figure 4.12: Cross-sectional discretisations for T-section beam.

trations. The reason for this difference is that LE and SLE models rely on local discretisations at cross-sectional level, whereas TE models are constructed with displacement shape functions spanning the entire cross-section from the beam reference axis, which detrimentally affects the conditioning number, thus preventing indefinite refinement.

In the remainder of this section, particular attention is given to τ_{yz}, which, as indicated by Table 4.2, is the most problematic field variable to be modelled accurately. Figure 4.13 and 4.14 show the variations of shear stress at the beam's mid span, respectively, along the flange and through the web at $x = 0.07$ and $x = 0.06$. In addition, the models are interrogated throughout the beam's length. Values of τ_{yz} through z, at 2%, 5% and 50% of the span from the clamped end, are reported in Figures 4.15 and 4.16. The latter, shows the shear stress distribution along the T-section's web. At $y = 0.5L$, such distributions can be calculated analytically using Jourawski's

Table 4.2: Displacement and stress components of the T-section beam.

	$u_z(f/2,L,0.025)$ [m] $\times 10^{-5}$	$\sigma_{yy}(f/2,L/5,w)$ [Pa]	$\tau_{yz}(f/2,L/2,0.025)$ [Pa]	$\tau_{yz}(f/2,L/2,0.01)$ [Pa]	DOFs #
ANSYS					
SOLID186	−2.6304	258410	−8830.4	-6266.3	7225431
Taylor Expansion					
T5	−2.6248	258323	−8520.6	-44031.3	5733
T6	−2.6268	258321	−8999.9	-4667.6	7644
T7	−2.6274	258327	−9080.2	-5061.7	9828
T8	−2.6280	258326	−8897.8	-5159.9	12285
T9	−2.6284	258324	−8802.7	-5485.1	15015
Lagrange Expansion					
40 L9	−2.6298	258326	−8973.3	-44031.3	52689
126 L9	−2.6301	258327	−8816.4	-6544.9	153699
184 L9	−2.6303	258327	−8843.8	-6247.3	221949
336 L9	−2.6303	258327	−8844.4	-6309.4	395577
432 L9	−2.6304	258327	−8844.9	-6304.8	502593
488 L9	−2.6304	258327	−8845.6	-6277.7	567021
Serendipity Lagrange Expansion					
66 SL5	−2.6304	258327	−8826.2	-5990.7	250614
66 SL6	−2.6305	258327	−8815.7	-6135.0	347529
66 SL7	−2.6305	258327	−8838.1	-6207.0	462462
66 SL8	−2.6305	258327	−8824.7	-6243.1	595413
66 SL9	−2.6305	258327	−8826.6	-6259.8	746382

formula [192]. This is done to highlight an example of the intrinsic limitations that may affect simplified models. Specifically, it is observed that the formula deviates from the numerical results, proceeding from the top of the section towards the flange. This result is as expected due to the assumptions in Jourawski's model.

In summary, shear stresses from the LE, SLE and 3D FE solutions match almost exactly and can capture localised features in the 3D stress field.

Finally, for further appraisal of SLE discretisations, 3D stress profiles across full cross-sections are compared to the reference ANSYS solution through contour plots of transverse shear and normal stresses at various span-wise locations. These positions are shown in Figures 4.17 to 4.19. Overall agreement is excellent, except at the corner between the flange and web, which theoretically is a singular point. No model is accurate in capturing stresses exactly in this location.

In conclusion, from the results presented in this section it is evident that the UF-SLE model is

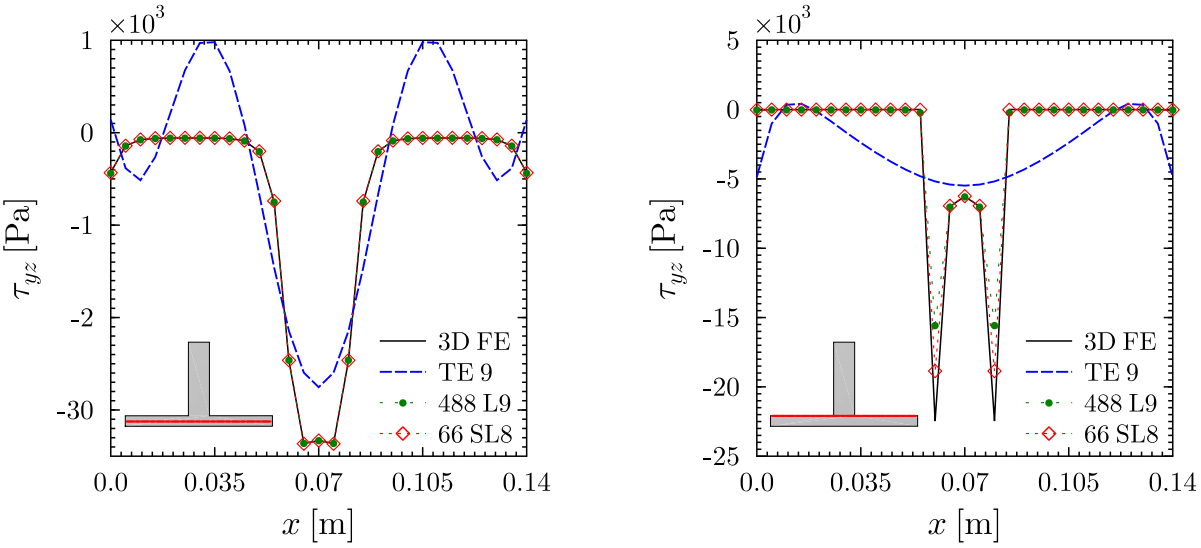

(a) τ_{yz} for $(y,z) = (L/2, t_f/2)$ and $x \in [0, f]$

(b) τ_{yz} for $(y,z) = (L/2, t_f)$ and $x \in [0, f]$

Figure 4.13: Variation of shear stress (τ_{yz}) along the T-section flange.

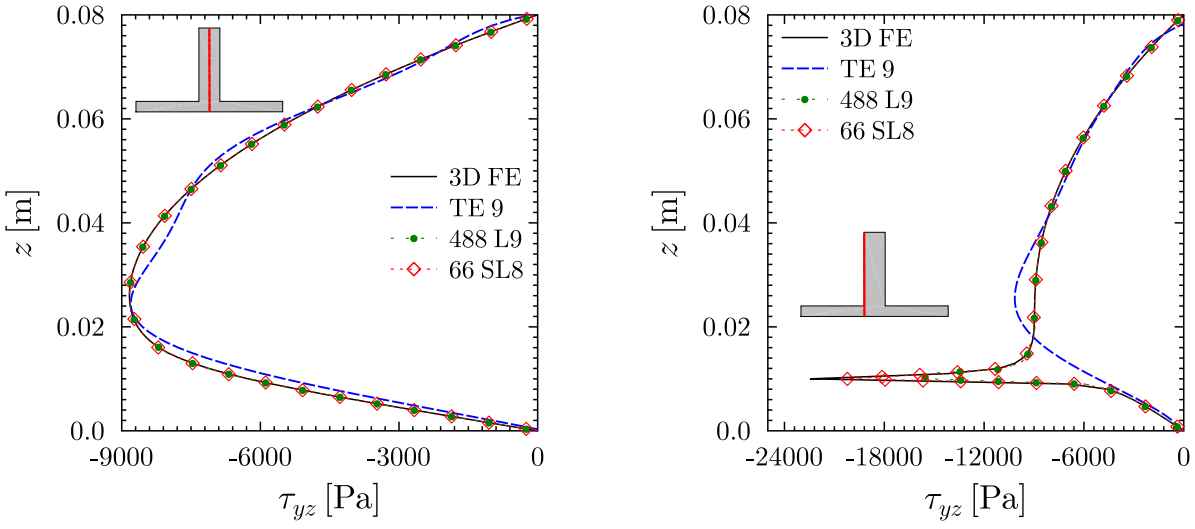

(a) τ_{yz} for $(x,y) = (0.07, L/2)$ and $z \in [0, t_f + w]$

(b) τ_{yz} for $(x,y) = (0.06, L/2)$ and $z \in [0, t_f + w]$

Figure 4.14: Through-thickness plot of shear stress (τ_{yz}).

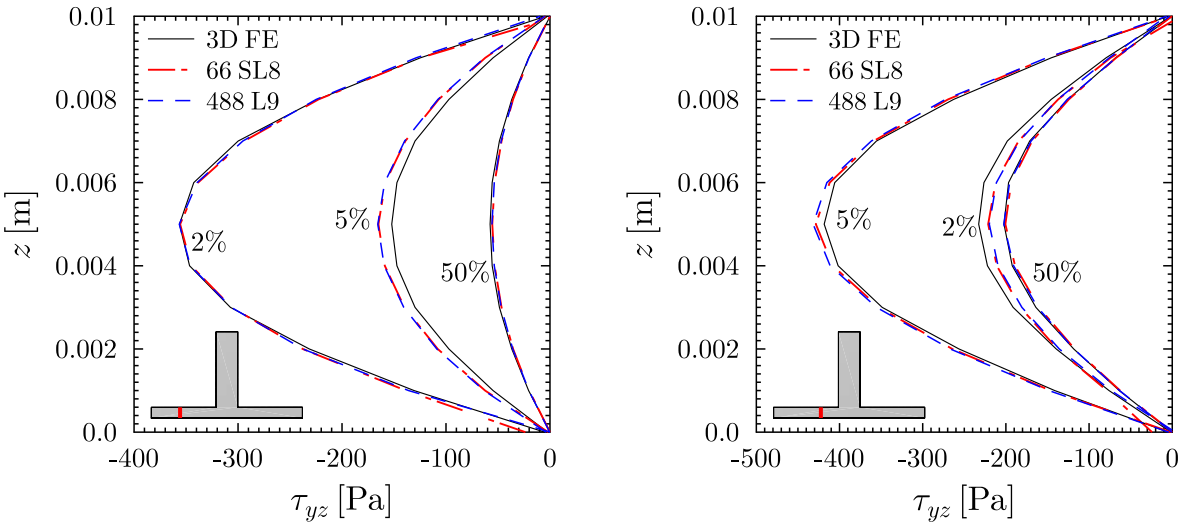

(a) τ_{yz} for $x = 0.03$ and $z \in [0, t_f]$

(b) τ_{yz} for $x = 0.05$ and $z \in [0, t_f]$

Figure 4.15: Through-thickness plot of shear stress (τ_{yz}) at locations 2%, 5% and 50% of the beam length from clamped end.

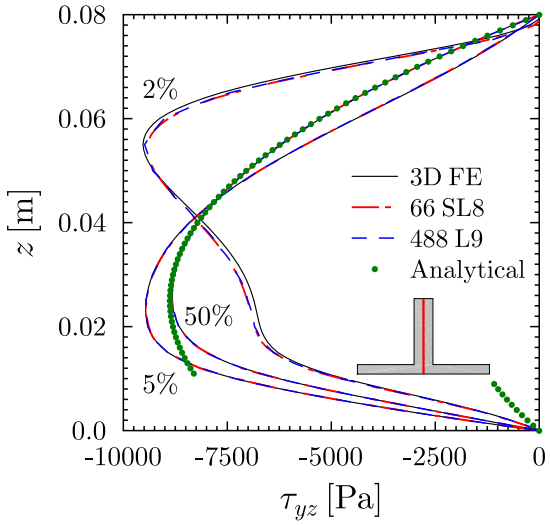

Figure 4.16: Through-thickness plot of shear stress (τ_{yz}) at locations 2%, 5% and 50% of the beam length from clamped end at $x = f/2$.

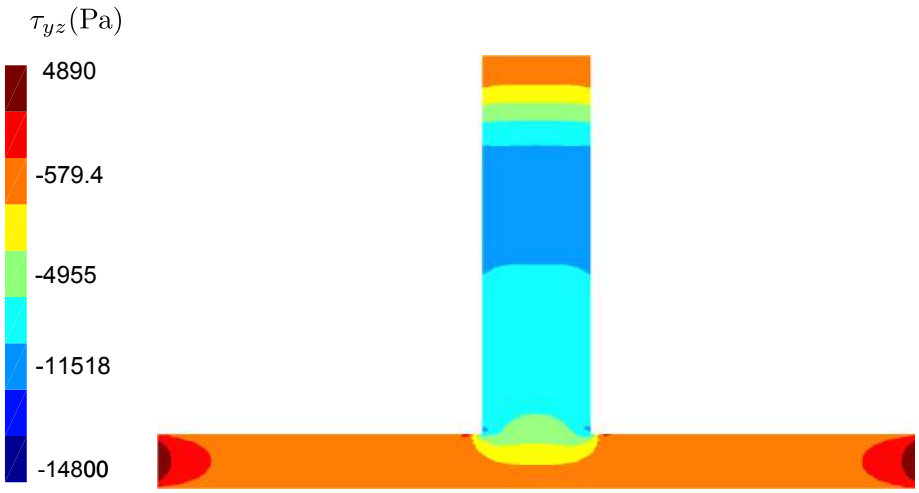

(a) 3D FE

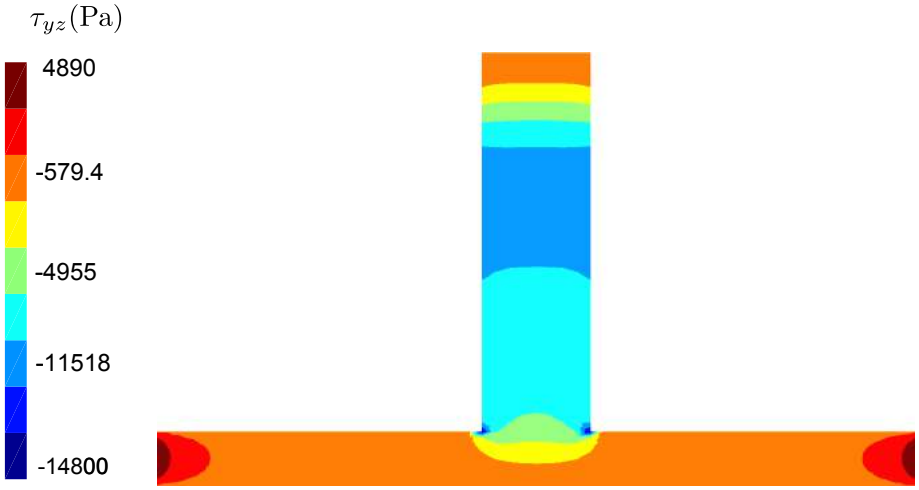

(b) UF-SLE

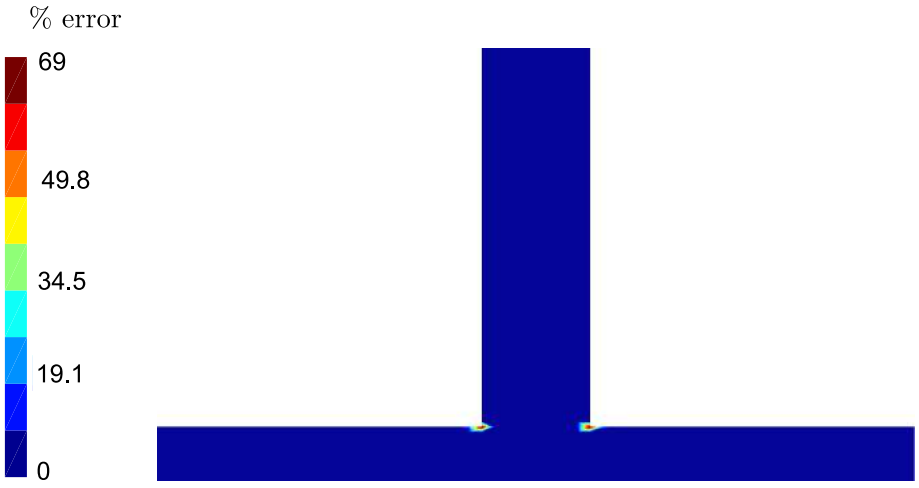

(c) Residual

Figure 4.17: Distribution of shear stress (τ_{yz}) in the cross-section at 2% of the beam length from the clamped end.

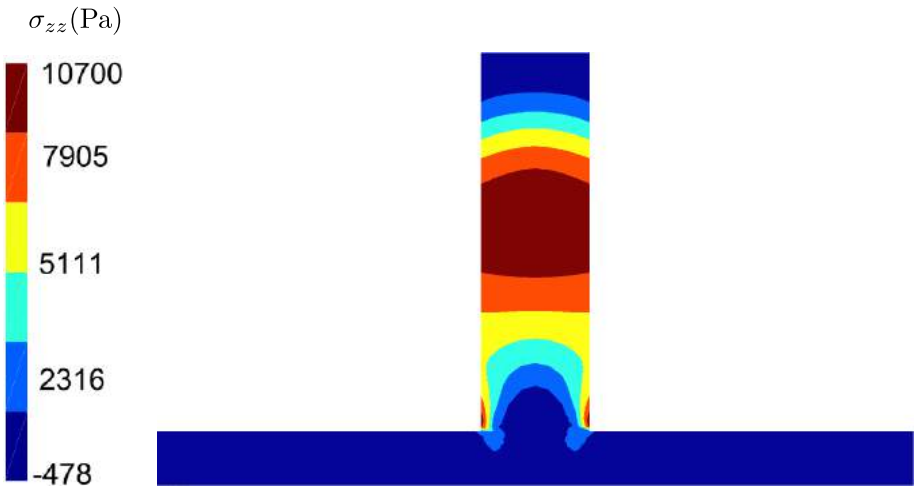

(a) 3D FE

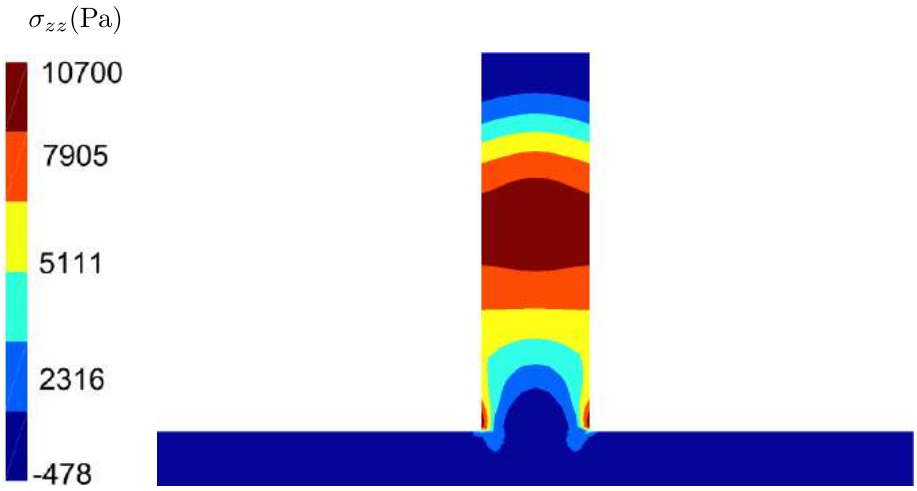

(b) UF-SLE

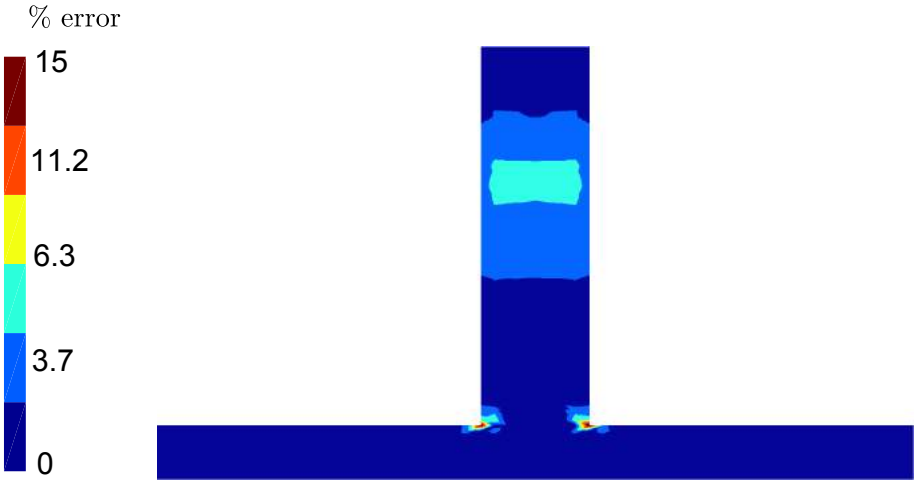

(c) Residual

Figure 4.18: Distribution of transverse normal stress (σ_{zz}) in the cross-section at 2% of the beam length from the clamped end.

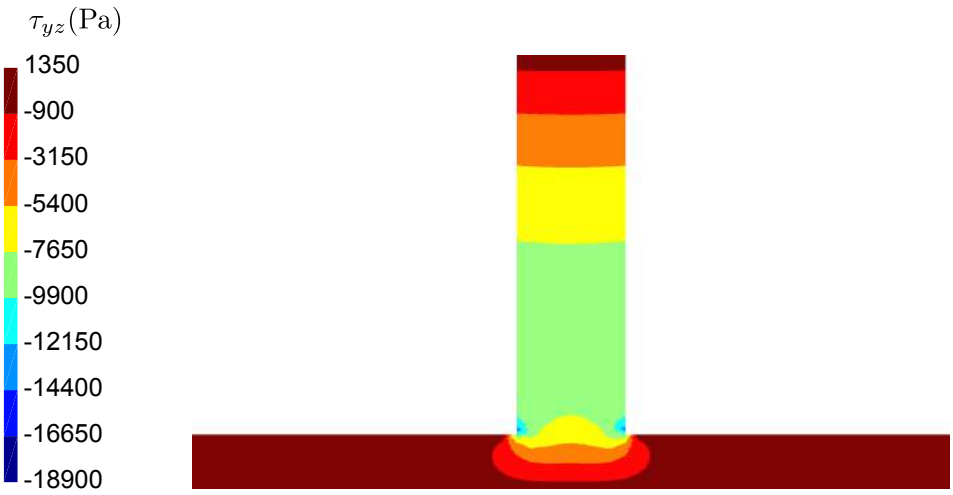

(a) 3D FE

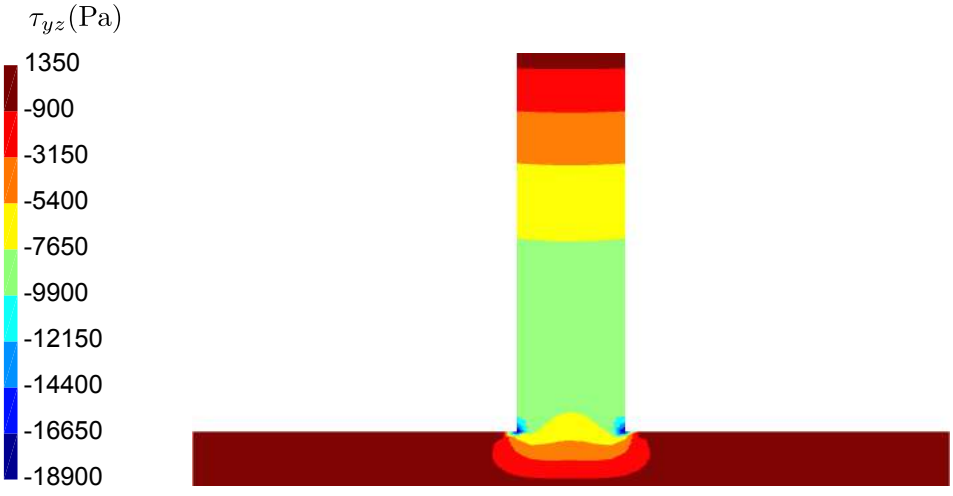

(b) UF-SLE

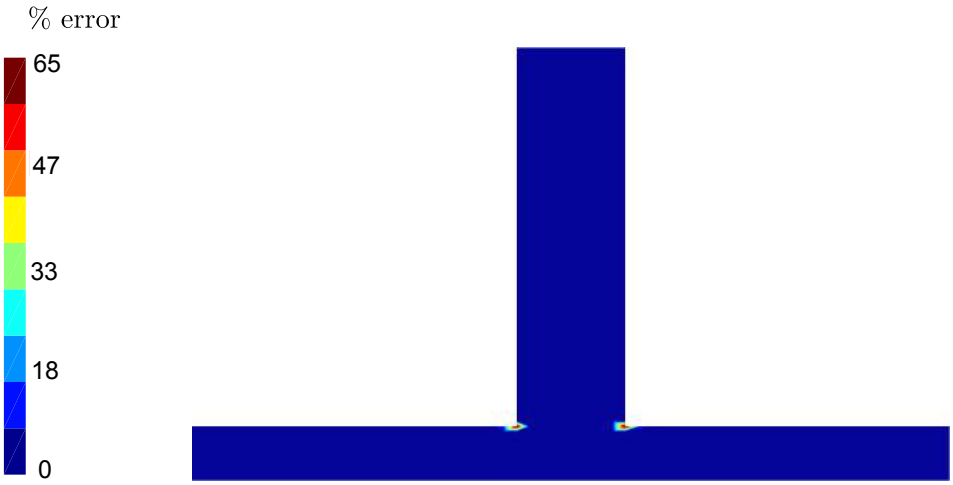

(c) Residual

Figure 4.19: Distribution of shear stress (τ_{yz}) in the cross-section at 50% of the beam length from the clamped end.

capable of accurate stress predictions with considerably less DOFs than 3D FE, which is a proxy for computational cost. From a numerical standpoint, SLE and LE models behave identically. This result allows either of the two models to be used with confidence. SLE meshes, however, give an extra advantage, because, unlike LE meshes, they facilitate element-wise hierarchical refinement thereby reducing the need for cross-sectional remeshing.

4.3 Capturing 3D Stress Fields in Stiffened Panels

This section aims to investigate the behaviour of previously introduced 1D UF, based on the Serendipity Lagrange expansion functions, in the analysis of stiffened structures. The first part of this section presents the static analysis of a flat panel with stiffeners reinforced in longitudinal and transverse directions. In the second part, a similar but curved panel is used to assess the validity of the mapping technique employed on the SLE model for analysing curved cross-section geometries. These examples have been selected to show the capabilities of the present formulation in representing a wide range of structures used in civil and aerospace industries. The present formulation requires these structures to be modelled as a 1D beam with different cross-sections running along the length. To understand this modelling strategy, consider two beam models, beam-A and beam-B. Beam-A represents the panel reinforced with longitudinal stringers, with the beam axis aligned along its length and cross-section as shown in Figure 4.20(b) and 4.21(b) for flat and curved panels, respectively. While beam-B represents the panel reinforced with a transverse stiffener, with beam axis aligned along the thickness direction and the section normal to it is treated as its cross-section as shown in Figure 4.20(c) for flat and Figure 4.21(c) for curved. These beam models are connected along the length to get the desired structures. The cross-section discretisation feature of the SLE model within the UF framework allows different cross-section beams to connect and maintain the displacement continuity at the interface.

All the essential geometrical parameters for stiffened flat and curved panels, considered in the present study, are described in Figures 4.20 and 4.21, respectively. The constituent material is isotropic with Young's modulus, $E = 71.7$ GPa and Poisson's ratio, $\nu = 0.3$. The structures are clamped at one end ($y = 0$) and a surface load of 1 kN is applied across the section at the other end ($y = 1$ m). The load applied in case of a flat panel is in the negative z-direction, whereas in case of a curved panel it is in the positive z-direction. For both cases, beam-A and beam-B are discretised using 5 and 3 B4 (four-noded cubic) elements, respectively, which adds up to 29 B4 elements for the complete structure. It is to be noted that the distribution of nodes, within each beam subset, follows the Chebyshev distribution, as described in Section 3.3. In doing so, the accuracy of the results increases near the stringer-rib interface as well as towards the clamped end, without the need to increase the total number of beam nodes. Furthermore, the cross-sections of beam-A and beam-B are discretised with 22 and 42 SL5 (fifth-order expansion) elements, respectively. This beam and cross-section discretisation results into a total of 110,220 unknown variables or

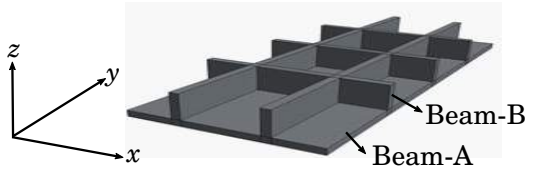

(a) Stiffened flat panel

All units in metres

$b = 0.4$	$h = 0.02$	$L_1 = 0.24$
$b_1 = 0.1$	$h_s = 0.04$	$L_2 = 0.23$
$b_s = 0.02$	$L = 1$	$L_s = 0.02$

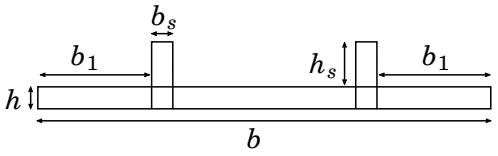

(b) Cross-section of Beam A

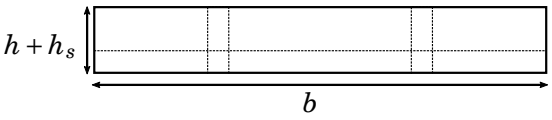

(c) Cross-section of Beam B

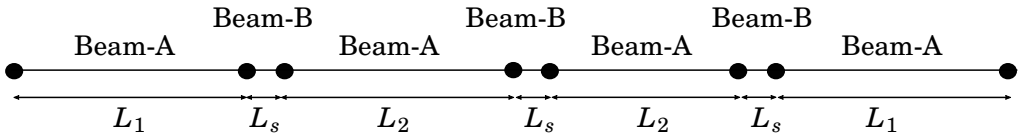

(d) Cross-section assembly along the length

Figure 4.20: Stiffened flat panel — Geometry.

degrees of freedom (DOFs). The number of beam elements, cross-sectional mesh and the order of expansion is decided by performing a convergence analysis. For the sake of brevity, only the converged results for all the cases are presented. For the curved stiffened panel, the 2D Jacobian transformation required to map the curved cross-section, as described in Section 3.5, is evaluated by employing the nonlinear function that exactly describes the arch (or curved cross-section geometry). In both the numerical cases assessed, stresses are computed at various locations along the beam and are compared with those obtained with high fidelity finite element analyses performed in ANSYS.

4.3.1 Stiffened Flat Panel

The static analysis of a stiffened flat panel is performed by employing the UF-SLE model and results obtained are presented in this section. To validate the present approach, a reference solution is required, which is obtained by discretising the structure with a finite number of 3D elements and analysing it using commercial finite element package, ANSYS. A mesh convergence analysis is performed which ensures that an optimum number of elements are employed to obtain accurate results. In this case, the model is discretised with 669,696 `SOLID186` (3D 20-node) elements, which leads to solving 8,832,243 equations (DOFs).

Normal stress, σ_{yy}, values are plotted along the length of the panel at two different locations, along the top surface of the stiffener and along the top surface of the skin, as shown in

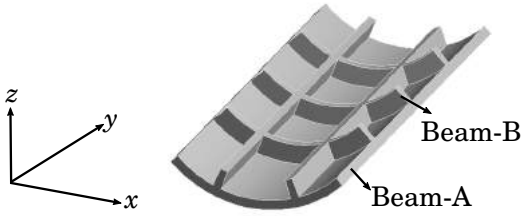

All units in metres

$b = 0.4$	$h = 0.02$	$L_1 = 0.24$
$b_1 = 0.1$	$h_s = 0.04$	$L_2 = 0.23$
$b_s = 0.02$	$L = 1$	$L_s = 0.02$

(a) Stiffened curved panel

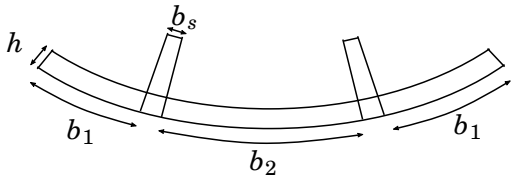

(b) Cross-section of Beam A

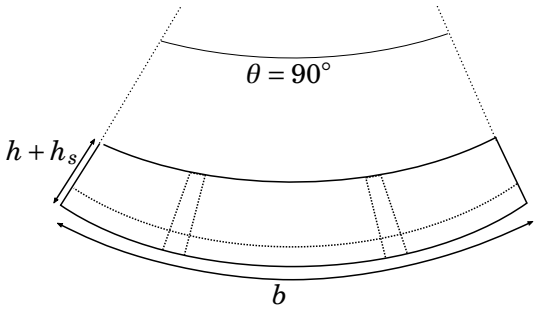

(c) Cross-section of Beam B

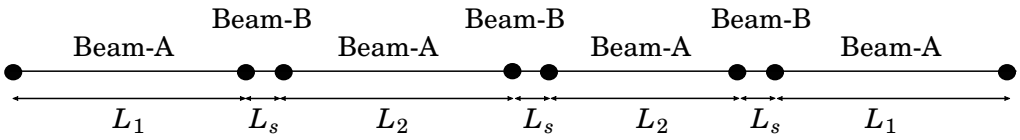

(d) Cross-section assembly along the length

Figure 4.21: Stiffened curved panel — Geometry.

Figure 4.22. These results are key towards the verification of the present modelling technique of connecting different cross-sections along the beam length. This displacement-based formulation naturally satisfies the displacement continuity requirement at the stringer-rib interface; however, a high-order displacement field approximation is required to obtain a continuous stress/strain distribution. The present model clearly meets this requirement, and therefore, no discrepancies are observed in the normal stress values along the length when compared to those obtained with ANSYS.

Furthermore, to demonstrate the capabilities of the proposed model in predicting the 3D stress fields in such structures, axial and transverse stress components are measured at several locations. The distribution of axial normal, σ_{yy}, transverse shear, τ_{yz}, and transverse normal, σ_{zz}, stresses are plotted, along the width of the panel at $(y,z) = (L/4,h/2)$ in Figur 4.23 and through-thickness at $(x,y) = (b/2,L/4)$ in Figure 4.24. To show the ability of the model in capturing the accurate structural response particularly at the rib-stringer junction, through-thickness normal and transverse stresses are presented in Figure 4.25. All these plots clearly show that the stress values are in an excellent agreement with those obtained with the 3D FE model. In

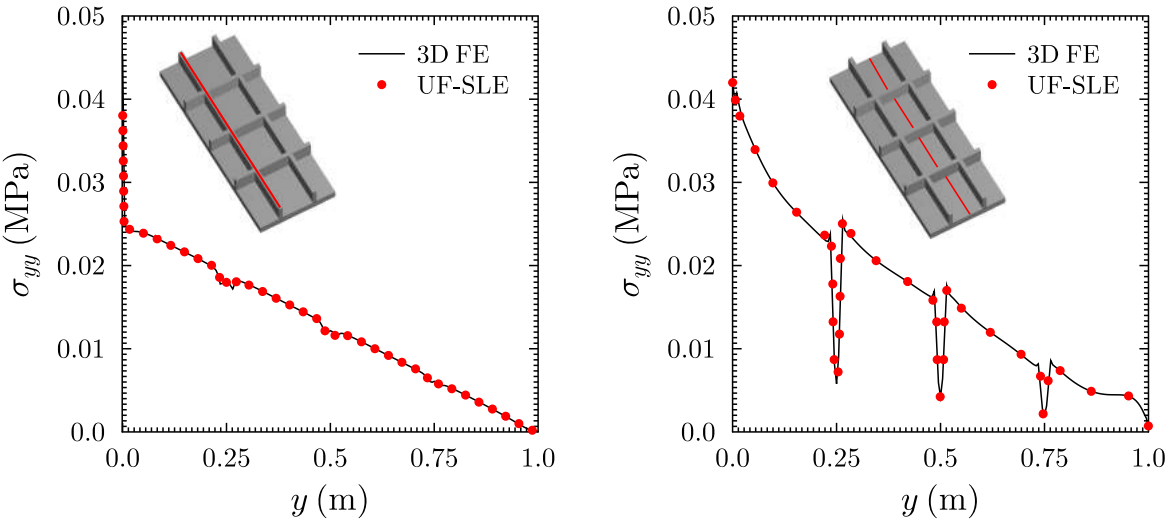

(a) σ_{yy} for $(x,z) = \left(b_1 + \frac{b_s}{2}, h + h_s\right)$ and $y \in [0, L]$

(b) σ_{yy} for $(x,z) = \left(\frac{b}{2}, h\right)$ and $y \in [0, L]$

Figure 4.22: Variation of axial normal stress, σ_{yy}, along the length of the flat panel.

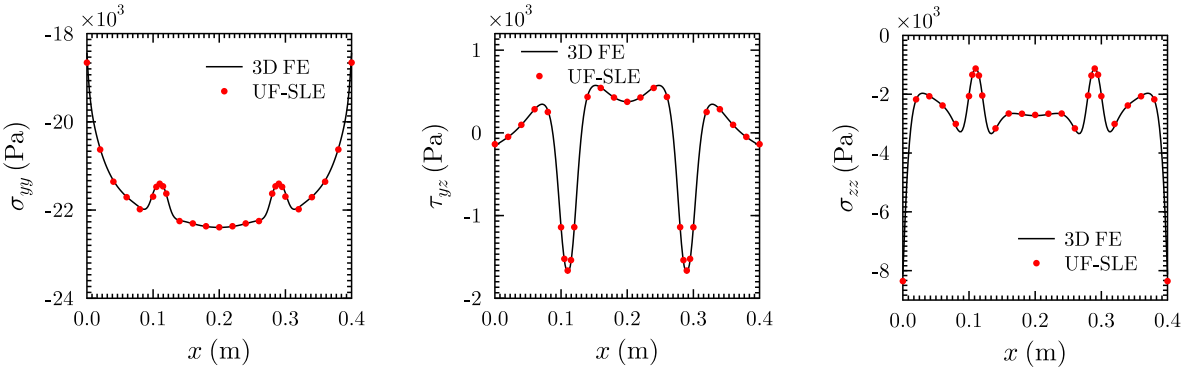

(a) Axial normal stress (σ_{yy})

(b) Transverse shear stress (τ_{yz})

(c) Transverse normal stress (σ_{zz})

Figure 4.23: Variation of normal and shear stresses across the panel width at $(y,z) = (L/4, h/2)$.

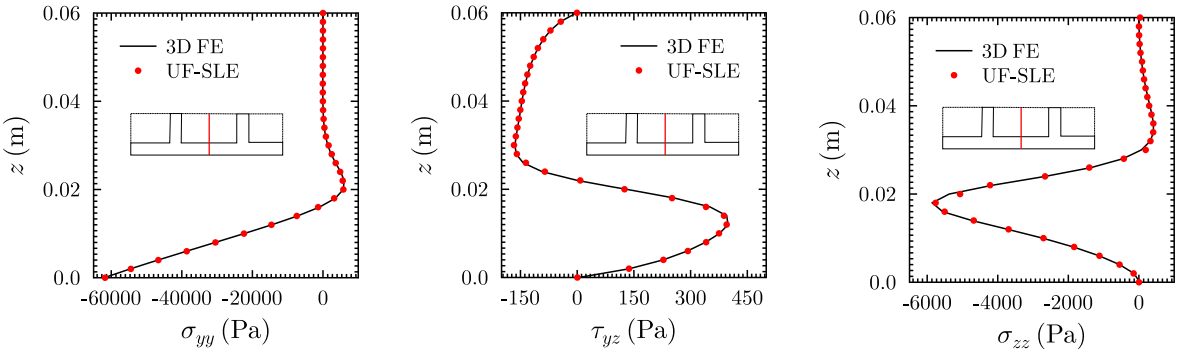

(a) Axial normal stress (σ_{yy}) (b) Transverse shear stress (τ_{yz}) (c) Transverse normal stress (σ_{zz})

Figure 4.24: Through-thickness distribution of normal and shear stresses at $(x, y) = (b/2, L/4)$.

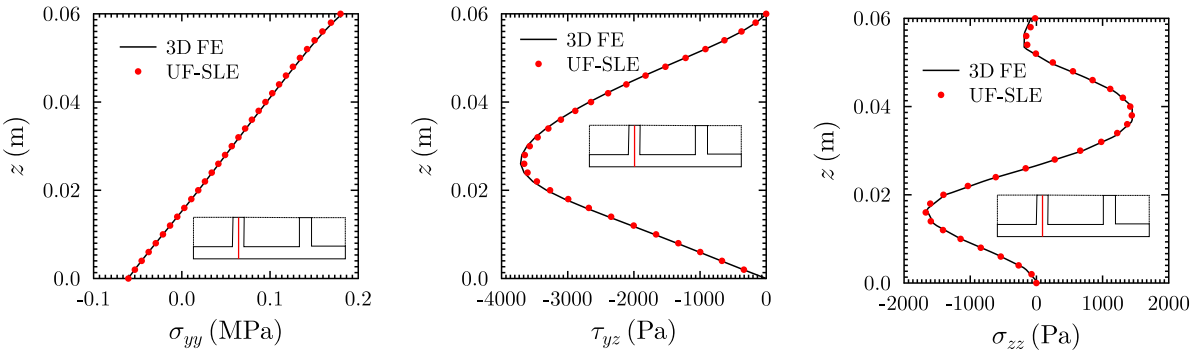

(a) Axial normal stress (σ_{yy}) (b) Transverse shear stress (τ_{yz}) (c) Transverse normal stress (σ_{zz})

Figure 4.25: Through-thickness distribution of normal and shear stresses at $(x, y) = (b_1 + b_s/2, L/4)$.

addition, the proposed high-order refined beam model can capture 3D stress fields accurately in a computationally efficient manner.

4.3.2 Stiffened Curved Panel

The scope of this section is to assess the proposed high-order UF-SLE model in capturing the structural response of a curved panel, stiffened with stringers and ribs, that usually require the use of 2D or 3D elements. A 3D FE analysis, performed is ANSYS, is used as a reference solution for validation, where the structure is discretised with `SOLID186` elements and 9,286,608 equations (DOFs) are solved to yield converged results.

Figure 4.26 shows the bending stress distribution at the top of a stringer along its length. Through-thickness variation of axial normal, σ_{yy}, transverse shear, τ_{yz}, and transverse normal, σ_{zz}, stresses, computed at the rib-stringer junction at $y = L/4$, is shown in Figure 4.27. It is to be noted that results shown in Figure 4.27(b) and 4.27(c) for τ_{yz} and σ_{zz} are computed in the local

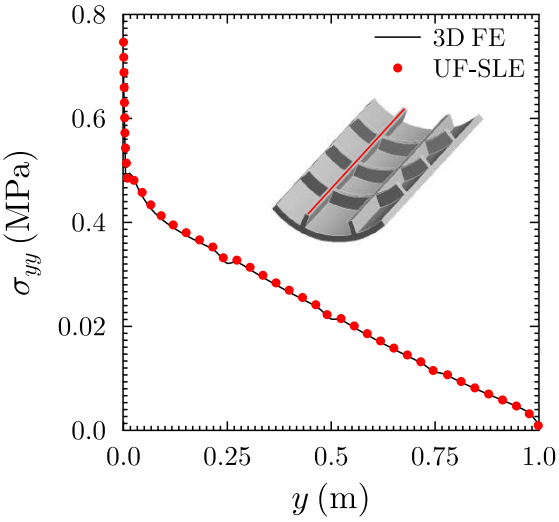

Figure 4.26: Variation of axial normal stress, σ_{yy}, along the length of the curved panel.

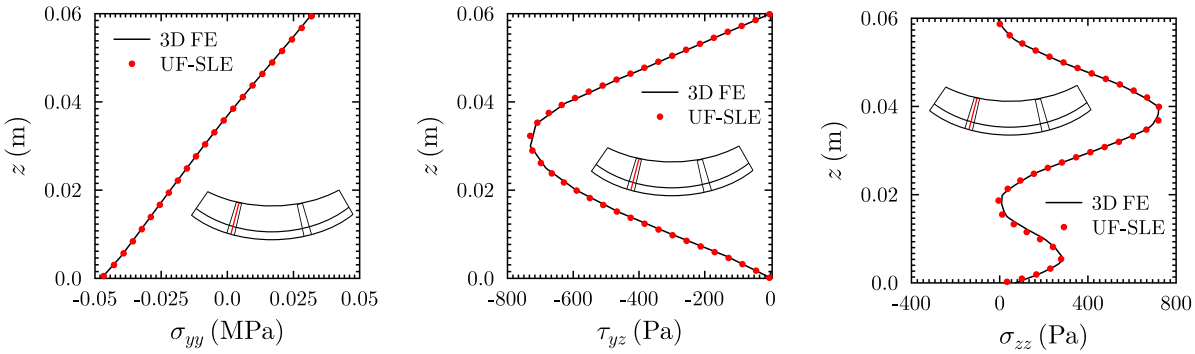

(a) Axial normal stress (σ_{yy}) (b) Transverse shear stress (τ_{yz}) (c) Transverse normal stress (σ_{zz})

Figure 4.27: Through-thickness distribution of normal and shear stresses at rib-stringer junction ($y = L/4$).

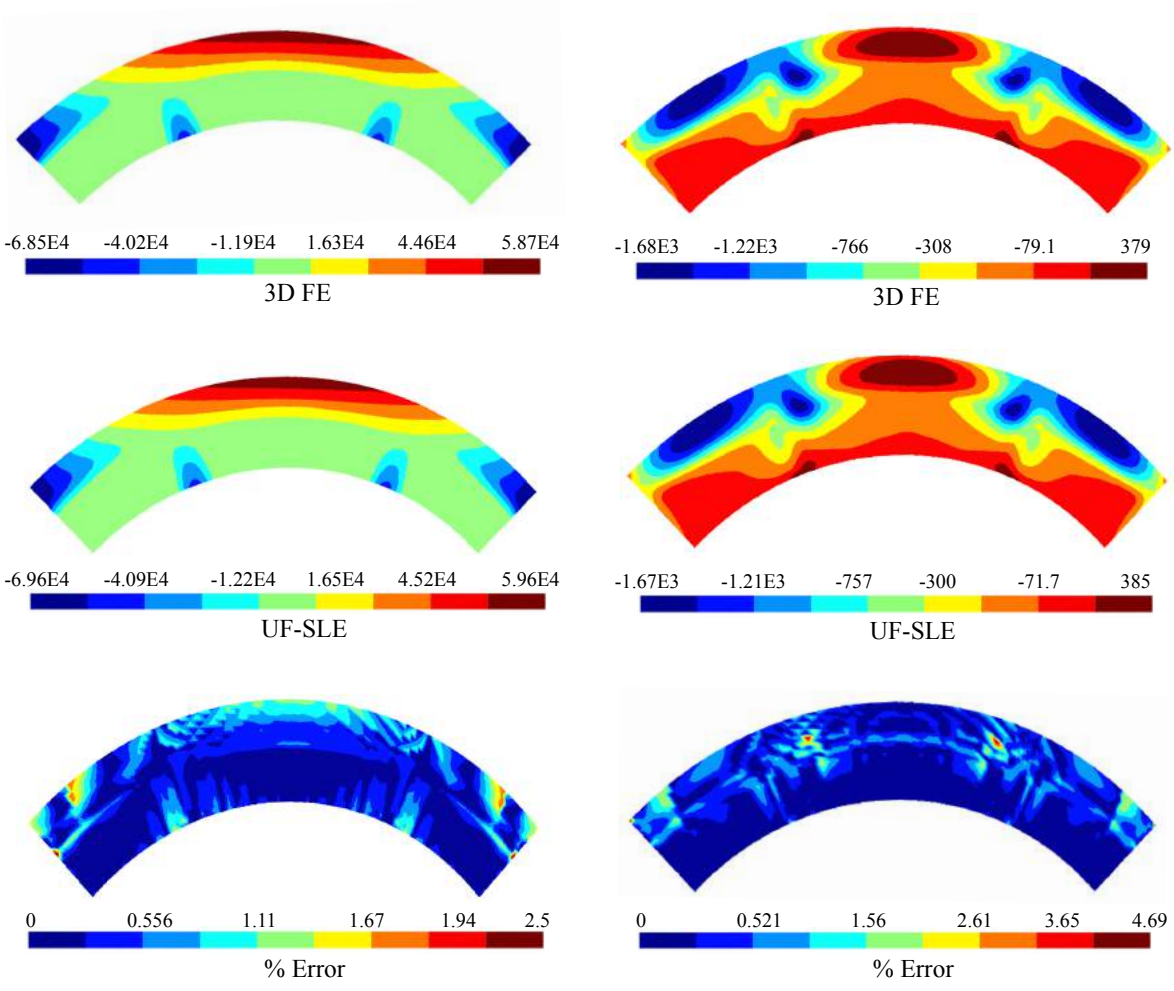

(a) σ_{yy} (Pa) at $(x, L/4, z)$ (b) τ_{yz} (Pa) at $(x, L/4, z)$

Figure 4.28: Distribution of axial normal, σ_{yy}, and transverse shear, τ_{yz}, stress across the section of the curved panel at 25% of the length from the clamped end.

coordinate system (obtained by rotating the global coordinate system about the y-axis such that the z-axis points towards the centre of curvature). To highlight the UF-SLE model's capability in capturing localised regions accurately, contour plots of normal and shear stresses (σ_{yy} and τ_{yz}) are computed across the entire cross-section at $y = L/4$. The stress distribution obtained using the UF-SLE model is compared with the 3D FE solution, and the percentage difference is evaluated as shown in Figure 4.28. From the contour plots, it is evident that the proposed model is capable of predicting an accurate response of the structure with less DOFs than the 3D FE model.

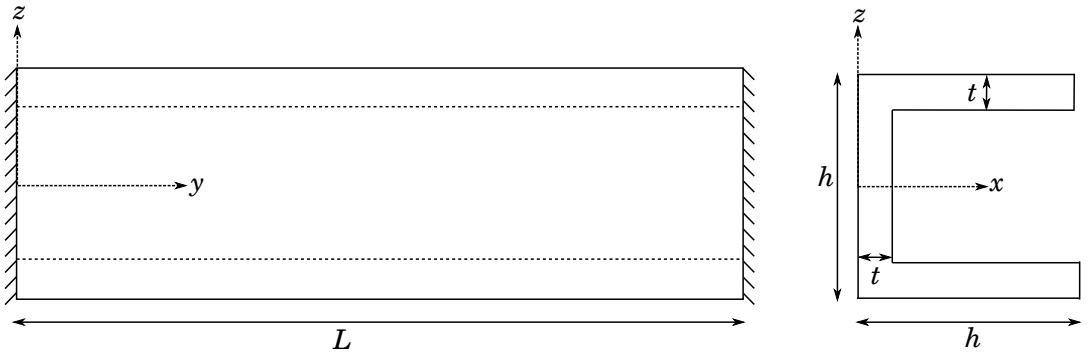

Figure 4.29: C-section beam clamped at both the ends.

Table 4.3: Displacement and stress components at various locations in a C-section beam.

Model					u_z (mm) $\left(h, \frac{L}{2}, \frac{h}{2}-t\right)$	σ_{xx} (MPa) $\left(t, \frac{L}{2}, \frac{h}{2}\right)$	σ_{yy} (MPa) $\left(t, \frac{L}{2}, t+\frac{h-t}{2}\right)$	DOFs #
3D FE (ANSYS)					-3.442	79.75	-18.14	2,020,923
SL2					-3.307	59.68	-16.39	17199
SL3					-3.379	61.23	-17.85	27300
SL4					-3.398	76.31	-17.79	40677
SL5					-3.410	78.90	-17.97	57330
SL6					-3.419	79.49	-18.09	77259
SL7					-3.425	79.58	-18.19	100464
Expansion order for beam elements								
EL 1-5	EL 6-14	EL 15-16	EL 17-25	EL 26-30				
SL2	SL4	SL5	SL4	SL2	-3.403	78.48	-18.03	31122

4.4 Assessment of the Unified Formulation with Variable Kinematics Model

The node-dependent (or variable) kinematics approach employed with the UF-SLE model, as described in Section 3.6, is assessed in predicting the static response of structures. The aim of this section is to assess the NDK methodology and highlight the computational efficiency gain achieved over the constant kinematics UF-SLE model. For this purpose, a C-section beam of length $L = 1\,\text{m}$, height $h = 0.1\,\text{m}$ and wall thickness $t = 0.005\,\text{m}$ is considered, as shown in Figure 4.29. The beam is clamped at both the ends and is subjected to a point load, $P_z = 1000$ N, at the mid-span $(h, \frac{L}{2}, \frac{h}{2})$. The constituent material is isotropic with Young's modulus $E = 71.7\,\text{GPa}$ and Poisson's ratio $\nu = 0.3$. The beam is discretised with 30 B4 elements along its length, 5 SLE elements in the cross-section and different expansion orders are used at different sections along the beam.

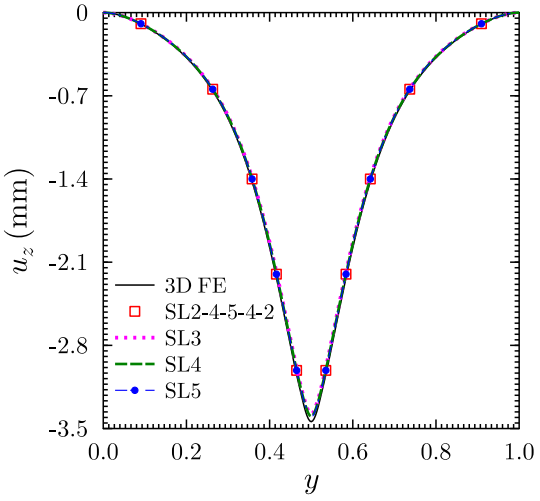

(a) u_z for $(x,z) = \left(h, \frac{h}{2} - t\right)$ and $y \in [0, L]$

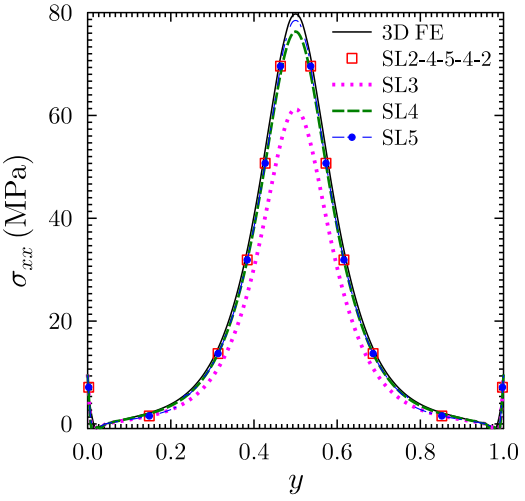

(b) σ_{xx} for $(x,z) = \left(t, \frac{h}{2}\right)$ and $y \in [0, L]$

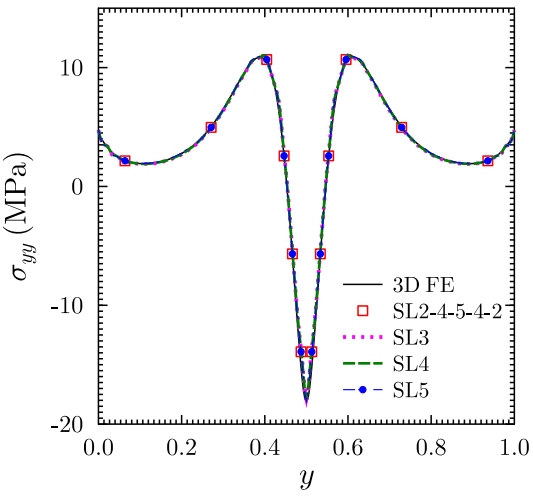

(c) σ_{yy} for $(x,z) = \left(h, t + \frac{h-t}{2}\right)$ and $y \in [0, L]$

Figure 4.30: Variation of transverse displacement and normal stresses along the length of a C-section beam

.

The vertical displacement, u_z at $(h, \frac{L}{2}, \frac{h}{2} - t)$, normal stress, σ_{xx} at $(t, \frac{L}{2}, \frac{h}{2})$ and σ_{yy} at $(t, \frac{L}{2}, t + \frac{h-t}{2})$ are evaluated for all the cases as shown in Table 4.3. A 3D FE analysis, performed with the commercial FE code, ANSYS, is used as a reference for validation. The displacement and stress distributions along the length are plotted in Figure 4.30 and are found to be in a good agreement with 3D FE solutions. From Table 4.3 and Figure 4.30, it is observed that at least a fifth-order expansion model is required to achieve convergence. The constant kinematics UF-SLE model of order 5 employs ~57,000 DOFs while the variable kinematics UF-SLE model of varying expansion order (SL-2, SL-4 and SL-5) employs ~31,000 DOFs. The accuracy of results in similar in both the cases. The local effects are expected due to the point load application at the mid-span, therefore, a refined SLE model is required only in the vicinity of this region. The variable kinematics approach offers increased flexibility to employ high-order models in specific regions to accurately capture local effects, and thereby, reduces the computational effort without compromising on the accuracy of the solution. However, applying this methodology requires prior knowledge of the structural response behaviour in order to decide the region where refinement is needed.

4.5 Conclusions

We have aimed to capture 3D stress fields accurately using 1D models with greater computational efficiency than 3D finite element analyses. The Serendipity Lagrange expansion model introduced in Chapter 3 within the framework of Carrera's Unified Formulation is employed to carry out the static analyses of isotropic beam-like structures. The examples are chosen such that they challenge and exemplify the merits of the proposed approach. The model is benchmarked against traditional Taylor and Lagrange expansions, 3D finite element solutions as well as analytical formulae (where available). The main findings from the present study are summarised as follows:

1. The effect of collocating beam nodes using a Chebyshev biased mesh has been studied. The mesh was refined in the regions where stress fields are expected to change rapidly. It has been observed that, by employing this node distribution, accurate results can be obtained near constraints, without the need to increase the total number of beam nodes. This type of discretisation also precludes spurious oscillations in the solutions, previously observed in CUF models.

2. For the numerical cases assessed, the Serendipity Lagrange expansion model retains benefits of both the Lagrange model (cross-sectional discretisation) and the Taylor model (hierarchical approximations), eliminating their disadvantages, as described in the following points.

3. In order to capture the response of beam-like structures accurately, high-order models may be required. For Taylor models, as the order of expansion increases, the conditioning number of the stiffness matrix decreases exponentially. This problem makes the system

ill-conditioned and numerically unstable. Serendipity Lagrange expansions overcome this limitation and are therefore suitable for analysing beams with complex cross-sections.

4. Similarly to Lagrange expansion models, the Serendipity Lagrange ones allow for cross-sectional discretisation. This feature, together with the hierarchical nature of the local expansions, makes Serendipity Lagrange elements particularly suited for capturing localised stress fields near boundaries, discontinuities and points of load application, unlike the Taylor expansion model. Cross-sections are also discretised in the Lagrange model, however model building is cumbersome because remeshing is the only way to improve accuracy.

5. Furthermore, the cross-section discretisation feature of the Serendipity Lagrange expansion model enables a beam to be modelled with different cross-sections along its length and maintains displacement and stress continuity at the interface. This feature makes it possible to analyse complex structures such as stiffened panels. Moreover, using different set of shape functions for geometric and kinematic description enables a broad class of structure to be modelled regardless of the geometrical complexity of the cross-section.

6. Finally, the node dependent kinematics approach allow different kinematic models do be used at each node of the beam element, thereby making it possible to use refined models at desired regions. The model is assessed by means of static analysis of a thin-walled C-section beam and results obtained clearly shows the improvement in performance compared to constant kinematics model.

The proposed Serendipity Lagrange expansion models proved to be an efficient and effective means for computing localised 3D stress fields for solid and thin-walled isotropic beam-like structures.

CHAPTER 5

THREE-DIMENSIONAL STRESS ANALYSIS FOR STRAIGHT-FIBRE COMPOSITE STRUCTURES

Accurate stress prediction in composite laminates is crucial for safe design under different loading conditions. Classical laminated theory, *i.e.* those based on the Euler-Bernoulli and Kirchhoff hypotheses, respectively for beams and plates/shells are inaccurate for relatively thick laminates as 3D effects such as transverse shear and normal deformations are neglected. Therefore, 3D finite element models are often employed for accurate stress analysis. However, these models are computationally expensive when used for laminates with a large number of layers, in optimisation studies, or for non-linear analyses. To address this issue, the Serendipity Lagrange expansion-based Unified Formulation (UF-SLE), introduced in Chapter 3, is presented for the analysis of straight-fibre, laminated composite and sandwich structures. Current focus is on prismatic, beam-like structures. However, the models presented herein are of broader interest because they can be extended to complex, non-prismatic geometries via geometric mapping discussed further in Chapter 9. A Layer-Wise approach is adopted, and together with the properties of SLE models, *i.e.* refinement by combined cross-sectional discretisation and hierarchical expansion, both local and global responses are obtained accurately and in a computationally efficient manner. The present formulation, which has displacements as degrees of freedom, does not ensure continuous transverse stresses across layer interfaces. Thus, in order to capture through-thickness transverse shear and normal stresses reliably, a post-processing step is employed where the transverse stresses are recovered by integrating the in-plane stresses in Cauchy's 3D indefinite equilibrium equations.

In Section 5.2, the UF-SLE model is benchmarked against Pagano's closed-form 3D elasticity solution [193] for simply-supported, straight-fibre laminated composite and sandwich beams. The results obtained are also compared to those available in the literature. Section 5.3 highlights

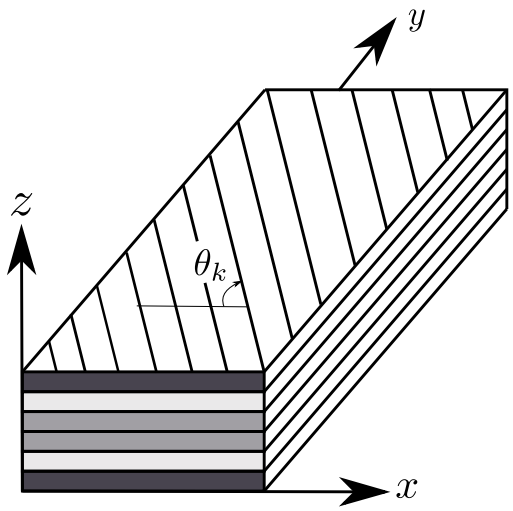

Figure 5.1: Reference system for a laminated composite beam.

the ability of the UF-SLE model in predicting the structure's response efficiently, including boundary layer regions, *i.e.* towards clamped ends, where 3D effects become relevant and computationally inexpensive classic theories are not applicable. As a result, global analyses (*e.g.* overall displacements, buckling, *etc.*) and local analyses (*e.g.* stress concentrations) are combined within a single, computationally efficient model. In this case the results are compared with high-fidelity, yet computationally expensive, finite element solutions. Finally, Section 5.4 presents through-thickness plots of the transverse normal stress computed for various laminated beams, by employing the stress recovery scheme using 3D equilibrium equations. The performance of the proposed approach, in terms of computational cost and precision, is assessed. Significant computational efficiency gains over 3D finite elements are observed for similar levels of accuracy.

5.1 Preliminaries

Consider a laminated beam of length L, rectangular cross-section of width b and thickness h, composed of N layers. The material properties and the thickness of each layer may be entirely different. The beam is referred to a Cartesian coordinate system (x,y,z), where the y-direction is defined to be along the principle beam axis, while the z-axis is in the transverse stacking direction as shown in Figure 5.1. Let θ denote the fibre orientation angle and the subscript k be used to refer to layer k.

The UF-SLE model allows a layer-wise approach to be implemented directly where each layer can be modelled as one sub-domain and the kinematics within each layer (or sub-domain) can be varied hierarchically as depicted in Figure 5.2 (where the shading denotes hierarchical functions spanning the sub-domain).

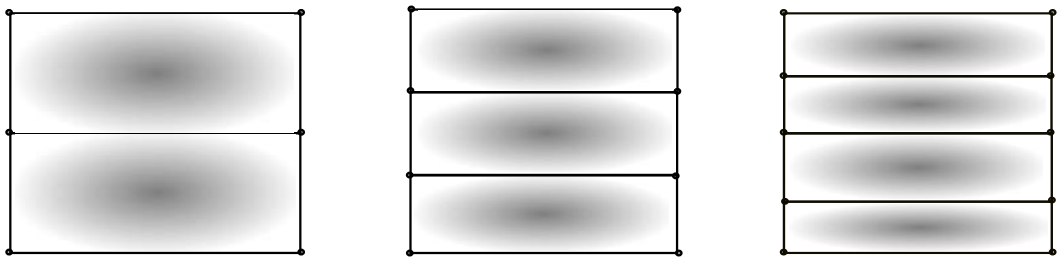

Figure 5.2: Cross-sectional discretisation using 4-noded SL elements

The laminates considered in the present study are assumed to be homogeneous and operate in the linear elastic range. The stress-strain relation for an orthotropic laminate takes the form as given below

$$\boldsymbol{\sigma} = \bar{\boldsymbol{C}}\boldsymbol{\varepsilon}, \tag{5.1}$$

or

$$\begin{Bmatrix} \sigma_{xx} \\ \sigma_{yy} \\ \sigma_{zz} \\ \tau_{yz} \\ \tau_{xz} \\ \tau_{xy} \end{Bmatrix} = \begin{bmatrix} \bar{C}_{11} & \bar{C}_{12} & \bar{C}_{13} & 0 & 0 & \bar{C}_{16} \\ \bar{C}_{21} & \bar{C}_{22} & \bar{C}_{23} & 0 & 0 & \bar{C}_{26} \\ \bar{C}_{31} & \bar{C}_{32} & \bar{C}_{33} & 0 & 0 & \bar{C}_{36} \\ 0 & 0 & 0 & \bar{C}_{44} & \bar{C}_{45} & 0 \\ 0 & 0 & 0 & \bar{C}_{54} & \bar{C}_{55} & 0 \\ \bar{C}_{61} & \bar{C}_{62} & \bar{C}_{63} & 0 & 0 & \bar{C}_{66} \end{bmatrix} \begin{Bmatrix} \varepsilon_{xx} \\ \varepsilon_{yy} \\ \varepsilon_{zz} \\ \gamma_{yz} \\ \gamma_{xz} \\ \gamma_{xy} \end{Bmatrix}, \tag{5.2}$$

where $\bar{\boldsymbol{C}}$ is the transformed material stiffness matrix that depends on the mechanical properties of the laminate material and fibre orientation angle. The coefficients $\bar{C}_{ij}$ are the transformed elastic coefficients referred to the (x,y,z) coordinate system, which are related to the elastic coefficients in the material coordinates C_{ij} by the transformation matrix $\boldsymbol{T}$ as given below

$$\bar{\boldsymbol{C}} = \boldsymbol{T}\boldsymbol{C}\boldsymbol{T}^{\top}, \tag{5.3}$$

The coefficients C_{ij} and the matrix $\boldsymbol{T}$ can be found in Appendix A or in the reference [194].

It is common practice to compute stresses using the constitutive relation as given by equation (7.17). However, this may lead to discontinuities of stresses at the interface of two adjacent layers (particularly in a displacement-based approach) and thus violates traction continuity. Accurate modelling of a laminated structure requires a description of interlaminar continuous transverse stresses (shear and normal components). In order to improve the 3D stress fields predicted by displacement-based models, transverse stresses can be recovered by employing the indefinite equilibrium equations of 3D elasticity and integrating in-plane stresses in the thickness direction. The 3D stress equilibrium equations for the static case, and in the absence of

volume forces, are

$$\frac{\partial \sigma_{xx}}{\partial x} + \frac{\partial \tau_{xy}}{\partial y} + \frac{\partial \tau_{xz}}{\partial z} = 0, \tag{5.4}$$

$$\frac{\partial \tau_{yx}}{\partial x} + \frac{\partial \sigma_{yy}}{\partial y} + \frac{\partial \tau_{yz}}{\partial z} = 0, \tag{5.5}$$

$$\frac{\partial \tau_{zx}}{\partial x} + \frac{\partial \tau_{zy}}{\partial y} + \frac{\partial \sigma_{zz}}{\partial z} = 0. \tag{5.6}$$

In-plane stresses, σ_{xx}, σ_{yy} and τ_{xy}, and their derivaties are computed conventionally using constitutive relations. Transverse shear stresses, τ_{xz} and τ_{yz}, are recovered from equations (5.4) and (5.5) and the transverse normal stress σ_{zz} is calculated afterwards from equation (5.6) as given by

$$\sigma^k_{zz}(z) = \sigma^k_{zz_b} - \int_{z^k_b}^{z} \left(\frac{\partial \tau_{zx}}{\partial x} + \frac{\partial \tau_{zy}}{\partial y} \right) dz, \tag{5.7}$$

where $\sigma^k_{zz}(z)$ is the stress value in the k^{th}-layer and $\sigma^k_{zz_b}$ is the stress value at the bottom of the k^{th}-layer.

Furthermore, it is noted that, in order to recover the transverse stresses accurately from the stress equilibrium equations, exact derivatives of the in-plane stresses are required. With the hierarchical nature of the SLE model, such accuracy can be achieved by including higher-order terms in the displacement field approximation. This level of accuracy is not possible for conventional 3D FE elements, as linear or quadratic elements are usually employed, the derivatives of the in-plane stresses are obtained by using numerical schemes, such as finite differences, which may not be sufficiently accurate.

5.2 Model Verification

The verification is carried out for a relatively thick square cross-section beam of length-to-thickness ratio, $L/t = 8$. The beam is aligned with the Cartesian y-axis and the cross-section is in the xz-plane. The layers are arranged in a general fashion with different ply thickness, material properties and material orientations. The beam is simply-supported at the two ends $y = 0$ and $y = L$ and is assumed to undergo static deformations in plane strain (x-direction) under a sinusoidal distributed load, equally divided between the top and the bottom surface, $P^{\mathrm{t}}_z = P^{\mathrm{b}}_z = -q_0/2 \cdot \sin(\pi y/L)$, as shown in Figure 5.3. It is to be noted that compared to Pagano's original benchmark [193], Groh and Weaver [89] split the sinusoidal load between the top and bottom surfaces to minimise through-thickness normal stretching. This loading condition allowed for a fairer comparison with their equivalent single layer (HR3-RZT) model and demonstrated that it could accurately capture the tractions on the top and bottom surfaces without *a priori* assumptions. As the HR3-RZT model is also used as a reference solution herein, we use the benchmark with split sinusoidal tractions (although this is not strictly necessary for the present

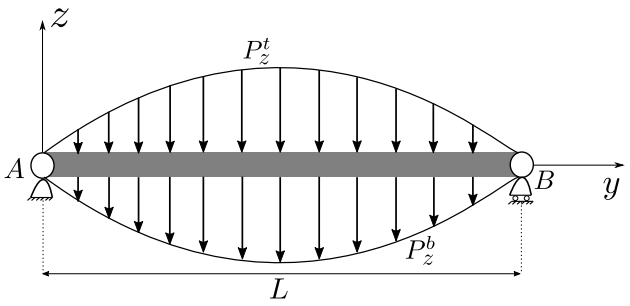

Figure 5.3: Representation of a simply-supported multi-layered beam subjected to a sinusoidal load at the top and the bottom surface.

UF-SLE model). The material properties and stacking sequences adopted are shown in Tables 6.1 and 6.2, respectively. This combination of materials, ply thickness and stacking sequence are taken from a recent paper by Groh and Weaver [89] on modelling highly heterogeneous laminated beams using the Hellinger-Reissner mixed formulation. The wide range of laminates considered, from simple to challenging, allows the full capabilities of the current formulation to be tested and validated. Material p represents a carbon-fibre reinforced plastic, material m a reinforced plastic with increased transverse stiffness, pvc is a poly-vinyl chloride foam modelled as an isotropic material and h represents a honey-comb core modelled as a transversely isotropic material. The plies made of these materials are stacked together in different combinations to form laminates as presented in Table 6.2. Laminates A-D are symmetric; I-J are non-symmetric cross-ply composites. Although these are not widely used in industry due to transverse cracking issues, it is a good test case for model validation as the $0^\circ/90^\circ$ sequence maximises the zig-zag effect. Laminates E-G are symmetric thick-core sandwich construction. In laminate F, the low transverse shear stiffness of material h compared to that of material p exacerbates the zig-zag effect. Laminate G is a challenging sandwich construction with a combination of three distinct materials. Finally, laminates K-M represent highly heterogeneous laminated plates.

The UF-SLE model is used for the analyses presented in this section. The structure is discretised with 30 B4 (four-noded) elements along the length; the cross-section is divided into sub-domains (one per layer). Within each sub-domain (Serendipity Lagrange element) a fifth-order expansion is employed. The number of beam elements and the order of expansion in the cross-section are decided by performing a convergence analysis. For the sake of brevity, only the converged results for all the cases are presented.

In this section and throughout the chapter, normalised quantities of the axial stress σ_{yy}, transverse shear stress τ_{yz} and transverse normal stress σ_{zz} are used as metrics to assess the accuracy of the UF-SLE model. The normalised quantities are defined as follows

$$\bar{\sigma}_{yy} = \frac{t^2}{q_0 L^2} \cdot \sigma_{yy}(x,y,z), \quad \bar{\tau}_{yz} = \frac{1}{q_0} \cdot \tau_{yz}(x,y,z), \quad \bar{\sigma}_{zz} = \frac{1}{q_0} \cdot \sigma_{zz}(x,y,z). \tag{5.8}$$

Table 5.3 shows the maximum through-thickness normalised axial stress $\bar{\sigma}_{yy}^{\max}$ and transverse

Table 5.1: Mechanical properties of the materials considered in the present study.

Material	E_x	E_y	E_z	G_{yz}	G_{xz}	G_{xy}
	[GPa]					
p	6.89	172.37	6.89	3.45	1.38	3.45
m	6.89	224.56	68.94	56.6	22.61	4.48
pvc	1.723	1.723	1.723	0.663	0.663	0.663
h	1.723×10^{-3}	1.723×10^{-3}	17.23×10^{-3}	6.03×10^{-3}	12.06×10^{-3}	6.9×10^{-6}
	ν_{yz}		ν_{xz}		ν_{xy}	
p	0.25		0.25		0.01	
m	0.25		0.025		7.676×10^{-3}	
pvc	0.3		0.3		0.3	
h	3.0×10^{-5}		3.0×10^{-5}		0.9	

Table 5.2: Stacking sequence for laminates considered in the present study. Subscripts indicate the repetition of a property over the corresponding number of layers.

Laminate	**Layer thickness ratio**	**Materials**	**Stacking sequence**
Symmetric			
A	$[(1/3)_3]$	$[p_3]$	[0/90/0]
B	$[0.2_5]$	$[p_5]$	[0/90/0/90/0]
C	$[0.2_5]$	$[p_5]$	[90/0/90/0/90]
D	$[(1/51)_{51}]$	$[p_{51}]$	$[0/(90/0)_{50}]$
E	$[(1/30)_3/0.8/(1/30)_3]$	$[p_3/pvc/p_3]$	$[0/90/0_3/90/0]$
F	$[(1/30)_3/0.8/(1/30)_3]$	$[p_3/h/p_3]$	$[0/90/0_3/90/0]$
G	$[0.1_2/0.2_3/0.1_2]$	$[p_2/pvc/h/pvc/p_2]$	$[90/0_5/90]$
H	$[(1/12)_{12}]$	$[p_{12}]$	$[\pm45/\mp45/0/90_2/0//\mp45/\pm45]$
Anti-Symmetric			
I	[0.3/0.7]	$[p_2]$	[0/90]
J	$[0.25_4]$	$[p_4]$	[0/90/0/90]
K	[0.1/0.3/0.35/0.25]	[p2/m/p]	$[0/90/0_2]$
L	[0.3/0.2/0.15/0.25/0.1]	[p3/m/p]	$[0/90/0_2/90]$
M	[0.1/0.7/0.2]	[m/pvc/p]	$[0_3]$

shear stress $\bar{\tau}_{yz}^{\max}$ at $y = L/2$ and $y = 0$, respectively. The results obtained are validated against Pagano's 3D elasticity solution and are also compared with those given by Groh and Weaver [89] using the Hellinger-Reissner third-order refined zig-zag theory (HR3-RZT). For all the cases assessed, the accuracy of results obtained with the proposed model is within 0.01%. Out of all the laminates, F and G are challenging constructions, and therefore, are considered as particularly important test cases for model validation. The normalised axial normal stress $\bar{\sigma}_{yy}$ (at $y = L/2$) and transverse shear stress $\bar{\tau}_{yz}$ (at $y = 0$) are plotted in Figures 5.4 and 5.5. From the plots, it is clearly shown that the commonly used Third-order Shear Deformation (TSDT), employed for laminated composites, is incapable of capturing the extreme cases of transverse orthotropy in laminates F and G, where a reversal of the transverse shear stress in the stiffer layers is observed. This stress distribution is due to the low transverse shear stiffness of the inner layer which makes it insufficient to support the peak transverse shear stress of the adjacent outer layer. Moreover, this behaviour cannot be predicted by a Reissner's Mixed-Variational Theory (RMVT) model implemented with zig-zag functions as the stress assumptions used in the variational statement are not inherently equilibrated [89]. However, the present model is able to capture the effect accurately and the results are in excellent agreement with 3D elasticity solution and those obtained by employing the HR3-RZT model. For more detailed comparisons of the 3D stress fields for laminates A-M, through-thickness distributions of normalised axial normal stress $\bar{\sigma}_{yy}$, transverse shear stress $\bar{\tau}_{yz}$ and transverse normal stress $\bar{\sigma}_{zz}$ are plotted in Figures 5.6 to 5.18. It is to be noted that all the results presented in this section are based on a plane strain assumption (to model an infinitely wide plate). This assumption simplifies the problem as there is no effect of the Poisson's coupling (C_{31}) term and the transverse normal–in-plane shear coupling (C_{36}) term, as shown in Appendix D. Thus, the current kinematic fidelity of the model is sufficient to naturally satisfy the stress equilibrium equations and to accurately capture the transverse stresses without employing the stress recovery post-processing step.

5.3 Localised Stress Fields Towards Clamped Ends

To assess the capability of the UF-SLE model in capturing boundary layer effects and localised stress gradients towards boundaries, the second validation example is carried out for a square section laminated beam of length-to-thickness ratio $L/t = 10$, clamped at both the ends. The beam is subjected to a uniformly distributed load, equally divided between the top and the bottom surface, $P_z^{\mathrm{t}} = P_z^{\mathrm{b}} = -q_0/2$ as shown in Figure 5.19. A plane strain condition is enforced as described in Appendix D. Two laminates as shown in Table 5.4 are considered, where laminates 1 and 2 are non-symmetric, composite and sandwich beams, respectively, comprised of materials p and pvc as defined in Table 6.1.

In the present approach, the beam is discretised using 40B4 elements and a fifth-order expansion is employed within each cross-section element (one element per layer). As Pagano's

Table 5.3: Normalised maximum absolute axial and transverse shear stresses. Percentage error with respect to Pagano's solution are shown in brackets for HR3-RZT and UF-SLE.

Laminate	**Model**	$\bar{\sigma}_{yy}^{\max}$	$\bar{\tau}_{yz}^{\max}$
	Pagano	**0.7913**	**3.3167**
A	HR3-RZT	0.7895 **(-0.23)**	3.3155 **(-0.04)**
	UF-SLE	0.7913 **(0.00)**	3.3167 **(0.00)**
	Pagano	**0.8672**	**3.3228**
B	HR3-RZT	0.8593 **(-0.92)**	3.3206 **(-0.23)**
	UF-SLE	0.8672 **(0.00)**	3.3228 **(0.00)**
	Pagano	**1.6307**	**5.3340**
C	HR3-RZT	1.6226 **(-0.49)**	5.3361 **(0.03)**
	UF-SLE	1.6307 **(0.00)**	5.3340 **(0.00)**
	Pagano	**1.2239**	**3.6523**
D	HR3-RZT	1.2280 **(0.34)**	3.6505 **(-0.05)**
	UF-SLE	1.2239 **(0.00)**	3.6523 **(0.00)**
	Pagano	**1.9593**	**2.8329**
E	HR3-RZT	1.9596 **(0.02)**	2.8300 **(-0.16)**
	UF-SLE	1.9592 **(-0.005)**	2.8329 **(0.00)**
	Pagano	**13.9883**	**8.1112**
F	HR3-RZT	13.9545 **(-0.24)**	8.1137 **(0.05)**
	UF-SLE	13.9885 **(0.001)**	8.1108 **(-0.005)**
	Pagano	**6.3417**	**5.6996**
G	HR3-RZT	6.3431 **(0.02)**	5.7019 **(0.04)**
	UF-SLE	6.3418 **(0.001)**	5.6999 **(0.005)**
	Pagano	**0.6157**	**4.0096**
H	HR3-RZT	0.6173 **(0.26)**	4.0117 **(0.05)**
	UF-SLE	0.6156 **(-0.01)**	4.0112 **(0.00)**
	Pagano	**2.0870**	**4.8799**
I	HR3-RZT	2.0748 **(-0.59)**	4.8882 **(0.17)**
	UF-SLE	2.0870 **(0.00)**	4.8789 **(0.04)**
	Pagano	**1.2175**	**4.3539**
J	HR3-RZT	1.2061 **(-0.94)**	4.3564 **(0.06)**
	UF-SLE	1.2175 **(0.00)**	4.3538 **(-0.002)**
	Pagano	**0.9566**	**4.1235**
K	HR3-RZT	0.9560 **(-0.06)**	4.1037 **(-0.48)**
	UF-SLE	0.9566 **(0.00)**	4.1223 **(-0.03)**
	Pagano	**1.0368**	**3.8037**
L	HR3-RZT	1.0431 **(0.61)**	3.7992 **(-0.12)**
	UF-SLE	1.0368 **(0.00)**	3.8035 **(-0.005)**
	Pagano	**1.4902**	**2.8969**
M	HR3-RZT	1.4978 **(0.51)**	2.8952 **(-0.06)**
	UF-SLE	1.4903 **(0.006)**	2.8969 **(0.00)**

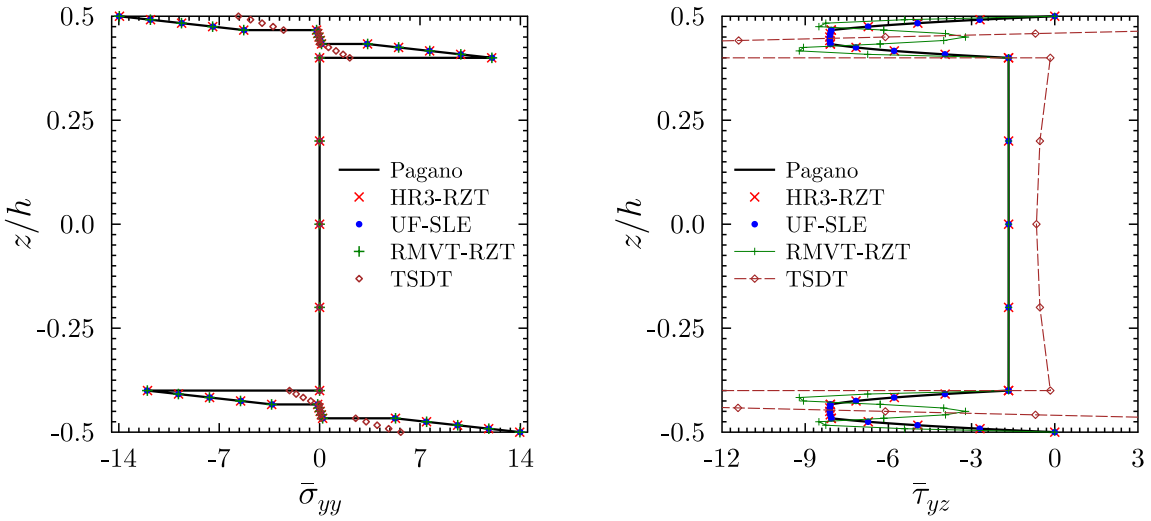

(a) Axial normal stress, $\bar{\sigma}_{yy}$ at $y = L/2$

(b) Transverse shear stress, $\bar{\tau}_{yz}$ at $y = 0$

Figure 5.4: Through-thickness distribution of the normalised axial and transverse shear stresses for laminate F.

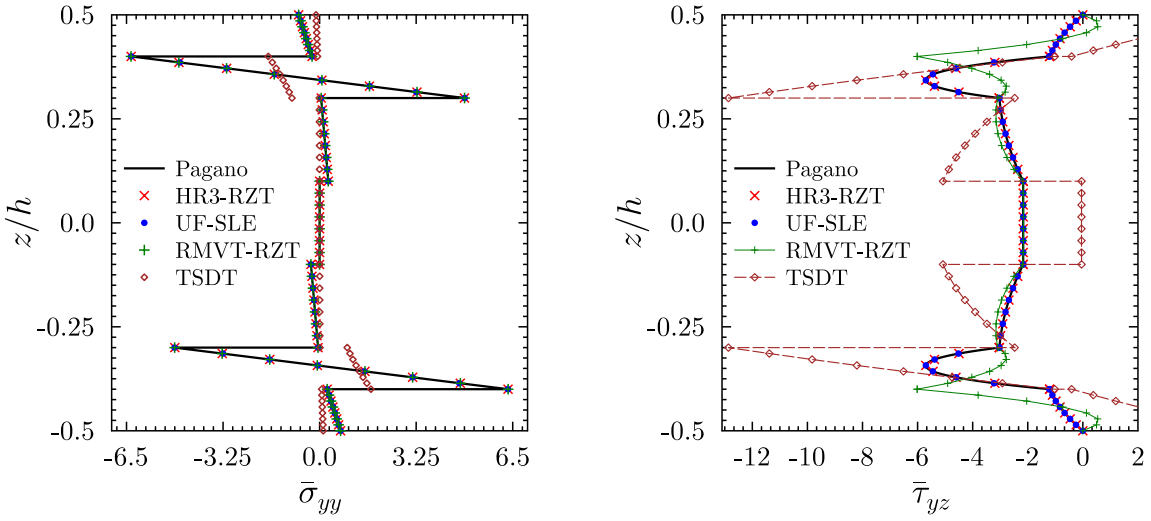

(a) Axial normal stress, $\bar{\sigma}_{yy}$ at $y = L/2$

(b) Transverse shear stress, $\bar{\tau}_{yz}$ at $y = 0$

Figure 5.5: Through-thickness distribution of the normalised axial and transverse shear stresses for laminate G.

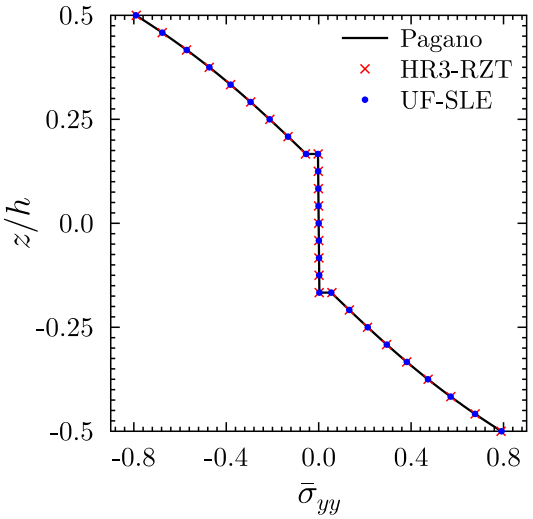

(a) Axial normal stress, $\bar{\sigma}_{yy}$ at $y = L/2$

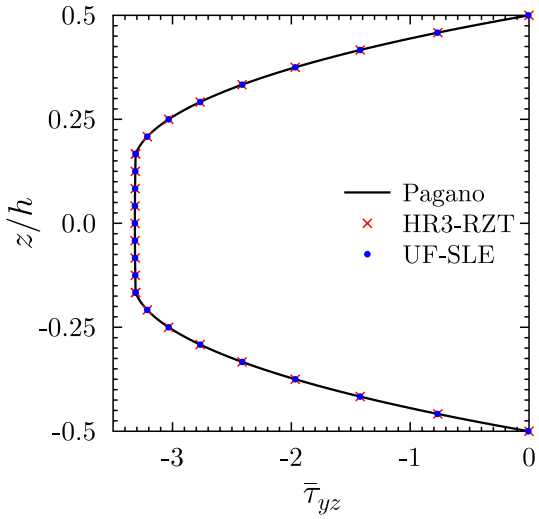

(b) Transverse shear stress, $\bar{\tau}_{yz}$ at $y = 0$

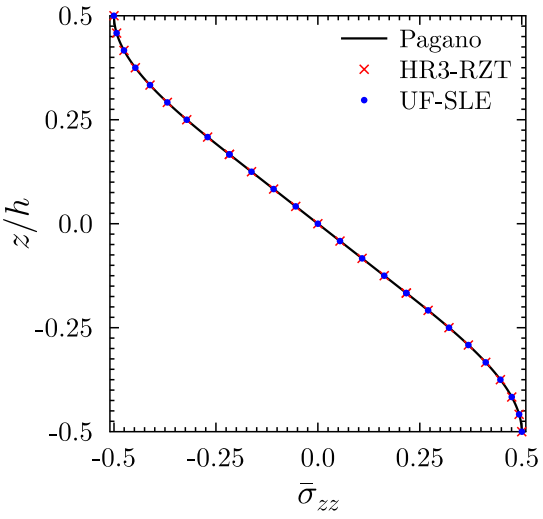

(c) Transverse normal stress, $\bar{\sigma}_{zz}$ at $y = L/2$

Figure 5.6: Through-thickness distribution of the normalized axial and transverse stresses for laminate A.

Table 5.4: Stacking sequence for laminate and sandwich beam considered in the present study. Subscripts indicate the repetition of a property over the corresponding number of layers.

Laminate	**Layer thickness ratio**	**Materials**	**Stacking sequence**
Laminate 1	$[(1/4)_4]$	$[p_4]$	[0/90/0/90]
Laminate 2	$[(1/8)_2/0.5/(1/8)_2]$	$[p_2/pvc/p_2]$	$[0/90/0_2/90]$

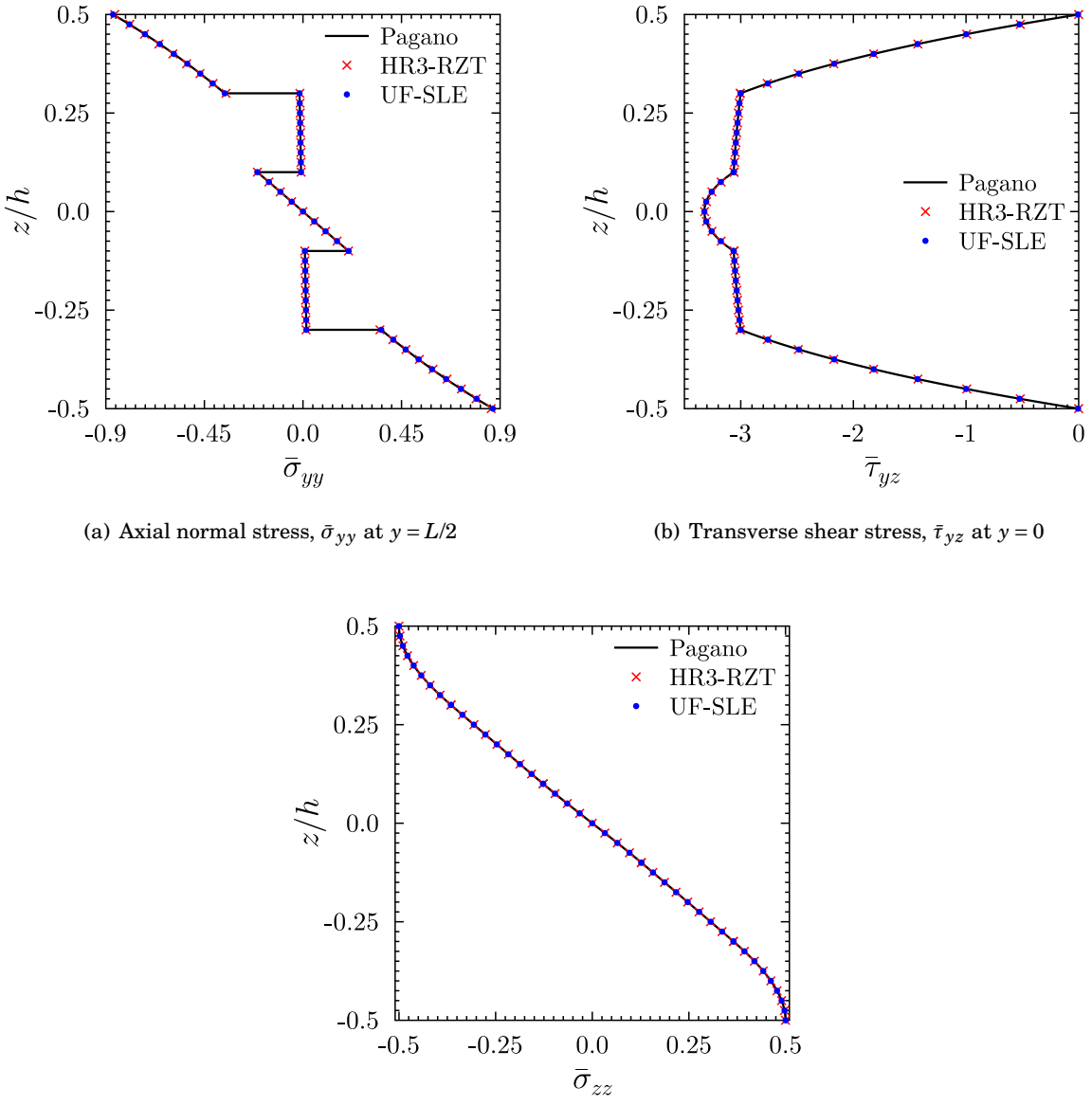

(a) Axial normal stress, $\bar{\sigma}_{yy}$ at $y = L/2$

(b) Transverse shear stress, $\bar{\tau}_{yz}$ at $y = 0$

(c) Transverse normal stress, $\bar{\sigma}_{zz}$ at $y = L/2$

Figure 5.7: Through-thickness distribution of the normalized axial and transverse stresses for laminate B.

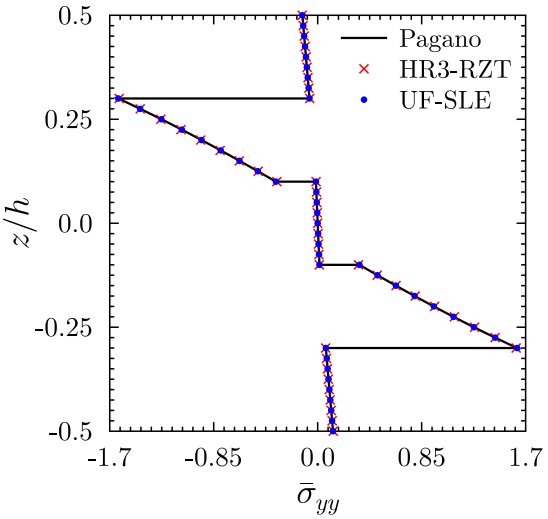

(a) Axial normal stress, $\bar{\sigma}_{yy}$ at $y = L/2$

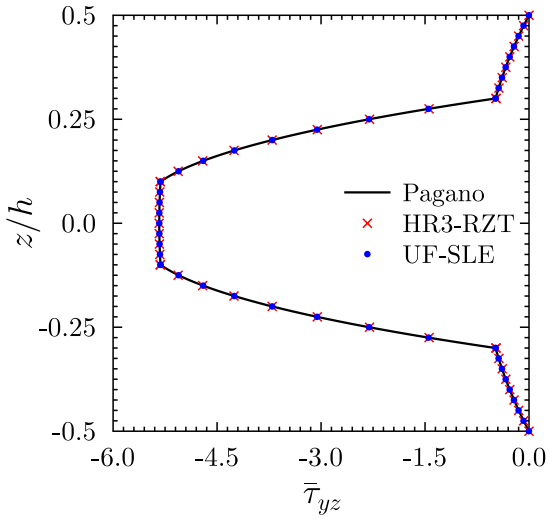

(b) Transverse shear stress, $\bar{\tau}_{yz}$ at $y = 0$

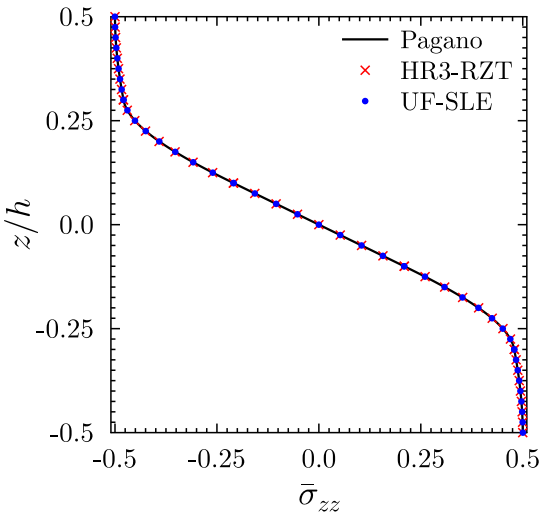

(c) Transverse normal stress, $\bar{\sigma}_{zz}$ at $y = L/2$

Figure 5.8: Through-thickness distribution of the normalized axial and transverse stresses for laminate C.

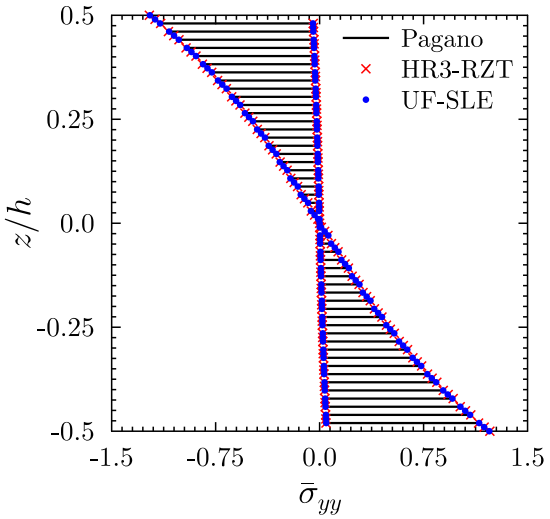

(a) Axial normal stress, $\bar{\sigma}_{yy}$ at $y = L/2$

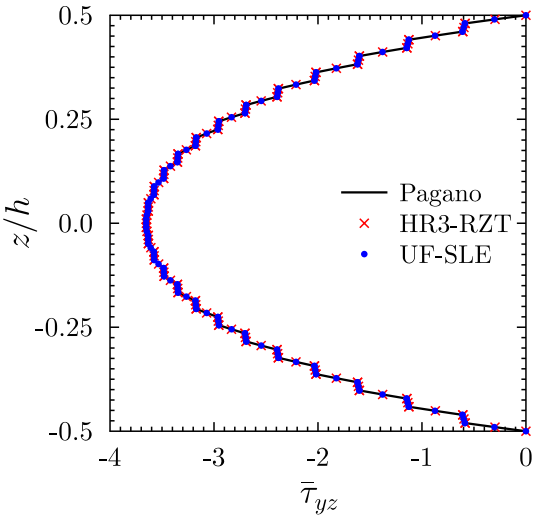

(b) Transverse shear stress, $\bar{\tau}_{yz}$ at $y = 0$

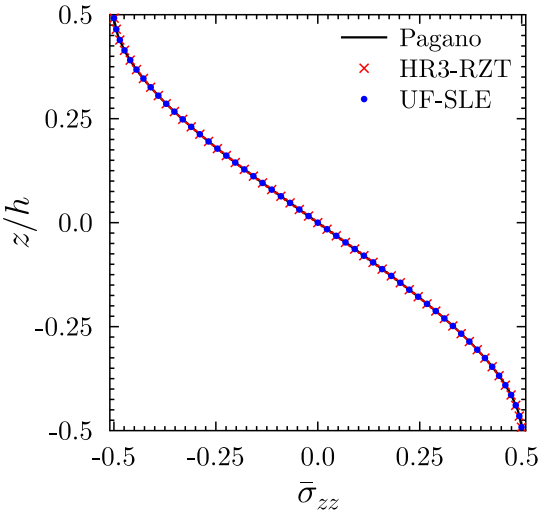

(c) Transverse normal stress, $\bar{\sigma}_{zz}$ at $y = L/2$

Figure 5.9: Through-thickness distribution of the normalized axial and transverse stresses for laminate D.

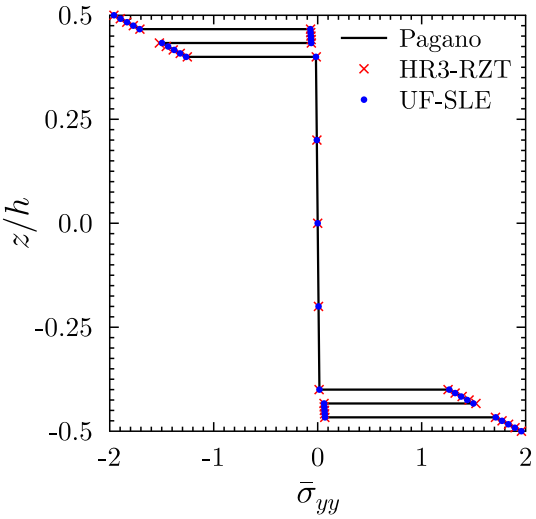

(a) Axial normal stress, $\bar{\sigma}_{yy}$ at $y = L/2$

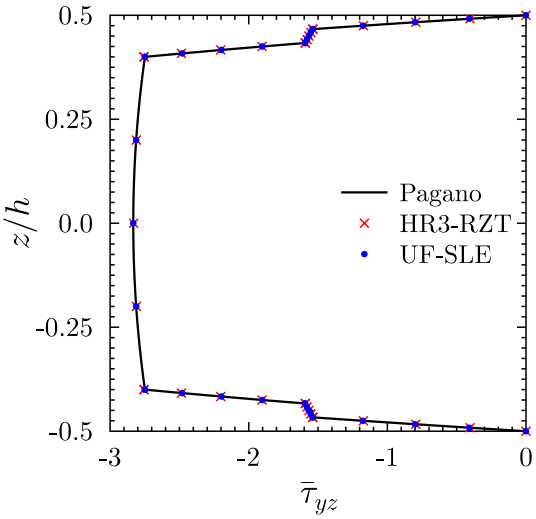

(b) Transverse shear stress, $\bar{\tau}_{yz}$ at $y = 0$

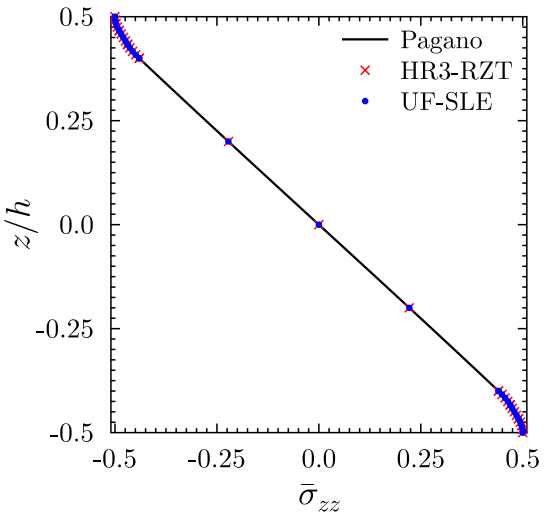

(c) Transverse normal stress, $\bar{\sigma}_{zz}$ at $y = L/2$

Figure 5.10: Through-thickness distribution of the normalized axial and transverse stresses for laminate E.

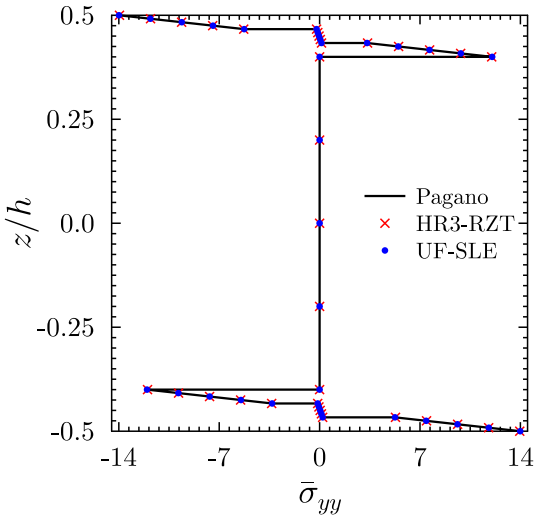

(a) Axial normal stress, $\bar{\sigma}_{yy}$ at $y = L/2$

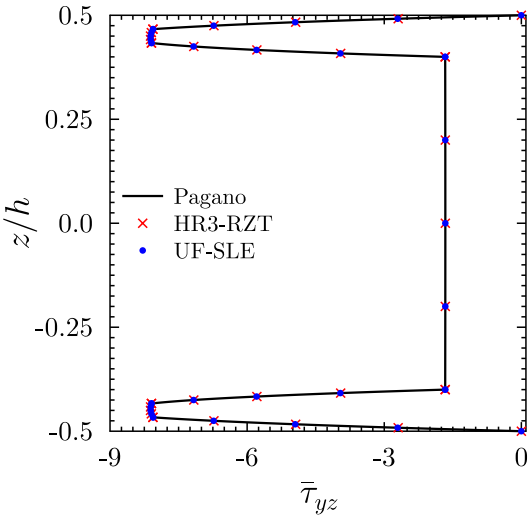

(b) Transverse shear stress, $\bar{\tau}_{yz}$ at $y = 0$

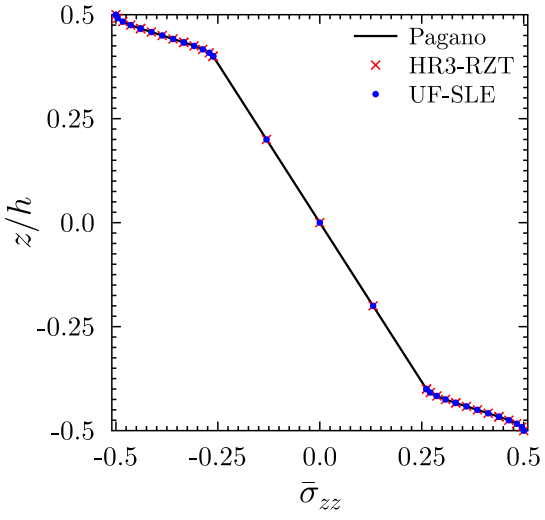

(c) Transverse normal stress, $\bar{\sigma}_{zz}$ at $y = L/2$

Figure 5.11: Through-thickness distribution of the normalized axial and transverse stresses for laminate F.

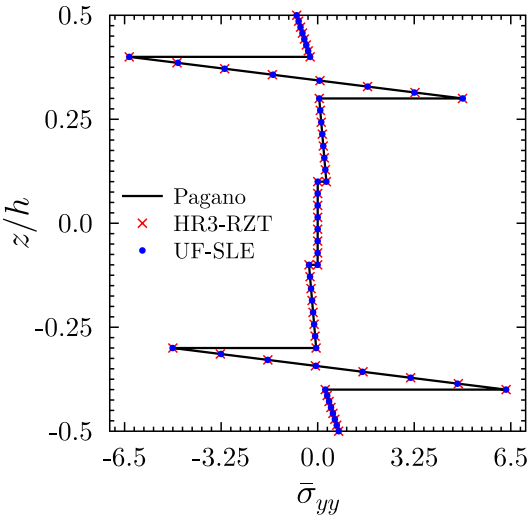

(a) Axial normal stress, $\bar{\sigma}_{yy}$ at $y = L/2$

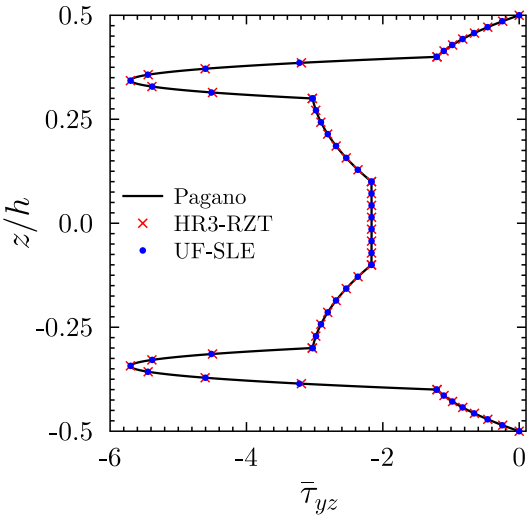

(b) Transverse shear stress, $\bar{\tau}_{yz}$ at $y = 0$

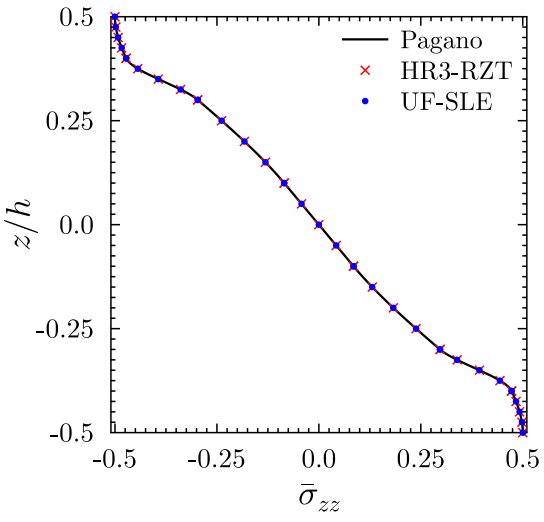

(c) Transverse normal stress, $\bar{\sigma}_{zz}$ at $y = L/2$

Figure 5.12: Through-thickness distribution of the normalized axial and transverse stresses for laminate G.

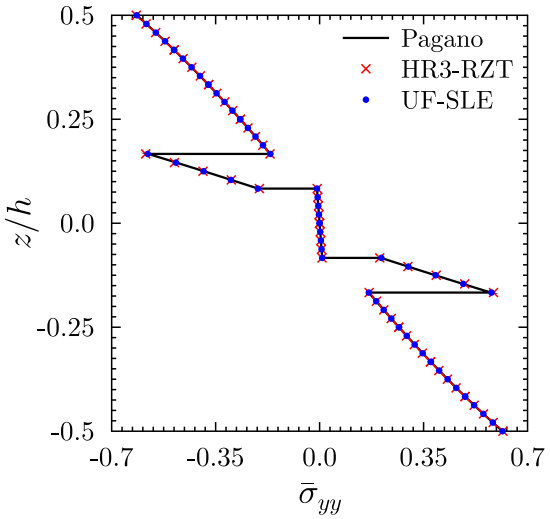

(a) Axial normal stress, $\bar{\sigma}_{yy}$ at $y = L/2$

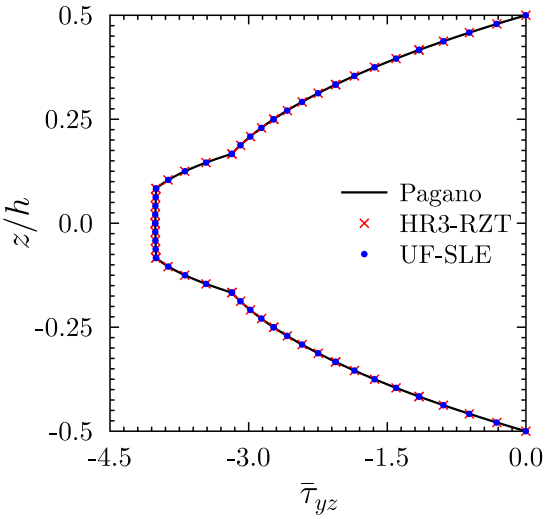

(b) Transverse shear stress, $\bar{\tau}_{yz}$ at $y = 0$

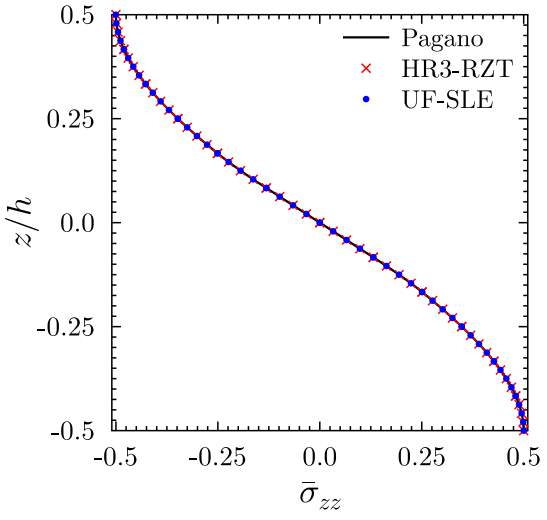

(c) Transverse normal stress, $\bar{\sigma}_{zz}$ at $y = L/2$

Figure 5.13: Through-thickness distribution of the normalized axial and transverse stresses for laminate H.

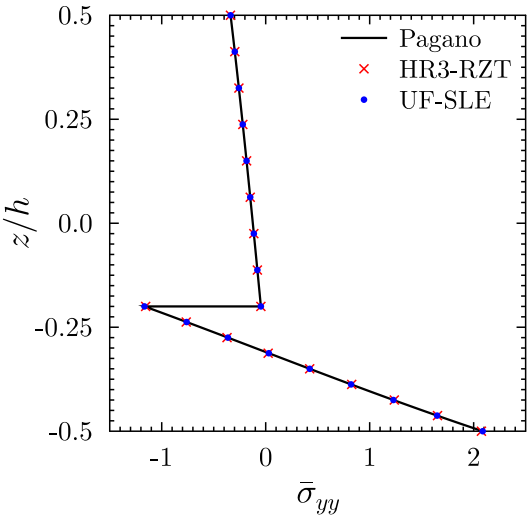

(a) Axial normal stress, $\bar{\sigma}_{yy}$ at $y = L/2$

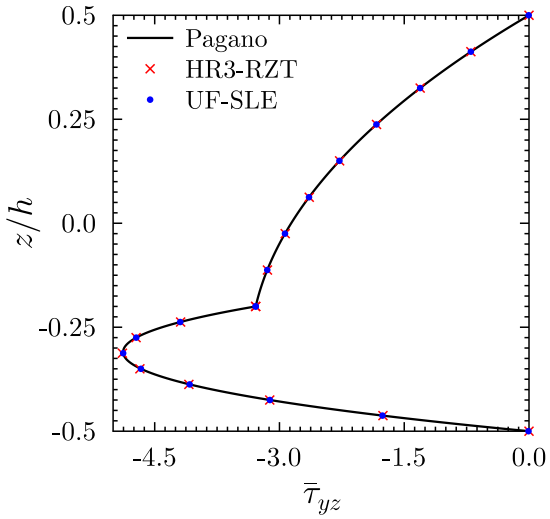

(b) Transverse shear stress, $\bar{\tau}_{yz}$ at $y = 0$

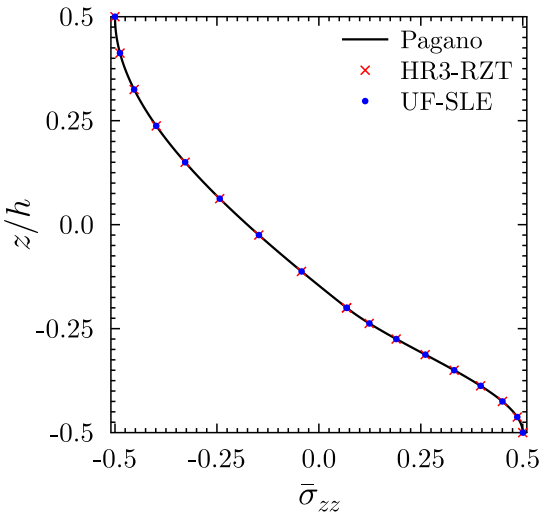

(c) Transverse normal stress, $\bar{\sigma}_{zz}$ at $y = L/2$

Figure 5.14: Through-thickness distribution of the normalized axial and transverse stresses for laminate I.

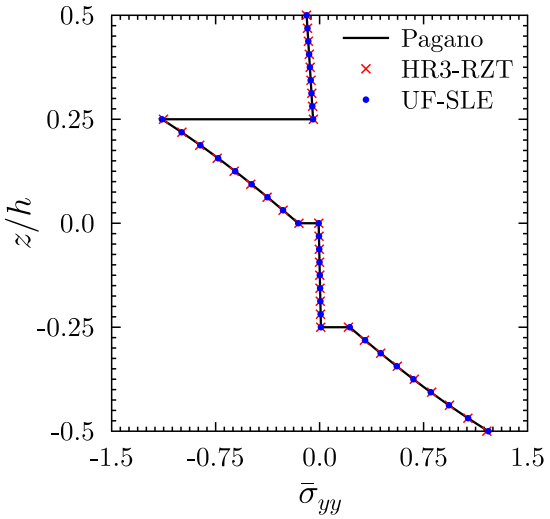

(a) Axial normal stress, $\bar{\sigma}_{yy}$ at $y = L/2$

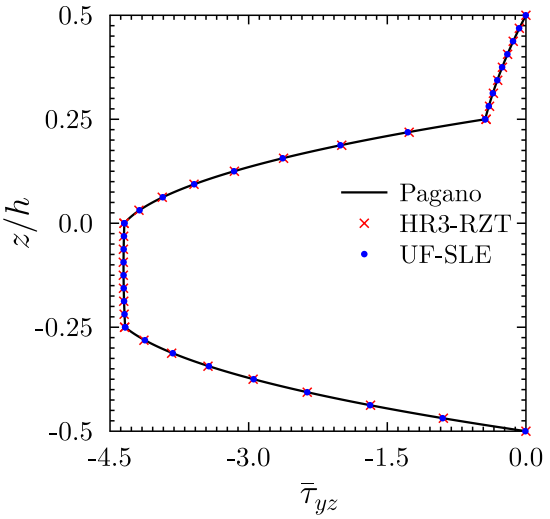

(b) Transverse shear stress, $\bar{\tau}_{yz}$ at $y = 0$

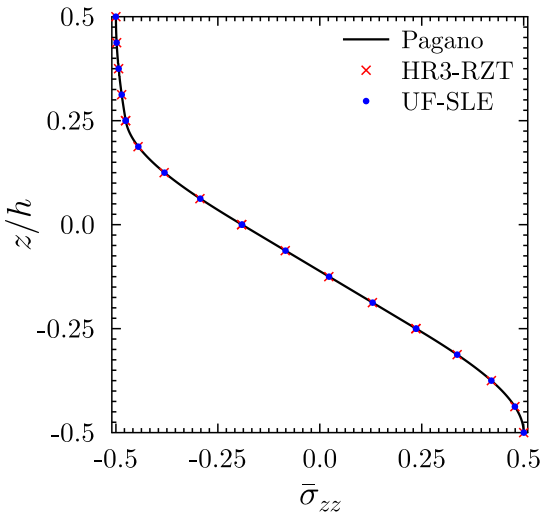

(c) Transverse normal stress, $\bar{\sigma}_{zz}$ at $y = L/2$

Figure 5.15: Through-thickness distribution of the normalized axial and transverse stresses for laminate J.

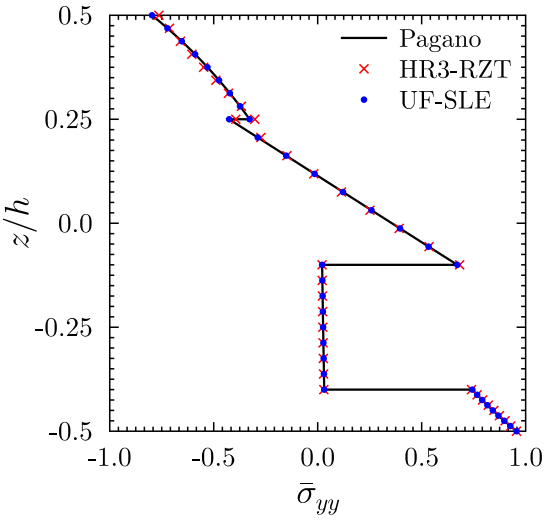

(a) Axial normal stress, $\bar{\sigma}_{yy}$ at $y = L/2$

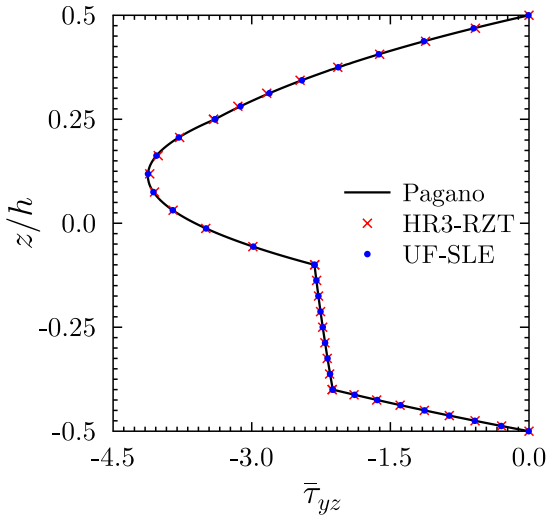

(b) Transverse shear stress, $\bar{\tau}_{yz}$ at $y = 0$

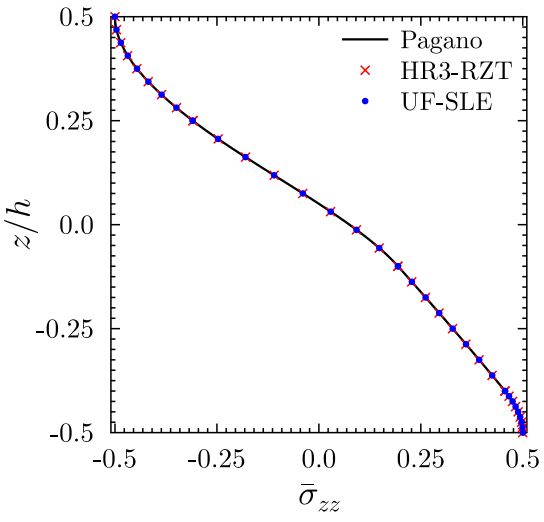

(c) Transverse normal stress, $\bar{\sigma}_{zz}$ at $y = L/2$

Figure 5.16: Through-thickness distribution of the normalized axial and transverse stresses for laminate K.

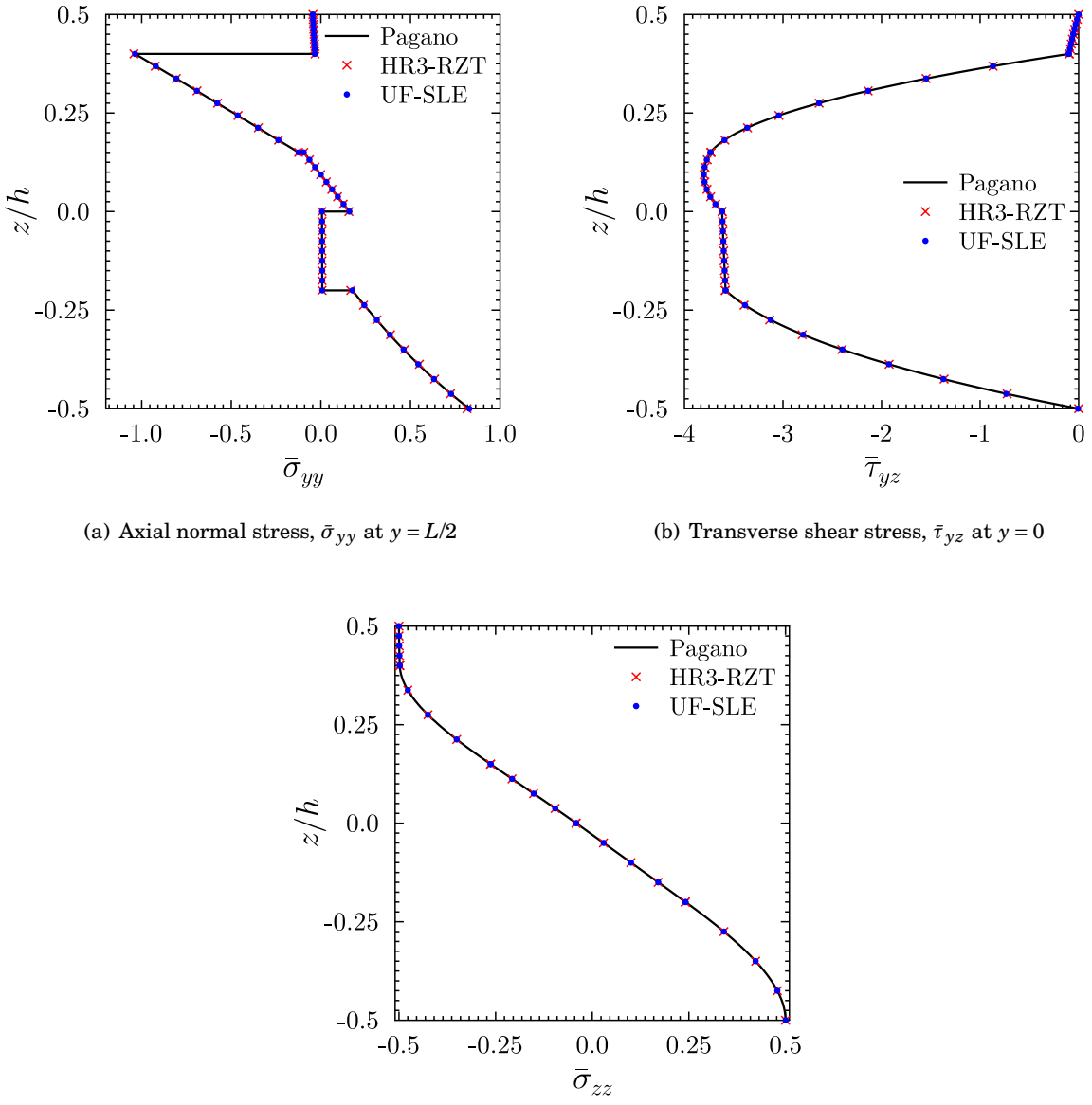

(a) Axial normal stress, $\bar{\sigma}_{yy}$ at $y = L/2$

(b) Transverse shear stress, $\bar{\tau}_{yz}$ at $y = 0$

(c) Transverse normal stress, $\bar{\sigma}_{zz}$ at $y = L/2$

Figure 5.17: Through-thickness distribution of the normalized axial and transverse stresses for laminate L.

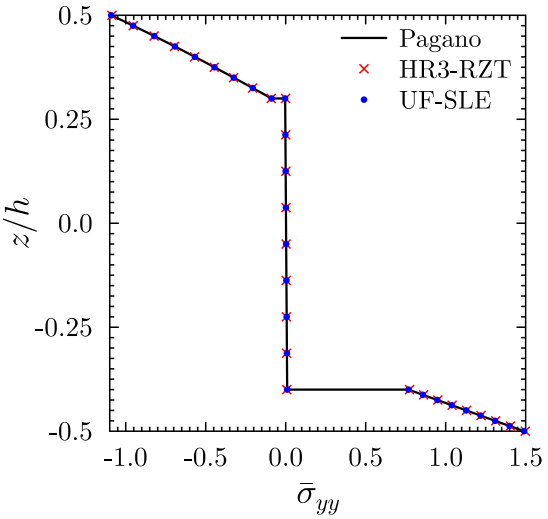

(a) Axial normal stress, $\bar{\sigma}_{yy}$ at $y = L/2$

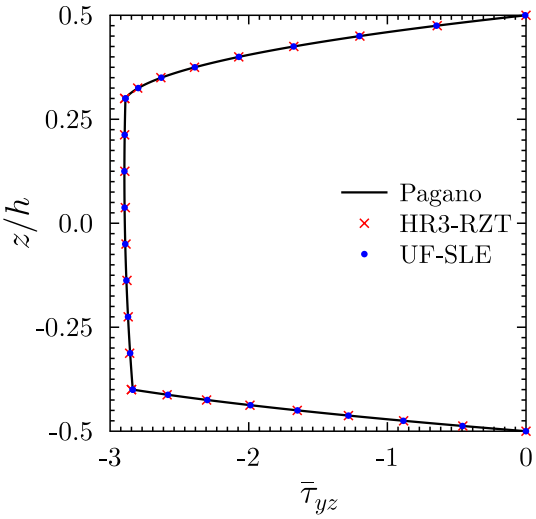

(b) Transverse shear stress, $\bar{\tau}_{yz}$ at $y = 0$

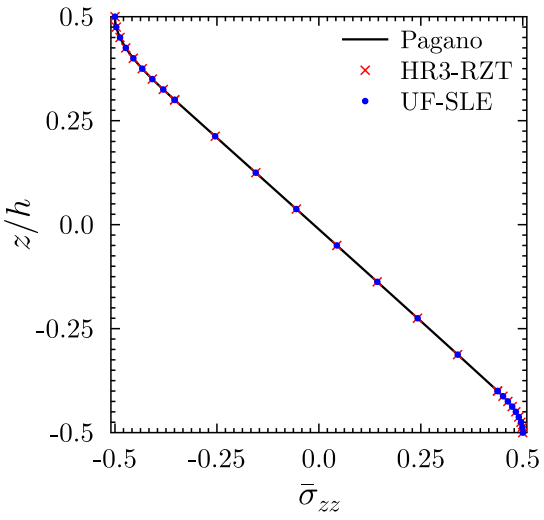

(c) Transverse normal stress, $\bar{\sigma}_{zz}$ at $y = L/2$

Figure 5.18: Through-thickness distribution of the normalized axial and transverse stresses for laminate M.

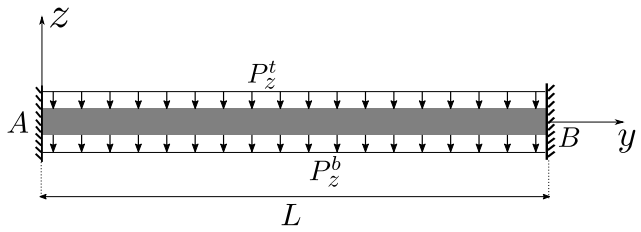

Figure 5.19: Representation of a multilayered beam clamped at both the ends subjected to a uniformly distributed load at the top and the bottom surface.

closed-form solutions are acceptable only for simply-supported beams, 3D FE results from the commercial code, ABAQUS as given in [11], are used as the reference solution. The 3D model, 1 m long, 0.1 m thick and 0.001 m wide, is meshed with 96,000 C3D8R brick elements. To model a plane strain condition, the lateral faces are restrained from expanding and one element is used in the width direction.

Through-thickness distribution of the stress fields, $\bar{\sigma}_{yy}$, $\bar{\tau}_{yz}$ and $\bar{\sigma}_{zz}$, at four locations 5%, 10%, 15% and 20% from the clamped end ($y = 0$) are plotted in figs. 5.20 to 5.25. The results obtained are also compared with those given in [11] using the HR3-RZT model. The boundary layer effect is clearly shown in these plots as there is a clear change in the stress profiles at different locations from the clamped support, for all three stress fields. In addition to the boundary layer effect, the high orthotropy ratio in a composite laminate causes channelling of the axial stress towards the surface [12, 28]. This effect requires the non-classical complexity of a higher-order model. Figure 5.20 shows the through-thickness distribution of the normalised axial stress $\bar{\sigma}_{yy}$ for laminate 1. The stress-channelling effect can be clearly observed in the 0° laminates, first and third layer from the bottom, with an orthotropy ratio $E_y/G_{yz} = 50$. However, near the clamped support, the linear behaviour of the zig-zag effect reduces the relative magnitude of these higher-order through-thickness variations. This effect can be observed by looking at the variation of $\bar{\sigma}_{yy}$ between 20% in Figure 5.20(d) and the 5% in Figure 5.20(a). To accurately capture this stress distribution, at least a fifth-order expansion function is required, as employed in the present formulation. In the case of the HR3-RZT model, based on a third-order theory, discrepancies with 3D FE results are observed. In contrast, the present results are in an excellent agreement with the 3D FE solutions.

The through-thickness profiles of $\bar{\tau}_{yz}$ and $\bar{\sigma}_{zz}$ for laminate 1 are plotted in Figure 5.21. The effect of the boundary layer induced by the clamped support is observed from the transverse shear and normal stress distributions at 5% location as shown in Figures 5.21(a) and 5.22(a), respectively. The clamped boundary condition exacerbates the zig-zag deformations within the laminate which results in the redistribution of the transverse shear and normal stresses across the section. This effect reduces as we move away from the clamped end. The plot for the 20% location in Figure 5.21(d) and 5.22(d) presents the converged solution free from boundary layer

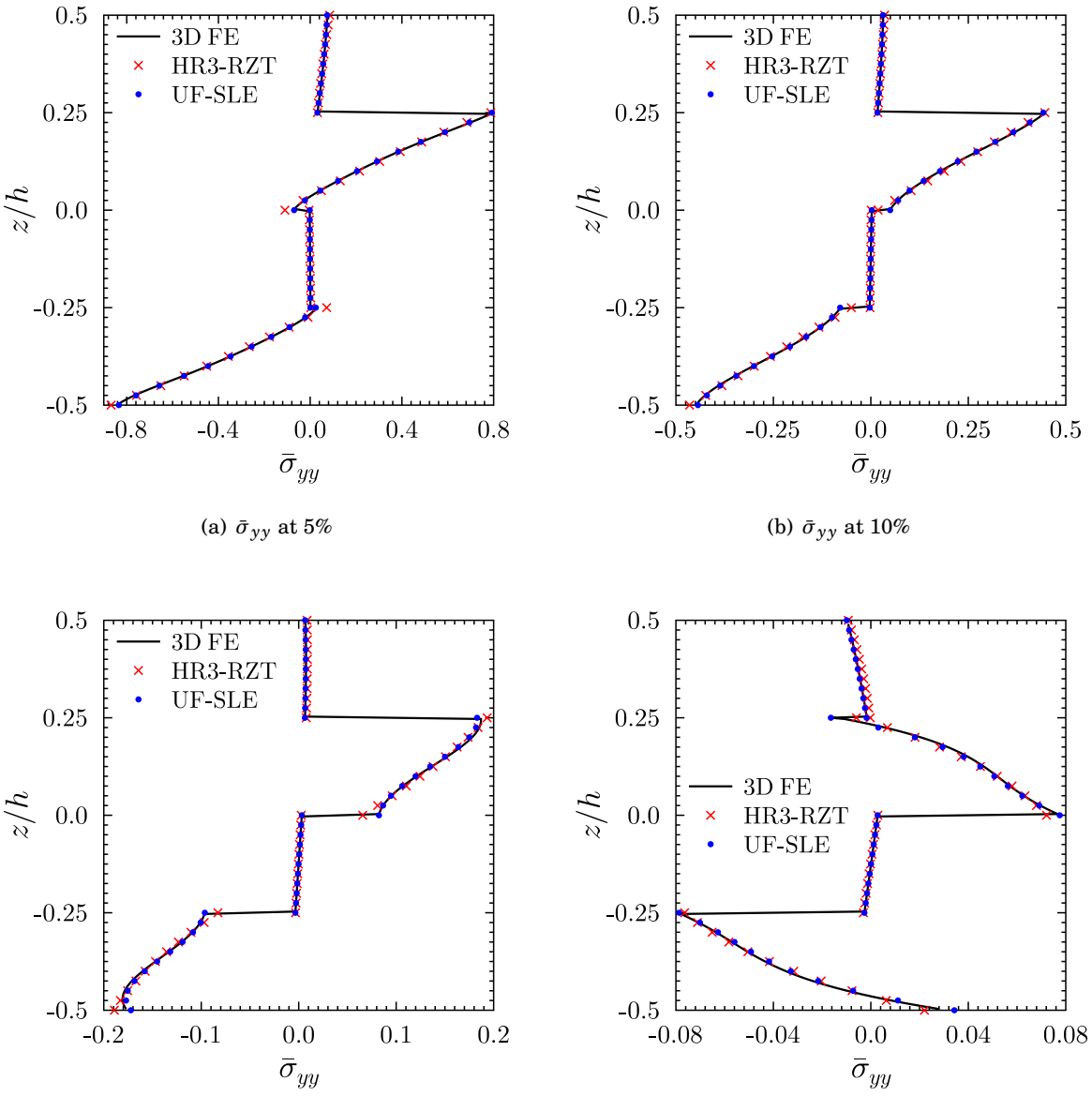

(a) $\bar{\sigma}_{yy}$ at 5%

(b) $\bar{\sigma}_{yy}$ at 10%

(c) $\bar{\sigma}_{yy}$ at 15%

(d) $\bar{\sigma}_{yy}$ at 20%

Figure 5.20: Through-thickness distribution of the normalised axial normal stress $\bar{\sigma}_{yy}$ at 5%, 10%, 15% and 20% from the clamped end A, for laminate 1.

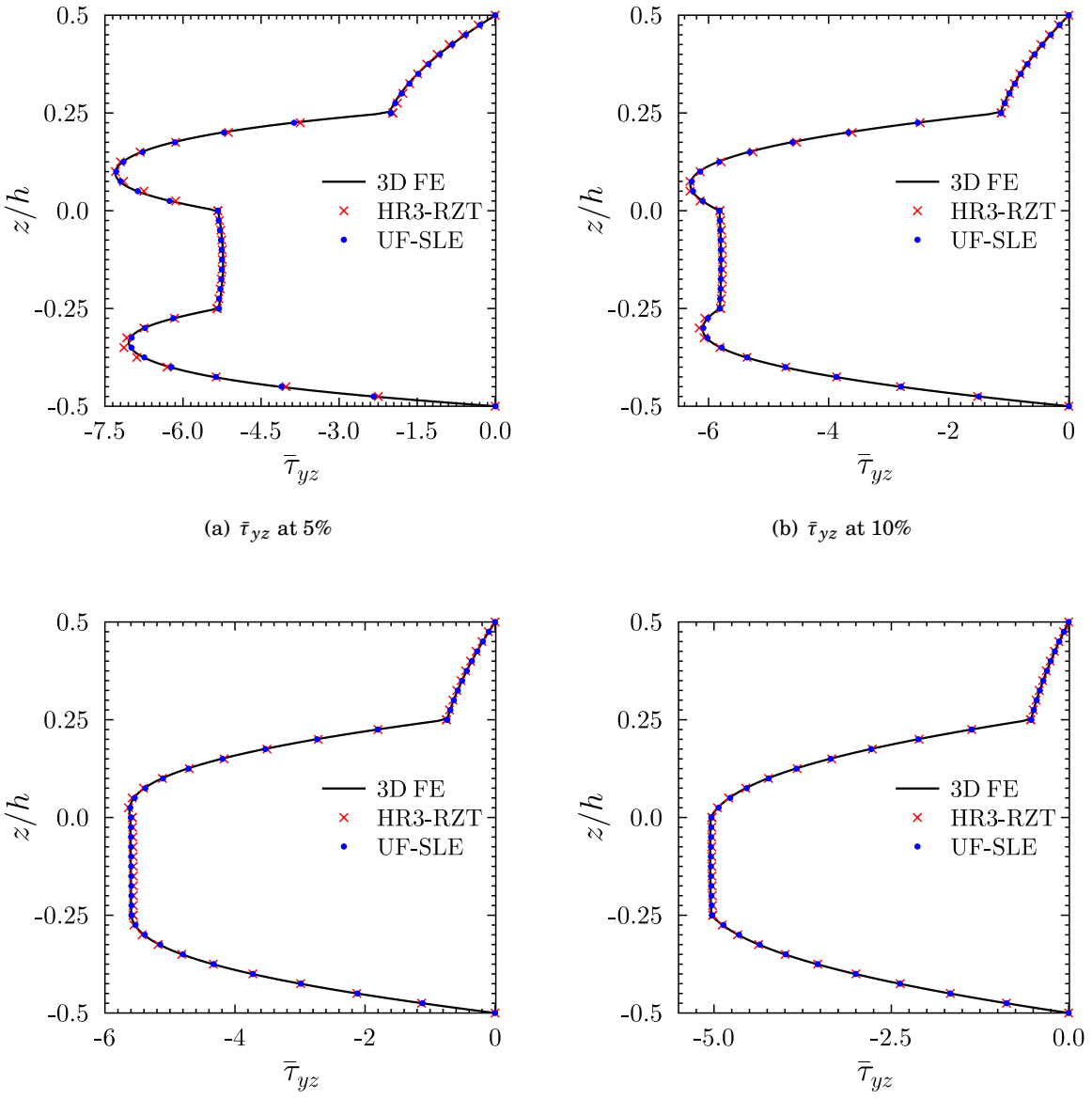

(a) $\bar{\tau}_{yz}$ at 5%

(b) $\bar{\tau}_{yz}$ at 10%

(c) $\bar{\tau}_{yz}$ at 15%

(d) $\bar{\tau}_{yz}$ at 20%

Figure 5.21: Through-thickness distribution of the normalised transverse shear stress $\bar{\tau}_{yz}$ at 5%, 10%, 15% and 20% from the clamped end A, for laminate 1.

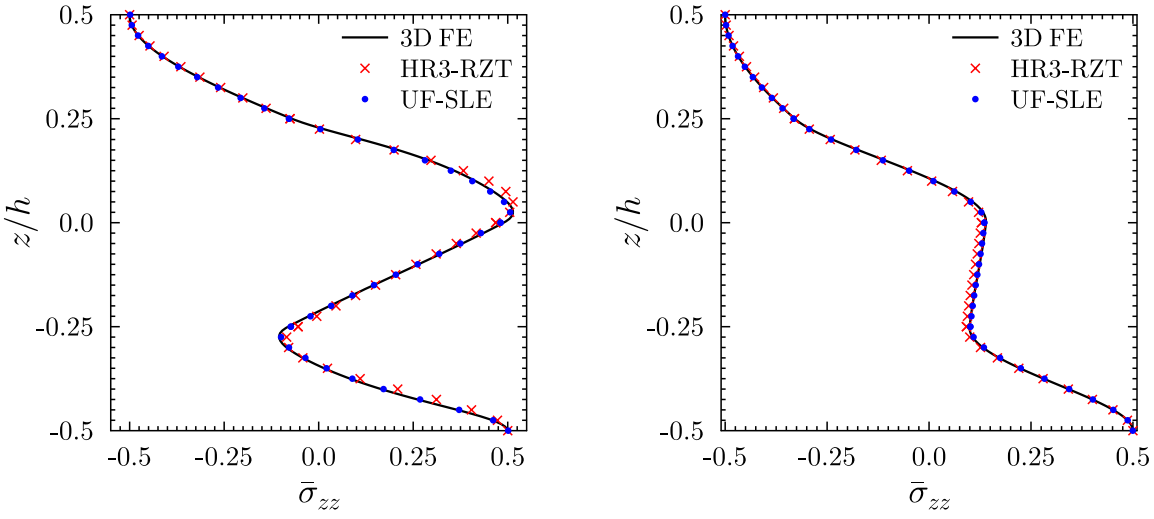

(a) $\bar{\sigma}_{zz}$ at 5%

(b) $\bar{\sigma}_{zz}$ at 10%

(c) $\bar{\sigma}_{zz}$ at 15%

(d) $\bar{\sigma}_{zz}$ at 20%

Figure 5.22: Through-thickness distribution of the normalised transverse normal stress $\bar{\sigma}_{zz}$ at 5%, 10%, 15% and 20% from the clamped end A, for laminate 1.

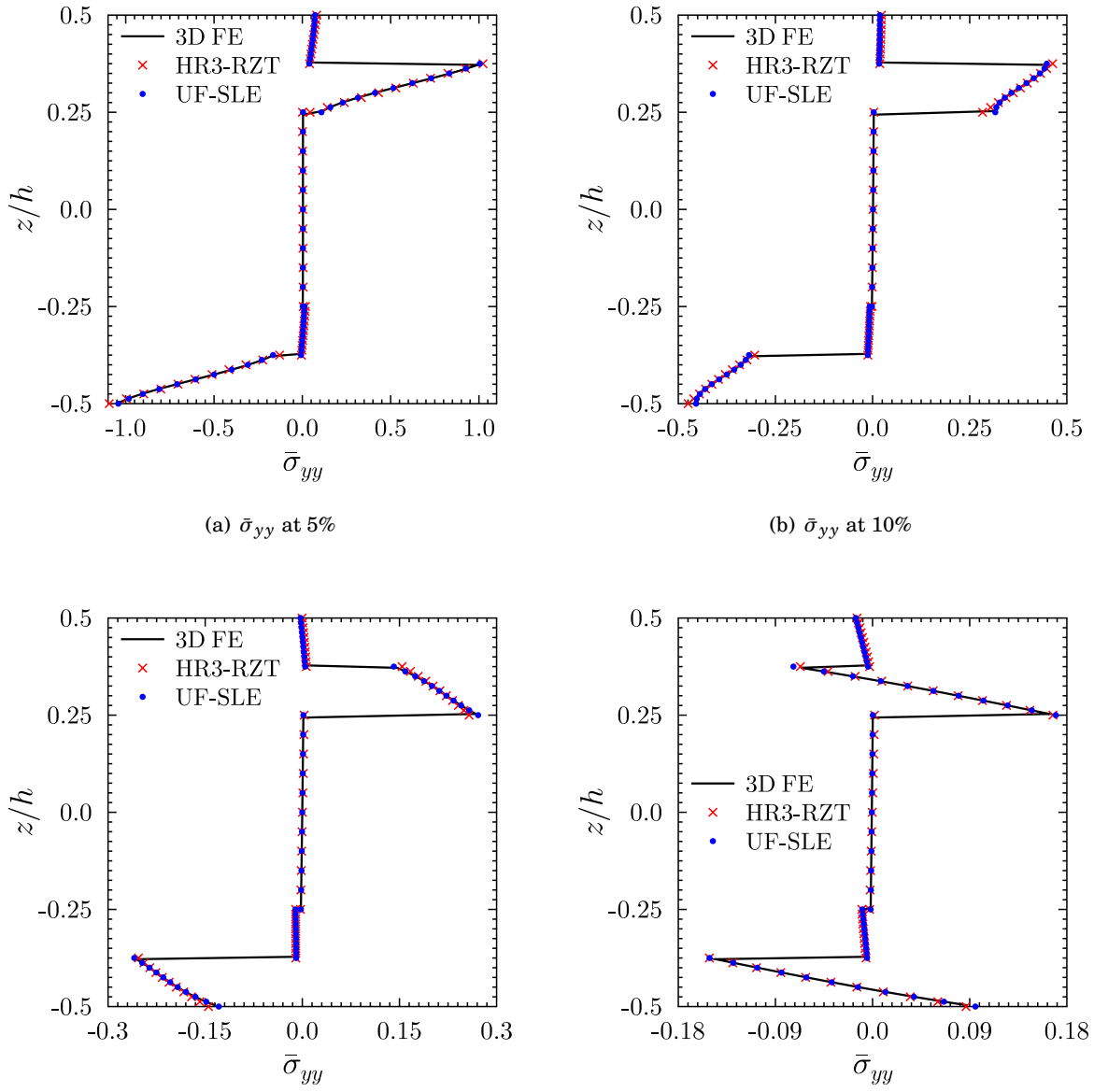

(a) $\bar{\sigma}_{yy}$ at 5%

(b) $\bar{\sigma}_{yy}$ at 10%

(c) $\bar{\sigma}_{yy}$ at 15%

(d) $\bar{\sigma}_{yy}$ at 20%

Figure 5.23: Through-thickness distribution of the normalised axial normal stress $\bar{\sigma}_{yy}$ at 5%, 10%, 15% and 20% from the clamped end A, for laminate 2.

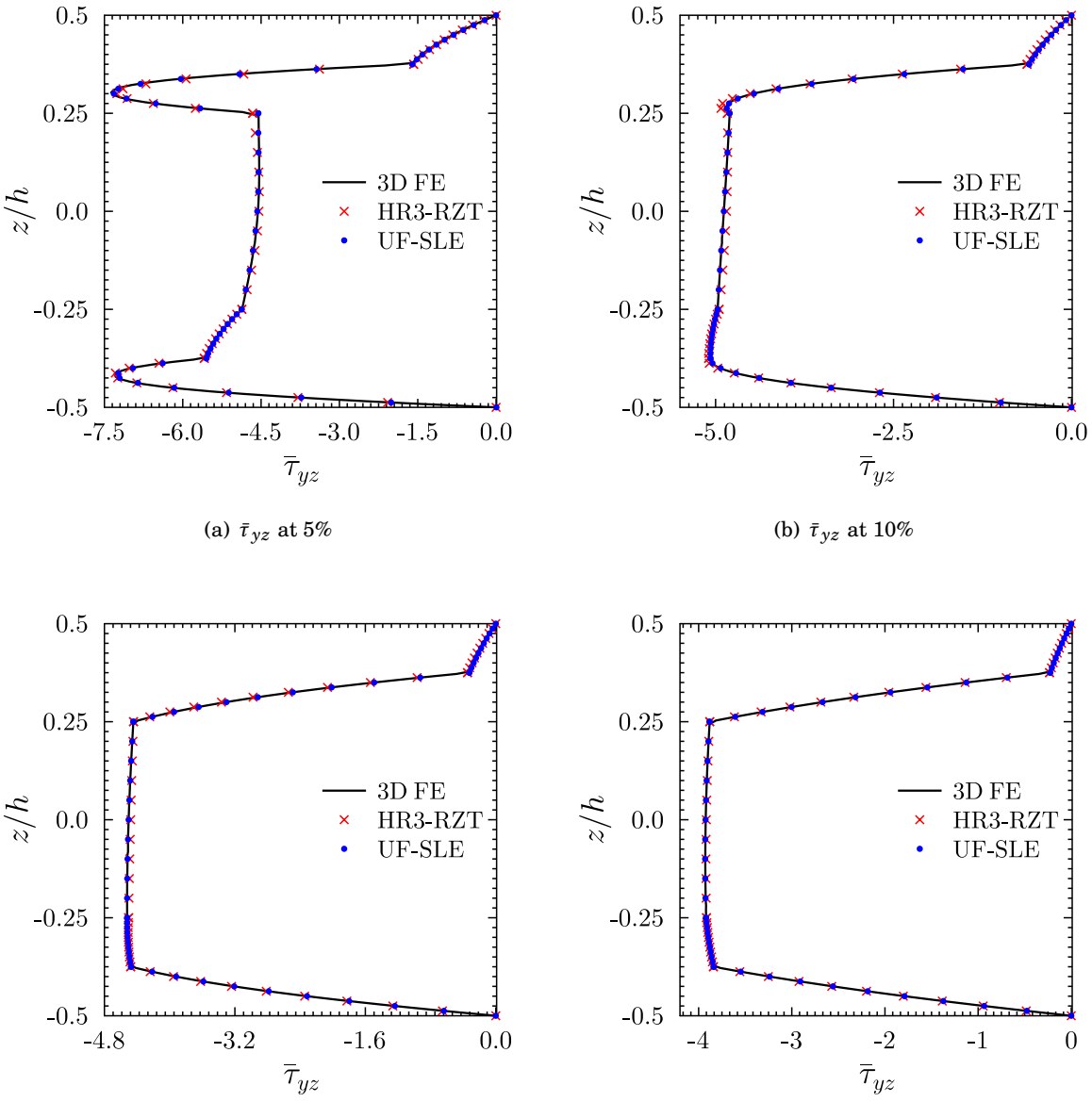

(a) $\bar{\tau}_{yz}$ at 5%

(b) $\bar{\tau}_{yz}$ at 10%

(c) $\bar{\tau}_{yz}$ at 15%

(d) $\bar{\tau}_{yz}$ at 20%

Figure 5.24: Through-thickness distribution of the normalised transverse shear stress $\bar{\tau}_{yz}$ at 5%, 10%, 15% and 20% from the clamped end A, for laminate 2.

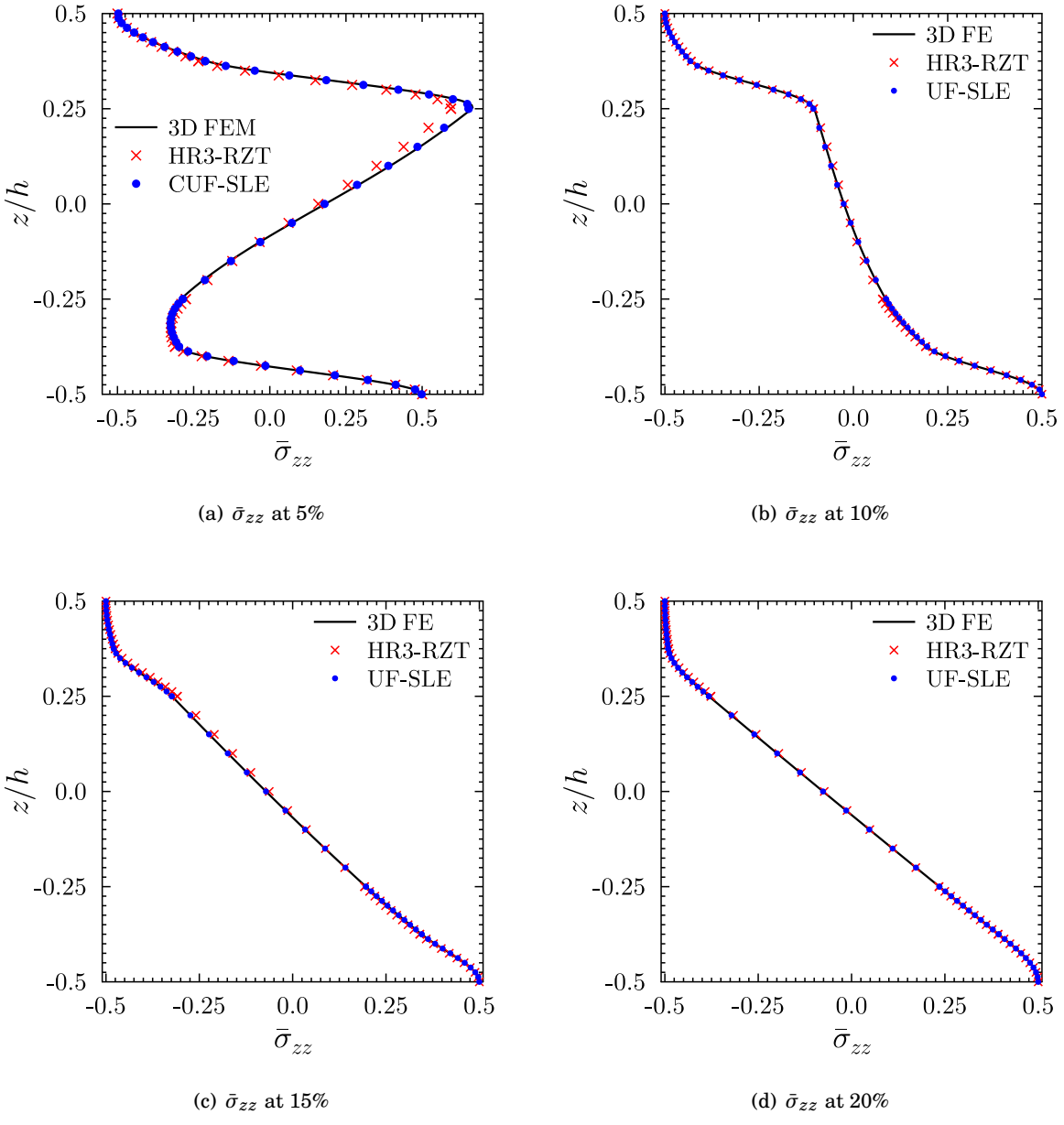

(a) $\bar{\sigma}_{zz}$ at 5%

(b) $\bar{\sigma}_{zz}$ at 10%

(c) $\bar{\sigma}_{zz}$ at 15%

(d) $\bar{\sigma}_{zz}$ at 20%

Figure 5.25: Through-thickness distribution of the normalised transverse normal stress $\bar{\sigma}_{zz}$ at 5%, 10%, 15% and 20% from the clamped end A, for laminate 2.

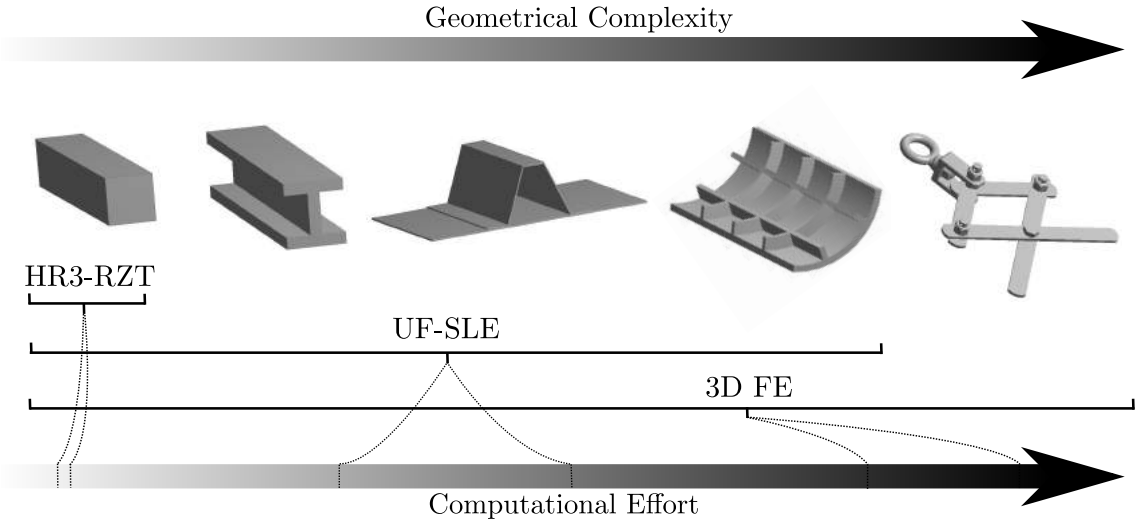

Figure 5.26: A tradeoff plot between geometrical complexity and computational efforts for 3D FE, UF-SLE model and mixed HR3-RZT formulation (where the arrows indicate increasing complexity or effort).

effects. Similarly, Figures 5.23 to 5.25 show through-thickness distributions of the three stress fields for the sandwich beam (laminate 2). The flexible core and the stiff face layers with clamped supports make this a challenging test case to analyse. The increasing effect of the zig-zag deformations towards the clamped ends is shown from the stress profiles from the 20% to 5% locations.

From the results presented in this section it is evident that the UF-SLE model is capable of accurate stress predictions compared to the HR3-RZT. However, this comparison is incomplete without highlighting the computational cost incurred by the models. Therefore, we compare the degrees of freedom (the number of unknown variables) required to solve the system, which gives an estimate of computational efficiency. The FE model requires 582,498 DOFs (for laminates 1 and 2), the UF-SLE model requires 26,862 DOFs (for laminate 1) and 33,033 DOFs (for laminate 2), and the HR3-RZT model employs only 217 DOFs (for laminates 1 and 2). Clearly, the HR3-RZT model, based on an equivalent single layer approach, is more computationally efficient than the UF-SLE model, followed by the 3D FE approach. However, the inability of the HR3-RZT model to analyse large and complex structures, subject to a variety of loads and boundary conditions, makes it unfit as a design tool for industrial applications. This requirement of solving complex structural problems is rather important and therefore, analysts often use alternative approaches, for example FE techniques. However, the present formulation can be a good compromise between the two numerical models discussed, when problem (or geometrical) complexity and computational efforts are of concern, as depicted in Figure 5.26.

5.4 Assessment of transverse normal stress via stress recovery

In previous sections, results for laminated composite and sandwich beams are computed and compared with the analytical and various numerical solutions available in the literature. All the analyses performed were based on the plane strain assumption in the beam's width direction (x-direction). This assumption forces the normal and shear strains with x-components (ε_{xx}, γ_{xz} and γ_{xz}) to be zero. In order to assess the performance of the present model in predicting the full 3D stress response of the structure, the analyses performed in Section 5.2 are repeated without any plane strain assumption.

The 3D finite element analysis is performed using the commercial code, ANSYS and the results are used as the reference solution. The 3D model is meshed with the `solid186` (20-noded brick) element and a mesh convergence analysis is performed to define the optimal mesh size for each laminate considered. In the present UF-SLE model, the beam is dicretised with 30B4 elements and a fifth-order expansion function is used within each Serendipity Lagrange element in the cross-section (one element per layer). Figures 5.27 to 5.30 present the converged solution for through-thickness transverse normal stress obtained from the 3D FEA and UF-SLE models.

From these figures, it can be clearly seen that like other displacement-based weak-form formulations, the SLE model based on the unified formulation approach, is unable to capture the transverse stresses accurately. The zig-zag effect due to the transverse anisotropy and the C^1-*discontinuous* displacements field make the transverse normal stress profile discontinuous at the laminar interfaces. This issue can be addressed either by increasing the fidelity of the model, which is a computationally expensive solution, or by employing the stress-recovery scheme, as used in the present case, where the stress equilibrium equations are integrated along the thickness direction as described in Section 5.1. This feature of recovering the transverse stresses from Cauchy's equilibrium equations creates a stronger condition than simply post-processing the stresses from the displacement unknowns in the kinematic and constitutive relations. The stress distribution profiles obtained are denoted by UF-SLE-SR in the plots, where SR denotes stress recovery. Results show an excellent agreement with the 3D FE solutions.

For all of the laminates considered, the number of unknowns required in the UF-SLE model is less than those required in 3D FEA. However, it is believed that comparing models based on DOFs only is not a fair assessment of computational efficiency. Instead, computational time must be the criterion for comparison. Because it is tricky to compare in-house codes with a commercial software, we compare other parameters which directly relate to computational time and memory requirements. For instance, to solve a linear static analysis, the most time consuming steps are the stiffness matrix inversion and multiplication, which further depends upon the solver type. The first choice employs a sparse direct solver as based on the direct elimination of equations (usually the Gaussian Elimination algorithm) and the solution obtained is stable without being affected by the numerical characteristics of the matrix. However, the direct solver demands a significant memory space and a large amount of calculations for large problems, in which case an

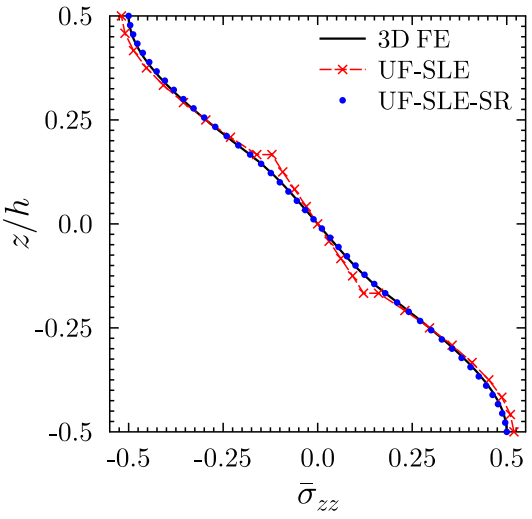

(a) Laminate A

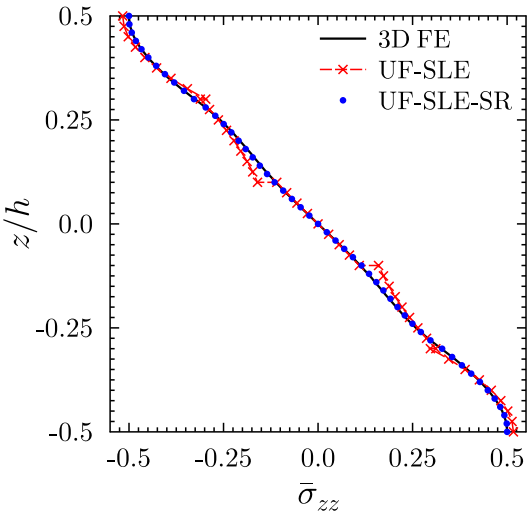

(b) Laminate B

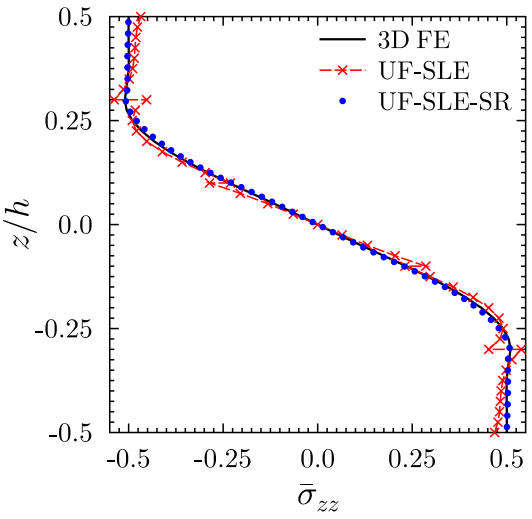

(c) Laminate C

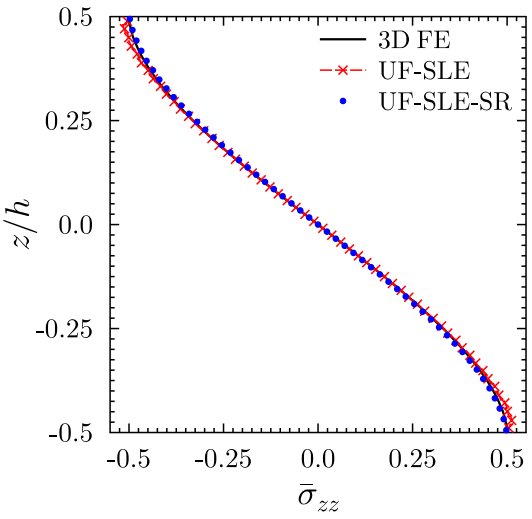

(d) Laminate D

Figure 5.27: Through-thickness distribution of the normalized transverse normal stress σ_{zz} at the mid-span for laminates A, B, C and D.

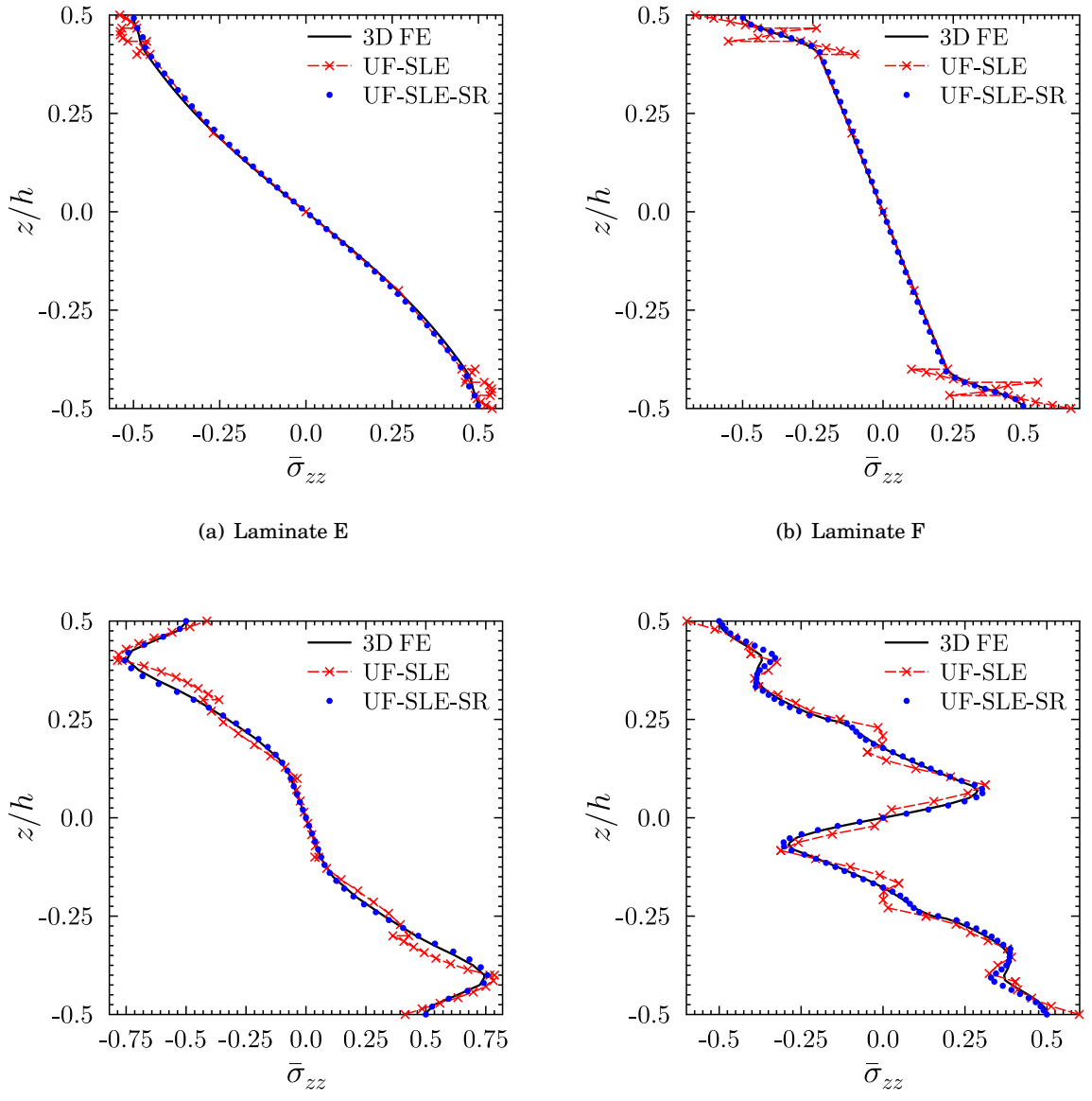

(a) Laminate E

(b) Laminate F

(c) Laminate G

(d) Laminate H

Figure 5.28: Through-thickness distribution of the normalized transverse normal stress σ_{zz} at the mid-span for laminates E, F, G and H.

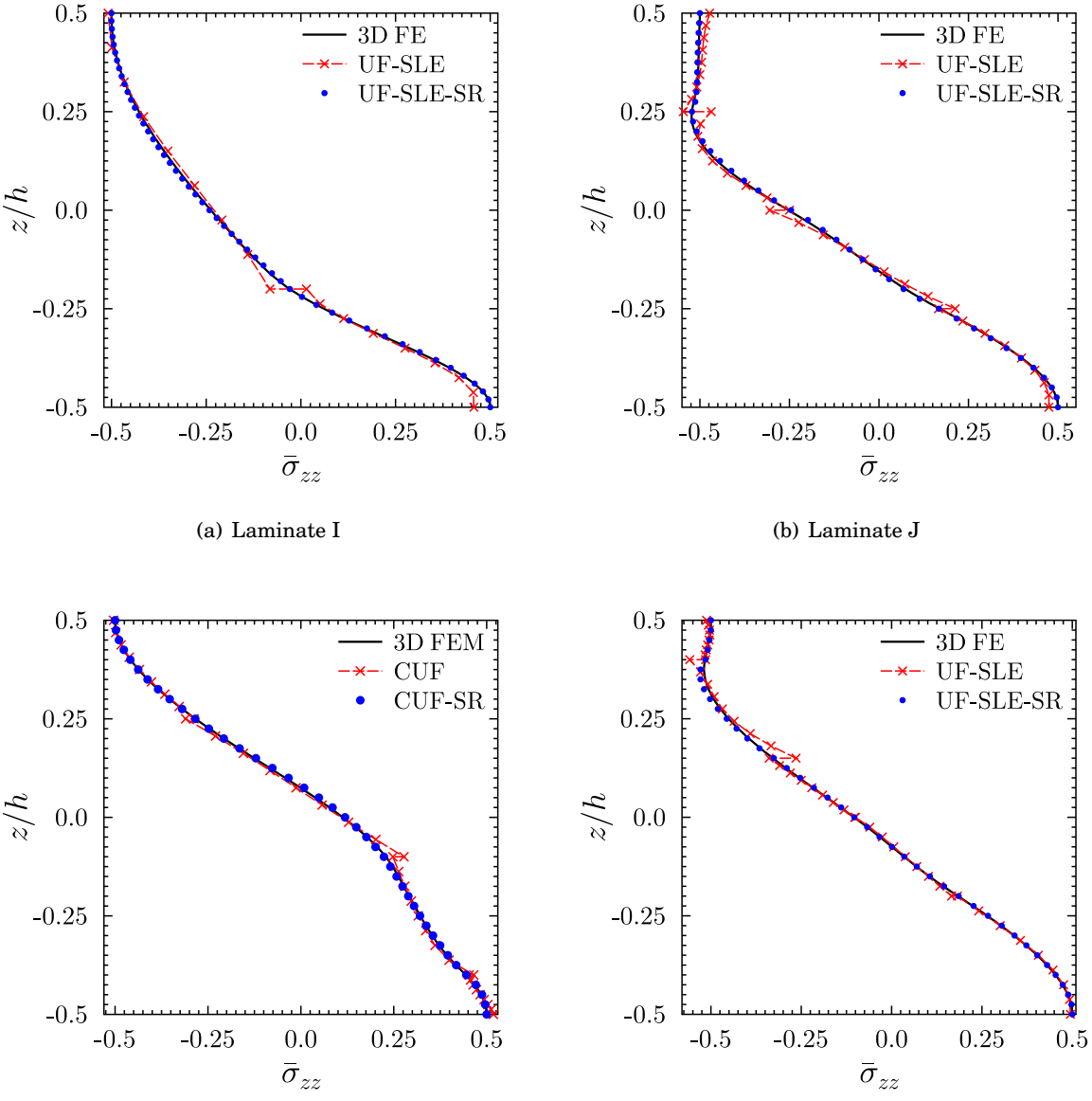

(a) Laminate I

(b) Laminate J

(c) Laminate K

(d) Laminate L

Figure 5.29: Through-thickness distribution of the normalized transverse normal stress σ_{zz} at the mid-span for laminates I, J, K and L.

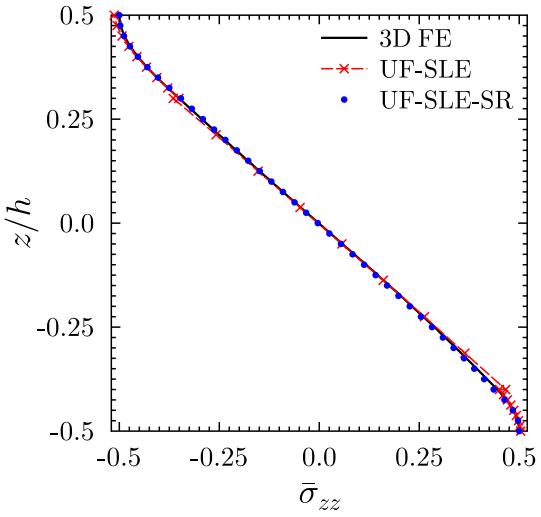

Figure 5.30: Through-thickness distribution of the normalized transverse normal stress σ_{zz} at the mid-span for laminate M.

Table 5.5: Assessment of the computational efficiency based on degrees of freedom and complexities associated with various algorithms.

Laminate	**Model**	**DOFs**	**Direct Solver Complexities**		**Iterative Solver Complexities**	
		n	Time $\sim \mathcal{O}(nb^2)$	Space $\sim \mathcal{O}(nb)$	*Time $\sim \mathcal{O}(n^2)$	*Space $\sim \mathcal{O}(nb)$
A	3D FE	5,241,615	10^{10}	10^{8}	10^{13}	10^{8}
	UF-SLE	15,561	10^{9}	10^{7}	10^{8}	10^{7}
B	3D FE	6,391,203	10^{10}	10^{8}	10^{13}	10^{8}
	UF-SLE	24,843	10^{10}	10^{7}	10^{8}	10^{7}
G	3D FE	9,988,575	10^{10}	10^{8}	10^{13}	10^{8}
	UF-SLE	34,125	10^{10}	10^{7}	10^{9}	10^{7}
K	3D FE	8,055,015	10^{10}	10^{8}	10^{13}	10^{8}
	UF-SLE	20,202	10^{10}	10^{7}	10^{8}	10^{7}

* complexity involved per iteration
b denotes the bandwidth of a matrix

iterative solver requiring less memory is more desirable (e.g. the Conjugate Gradient method). To give a detailed mathematical insight into these algorithms is beyond the scope of this work. The reader is referred to [195, 196] for more details.

For both cases, the time and space complexities are measured, which quantifies the amount of time and storage taken by an algorithm [196, 197]. The time complexity is estimated by counting the number of elementary operations performed and the space complexity is measured by the input size. Both are commonly expressed using a big $\mathcal{O}$ notation [198]. These quantities are

calculated for a few laminates as shown in Table 5.5 for the UF-SLE and the 3D FE model. Despite the large number of degrees of freedom in the 3D FE model, the time required for matrix inversion in both models is the same. This result is due to the fact that in the 3D FE model, the stiffness matrix is more sparse than the UF-SLE model. However, the advantage of the present approach becomes clear when memory requirements are considered. Due to the huge number of degrees of freedom in 3D FE, the memory required is 10 times more than the case of the UF-SLE model. Moreover, the direct solver uses computer's RAM for storing the matrix and for performing other operations. If sufficient RAM is not available, the solver must be changed to iterative, which in turn makes the computation more expensive in case of 3D FE compared to the UF-SLE model.

5.5 Conclusions

The aim of this chapter was to capture three-dimensional stress fields accurately in laminated composite and sandwich beam-like structures and with greater computational efficiency than 3D finite element analysis. The Serendipity Lagrange expansion-based Unified Formulation model is benchmarked against a 3D elasticity solution, 3D finite element solutions and a mixed formulation based on a Hellinger-Reissner third-order refined zig-zag model. The findings from the present study can be summarised as follows:

1. The UF-SLE model is sufficient to obtain a Layer-Wise model and therefore captures the zig-zag effect. The beam's cross-section is discretised such that each layer represents a four-node Lagrange element and the precision of the solution is tuned by varying the polynomial order. In contrast, 3D FE models require a large number of elements per layer and furthermore, the condition on the aspect ratio of a 3D brick element increases overall mesh density.

2. For all of the laminates considered, the UF-SLE model predicts 3D stress fields accurately and the results are in excellent agreement with Pagano's 3D elasticity solution. In most cases, the results are more accurate than those obtained by the mixed beam benchmark problem.

3. The UF-SLE model is a displacement-based layer-wise approach and the HR3-RZT is a mixed-variational equivalent single layer theory. Both models provide similar levels of accuracy and the HR3-RZT is shown to be computationally more efficient. Despite this relative inefficiency, the present approach has significant benefits as it is more general in terms of the variety of structural mechanics problems that can be solved.

4. As the present approach is displacement-based, *i.e.* the equilibrium of stresses is guaranteed in a weak sense, the inter-laminar continuity condition of transverse stresses is not satisfied. To ensure that the transverse stresses are captured accurately, a posteriori stress recovery step is employed.

5. The proposed model accurately predicts the boundary layer effects that arise due to local variations in the 3D stresses towards clamped ends. The boundary layer intensifies the through-thickness transverse shear and normal stresses. These stresses play an important role in delamination initiation, thus robust numerical models that capture these effects are essential.

6. With the UF-SLE formulation, global stiffness and buckling, as well as detailed localised stress analyses can be performed in a single model. As such, the need for running low-fidelity models for global response, and high-fidelity models for accurate stress predictions is removed. Potentially, the modelling approach for structural analysts in industry could be simplified.

7. All of the above mentioned points are valid for a 3D finite element model. However, the computational efficiency gain obtained with the proposed model in comparison with finite elements is significant. Thus, the combination of accuracy and computational expense makes the Unified Formulation, based on Serendipity Lagrange expansion model, an attractive method for industrial design tools.

Another class of cross-sectional expansions based on Legendre polynomials, the so-called Hierarchical Legendre Expansion (HLE), and developed within the Unified Formulation framework shows similar advanced capabilities [199]. However, compared to HLE, SLE expansions are easier to implement as they are obtained in a straightforward manner from the product of linear two-dimensional Lagrange polynomials. Moreover, the numerical stability of HLE models is yet to be investigated, whereas, as demonstrated in [149], SLE models remain numerically stable increasing their order.

CHAPTER 6

THREE-DIMENSIONAL STRESS ANALYSIS FOR TOW-STEERED COMPOSITE STRUCTURES

Variable Angle Tow (VAT) composites offer increased freedom for tailoring material properties compared to traditional straight-fibre composites. This increased freedom leads to greater design flexibility for enhanced structural performance but comes at the cost of more complex, spatially-varying displacement, strain and stress fields. To maximise the utility of VAT composites, a computationally efficient, yet accurate, numerical framework is needed. To this end, the layer-wise form of the UF-SLE, from the previous chapter, is extended to account for tow-steered laminated composite structures. With the aim of assessing the accuracy and robustness of the UF-SLE model in analysing VAT structures, static analysis results of VAT composite beam- and plate-like structures are presented in Sections 6.2 and 6.3, respectively. Results obtained using the present approach are validated with 3D FE solutions and are compared with a mixed displacement/stress-based, third-order zig-zag theory available in the literature [11]. A key advantage of the present approach is the ability to predict accurate 3D stress fields efficiently, *i.e.* with reduced computational effort, including around local features such as geometric, kinematic or constitutive boundaries. Moreover, the work in this chapter concerns the peculiarities of commonly used mathematical expressions for describing spatially varying fibre orientations across VAT laminates. The presence of an absolute value in the function used to describe fibre orientation can lead to discontinuities in fibre angle slope and curvature. In turn, these discontinuities lead to mathematical singularities in the constitutive relations along the laminate. If this singularity is not appropriately modelled as a boundary of the continuum, but rather as an interior point of the continuum, stresses may be predicted inaccurately. Compared to other models in the literature, our method is capable of unveiling detailed 3D stresses readily and accurately also in the vicinity of this singularity.

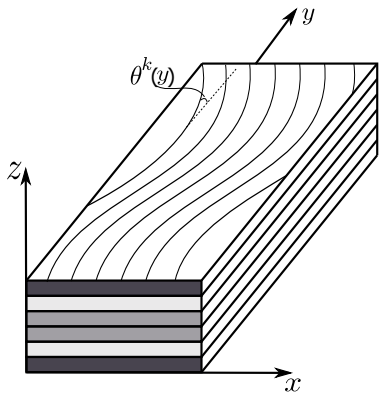

Figure 6.1: Reference system for a VAT laminated beam.

6.1 Preliminaries

Consider a variable angle tow laminated beam of length L, rectangular cross-section of width b and thickness h, composed of N layers. The material properties and the thickness of each layer may be entirely different. The beam is referred to a Cartesian coordinate system (x,y,z), where the y-direction is defined to be along the principle beam axis, while the z-axis is in the transverse stacking direction as shown in Figure 6.1. Let θ denote the fibre angle measured with respect to the y direction and varying along the beam's span. Finally, let the superscript k be used to refer to layer k.

In this work, VAT composite structures with linear fibre angle variation along one direction and constant stiffness properties in the orthogonal direction are considered. The angle variation along the spanwise direction, y, of each ply, k, is defined using the notation given by Gürdal and Olmedo [96],

$$\theta^{(k)}(y) = \frac{2(T_1^{(k)} - T_0^{(k)})}{L} \left| y - \frac{L}{2} \right| + T_0^{(k)}, \tag{6.1}$$

where $\theta^{(k)}(y)$ is the local fibre angle at y, and $T_0^{(k)}$ and $T_1^{(k)}$, written as $\langle T_0^{(k)} | T_1^{(k)} \rangle$, are the fibre angles at the beam midspan $y = L/2$ and ends $y = 0, L$, respectively. Hence, the fibre angle in each ply takes the value $T_1^{(k)}$ at one end of the beam, being steered to $T_0^{(k)}$ at the mid-span, and returning to $T_1^{(k)}$ at the other end. Due to the variable-stiffness design of the curvilinear tow paths, the material stiffness tensor $\boldsymbol{C}$ is a function of the y-location. It follows that in the analysis of VAT composites, the material stiffness matrix needs to be evaluated at each integration point that is employed in the numerical integration of the stiffness matrix (See Appendix B). It is to be noted that, the explicit expressions of the fundamental nucleus of the stiffness matrix given in Appendix B are applicable to straight-fibre (or constant-stiffness) laminates. In order to analyse VAT composites, the coefficients $\bar{C}(i,j)$ must be inside 1D integrals. For instance, equation (B.1)

Table 6.1: Mechanical properties of the materials considered in the present study. Materials p, pvc, h and IM7 stands for carbon-fibre reinforced plastic, poly-vinyl chloride foam, honeycomb and IM7/8552 composite, respectively.

Material	E_x	E_y	E_z	G_{yz}	G_{xz}	G_{xy}
	[GPa]					
p	6.9	172.37	6.9	3.45	1.38	3.45
pvc	1.723	1.723	1.723	0.663	0.663	0.663
h	1.723×10^{-3}	1.723×10^{-3}	17.23×10^{-3}	6.03×10^{-3}	12.06×10^{-3}	6.9×10^{-6}
IM7	12.0	163.0	12.0	4.0	3.2	5.0
	ν_{yz}		ν_{xz}		ν_{xy}	
p	0.25		0.25		0.01	
pvc	0.3		0.3		0.3	
h	3.0×10^{-5}		3.0×10^{-5}		0.9	
IM7	0.3		0.3		0.022	

of Appendix B becomes

$$\begin{aligned} K_{xy}^{\tau sij} = &\int_A F_{\tau,z} F_s dx dz \int_l \bar{C}(4,6) N_i N_{j,y} dy + \int_A F_{\tau,x} F_s dx dz \int_l \bar{C}(6,6) N_i N_{j,y} dy \\ &+ \int_A F_\tau F_{s,z} dx dz \int_l \bar{C}(2,5) N_{i,y} N_j dy + \int_A F_\tau F_{s,x} dx dz \int_l \bar{C}(1,2) N_{i,y} N_j dy \\ &+ \int_A F_{\tau,z} F_{s,z} dx dz \int_l \bar{C}(4,5) N_i N_j dy + \int_A F_{\tau,z} F_{s,x} dx dz \int_l \bar{C}(1,4) N_i N_j dy \\ &+ \int_A F_{\tau,x} F_{s,z} dx dz \int_l \bar{C}(5,6) N_i N_j dy + \int_A F_\tau F_s dx dz \int_l \bar{C}(2,6) N_{i,y} N_{j,y} dy \\ &+ \int_A F_{\tau,x} F_{s,x} dx dz \int_l \bar{C}(1,6) N_i N_j dy, \end{aligned} \tag{6.2}$$

and so on.

The material properties and stacking sequences modelled in this section are shown in Tables 6.1 and 6.2, respectively. Materials p, pvc, h represent an orthotropic carbon-fibre reinforced plastic, isotropic poly-vinyl chloride foam, and transversely isotropic honey-comb core, respectively. IM7 stands for IM7 8852, a carbon-fibre reinforced plastic material commonly used in industry. In most of the laminates considered herein, the variation in fibre angle along the length of the beam is 90°, which is greater than the manufacturing capability of most tow-steering machines. However, this extreme case of stiffness variation along the beam length provides a good test case for model verification.

6.2 Tow-Steered Composite Beam-like Structure

A multilayered beam-like 3D structure with length-to-thickness ratio $L/h = 10$, comprising N_l VAT composite layers is considered in the present study. The beam, aligned with the Cartesian

Table 6.2: Stacking sequence for laminates considered in the present study. Subscripts indicate the repetition of a property over the corresponding number of layers.

Laminate	Layer thickness ratio	Material	Stacking sequence
VAT Beam			
A	$[(1/8)_8]$	$[IM7_8]$	$[\langle 90\|0\rangle/\langle -90\|0\rangle/\langle 45\|\text{-}45\rangle/\langle -45\|45\rangle]_s$
B	$[(1/8)_8]$	$[IM7_8]$	$[\langle 90\|20\rangle/\langle 45\|-25\rangle/\langle -90\|-20\rangle/\langle -45\|25\rangle]_s$
C	$[(1/3)_3]$	$[IM7_3]$	$[\langle 0\|90\rangle/\langle 90\|0\rangle/\langle 0\|90\rangle]$
D	$[(1/3)_3]$	$[IM7_3]$	$[\langle 90\|0\rangle/\langle 0\|90\rangle/\langle 90\|0\rangle]$
E	$[(1/5)_5]$	$[IM7_5]$	$[\langle 90\|30\rangle/\langle -70\|50\rangle/\langle 60\|0\rangle/\langle -25\|35\rangle/\langle 80\|10\rangle]$
F	$[(1/4)_4]$	$[IM7_4]$	$[\langle 0\|70\rangle/\langle 90\|50\rangle/\langle 20\|-40\rangle/\langle 50\|0\rangle]$
G	$[(1/8)_2/0.5/(1/8)_2]$	$[p_2/pvc/p_2]$	$[\langle 45\|-45\rangle/\langle -45\|45\rangle/0/\langle -45\|45\rangle/\langle 45\|-45\rangle]$
H	$[(1/12)_4/(1/3)/(1/12)_4]$	$[p_4/pvc/p_4]$	$[\langle 0\|90\rangle/\langle 90\|0\rangle/\langle 0\|-90\rangle/\langle -90\|0\rangle/\ldots$ $0/\langle -90\|0\rangle/\langle 0\|-90\rangle/\langle 90\|0\rangle/\langle 0\|90\rangle]$
I	$[(1/8)_2/0.5/(1/8)_2]$	$[p_2/pvc/p_2]$	$[\langle 20\|-60\rangle/\langle -20\|60\rangle/0/0/90]$
J	$[(1/12)_4/(1/3)/(1/12)_4]$	$[p_4/pvc/p_4]$	$[\langle 20\|-60\rangle/\langle -20\|60\rangle/\langle 45\|-45\rangle/\langle -45\|45\rangle/\ldots$ $0/0/90/\langle 35\|-35\rangle/\langle -35\|35\rangle]$
VAT Plate			
K	$[(1/4)_4]$	$[IM7_4]$	$[\langle 0\|90\rangle/\langle 0\|-90\rangle]_s$
L	$[(1/8)_8]$	$[IM7_8]$	$[\langle 0\|70\rangle/\langle 0\|-70\rangle/\langle 90\|20\rangle/\langle -90\|-20\rangle]_s$
M	$[(1/16)_4/0.5/(1/16)_4]$	$[IM7_4/h/IM7_4]$	$[\langle 0\|70\rangle/\langle 0\|-70\rangle/\langle 45\|-20\rangle/\langle -45\|20\rangle/0/\ldots]$ $\langle -45\|20\rangle/\langle 45\|-20\rangle/\langle 0\|-70\rangle/\langle 0\|70\rangle]$

y-axis, is clamped at both ends, $y = 0$ and $y = L$, and is assumed to undergo static deformations in plane strain (x-direction), under a uniformly distributed load equally divided between the top and the bottom surfaces $P_z^{\mathrm{t}} = P_z^{\mathrm{b}} = -q_0/2$, as shown in Figure 6.2. To test the general applicability of the Unified Formulation based on the Serendipity Lagrange expansion functions (UF-SLE), a variety of symmetric and non-symmetric VAT composite beams are analysed. These laminates are defined by items A-J in Table 6.2, where VAT beams A-D are symmetric, E-F are non-symmetric, G-H are symmetric sandwich construction with variable stiffness face layers, and I-J are non-symmetric sandwich construction with hybrid constant-stiffness/variable-stiffness face layers.

In our UF-SLE models, the structures are discretised with 40 B4 (four-noded 1D Lagrange) elements along their length. The cross-sections are divided into sub-domains (one per layer). Within each sub-domain (Serendipity Lagrange element) a fourth-order expansion function is employed (SL4). The number of beam elements and the order of expansion in the cross-section

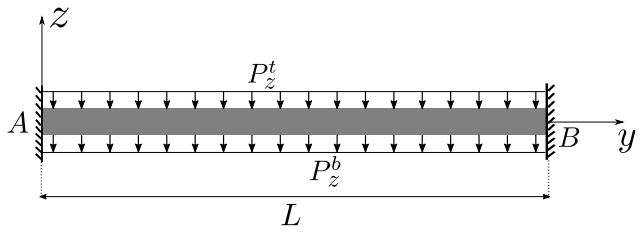

Figure 6.2: Representation of a multilayered beam-like structure, length-to-thickness ratio $L/h = 10$, clamped at both ends and subjected to a uniformly distributed load over the top and bottom surface.

were set through a convergence analysis. For the sake of brevity, only converged results are presented for all cases. To the authors' knowledge there are no 3D closed-form solutions for VAT composite beams under bending. Therefore, the bending deflection and stress results obtained are compared with a mixed formulation approach based on the Hellinger-Reissner third-order theory [200] with Murakami Zig-Zag function [201] (HR3-MZZF) and 3D FE solutions as given in [11]. It is to be noted that the results available in the literature are based on a plane-strain assumption in the x-direction. Thus, to mimic the plane-strain condition in the present approach, appropriate coupling terms are removed from the material stiffness matrix as described in Appendix D.

Normalised metrics of the bending deflection, u_z, axial stress, σ_{yy}, transverse shear stress, τ_{yz} and transverse normal stress, σ_{zz}, are used for our comparisons as given by

$$\begin{aligned} \bar{u}_z = \frac{10^6 h^2}{q_0 L^4} \int_{-h/2}^{h/2} u_z(x,y,z), \quad \bar{\sigma}_{yy} = \frac{h^2}{q_0 L^2} \cdot \sigma_{yy}(x,y,z), \\ \bar{\tau}_{yz} = \frac{1}{q_0} \cdot \tau_{yz}(x,y,z), \quad \bar{\sigma}_{zz} = \frac{1}{q_0} \cdot \sigma_{zz}(x,y,z). \end{aligned} \tag{6.3}$$

Figures 6.3 to 6.12 show plots of the spanwise bending deflection, $\bar{u}_z$, through-thickness in-plane stress, $\bar{\sigma}_{yy}$, and transverse normal stress, $\bar{\sigma}_{zz}$, at the mid-span of the beam, and through-thickness transverse shear stress, $\bar{\tau}_{yz}$, at the quarter-span of the beam. From these plots, it is evident that the displacement and stress distributions computed using the UF-SLE model are in an excellent agreement with 3D FE solutions. Furthermore, generally, the UF-SLE model correlates with the 3D FE solutions better than the HR3-MZZF model, particularly for transverse normal stresses, $\bar{\sigma}_{zz}$. Overall, for displacement, $\bar{u}_z$, axial normal stress, $\bar{\sigma}_{yy}$, and transverse shear stress, $\bar{\tau}_{yz}$, Figures 6.3 to 6.8 show a good correlation between 3D FE, HR3-MZZF and UF-SLE models. However, for VAT sandwiches, *i.e.* VAT G, VAT H, VAT I and VAT J, the UF-SLE model (layer-wise approach) is more accurate than the HR3-MZZF model (equivalent single layer approach), due to higher degrees of transverse orthotropy. The greatest differences are observed for the most challenging test case, the non-symmetric sandwich beam VAT J, as shown in Figure 6.12. These differences are clearly due to the inability of the Murakami's Zig-Zag function (MZZF) to capture the zig-zag effect accurately, when employed for highly heterogeneous sandwich beams.

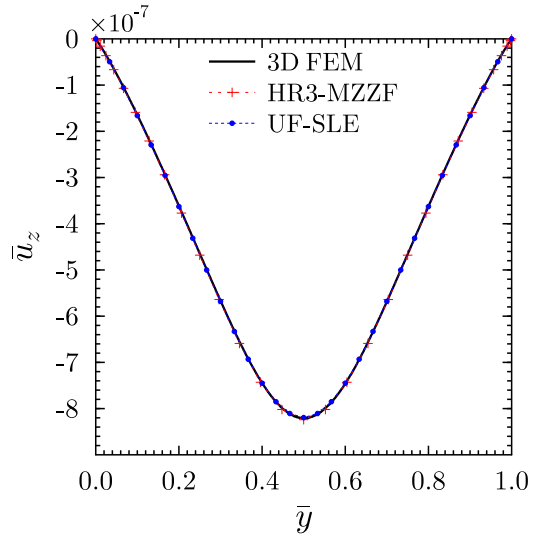

(a) Normalised bending deflection, $\bar{u}_z$

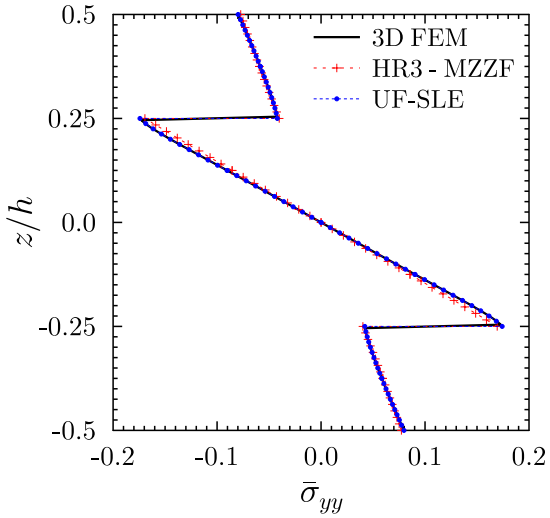

(b) Axial normal stress, $\bar{\sigma}_{yy}$ at $y = L/2$

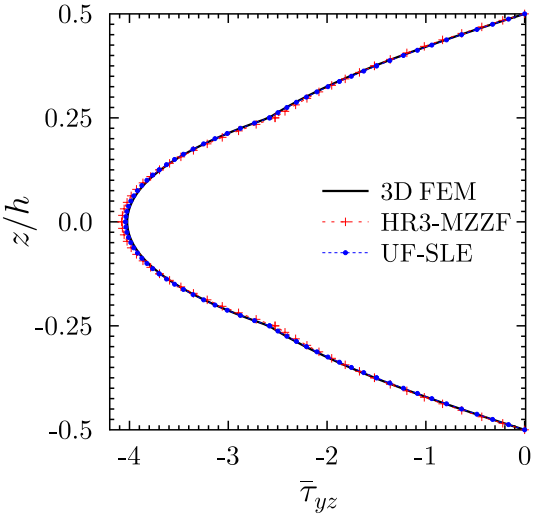

(c) Transverse shear stress, $\bar{\tau}_{yz}$ at $y = L/4$

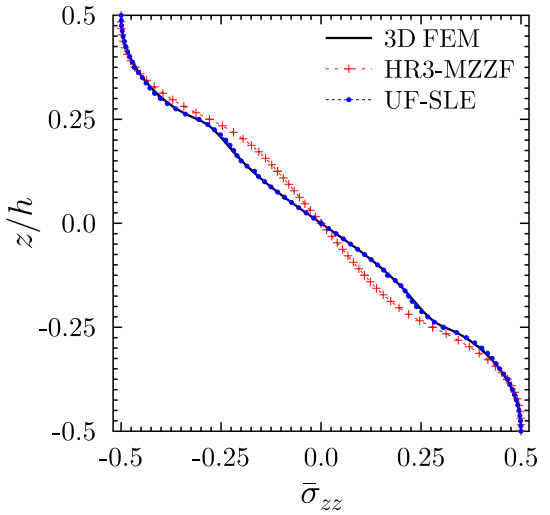

(d) Transverse normal stress, $\bar{\sigma}_{zz}$ at $y = L/2$

Figure 6.3: Normalised bending deflection and through-thickness distribution of the normalized axial and transverse stresses for VAT laminate A.

It is noted, however, that the refined zig-zag theory (RZT) introduced by Tessler [202] has been shown to solve this shortcoming and to be capable of predicting the stress response accurately even for highly heterogeneous laminates.

The remainder of this section focuses on: (i) the accuracy of the distributions of through-thickness transverse normal stress, and (ii) a comparison of the 3D FE, HR3-MZZF and UF-SLE, models in term of general accuracy. It is well known that in a displacement-based 3D FE approach,

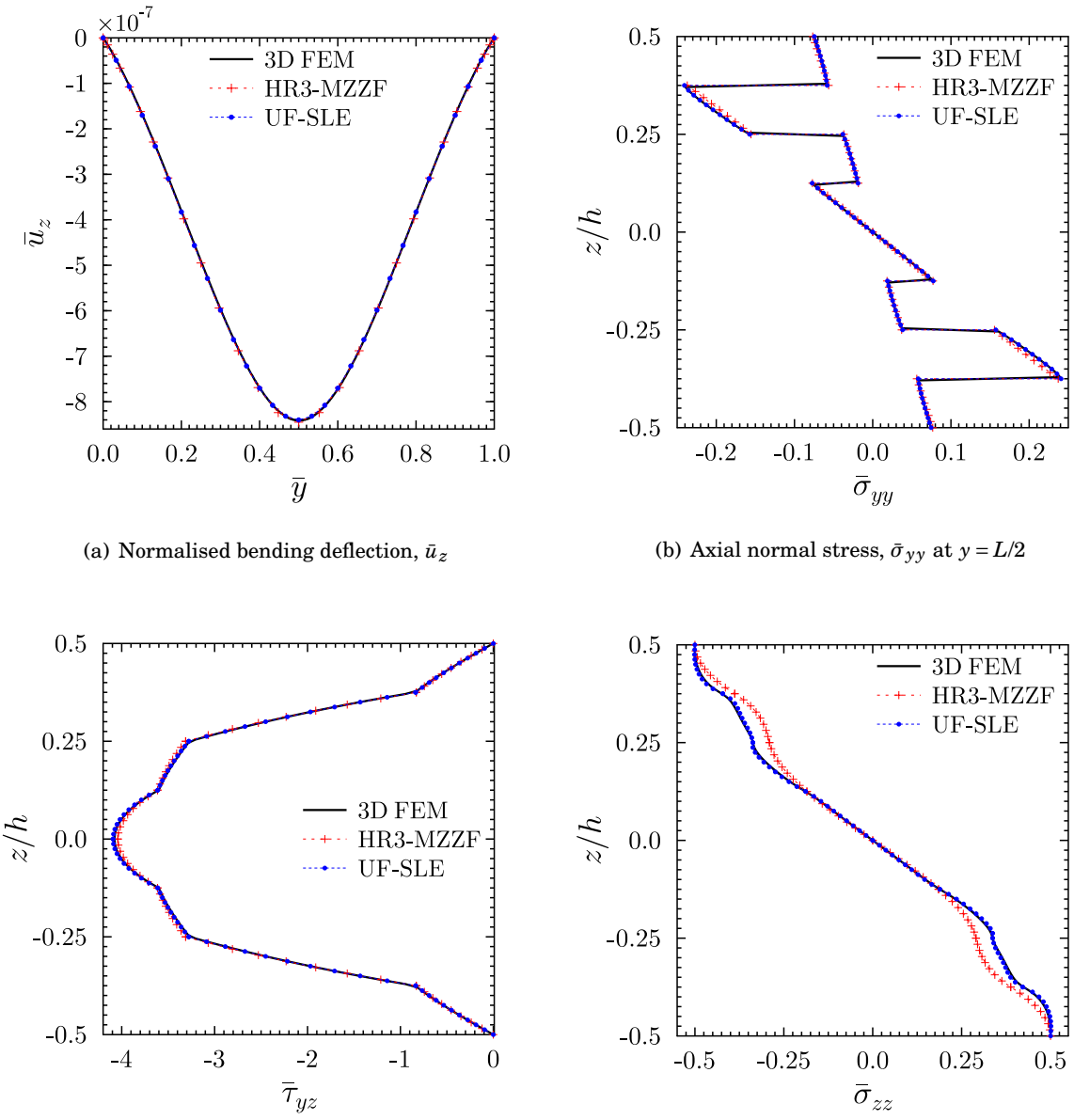

(a) Normalised bending deflection, $\bar{u}_z$

(b) Axial normal stress, $\bar{\sigma}_{yy}$ at $y = L/2$

(c) Transverse shear stress, $\bar{\tau}_{yz}$ at $y = L/4$

(d) Transverse normal stress, $\bar{\sigma}_{zz}$ at $y = L/2$

Figure 6.4: Normalised bending deflection and through-thickness distribution of the normalized axial and transverse stresses for VAT laminate B.

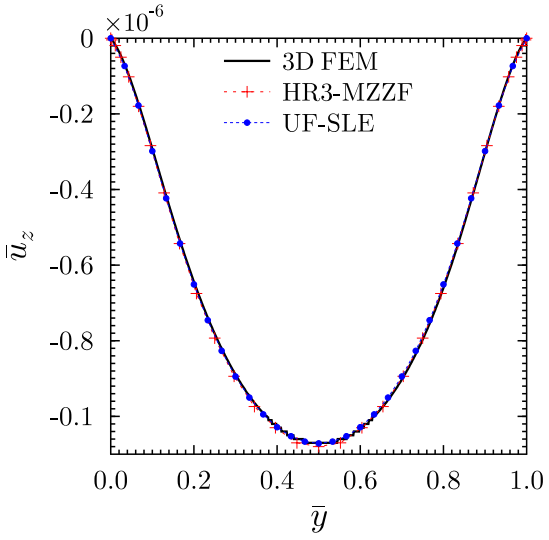

(a) Normalised bending deflection, $\bar{u}_z$

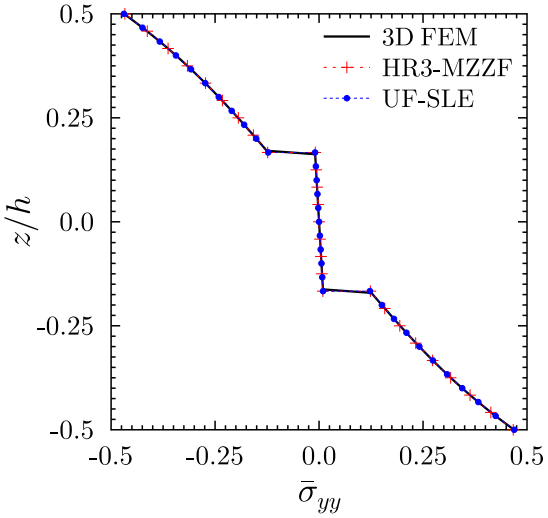

(b) Axial normal stress, $\bar{\sigma}_{yy}$ at $y = L/2$

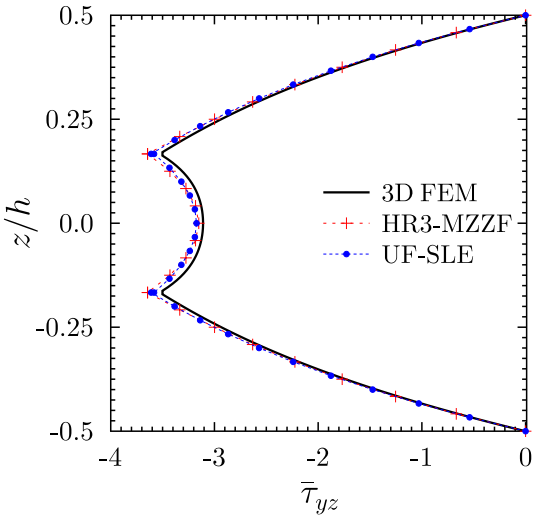

(c) Transverse shear stress, $\bar{\tau}_{yz}$ at $y = L/4$

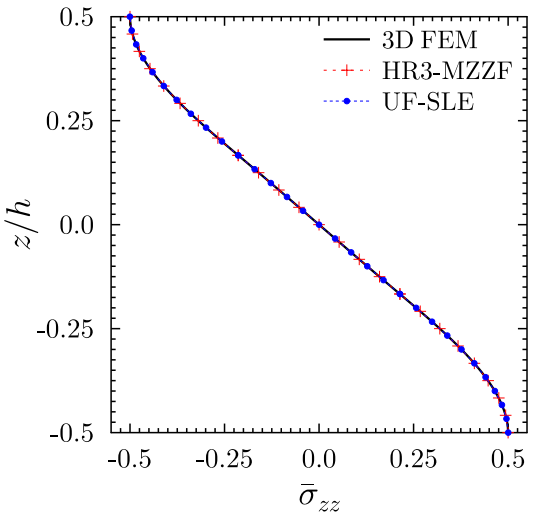

(d) Transverse normal stress, $\bar{\sigma}_{zz}$ at $y = L/2$

Figure 6.5: Normalised bending deflection and through-thickness distribution of the normalized axial and transverse stresses for VAT laminate C.

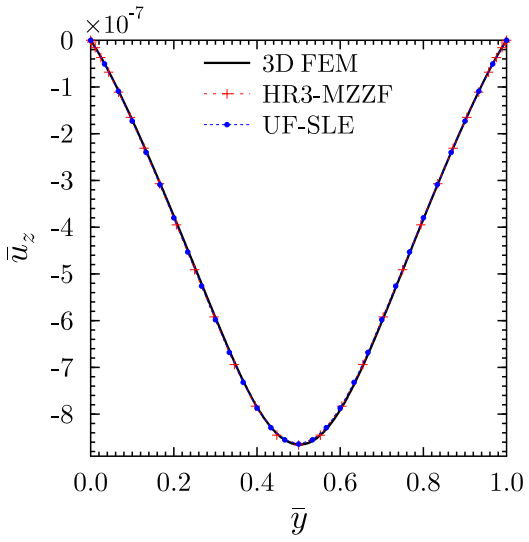

(a) Normalised bending deflection, $\bar{u}_z$

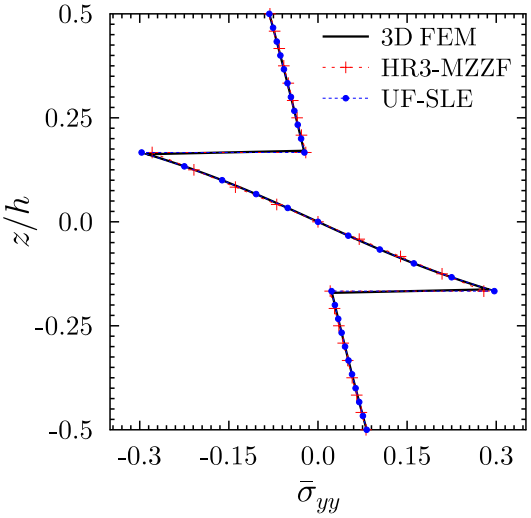

(b) Axial normal stress, $\bar{\sigma}_{yy}$ at $y = L/2$

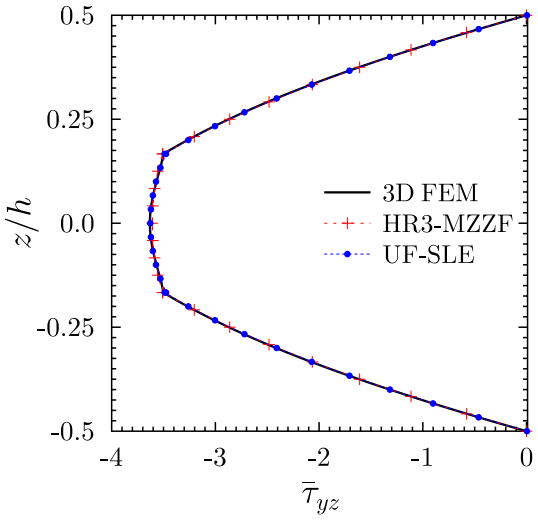

(c) Transverse shear stress, $\bar{\tau}_{yz}$ at $y = L/4$

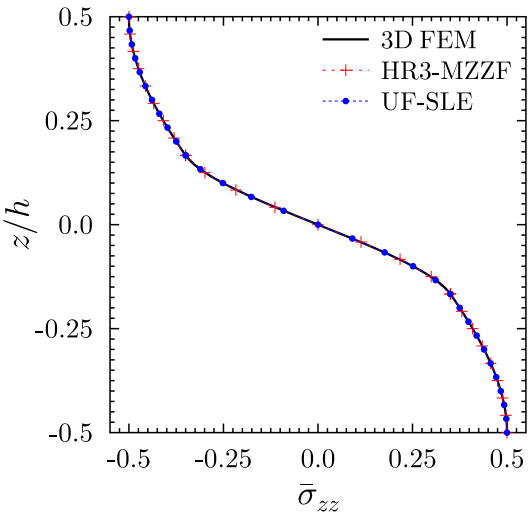

(d) Transverse normal stress, $\bar{\sigma}_{zz}$ at $y = L/2$

Figure 6.6: Normalised bending deflection and through-thickness distribution of the normalized axial and transverse stresses for VAT laminate D.

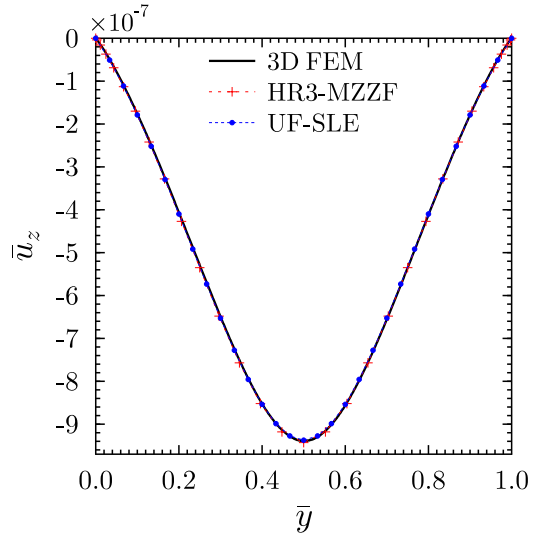

(a) Normalised bending deflection, $\bar{u}_z$

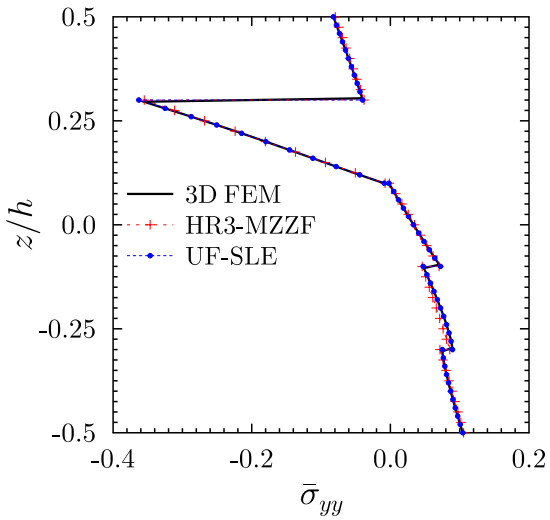

(b) Axial normal stress, $\bar{\sigma}_{yy}$ at $y = L/2$

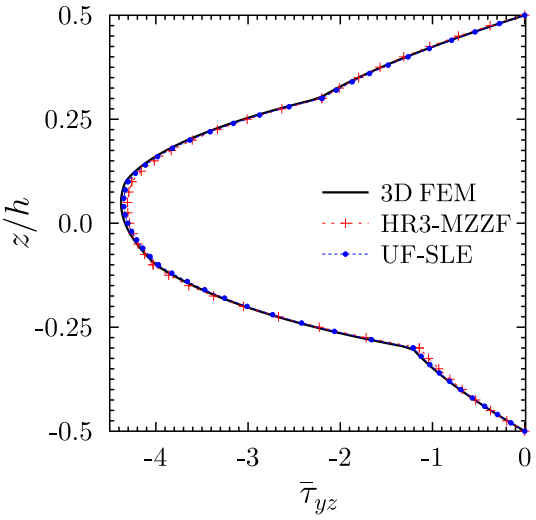

(c) Transverse shear stress, $\bar{\tau}_{yz}$ at $y = L/4$

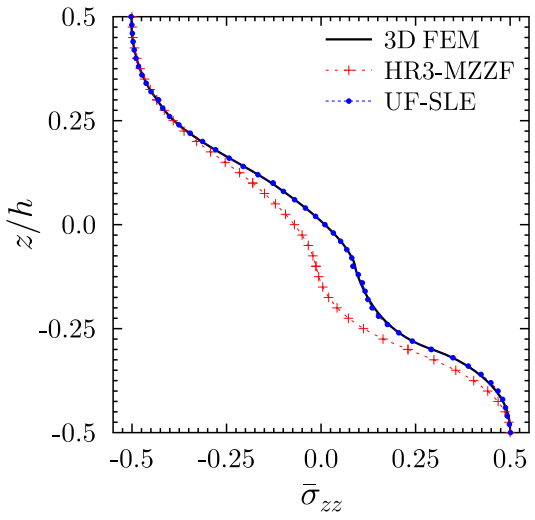

(d) Transverse normal stress, $\bar{\sigma}_{zz}$ at $y = L/2$

Figure 6.7: Normalised bending deflection and through-thickness distribution of the normalized axial and transverse stresses for VAT laminate E.

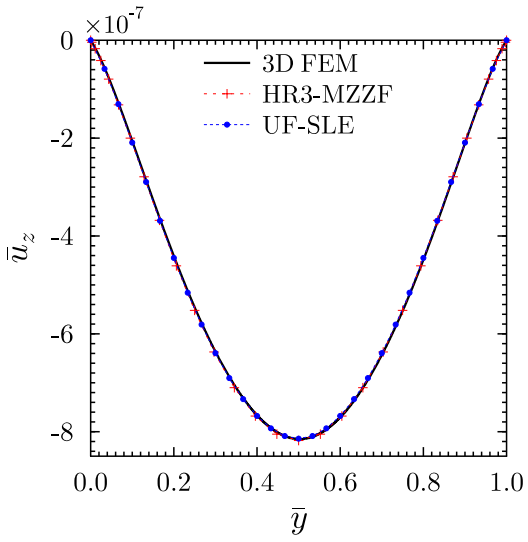

(a) Normalised bending deflection, $\bar{u}_z$

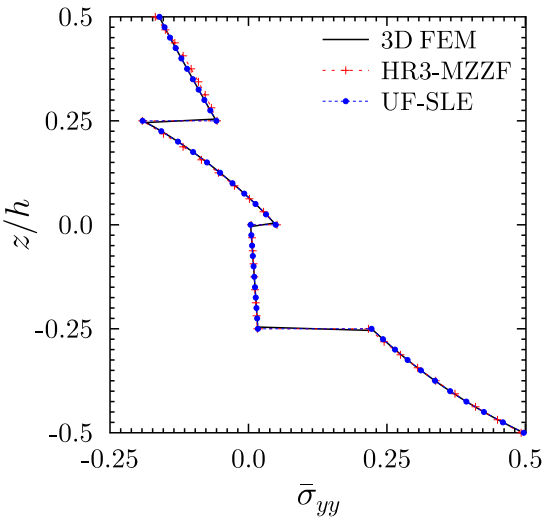

(b) Axial normal stress, $\bar{\sigma}_{yy}$ at $y = L/2$

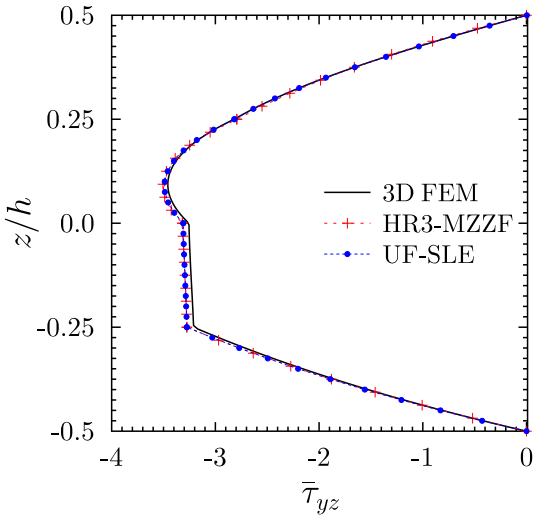

(c) Transverse shear stress, $\bar{\tau}_{yz}$ at $y = L/4$

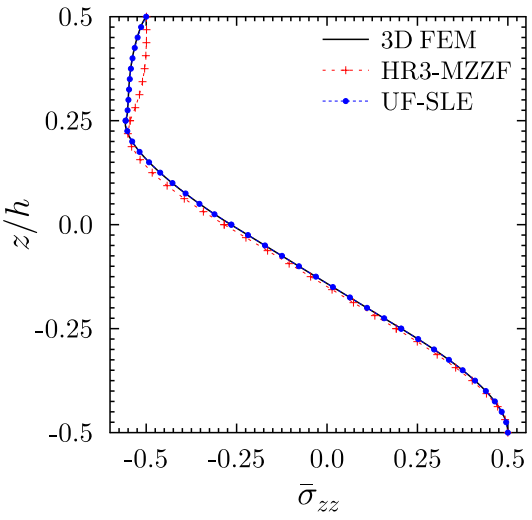

(d) Transverse normal stress, $\bar{\sigma}_{zz}$ at $y = L/2$

Figure 6.8: Normalised bending deflection and through-thickness distribution of the normalized axial and transverse stresses for VAT laminate F.

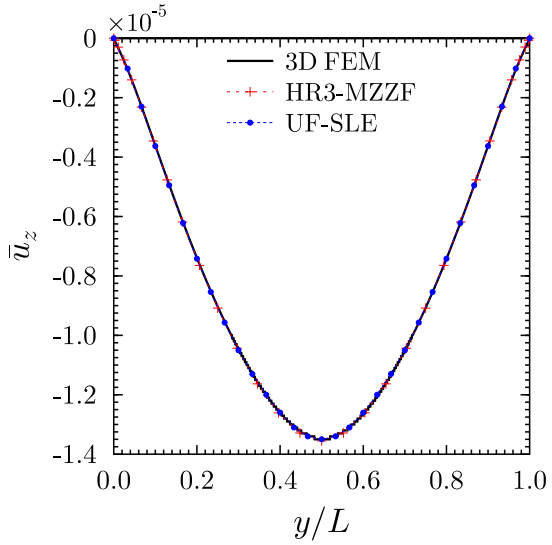

(a) Normalised bending deflection, $\bar{u}_z$

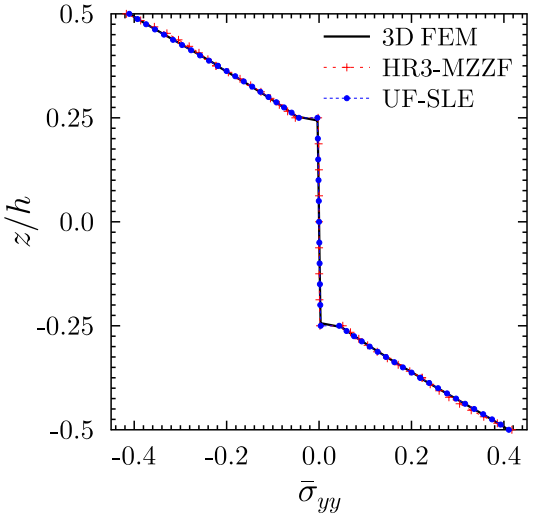

(b) Axial normal stress, $\bar{\sigma}_{yy}$ at $y = L/2$

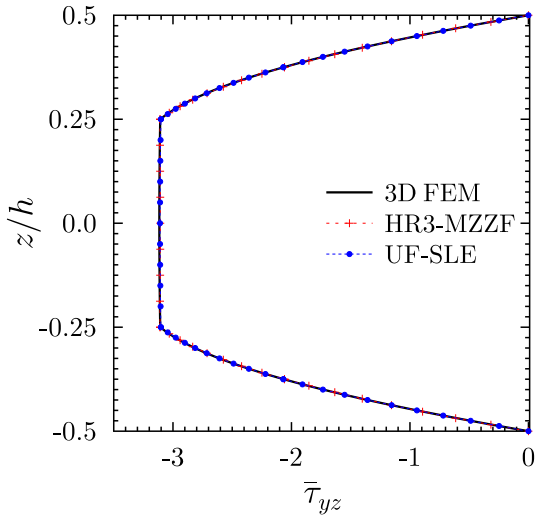

(c) Transverse shear stress, $\bar{\tau}_{yz}$ at $y = L/4$

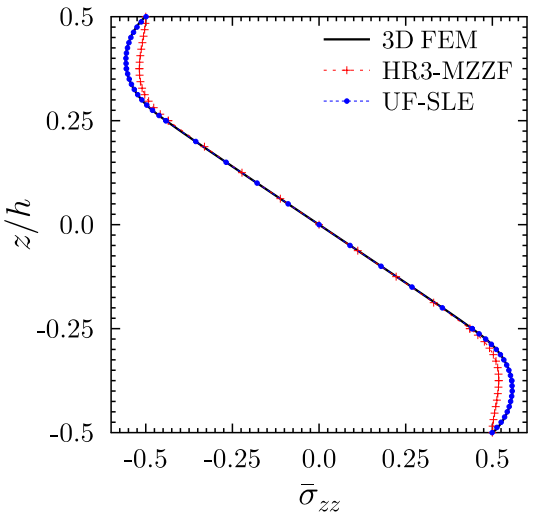

(d) Transverse normal stress, $\bar{\sigma}_{zz}$ at $y = L/2$

Figure 6.9: Normalised bending deflection and through-thickness distribution of the normalized axial and transverse stresses for VAT laminate G.

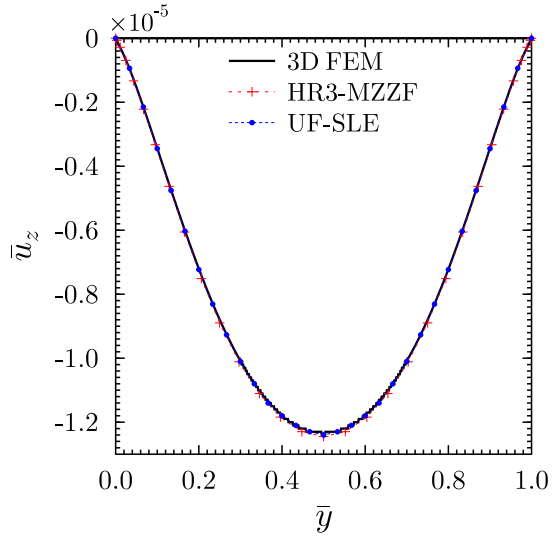

(a) Normalised bending deflection, $\bar{u}_z$

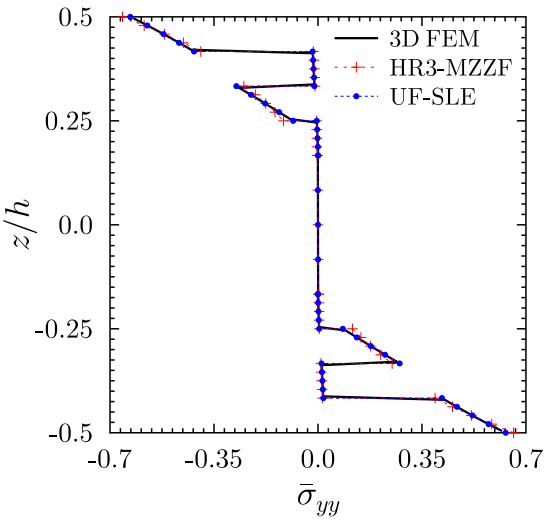

(b) Axial normal stress, $\bar{\sigma}_{yy}$ at $y = L/2$

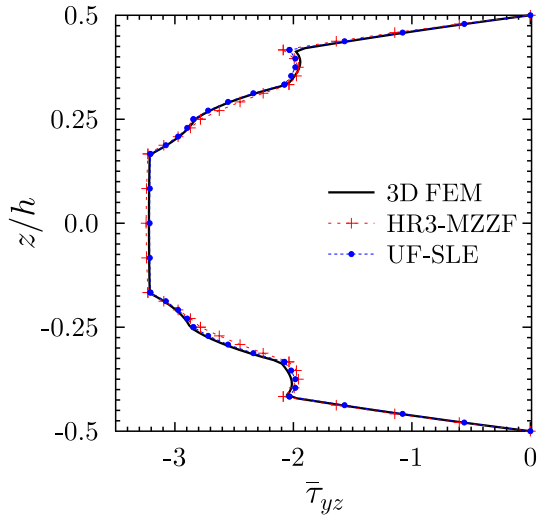

(c) Transverse shear stress, $\bar{\tau}_{yz}$ at $y = L/4$

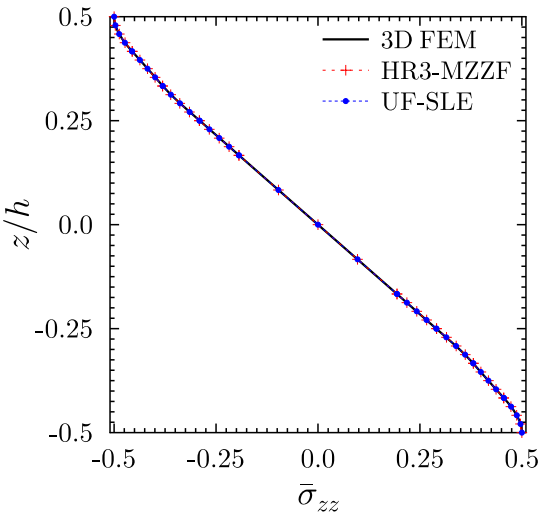

(d) Transverse normal stress, $\bar{\sigma}_{zz}$ at $y = L/2$

Figure 6.10: Normalised bending deflection and through-thickness distribution of the normalized axial and transverse stresses for VAT laminate H.

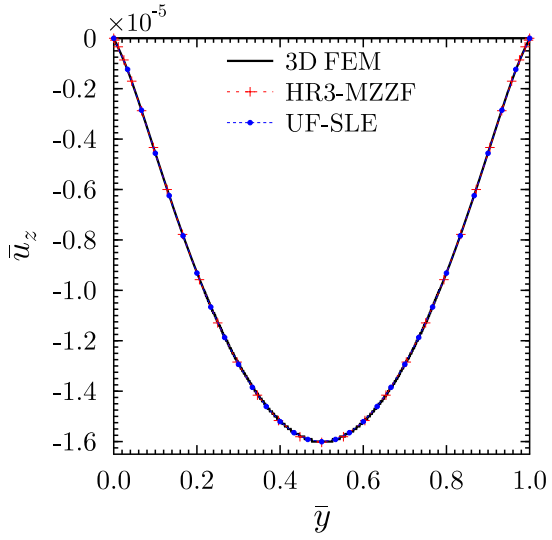

(a) Normalised bending deflection, $\bar{u}_z$

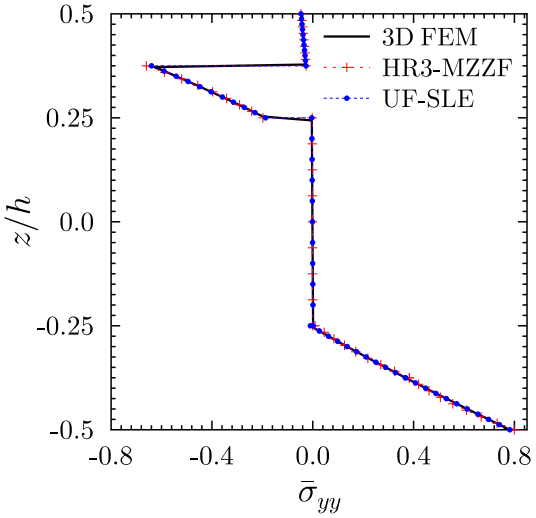

(b) Axial normal stress, $\bar{\sigma}_{yy}$ at $y = L/2$

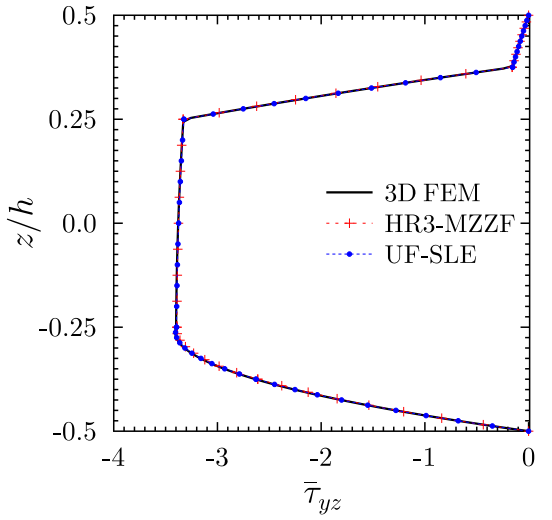

(c) Transverse shear stress, $\bar{\tau}_{yz}$ at $y = L/4$

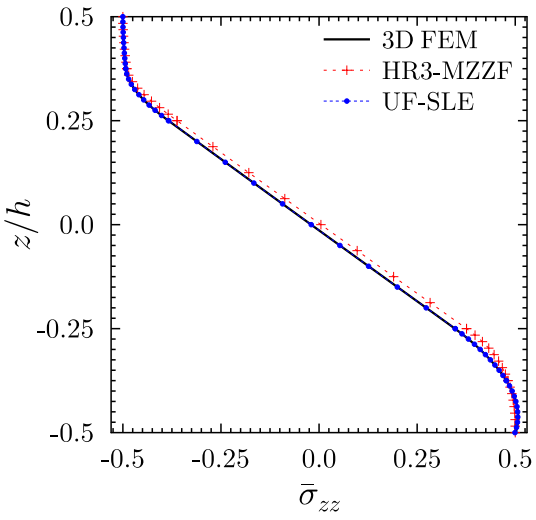

(d) Transverse normal stress, $\bar{\sigma}_{zz}$ at $y = L/2$

Figure 6.11: Normalised bending deflection and through-thickness distribution of the normalized axial and transverse stresses for VAT laminate I.

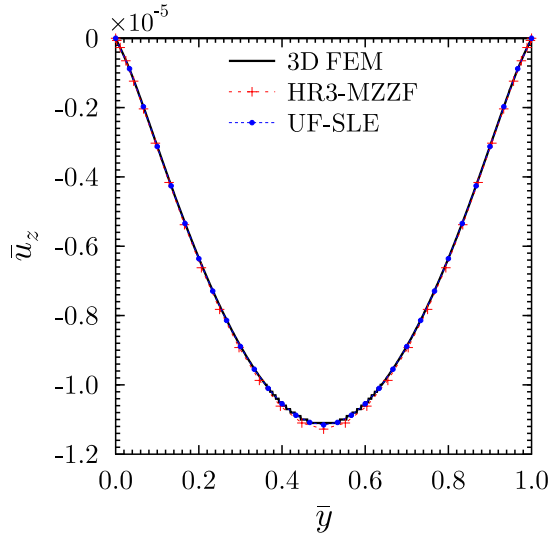

(a) Normalised bending deflection, $\bar{u}_z$

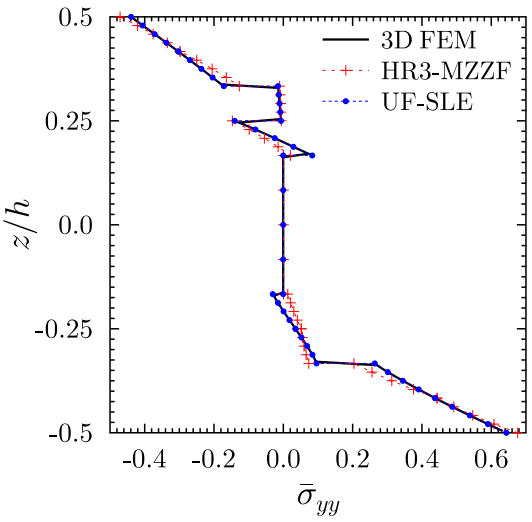

(b) Axial normal stress, $\bar{\sigma}_{yy}$ at $y = L/2$

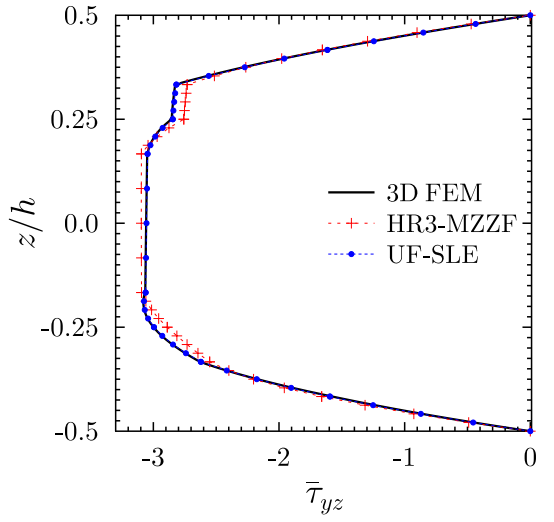

(c) Transverse shear stress, $\bar{\tau}_{yz}$ at $y = L/4$

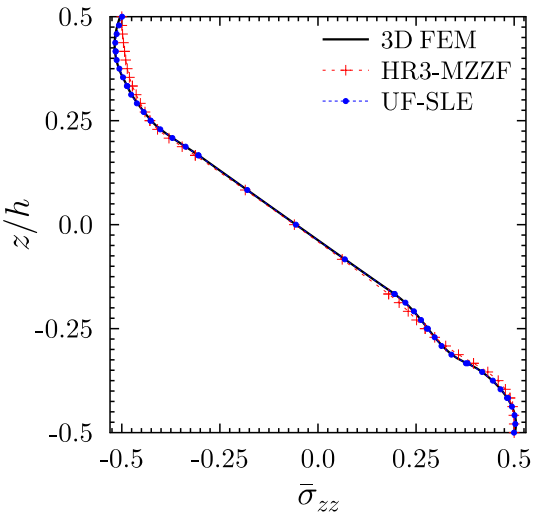

(d) Transverse normal stress, $\bar{\sigma}_{zz}$ at $y = L/2$

Figure 6.12: Normalised bending deflection and through-thickness distribution of the normalized axial and transverse stresses for VAT laminate J.

stresses are derived from displacement variables using kinematic and constitutive equations, and therefore, the equilibrium of stresses is only satisfied in a weak (average integral) sense. This means that the residual in the 3D equilibrium equations decreases asymptotically with mesh refinement. In the Hellinger-Reissner (HR) mixed formulation proposed by Groh & Weaver [11], the individual stress assumptions inherently satisfy Cauchy's equilibrium equations. The statement is substantiated in Chapter 6 of [11] by computing residuals of Cauchy's equilibrium equations for all VAT beams A-J in case of the 3D FE and the HR model. In addition to the residual, the total strain energy was also used to assess the accuracy of the two models. These quantitative findings clearly showed that the HR model obeys the stress equilibrium equations more accurately, and at the same time corresponds to a lower strain energy configuration than 3D FE. Hence, it was inferred that the HR3-MZZF solution provides a more accurate representation of the 3D stress field within the structures analysed than the purely displacement-based 3D FE formulation. However, let us now consider the transverse stress plots for VAT beams F, G and J (Figures 6.8, 6.9 and 6.12), which show the greatest discrepancy between the two weak, displacement-based formulations (3D FE and the UF-SLE) and the HR model. Groh & Weaver [11] originally argued that the 3D FE model does not obey the traction equilibrium condition on the top and bottom surfaces (top for F and J, top and bottom for G). Their argument was based on analysing Cauchy's transverse equilibrium equation in the absence of body forces as given by

$$\frac{\partial \tau_{xz}}{\partial x} + \frac{\partial \tau_{yz}}{\partial y} + \frac{\partial \sigma_{zz}}{\partial z} = 0, \tag{6.4}$$

and went as follows. The test case considered here assumes a plane strain condition in the lateral x-direction, hence $\tau_{xz} = 0$. Also, due to the absence of shear tractions on the top and bottom surfaces, $\tau_{yz}(z = \pm h/2) = 0$. It follows that the axial derivative of the transverse shear stress vanishes on the top and bottom surfaces, $\partial \tau_{yz}/\partial y(z = \pm h/2) = 0$. Groh & Weaver therefore argued that the z-wise derivative of the transverse normal stress $\partial \sigma_{zz}/\partial z$ must be zero at the top and bottom surfaces. The plots of $\bar{\sigma}_{zz}$ in Figures 6.8, 6.9 and 6.12 show that this condition does not hold true for the 3D FE and the UF-SLE model, whereas the HR3-MZZF model satisfies this boundary condition for all cases. However, for a 3D body, equation (6.4) describes the equilibrium within the interior of the continuum, whereas the top and bottom surfaces are on the boundary. Hence, equation (6.4) is in fact not applicable at these points and only the traction boundary conditions need to be satisfied. Both 3D FE and UF-SLE models satisfy the transverse traction conditions. Even though the z-wise derivative of the transverse normal stress $\partial \sigma_{zz}/\partial z$ is often zero for isotropic structures and straight-fibre laminates, the traction boundary conditions do not require this to be so, and indeed for some VAT laminates (F, G and J) the condition does not hold.

To elucidate this point further we compute the transverse normal stress using the UF-SLE model, not from the constitutive relation, but from the transverse stress equilibrium equation, hence mimicking the HR approximation. This approach is commonly termed as Stress Recovery (SR), which ensures that the 3D stress equilibrium equations are satisfied. The stress recovery technique applied in the Unified formulation framework is described in Section 5.1 of the

previous chapter. The transverse normal stress recovered is shown as the "UF-SR (40B4)" curve in Figure 6.13, a close-up on surface stresses for VAT beams F and G. It is observed that the through-thickness gradient of $\bar{\sigma}_{zz}$ approaches zero at the top surface. However, with an increase in the number of beam elements along the length from 40 to 200 it is observed, in contrast, that the curve progressively approaches the transverse normal stress distribution obtained from 3D FE and UF-SLE models (using the constitutive relation). From these results, a couple of important conclusions can be drawn. Firstly, the initial solution obtained from the constitutive relations has already converged and there is no further need to employ the SR step. Secondly, the shift in the curve of $\bar{\sigma}_{zz}$ (obtained by SR) with increasing beam elements indicates that the spanwise distribution of the transverse shear stress is indeed varying such as to satisfy equilibrium (equation (6.4)).

Shifting our attention on the transverse shear stress, Figure 6.14(a) shows the variation of $\bar{\tau}_{yz}$ along the beam, just below the top surface ($z/h = 0.499$). The distribution is shown to be continuous but non-differentiable at the mid-span of the beam. A similar behaviour is observed by plotting the variation of $\bar{\sigma}_{yy}$ in Figure 6.14(b), implying that $\frac{\partial \sigma_{yy}}{\partial y}$ and $\frac{\partial \tau_{yz}}{\partial y}$ are not defined at $y = L/2$. For the same reason one can deduce that the residuals

$$\frac{\partial \tau_{xy}}{\partial x} + \frac{\partial \sigma_{yy}}{\partial y} + \frac{\partial \tau_{yz}}{\partial z} = R_y, \qquad \frac{\partial \tau_{xz}}{\partial x} + \frac{\partial \tau_{yz}}{\partial y} + \frac{\partial \sigma_{zz}}{\partial z} = R_z, \tag{6.5}$$

are also not defined at $y = L/2$. This hypothesis is examined quantitatively and confirmed by plotting residuals R_y and R_z at various locations along the beam length, just below the top surface ($z/h = 0.499$) in Figure 6.15. Therefore, in such cases the stress distribution is incorrect if recovered from Cauchy's equilibrium equations. The HR formulation uses a similar approach as the SR technique as Cauchy's equilibrium equations are used to inform the stress assumptions, and incorrectly enforces field equilibrium rather than boundary (traction) equilibrium on the top and bottom surface. Hence, the normal stress distribution obtained from the HR3-MZZF model at the beam's mid-span is inaccurate for VAT laminates F, G and J, and the through-thickness gradient of $\bar{\sigma}_{zz}$ is not zero towards the surfaces, as correctly obtained from 3D FE and UF-SLE models. At locations other than the mid-span, since $\frac{\partial \tau_{yz}}{\partial y}$ is defined, a boundary layer, defined as the region below the top surface up to the point where $\frac{\partial \sigma_{zz}}{\partial z}$ goes to zero, does exist. The boundary layer thickness, t_{BL}, calculated from the top surface is shown in Figure 6.16.

The reason for $\bar{\tau}_{yz}$ and $\bar{\sigma}_{yy}$ to be continuous but non-differentiable at the mid-span is the linear fibre angle variation definition by Gürdal and Olmedo [96]. This is illustrated by Figures 6.17 and 6.18(a). The former shows the representation of spatially steered fibres in the plane of a composite lamina, while Figure 6.18(a) shows the spanwise variation of fibre angle as calculated from equation (6.1) for different combinations of $T_0|T_1$. One of the combinations considered is for the top layer of VAT beam G, where the fibre angle starts at $-45°$, is steered linearly to $45°$ at the mid-span, and then ends at $-45°$. In other cases, T_0 is varied from $0°$ to $90°$, while T_1 is kept fixed at $-45°$, so as to understand the reason for the typical behaviour

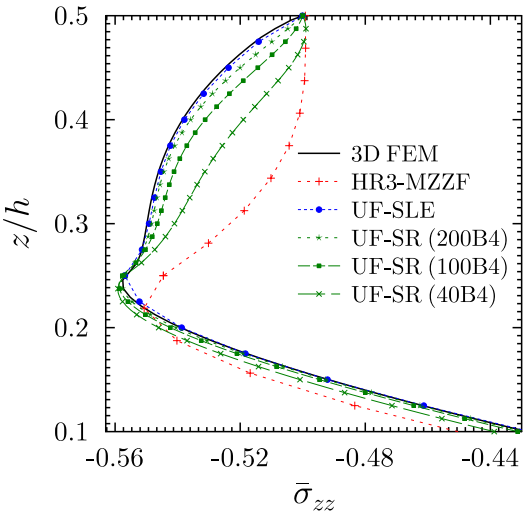

(a) VAT beam F: Transverse normal stress, $\bar{\sigma}_{zz}$

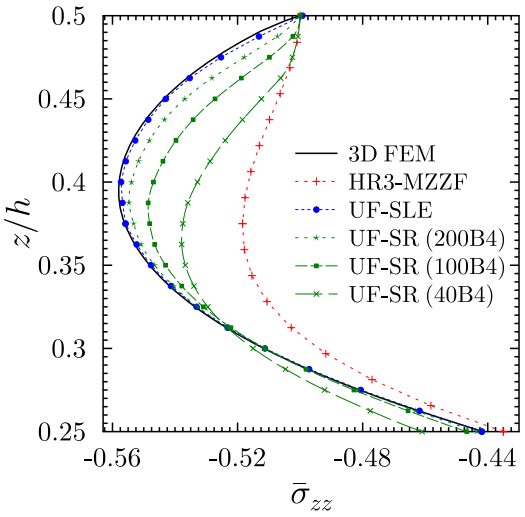

(b) VAT beam G: Transverse normal stress, $\bar{\sigma}_{zz}$

Figure 6.13: A close-up plot focusing on the distribution of the normalized transverse normal stress near the top surface at $y = L/2$, for VAT laminates F and G.

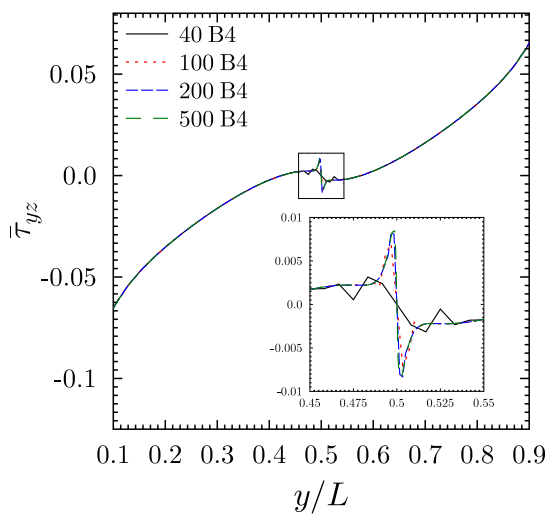

(a) Transverse shear stress, $\bar{\tau}_{yz}$

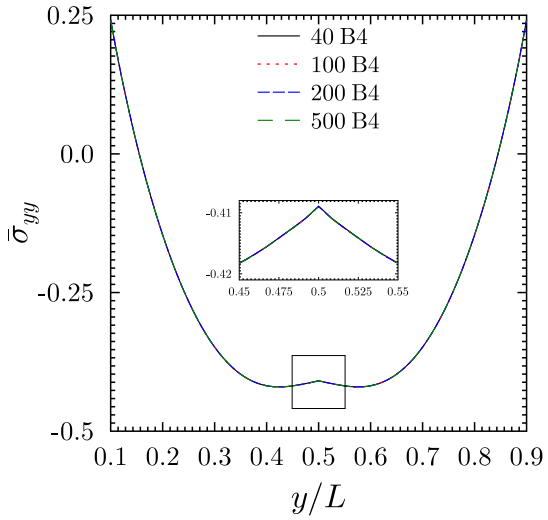

(b) Axial normal stress, $\bar{\sigma}_{yy}$

Figure 6.14: Variation of transverse shear and axial normal stresses along the beam length $y/L \in [0.1, 0.9]$ at $z/h = 0.499$ (just below the top surface) for VAT laminate G as calculated from the UF-SLE model.

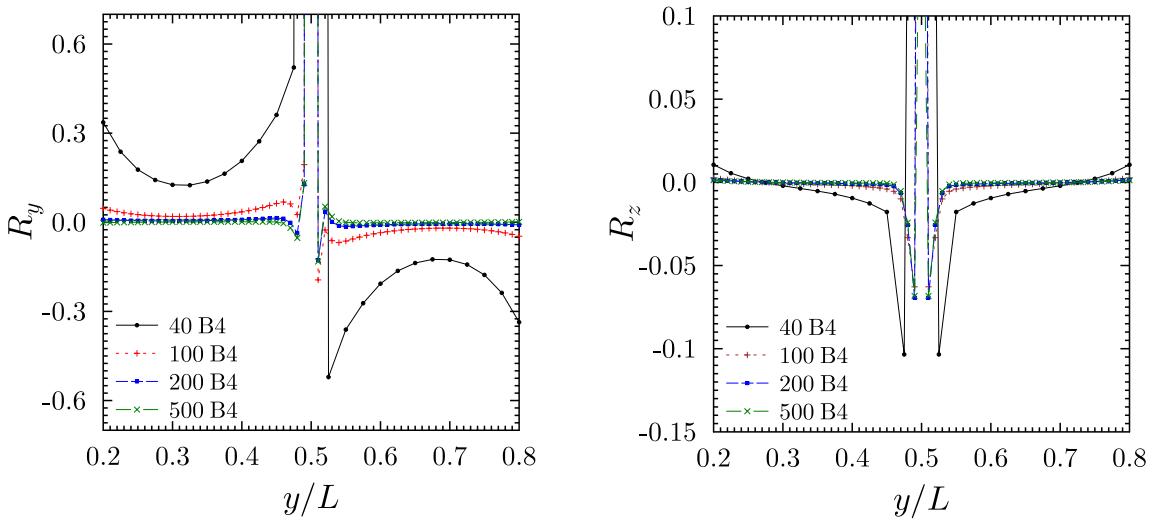

(a) Residual, R_y

(b) Residual, R_z

Figure 6.15: Spanwise distribution of residuals of Cauchy's y- and z-direction equilibrium equations just below the top surface at $z/h = 0.499$ for VAT laminate G as calculated from the UF-SLE model.

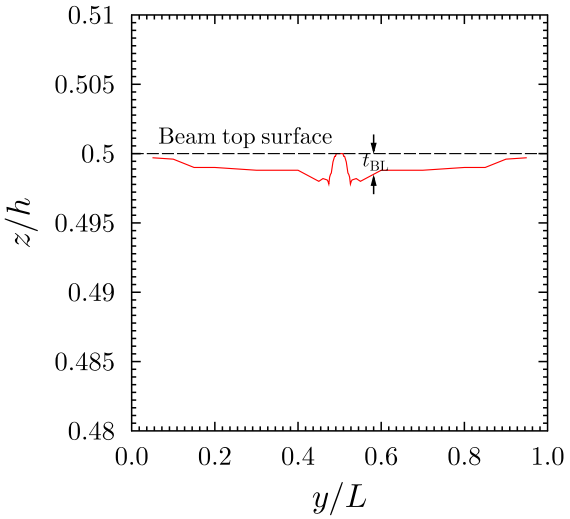

Figure 6.16: The boundary layer below the top surface along the beam length for VAT laminate G as calculated from the UF-SLE model.

observed at the beam's mid-span. Figures 6.18(d) and 6.18(e) show the spanwise variation of the transformed in-plane normal stiffness $\bar{C}_{22}$ and transverse shear stiffness $\bar{C}_{44}$. Mathematically, the transformed elastic coefficients $\bar{C}_{22}$ and $\bar{C}_{44}$ for an orthotropic material, can be obtained from the elastic coefficients in the material coordinates C_{ij} by means of equation (6.6) [194],

$$\begin{aligned} \bar{C}_{22} &= C_{22}\cos^4\theta_y + 2(C_{11}+2C_{66})\cos^2\theta_y \sin^2\theta_y + C_{11}\sin^4\theta_y, \\ \bar{C}_{44} &= C_{44}\cos^2\theta_y + C_{55}\sin^2\theta_y, \end{aligned} \tag{6.6}$$

where $\theta_y = \theta(y)$ is the fibre angle orientation. Substituting the expression of $\bar{C}_{44}$ from equation (6.6) in equation (D.3) of Appendix D, the expression of transverse shear stress and its derivative with respect to the y-coordinate can be written as

$$\begin{aligned} \tau_{yz} &= \bar{C}_{44}\gamma_{yz}, \\ \frac{\partial \tau_{yz}}{\partial y} &= \gamma_{yz}\frac{\partial \bar{C}_{44}}{\partial y} + \bar{C}_{44}\frac{\partial \gamma_{yz}}{\partial y}. \end{aligned} \tag{6.7}$$

In case of straight fibre laminates, $\frac{\partial \bar{C}_{44}}{\partial y} = 0$. But for a VAT laminate $\frac{\partial \bar{C}_{44}}{\partial y}$ is given by

$$\begin{aligned} \frac{\partial \bar{C}_{44}}{\partial y} &= -C_{44}\sin(2\theta_y)\,\frac{\partial \theta_y}{\partial y} + C_{55}\sin(2\theta_y)\,\frac{\partial \theta_y}{\partial y}, \\ &= (C_{55}-C_{44})\sin(2\theta_y)\frac{\partial \theta_y}{\partial y}. \end{aligned} \tag{6.8}$$

Clearly, equation (6.8) and Figure 6.18(a), show that $\frac{\partial \theta_y}{\partial y}$ does not exist at $y = L/2$ because this is the apex of the absolute function that describes θ_y in equation (6.1). Indeed, Figures 6.18(b) and 6.18(c) show the nature of the fibre angle slope and curvature at the midspan as a Heaviside function and Dirac function, respectively. If Cauchy's equilibrium equations are therefore used across this fibre angle singularity at the midspan, then the derivatives are incorrectly computed numerically. Hence, under such circumstances, both, the SR technique and the HR model, lead to incorrect results. In fact, because there is a constitutive singularity at the midspan, the continuity condition of a continuum is broken such that the midspan needs to be treated as a boundary and not as an interior point. This condition is inherently satisfied in 3D FE and UF-SLE models if an elemental boundary node is placed at the midspan and the transverse stress results are computed from the underlying constitutive equations.

This study highlights crucial intricacies in modelling VAT laminates. Even though the structure may seem like a global continuum, singularities in the angle description can break the fundamental assumptions underlying a mechanical continuum, such that internal boundaries need to placed within the structure to correctly model its mechanical behaviour. Such behaviour leads to highly localised raised levels of transverse shear stress (see Figure 6.14) with ensuing implications for failure prediction and design. Indeed, such considerations are necessary whenever a linear variation of fibre orientation is used (equation (6.1)). Appropriate mechanical response is accomplished using a weak-form finite element approach as long as exterior elemental nodes

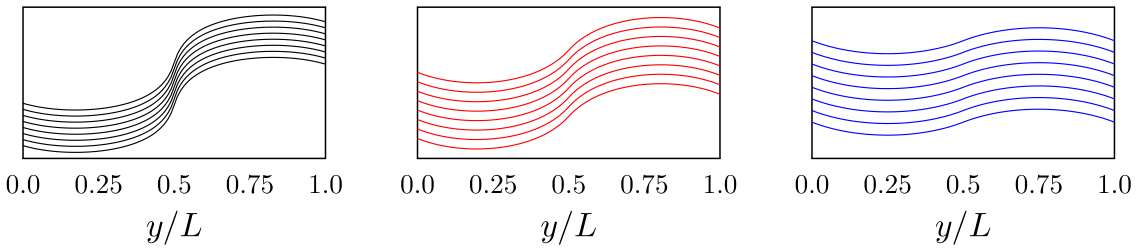

(a) $\langle T_0|T_1\rangle$:⟨90|-45⟩ (b) $\langle T_0|T_1\rangle$:⟨70|-45⟩ (c) $\langle T_0|T_1\rangle$:⟨45|-45⟩

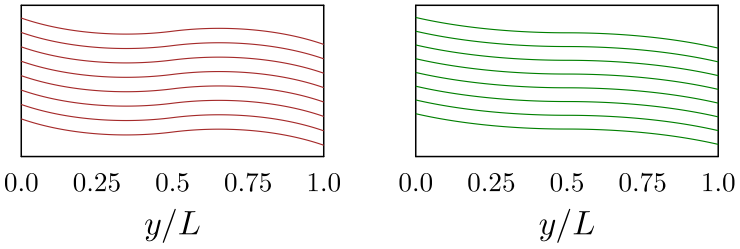

(d) $\langle T_0|T_1\rangle$:⟨20|-45⟩ (e) $\langle T_0|T_1\rangle$:⟨0|-45⟩

Figure 6.17: Representation of spatially steered fibres in the plane of a composite lamina for various combinations of T_0 and T_1.

are placed at singularity locations. Furthermore, this discussion addresses the issues regarding discrepancies between HR3-MZZF and UF-SLE models in computing the transverse normal stress $\bar{\sigma}_{zz}$ for VAT beams A, B, E, F, G, I and J. The discrepancies occur at specific positions through the thickness, where the fibre angle at the mid-span T_0 differs from 0° and 90°, as shown in Figures 6.3(d), 6.4(d), 6.7(d), 6.8(d), 6.9(d), 6.11(d) and 6.12(d). For the VAT beams C, D and H, all layers have T_0 values with either 0° or 90°, so that the transverse normal stress correlates well for all models as shown in Figures 6.5(d), 6.6(d) and 6.10(d).

6.3 Tow-Steered Composite Plate-like Structure

This section aims to assess the capability of the UF-SLE model in computing the 3D stress fields in tow-steered plates and compares these against 3D FE and HR3-MZZF models. Consider a square plate-like 3D structure, as shown in Figure 6.19, with side length-to-thickness ratio $a/t = b/t = 10$. The plate comprises N_l orthotropic, tow-steered laminae of arbitrary thickness t^k with the fibre orientation angle $\theta^k(y)$ varying linearly along the y-direction as given by equation (6.1). The plate is clamped along all four faces and is subjected to a uniformly distributed pressure load, P_0, on the top surface. The laminates investigated here are restricted to symmetric stacking sequences for both composites and sandwich plates, designated as VAT K, L and M. The material properties and stacking sequences are shown in Tables 6.1 and 6.2.

In the UF-SLE model, the plate structure is discretised with 20 B4 elements along the length

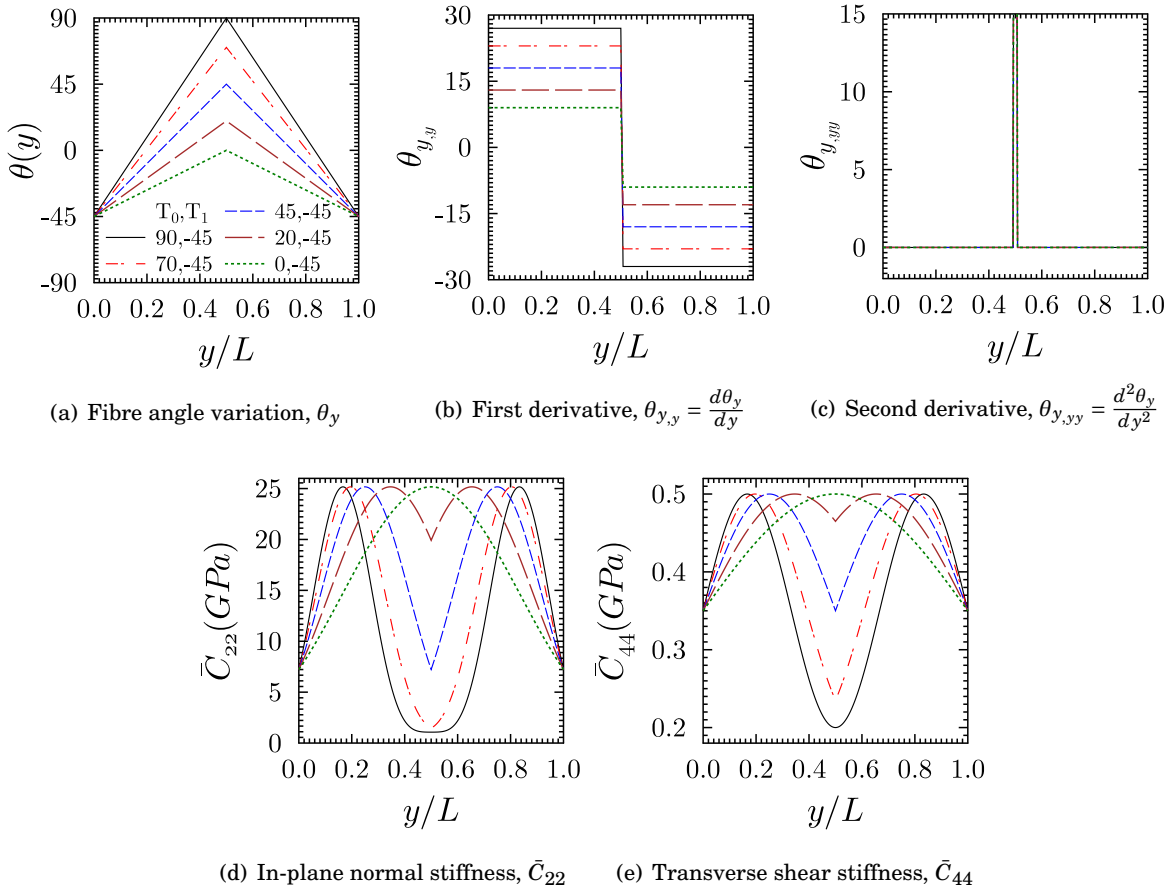

(a) Fibre angle variation, θ_y

(b) First derivative, $\theta_{y,y} = \frac{d\theta_y}{dy}$

(c) Second derivative, $\theta_{y,yy} = \frac{d^2\theta_y}{dy^2}$

(d) In-plane normal stiffness, $\bar{C}_{22}$

(e) Transverse shear stiffness, $\bar{C}_{44}$

Figure 6.18: Spanwise distribution of (a) fibre angle, (b) first derivative of fibre angle, (c) second derivative of fibre angle (d) in-plane normal stiffness term and (e) transverse shear stiffness term for various combinations of T_0 and T_1.

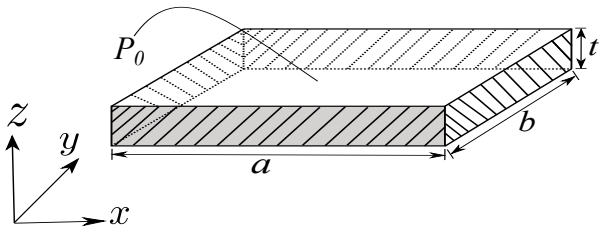

Figure 6.19: Representation of a laminated square plate-like structure ($a/t = b/t = 10$), clamped along all four faces and subjected to a uniformly distributed load at the top surface.

(y-direction), whereas the cross-section is divided into $3\times N_l$ sub-domains (three elements along the x-direction and one element per layer). Within each sub-domain (Serendipity Lagrange element), a seventh-order expansion is employed. The number of elements and the order of expansion are prescribed by performing a convergence analysis. The model is verified against 3D FE analysis performed in ABAQUS [11], where the structure is meshed with 1,776,080 linear C3D8R reduced integration brick elements. All stress results are presented as normalised metrics, which are defined as follows:

$$\begin{aligned} \bar{\sigma}_{xx} &= \frac{t^2}{P_0 a^2}\cdot\sigma_{xx}(x,y,z), \quad \bar{\sigma}_{yy} = \frac{t^2}{P_0 b^2}\cdot\sigma_{yy}(x,y,z), \quad \bar{\tau}_{xy} = \frac{t^2}{P_0 ab}\cdot\tau_{xy}(x,y,z), \\ \bar{\tau}_{xz} &= \frac{1}{P_0}\cdot\tau_{xz}(x,y,z), \quad \bar{\tau}_{yz} = \frac{1}{P_0}\cdot\tau_{yz}(x,y,z), \quad \bar{\sigma}_{zz} = \frac{1}{P_0}\cdot\sigma_{zz}(x,y,z). \end{aligned} \tag{6.9}$$

Through-thickness variations of all six stress fields for VAT plates K, L and M are plotted in Figures 6.20 to 6.22. The planar (x,y) locations of each plot are indicated in the figure captions.

The transverse pressure applied on the top surface locally affects the in-plane stress field due to Poisson's coupling. This local effect is pronounced for VAT K and is clearly shown in the in-plane $\bar{\sigma}_{xx}$ stress plot (Figure 6.20), where the compressive stress on the top surface is greater than the tensile stress on the bottom surface. The UF-SLE model, being hierarchical in nature, allows higher-order terms to be readily added to the displacement field approximation, and is therefore capable of capturing these localised effects more readily compared to the HR3-MZZF model, which is based on a third-order equivalent single-layer theory. Furthermore, for sandwich plate VAT M, the accuracy obtained with the present modelling approach is superior in contrast to the HR3-MZZF model, particularly for in-plane stress fields $\bar{\sigma}_{xx}$, $\bar{\sigma}_{yy}$ and $\bar{\tau}_{xy}$, as shown in Figure 6.22. For all VAT composite and sandwich plates analysed herein, the UF-SLE model results correlate better with the 3D FE solutions than to those obtained by the HR3-MZZF model.

6.4 Computational Efficiency Gain over 3D FE Model

To analyse tow-steered composite structures, a 3D finite element model requires a refined in-plane mesh to guarantee sufficiently smooth fibre variations after discretisation. Additionally, the limitation on the aspect ratio of a 3D brick element further necessitates a refined mesh in the thickness direction, which thereby increases the overall mesh density. In contrast, the UF-SLE model describes the fibre variation smoothly, as the angle is defined at Gauss points and is interpolated using the traditional cubic 1D Lagrange shape functions within the element. Moreover, as discussed in Section 3.2, decoupling the shape functions along the longitudinal axis from the transverse plane removes the limitation of maintaining square element aspect ratios. Hence, the UF-SLE approach has certain advantages in analysing VAT laminated structures in a computationally efficient manner. The previous chapter highlighted the computational efficiency of the UF-SLE model compared to 3D finite elements for laminated composite and sandwich structures. For comparison purposes, computational time and algebraic system complexity were

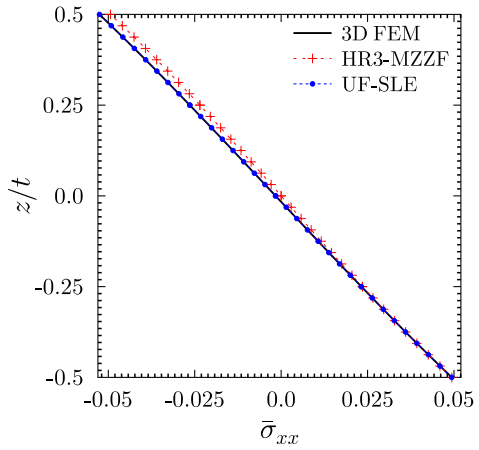

(a) Lateral normal stress, $\bar{\sigma}_{xx}(a/2, b/2, z)$

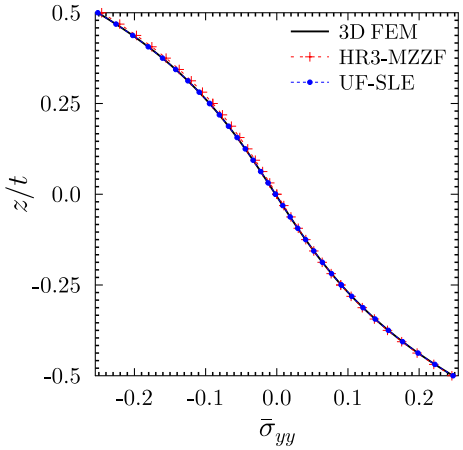

(b) Axial normal stress, $\bar{\sigma}_{yy}(a/2, b/2, z)$

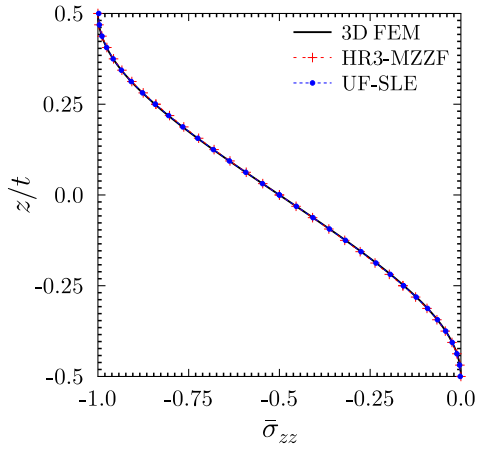

(c) Transverse normal stress, $\bar{\sigma}_{zz}(a/2, b/2, z)$

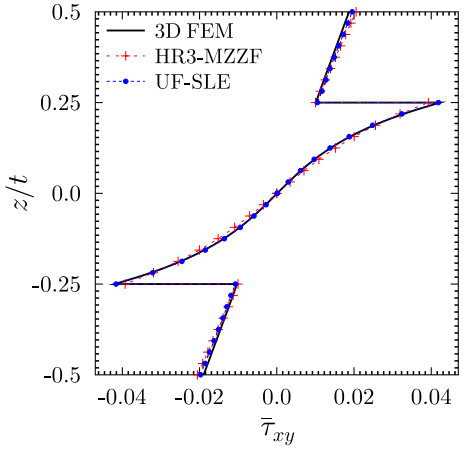

(d) In-plane shear stress, $\bar{\tau}_{xy}(a/4, b/4, z)$

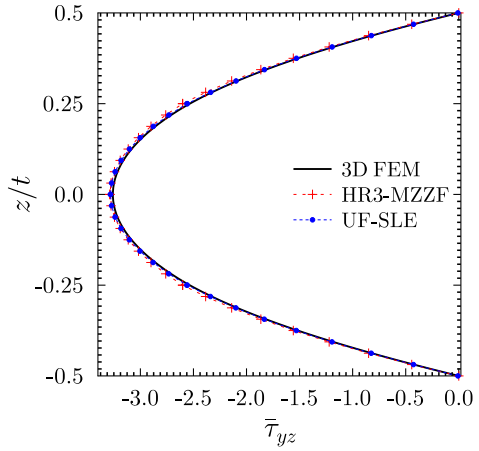

(e) Transverse shear stress, $\bar{\tau}_{yz}(a/2, b/4, z)$

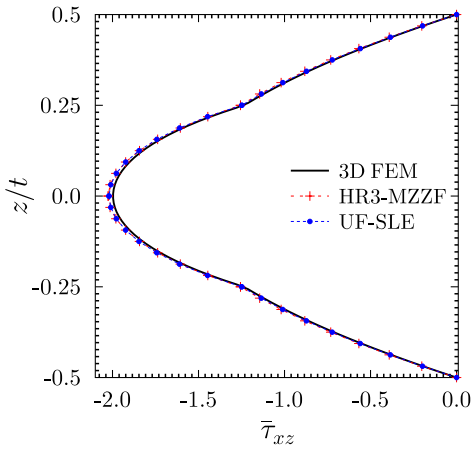

(f) Transverse shear stress, $\bar{\tau}_{xz}(a/4, b/2, z)$

Figure 6.20: Through-thickness distribution of the 3D stress field at different planar locations for VAT plate K.

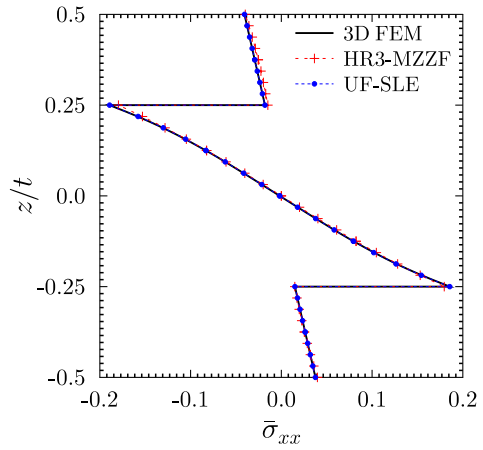

(a) Lateral normal stress, $\bar{\sigma}_{xx}(a/2, b/2, z)$

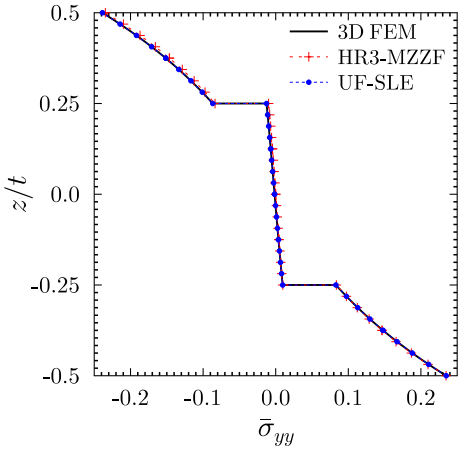

(b) Axial normal stress, $\bar{\sigma}_{yy}(a/2, b/2, z)$

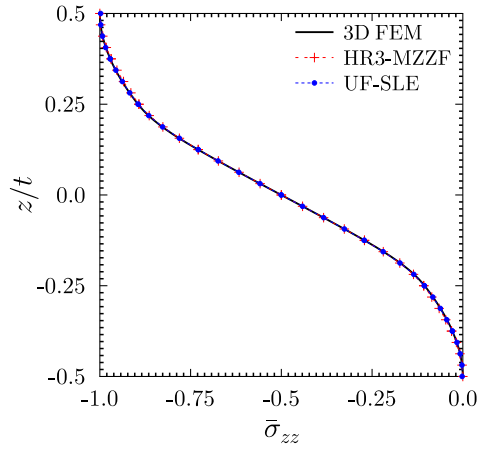

(c) Transverse normal stress, $\bar{\sigma}_{zz}(a/2, b/2, z)$

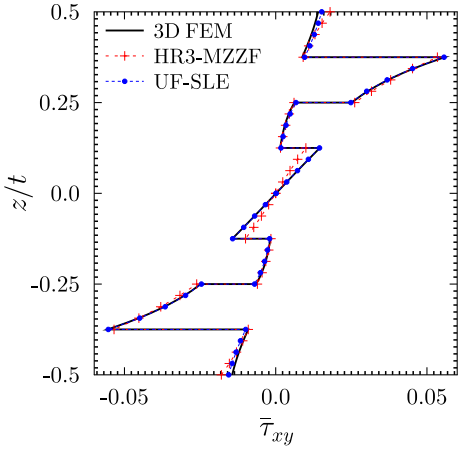

(d) In-plane shear stress, $\bar{\tau}_{xy}(a/4, b/4, z)$

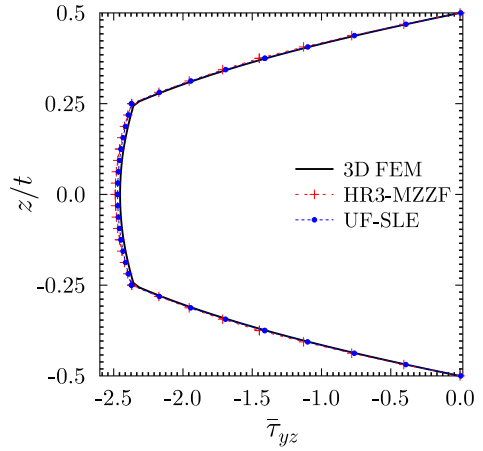

(e) Transverse shear stress, $\bar{\tau}_{yz}(a/2, b/4, z)$

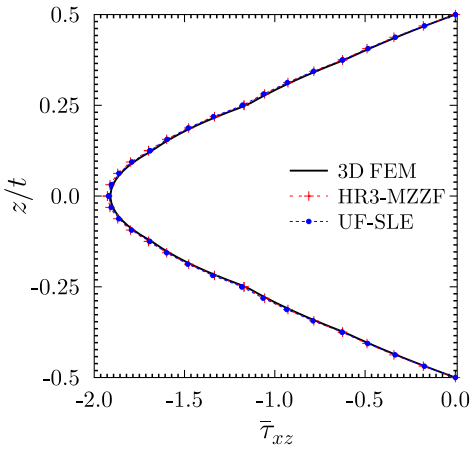

(f) Transverse shear stress, $\bar{\tau}_{xz}(a/4, b/2, z)$

Figure 6.21: Through-thickness distribution of the 3D stress field at different planar locations for VAT plate L.

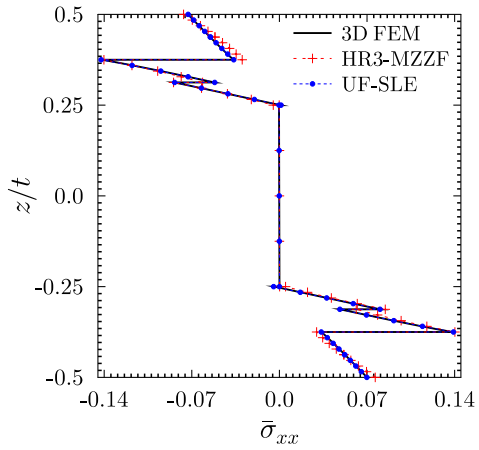

(a) Lateral normal stress, $\bar{\sigma}_{xx}(a/2, b/2, z)$

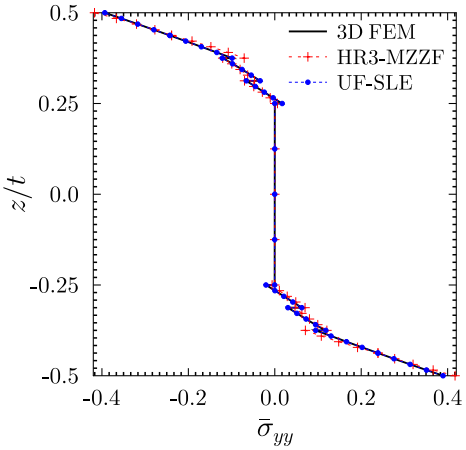

(b) Axial normal stress, $\bar{\sigma}_{yy}(a/2, b/2, z)$

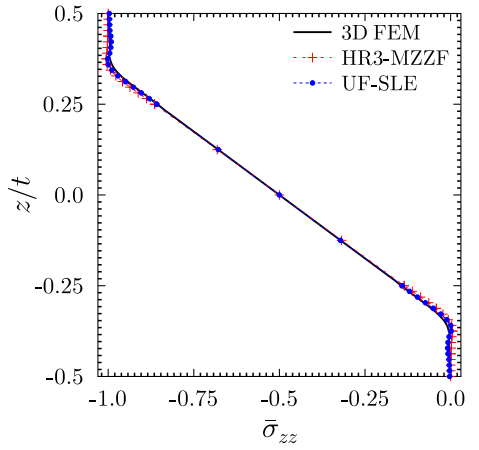

(c) Transverse normal stress, $\bar{\sigma}_{zz}(a/2, b/2, z)$

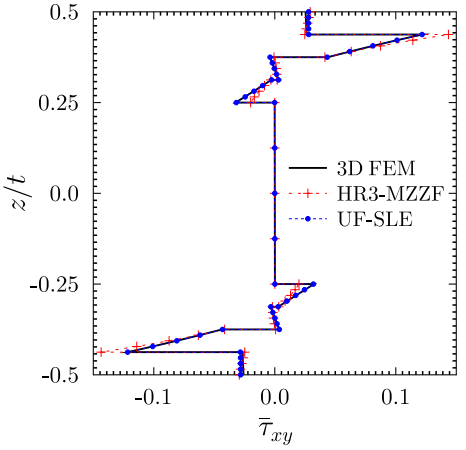

(d) In-plane shear stress, $\bar{\tau}_{xy}(a/4, b/4, z)$

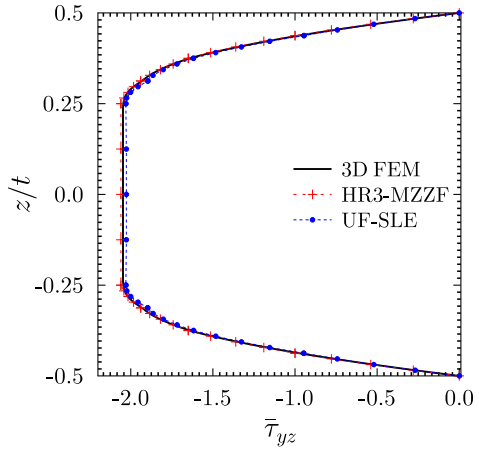

(e) Transverse shear stress, $\bar{\tau}_{yz}(a/2, b/4, z)$

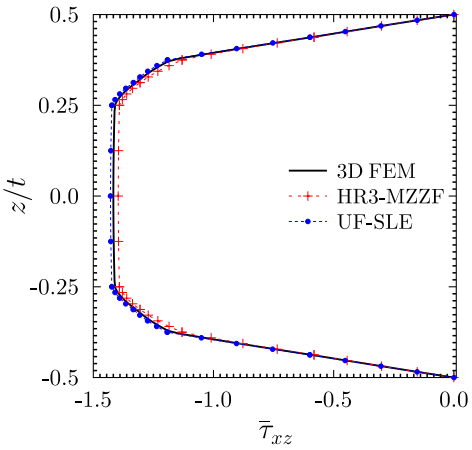

(f) Transverse shear stress, $\bar{\tau}_{xz}(a/4, b/2, z)$

Figure 6.22: Through-thickness distribution of the 3D stress field at different planar locations for VAT plate M.

measured, which quantify the amount of time and storage required by an algorithm. In this chapter, we compare the degrees of freedom (or the number of unknown variables) required to solve the system, which gives an estimate of the relative time and space complexity and thus, predicts overall computational efficiency.

The deflection and stress response obtained for VAT beams A-J, presented in Section 6.2, are computed by discretising the structure with 95,880 linear C3D8R elements in ABAQUS, which results in 580,800 DOFs. On the other hand, a fourth-order SLE model with one cross-section element per layer is used within the Unified Formulation framework with 40 B4 elements along its length to obtain the structural response as shown in Figures 6.3 to 6.12. This setting results in 14,883 DOFs (lowest) and 41,019 DOFs (highest) for VAT D (3 layers) and VAT H, J (9 layers), respectively. Furthermore, accurately computing the localised 3D stress fields in VAT plates K-M demands high-fidelity models. Therefore, in the case of 3D FE analysis, 1,776,080 linear C3D8R elements are used, resulting in 5,467,500 DOFs, and a seventh-order SLE model is employed in the UF framework with 20 B4 elements, leading to 129,198 DOFs for VAT M (9 layers). These numbers clearly demonstrate the computational benefit attained by using the UF-SLE model over the 3D FE model. On the other hand, the HR model is slightly less accurate than the SLE approach but also requires an order of magnitude fewer DOFs.

6.5 Conclusions

Previous chapters highlighted the ability of the Unified Formulation, based on Serendipity Lagrange expansions (UF-SLE), in capturing localised three-dimensional (3D) stress fields accurately in isotropic, laminated composite and sandwich structures. In this chapter, the UF-SLE model is extended for analysing Variable Angle Tow (VAT) structures and is benchmarked against 3D Finite Element (FE) solutions and an equivalent single-layer mixed formulation based on the Hellinger-Reissner principle. The hierarchical nature of the present approach allows the fidelity of the model to be tuned, such that low-fidelity and high-fidelity models can be used concurrently to assess global response and 3D stresses, even when highly localised. Moreover, this feature offers computational benefits over 3D FE models while maintaining a similar level of accuracy.

The present study also highlights the subtle implications of the commonly used linear fibre-orientation expression for VAT laminates, as given by equation (6.1). The presence of an absolute function in the expression introduces a mathematical singularity within the domain of a continuous fibre distribution, which leads to localised stress concentrations in the transverse stresses, and which may have implications for failure prediction and design considerations. This condition is often overlooked by researchers when modelling VAT composites. For instance, in the case of the HR3-MZZF model [11], a Differential Quadrature method (DQM) was employed to model the beam structure using a single continuous domain. This modelling technique yielded

inaccurate transverse shear stress distributions at the beam's mid-span where the singularity, and hence a mathematical boundary, is present. This inaccuracy in the transverse shear stress calculation was further amplified in the computation of the transverse normal stress. In contrast, the present approach uses a finite element discretisation along the beam direction, and therefore, separates the domain at the point of mathematical singularity. Hence, such an approach is also required for the DQM-based HR model and can readily be implemented using an element-based domain decomposition such as the differential quadrature-based FE method [203].

CHAPTER 7

THREE-DIMENSIONAL STRESS CAPTURE OF LAMINATED COMPOSITES VIA EQUIVALENT SINGLE LAYER MODEL

In Chapters 5 and 6, the layer-wise (LW) approach of the UF-SLE is shown to yield accurate localised 3D stress fields in constant- and variable-stiffness laminated composites. Although the model is computationally efficient compared to a 3D FE method, the LW approach is still expensive for preliminary design studies since the computational cost multiplies with the number of layers. In order to provide an efficient framework for modelling constant- and variable-stiffness (straight-fibre and tow-steered) laminates as well as sandwich structures, in this chapter, we propose an Equivalent Single-Layer (ESL) approach implemented within the UF-SLE model. The hierarchical capability of this expansion model provides significant versatility with respect to the structural modelling. To enhance the capability of the ESL model in accounting for the through-thickness transverse anisotropy, two Zig-Zag (ZZ) functions, namely Murakami's ZZ function (MZZF) and the Refined ZZ theory function (RZT), are implemented.

Sections 7.1.1 and 7.1.2 provide the displacement field approximation for LW, ESL-MZZF and ESL-RZT models within the UF framework. Sections 7.1.3 and 7.1.4 provide an overview of the stiffness matrix, strain and stress computations, respectively. Furthermore, as described in Chapters 5 and 6, the present displacement-based formulation does not ensure continuous transverse stresses across layer interfaces. Therefore, in order to capture through-thickness transverse shear and normal stresses reliably, a post-processing step is employed where the transverse stresses are recovered by integrating the in-plane stresses in Cauchy's 3D indefinite equilibrium equations. Finally, in Section 9.2, results obtained using the present modelling approaches, for constant- and variable-stiffness laminates, are discussed and compared with 3D closed-form and 3D FE solutions. For similar levels of accuracy, significant gains in computational efficiency are achieved over 3D FE and LW models by using the ESL approach with RZT ZZ

functions.

7.1 Numerical Formulation

7.1.1 Displacement Field Approximation

Consider a constant- and a variable-stiffness laminated beams of length L, rectangular cross-section of width b and thickness h, composed of N_l layers. The beams are referred to a Cartesian coordinate system (x,y,z), where the y-direction is defined to be along the principle beam axis, while the z-axis is in the transverse stacking direction as shown in Figures 5.1 and 6.1.

The Unified Formulation model relies on a displacement-based version of the finite element method. The three-dimensional displacement field is given as

$$\boldsymbol{u}(x,y,z) = \{u \quad v \quad w\}^{\top}. \tag{7.1}$$

In the current setting, the longitudinal axis of the structure is discretized with four-noded, Lagrange 1D finite elements, so that the displacement field can be approximated element-wise by means of local shape functions $N_i(y)$, and generalized nodal displacements, $\boldsymbol{u}_i(x,z)$, such that

$$\boldsymbol{u}(x,y,z) = \sum_{i=1}^{4} N_i(y)\boldsymbol{u}_i(x,z). \tag{7.2}$$

The transverse, or cross-sectional, deformations are approximated using hierarchical Serendipity Lagrange Expansion (SLE) functions $F_\tau(x,z)$, as described in Chapter 3. Adopting this expansion model, cross-sections are discretized using four-noded Lagrange sub-domains and the displacement field within each sub-domain can be enriched by increasing the order of the local Serendipity Lagrange expansion. The cross-sectional displacement field at the i^{th} beam node is expressed as

$$\boldsymbol{u}_i(x,z) = \sum_{\tau=1}^{m} F_\tau(x,z)\boldsymbol{u}_{i\tau}, \tag{7.3}$$

where m is the number of terms depending on the order of expansion and $\boldsymbol{u}_{i\tau}$ are generalized displacement vectors. By introducing the cross-sectional approximation of equation (7.3) into the FE discretization along the beam axis of equation (7.2), the displacement field reads

$$\boldsymbol{u}(x,y,z) = \sum_{i=1}^{4}\sum_{\tau=1}^{m} N_i(y)F_\tau(x,z)\boldsymbol{u}_{i\tau}. \tag{7.4}$$

The UF-SLE model allows a LW approach to be implemented directly with each layer modelled as one sub-domain and the kinematics within each layer (or sub-domain) varied hierarchically. This representation allows for an accurate strain field by satisfying the ZZ requirement and an accurate determination of 3D stresses at layer level. However, the number of variables in the model scales with the number of layers in the laminate and thus, the added accuracy comes at greater computational cost. To overcome this issue, an ESL approach is implemented within the

UF-SLE framework, *i.e.* a single 4−noded Serendipity Lagrange element is used to model the beam's cross-section. Thus, the number of unknowns in the model becomes independent of the number of layers. Furthermore, the hierarchical nature of the SLE function allows higher-order terms to be added in the displacement field to account for severe transverse shear and normal deformations. While the higher-order terms in the displacement field provide accurate modelling of global structural effects, they are not capable of explicitly capturing ZZ effects. Therefore, there is a need to incorporate ZZ kinematics within the ESL approach in order to present it as a good compromise between local, layer-wise accuracy and computational cost, as discussed in the following section.

7.1.2 Zig-Zag Kinematics

The most commonly used ZZ function is Murakami's ZZ function (MZZF) [201], which is given by

$$\phi^{M^k}(z) = (-1)^k \frac{2}{h^k}(z - z_m^k), \tag{7.5}$$

where z_m^k is the mid-plane coordinate and h^k is the thickness of layer k. MZZF assumes alternating values of $+1$ and -1 at the top and bottom interfaces regardless of the planar location. Also, it does not depend on the mechanical properties of layers and is often presented as an effective enrichment of the displacement field, regardless of the type of stacking sequence. Numerous studies in literature [83, 204] show that superior representation of displacements and stresses, combined with less computational cost, can be achieved by including MZZF for constant- and variable-stiffness laminates and sandwich structures. However, for symmetric (with more than three layers) and unsymmetric sandwich lay-ups, or for laminates with externally weak layers, MZZF fails to predict the stress response accurately [86]. Therefore, another class of zig-zag function, introduced by Tessler *et al.* [87], termed Refined Zig-Zag Theory (RZT), is incorporated within the UF-SLE ESL model. In RZT, the zig-zag slopes m_i^k are defined by the difference between the transverse shear rigidities G_{iz}^k of layer k, and effective transverse shear rigidity G_i of the entire layup [90]

$$m_i^k = \frac{G_i}{G_{iz}^k} - 1, \qquad \text{with} \quad G_i = \left[\frac{1}{h}\sum_{k=1}^{N_l}\frac{h^k}{G_{iz}^k}\right]^{-1}, \quad i = x, y, \tag{7.6}$$

where N_l is the total number of layers, and h_k and h are the thickness of layer k and total laminate thickness, respectively. The ZZ function is defined by

$$\phi_i^{R^k}(z) = z m_i^k + c_i^k, \quad i = x, y \tag{7.7}$$

where c_i^k enforces interlaminar continuity and is given as

$$c_i^k = m_i^k \frac{h}{2} + \sum_{j=2}^{k} h^{j-1}\Big(\frac{G_i}{G_{iz}^{j-1}} - \frac{G_i}{G_{iz}^k}\Big). \tag{7.8}$$

It is to be noted that the RZT ZZ function $\phi_i^{R^k}(z)$ is derived from transverse material properties, therefore in case of variable-stiffness laminates, the function varies with the in-plane location, *i.e.* $\phi_i^{R^k}(x,y,z)$.

Following the standard definition of the MZZF and RZT ZZ functions, and incorporating these within the UF-SLE framework, the assumed displacement field, as given by equation (7.4), can now be written:

$$\begin{aligned} u(x,y,z) &= \sum_{i=1}^{4} N_i(y)\left(\sum_{\tau=1}^{m} F_\tau(x,z)u_{i\tau} + \phi^M(z)\psi_{x_i}\right) \\ v(x,y,z) &= \sum_{i=1}^{4} N_i(y)\left(\sum_{\tau=1}^{m} F_\tau(x,z)v_{i\tau} + \phi^M(z)\psi_{y_i}\right) \\ w(x,y,z) &= \sum_{i=1}^{4} N_i(y)\left(\sum_{\tau=1}^{m} F_\tau(x,z)w_{i\tau}\right), \end{aligned} \tag{7.9}$$

and

$$\begin{aligned} u(x,y,z) &= \sum_{i=1}^{4} N_i(y)\left(\sum_{\tau=1}^{m} F_\tau(x,z)u_{i\tau} + \phi_x^R(x,y,z)\psi_{x_i}\right) \\ v(x,y,z) &= \sum_{i=1}^{4} N_i(y)\left(\sum_{\tau=1}^{m} F_\tau(x,z)v_{i\tau} + \phi_y^R(x,y,z)\psi_{y_i}\right) \\ w(x,y,z) &= \sum_{i=1}^{4} N_i(y)\left(\sum_{\tau=1}^{m} F_\tau(x,z)w_{i\tau}\right), \end{aligned} \tag{7.10}$$

where ψ_{x_i} and ψ_{y_i} are ZZ rotations at the i^{th} beam node. Finally, we now have three displacement field approximations in the UF-SLE model as given by equations (7.4), (7.9) and (7.10) which correspond to the LW, the ESL-MZZF and the ESL-RZT theories, respectively. In the remainder of this paper, these models are referred as UF-LW, UF-MZZF and UF-RZT.

7.1.3 Fundamental Nucleus of the Stiffness Matrix

Elastic equilibrium is enforced via the Principle of Virtual Displacements, which, in a quasi-static setting, states that

$$\delta W_{\text{int}} = \delta W_{\text{ext}}, \tag{7.11}$$

where δ denotes the first variation with respect to displacements, and W_{int} and W_{ext} denote the internal and external work, respectively.

By definition, the internal work is the work done by the internal stresses over the corresponding internal strains and is equivalent to the elastic strain energy. Noting that $W_{\text{int}} = \sum_{\text{e}} W_{\text{int}}^{\text{e}}$ and letting l_{e} be the length of the generic beam element and A be the cross-sectional area,

$$\delta W_{\text{int}}^{\text{e}} = \int_{l_{\text{e}}} \int_A \delta \boldsymbol{\varepsilon}^\top \boldsymbol{\sigma}\, dA\, dl. \tag{7.12}$$

In the Unified Formulation notation, the internal work can be re-written as

$$\delta W_{\text{int}}^{\text{e}} = \delta \boldsymbol{u}_{js\varphi}^\top \boldsymbol{K}_{\text{e}}^{\tau s \phi \varphi i j} \boldsymbol{u}_{i\tau\phi}, \tag{7.13}$$

where

$$\boldsymbol{u}_{js\varphi} = \left\{ \begin{array}{ccccc} u_{js} & v_{js} & w_{js} & \psi_{x_j} & \psi_{y_j} \end{array} \right\}^\top, \qquad \boldsymbol{u}_{i\tau\phi} = \left\{ \begin{array}{ccccc} u_{i\tau} & v_{i\tau} & w_{i\tau} & \psi_{x_i} & \psi_{y_i} \end{array} \right\}^\top,$$

and

$$\boldsymbol{K}_{\mathrm{e}}^{\tau s\phi\varphi ij} = \left[\begin{array}{cc} \boldsymbol{K}^{\tau sij} & \boldsymbol{K}^{\tau\varphi ij} \\ \boldsymbol{K}^{\phi sij} & \boldsymbol{K}^{\phi\varphi ij} \end{array} \right].$$

Matrices $\boldsymbol{K}^{\tau sij}$, $\boldsymbol{K}^{\tau\varphi ij}$, $\boldsymbol{K}^{\phi sij}$ and $\boldsymbol{K}^{\phi\varphi ij}$ are referred to as the *Fundamental Nuclei* of the stiffness matrix. For a given τ, s, i, j and ϕ, φ these matrices are of size 3×3, 3×2, 2×3 and 2×2, respectively. These *fundamental nuclei* are expanded by using the indices $\tau, s = 1, \ldots, m$; $\phi, \varphi = m+1$ and $i, j = 1, \ldots, 4$; in order to obtain the elemental stiffness matrix, $\boldsymbol{K}_{\mathrm{e}}^{\tau s\phi\varphi ij}$. The layer-wise model is obtained by removing stiffness terms, $\boldsymbol{K}^{\tau\varphi ij}$, $\boldsymbol{K}^{\phi sij}$ and $\boldsymbol{K}^{\phi\varphi ij}$, that account for the zig-zag kinematics. The explicit form for matrices, $\boldsymbol{K}^{\tau sij}$, $\boldsymbol{K}^{\tau\varphi ij}$, $\boldsymbol{K}^{\phi sij}$ and $\boldsymbol{K}^{\phi\varphi ij}$, can be found in Appendix B. The elemental stiffness matrix, so-obtained, is assembled in a global stiffness matrix following the standard finite element procedure.

7.1.4 Strain and Stress Components

From basic elasticity, the generalized strain component vector can be written as

$$\boldsymbol{\varepsilon} = \mathscr{D}\boldsymbol{u}, \tag{7.14}$$

where $\boldsymbol{\varepsilon}^\top = \{\varepsilon_{xx}, \varepsilon_{yy}, \varepsilon_{zz}, \gamma_{yz}, \gamma_{zx}, \gamma_{xy}\}$ and $\mathscr{D}$ is the kinematic partial differential operator

$$\mathscr{D} = \left[\begin{array}{cccccc} \frac{\partial}{\partial x} & 0 & 0 & 0 & \frac{\partial}{\partial z} & \frac{\partial}{\partial y} \\ 0 & \frac{\partial}{\partial y} & 0 & \frac{\partial}{\partial z} & 0 & \frac{\partial}{\partial x} \\ 0 & 0 & \frac{\partial}{\partial z} & \frac{\partial}{\partial y} & \frac{\partial}{\partial x} & 0 \end{array} \right]^\top. \tag{7.15}$$

By substituting equations (7.4), (7.9) and (7.10), in equation (7.14), the elemental strain component vector for UF-LW, UF-MZZF and UF-RZT models is given by

$$\boldsymbol{\varepsilon} = \boldsymbol{G}_{i\tau}\boldsymbol{u}_{i\tau}, \quad \boldsymbol{\varepsilon} = \boldsymbol{G}_{i\tau}\boldsymbol{u}_{i\tau} + \boldsymbol{G}_i^M\boldsymbol{\psi}_i, \quad \text{and } \boldsymbol{\varepsilon} = \boldsymbol{G}_{i\tau}\boldsymbol{u}_{i\tau} + \boldsymbol{G}_i^R\boldsymbol{\psi}_i, \tag{7.16}$$

respectively, where

$$\boldsymbol{G}_{i\tau} = \left[\begin{array}{ccc} N_i F_{\tau,x} & 0 & 0 \\ 0 & N_{i,y} F_\tau & 0 \\ 0 & 0 & N_i F_{\tau,z} \\ 0 & N_i F_{\tau,z} & N_{i,y} F_\tau \\ N_i F_{\tau,z} & 0 & N_i F_{\tau,x} \\ N_{i,y} F_\tau & N_i F_{\tau,x} & 0 \end{array} \right], \quad \boldsymbol{u}_{i\tau} = \left\{ \begin{array}{c} u_{i\tau} \\ v_{i\tau} \\ w_{i\tau} \end{array} \right\},$$

$$\boldsymbol{G}_i^M = \begin{bmatrix} 0 & 0 & 0 \\ 0 & 0 & 0 \\ 0 & 0 & 0 \\ 0 & N_i\phi_{,z}^M & 0 \\ N_i\phi_{,z}^M & 0 & 0 \\ 0 & 0 & 0 \end{bmatrix}, \quad \boldsymbol{G}_i^R = \begin{bmatrix} N_i\phi_{x,x}^R & 0 & 0 \\ 0 & N_i\phi_{y,y}^R + N_{i,y}\phi_y^R & 0 \\ 0 & 0 & 0 \\ 0 & N_i\phi_{y,z}^R & 0 \\ N_i\phi_{x,z}^R & 0 & 0 \\ N_i\phi_{x,y}^R + N_{i,y}\phi_x^R & N_i\phi_{y,x}^R & 0 \end{bmatrix}, \quad \boldsymbol{\psi}_i = \begin{Bmatrix} \psi_{x_i} \\ \psi_{y_i} \\ 0 \end{Bmatrix}.$$

Equation (7.16) use Einstein's summation notation over repeated indices and a subscript preceded by a comma denotes differentiation with respect to the corresponding spatial coordinate. It is noted that in case of constant-stiffness (straight fibre) laminate, the RZT ZZ functions depend only on the thickness coordinate, and therefore, derivatives of ϕ_x^R and ϕ_y^R with respect to x and y are zero. Furthermore, in the present study, we have considered variable-stiffness laminates with fibre-angle variation only along the spanwise direction y, and thus, $\phi_{x,x}^R$ and $\phi_{y,x}^R$ are zero.

For a linear elastic material undergoing infinitesimal strains and small displacements, the stresses are derived from the constitutive relation as given below,

$$\boldsymbol{\sigma} = \bar{\boldsymbol{C}}\boldsymbol{\varepsilon}, \tag{7.17}$$

or

$$\begin{Bmatrix} \sigma_{xx} \\ \sigma_{yy} \\ \sigma_{zz} \\ \tau_{yz} \\ \tau_{xz} \\ \tau_{xy} \end{Bmatrix} = \begin{bmatrix} \bar{C}_{11} & \bar{C}_{12} & \bar{C}_{13} & \bar{C}_{14} & \bar{C}_{15} & \bar{C}_{16} \\ & \bar{C}_{22} & \bar{C}_{23} & \bar{C}_{24} & \bar{C}_{25} & \bar{C}_{26} \\ & & \bar{C}_{33} & \bar{C}_{34} & \bar{C}_{35} & \bar{C}_{36} \\ & & & \bar{C}_{44} & \bar{C}_{45} & \bar{C}_{46} \\ & Symmetric & & & \bar{C}_{55} & \bar{C}_{56} \\ & & & & & \bar{C}_{66} \end{bmatrix} \begin{Bmatrix} \varepsilon_{xx} \\ \varepsilon_{yy} \\ \varepsilon_{zz} \\ \gamma_{yz} \\ \gamma_{xz} \\ \gamma_{xy} \end{Bmatrix}, \tag{7.18}$$

where coefficients $\bar{C}_{ij}$ are the transformed elastic coefficients referred to the global (x,y,z) coordinate system that depends on the mechanical properties of the laminate material and fibre orientation angle. The explicit expression for coefficients C_{ij}^k can be found in Appendix A.

Furthermore, as described previously, computing stresses using the constitutive relation may lead to discontinuities in the transverse stresses at the interface between two adjacent layers. Therefore, transverse stresses are recovered by employing the indefinite equilibrium equations of 3D elasticity and integrating in-plane stresses in the thickness direction. The 3D stress equilibrium equations for the static case, and in the absence of body forces, are

$$\sigma_{ij_{,j}} = 0, \quad i,j = x,y,z, \tag{7.19}$$

where a comma denotes differentiation and Einstein's summation notation has been used. In summary, the in-plane stresses, σ_{xx}, σ_{yy} and τ_{xy}, are computed conventionally using the constitutive relations. Transverse shear and normal stresses, τ_{xz}, τ_{yz}, and σ_{zz} are calculated as

$$\sigma_{iz}^k(z) = \sigma_{iz_b}^k - \int_{z_b^k}^{z} \left(\sigma_{ix,x} + \sigma_{iy,y}\right) dz, \tag{7.20}$$

where $\sigma^k_{iz}(z)$ is the stress in the k^{th}-layer and $\sigma^k_{iz_b}$ is the stress at the bottom of the k^{th}-layer.

Adopting this methodology requires the derivatives of in-plane stresses to be verified while modelling variable-stiffness composite structures. Because the material properties vary spatially in VS laminates, implying the variability of Hooke's coefficients at element level, the derivatives of material stiffness coefficients must be taken into account. For instance, to recover transverse shear stress τ_{yz} using equation (7.20), derivatives of in-plane stresses are calculated as

$$\begin{aligned}\frac{\partial \tau_{xy}}{\partial x} =& \left(\bar{C}_{61}\frac{\partial \varepsilon_{xx}}{\partial x} + \bar{C}_{62}\frac{\partial \varepsilon_{yy}}{\partial x} + \bar{C}_{63}\frac{\partial \varepsilon_{zz}}{\partial x} + \bar{C}_{66}\frac{\partial \gamma_{xy}}{\partial x}\right) \\ &+ \left(\varepsilon_{xx}\frac{\partial \bar{C}_{61}}{\partial x} + \varepsilon_{yy}\frac{\partial \bar{C}_{62}}{\partial x} + \varepsilon_{zz}\frac{\partial \bar{C}_{63}}{\partial x} + \gamma_{xy}\frac{\partial \bar{C}_{66}}{\partial x}\right),\end{aligned} \tag{7.21}$$

$$\begin{aligned}\frac{\partial \sigma_{yy}}{\partial y} =& \left(\bar{C}_{21}\frac{\partial \varepsilon_{xx}}{\partial y} + \bar{C}_{22}\frac{\partial \varepsilon_{yy}}{\partial y} + \bar{C}_{23}\frac{\partial \varepsilon_{zz}}{\partial y} + \bar{C}_{26}\frac{\partial \gamma_{xy}}{\partial y}\right) \\ &+ \left(\varepsilon_{xx}\frac{\partial \bar{C}_{21}}{\partial y} + \varepsilon_{yy}\frac{\partial \bar{C}_{22}}{\partial y} + \varepsilon_{zz}\frac{\partial \bar{C}_{23}}{\partial y} + \gamma_{xy}\frac{\partial \bar{C}_{26}}{\partial y}\right).\end{aligned} \tag{7.22}$$

The derivatives of material stiffness coefficients can be computed exactly as given in [204] or by employing finite differences. In the present work, finite differences are used for evaluating these derivatives.

7.2 Modelling Straight-Fibre and Tow-Steered Laminated Composites

The two equivalent single layer models introduced in this chapter, namely UF-MZZF and UF-RZT, are employed for analyzing constant- and variable-stiffness composite laminates. In order to verify the applicability of these models, constant-stiffness (CS) laminates, CS A and CS B, from Chapter 5 and variable-stiffness (VS) laminates, VS C, VS D, VS E and VS F, from Chapter 6 are considered. The geometry, material properties, loads and boundary conditions for respective laminates are defined in Sections 5.2 and 6.2. For the sake of convenience, the stacking sequence of the laminates considered are shown in Table 7.1.

Layer-wise stresses are usually computed using the constitutive relation as given by Eq. (7.17). However, if the modelling fidelity is not sufficient most displacement-based approaches produce discontinuous transverse stresses at the layer interfaces, which violates the traction equilibrium condition between layers. The accuracy of the transverse stresses evaluated via Hooke's law is not acceptable when ESL models are employed. Moreover, transverse stresses calculated by integration of the equilibrium equations were shown to provide, in general, the best overall results, as also confirmed in [204]. For this reason, the in-plane stresses are herein calculated by using Hooke's law, whereas the transverse stresses are obtained via integration of the equilibrium equations.

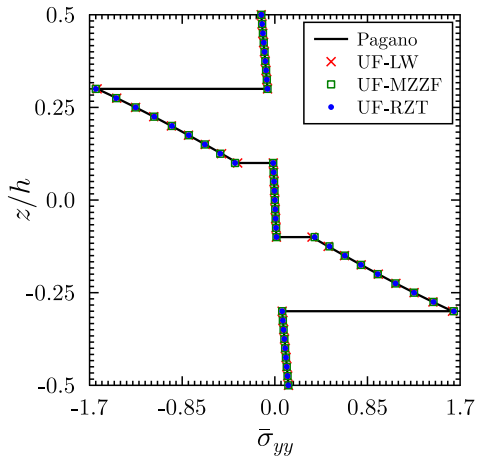

(a) Lam A: $\bar{\sigma}_{yy}$ at $y = L/2$

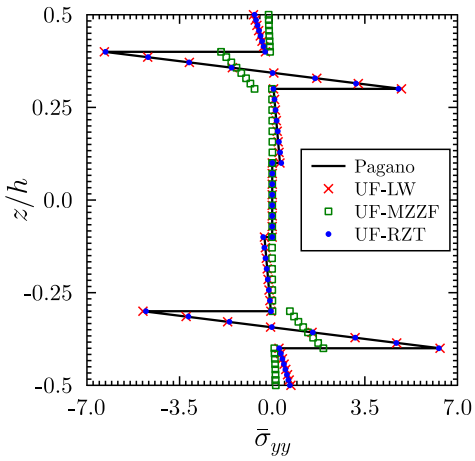

(b) Lam B: $\bar{\sigma}_{yy}$ at $y = L/2$

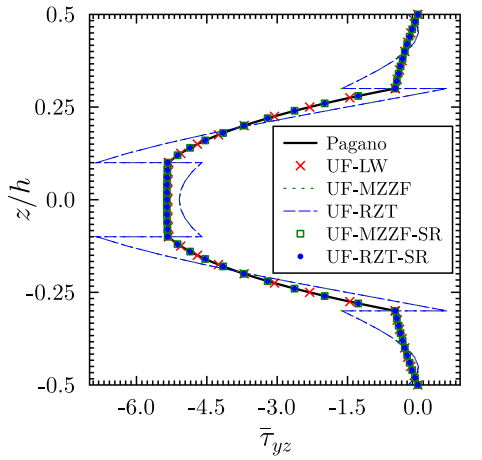

(c) Lam A: $\bar{\tau}_{yz}$ at $y = 0$

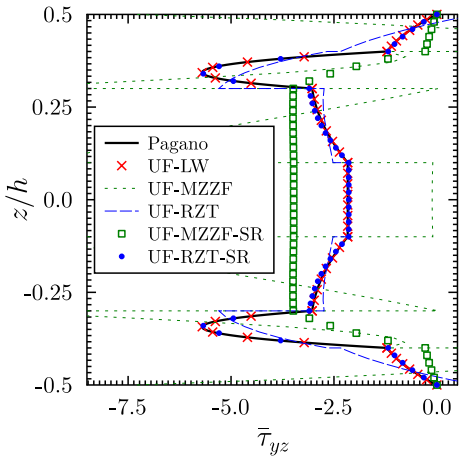

(d) Lam B: $\bar{\tau}_{yz}$ at $y = 0$

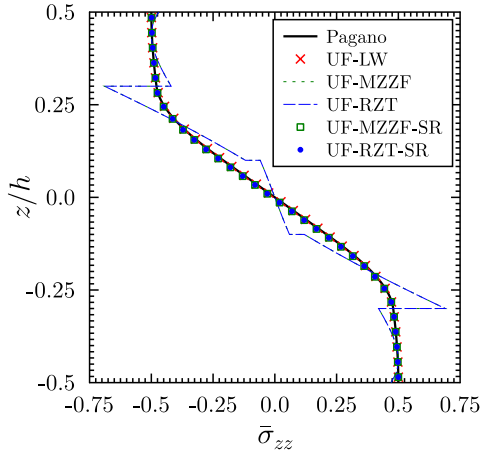

(e) Lam A: $\bar{\sigma}_{zz}$ at $y = L/2$

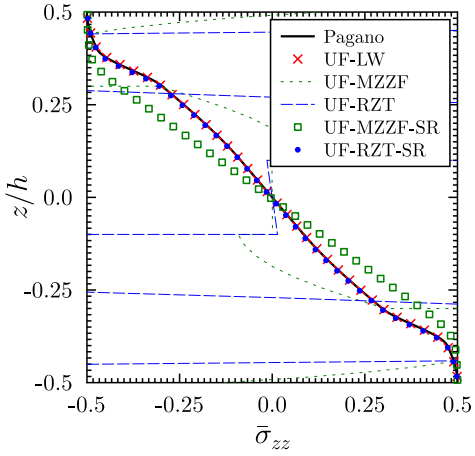

(f) Lam B: $\bar{\sigma}_{zz}$ at $y = L/2$

Figure 7.1: Through-thickness distribution of the normalized axial, transverse shear and transverse normal stresses for constant-stiffness laminates A and B.

Table 7.1: Stacking sequence for constant- and variable-stiffness laminates considered in the present study. Subscripts indicate the repetition of a property over the corresponding number of layers.

Laminate	**Layer thickness ratio**	**Material**	**Stacking sequence**
CS A	$[0.2_5]$	$[p_5]$	[90/0/90/0/90]
CS B	$[0.1_2/0.2_3/0.1_2]$	$[p_2/pvc/h/pvc/p_2]$	$[90/0_5/90]$
VS C	$[(1/8)_8]$	$[IM7_8]$	$[\langle 90\vert 0\rangle/\langle -90\vert 0\rangle/\langle 45\vert$-$45\rangle/\langle -45\vert 45\rangle]_s$
VS D	$[(1/12)_4/(1/3)/(1/12)_4]$	$[p_4/pvc/p_4]$	$[\langle 0\vert 90\rangle/\langle 90\vert 0\rangle/\langle 0\vert -90\rangle/\langle -90\vert 0\rangle/\ldots$ $0/\langle -90\vert 0\rangle/\langle 0\vert -90\rangle/\langle 90\vert 0\rangle/\langle 0\vert 90\rangle]$
VS E	$[(1/8)_2/0.5/(1/8)_2]$	$[p_2/pvc/p_2]$	$[\langle 45\vert -45\rangle/\langle -45\vert 45\rangle/0/\langle -45\vert 45\rangle/\langle 45\vert -45\rangle]$
VS F	$[(1/12)_4/(1/3)/(1/12)_4]$	$[p_4/pvc/p_4]$	$[\langle 20\vert -60\rangle/\langle -20\vert 60\rangle/\langle 45\vert -45\rangle/\langle -45\vert 45\rangle/\ldots$ $0/0/90/\langle 35\vert -35\rangle/\langle -35\vert 35\rangle]$

All results for axial normal, σ_{yy}, transverse shear, τ_{yz}, and transverse normal, σ_{zz}, stress presented in this chapter are normalized as follows

$$\bar{\sigma}_{yy} = \frac{h^2}{q_0 L^2} \cdot \sigma_{yy}(x,y,z), \quad \bar{\tau}_{yz} = \frac{1}{q_0} \cdot \tau_{yz}(x,y,z), \quad \bar{\sigma}_{zz} = \frac{1}{q_0} \cdot \sigma_{zz}(x,y,z), \tag{7.23}$$

where h is the total laminate thickness, L is the beam length and q_0 is the applied loading magnitude.

The stress response obtained from the UF-SLE ESL models (UF-MZZF and UF-RZT) are compared with those obtained by employing the Layer-Wise approach (UF-LW). Furthermore, the results for constant- and variable-stiffness beams are verified against Pagano's 3D elasticity and 3D FE solutions, respectively. The beam and cross-section discretisation employed for each case are shown in Table 7.2. Moreover, from the table, the computational expense incurred by each model, for all the cases analysed herein, are compared by means of DOFs, time and space complexities.

Through-thickness distribution of normalized axial stress $\bar{\sigma}_{yy}$ (at $y = L/2$), transverse shear stress $\bar{\tau}_{yz}$ (at $y = 0$) and transverse normal stress $\bar{\sigma}_{zz}$ (at $y = L/2$) for constant-stiffness laminates A and B are plotted in Figure 7.1. From the plots, it can be clearly seen that the LW approach of the UF-SLE model (UF-LW) shows excellent correlation with Pagano's 3D elasticity solution, as given in [89]. Moreover, the current fidelity of the model (with 30 B4 beam elements and fifth-order expansion) is sufficient to capture the transverse shear and normal stress profile accurately without any *posteriori* stress recovery step. For the ESL models with MZZF and RZT ZZ function, on the other hand, there is a need to recover the transverse stresses from the 3D stress equilibrium equations. However, a much greater gain in computational efficiency is obtained with the UF-MZZF and UF-RZT compared to the UF-LW model, as shown in Table 7.2, where the number of beam and cross-section elements, order of expansion, degrees of freedom

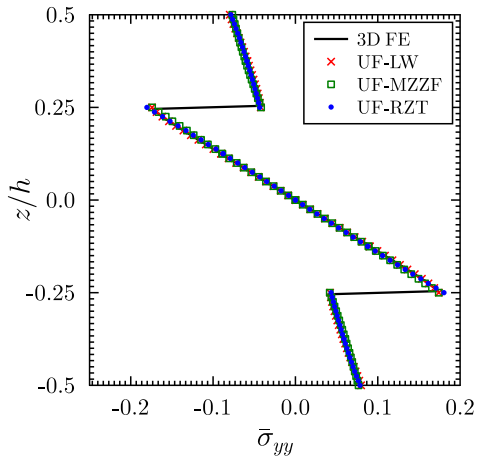

(a) VS Lam C: $\bar{\sigma}_{yy}$ at $y = L/2$

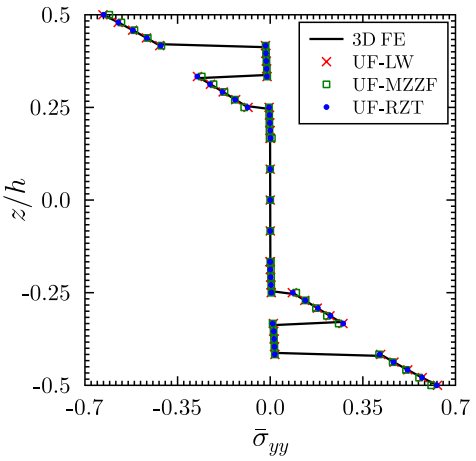

(b) VS Lam D: $\bar{\sigma}_{yy}$ at $y = L/2$

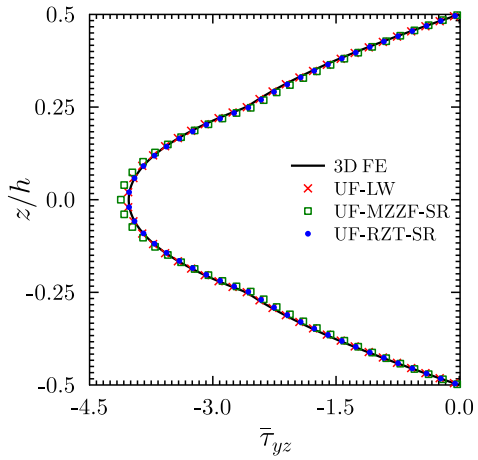

(c) VS Lam C: $\bar{\tau}_{yz}$ at $y = L/4$

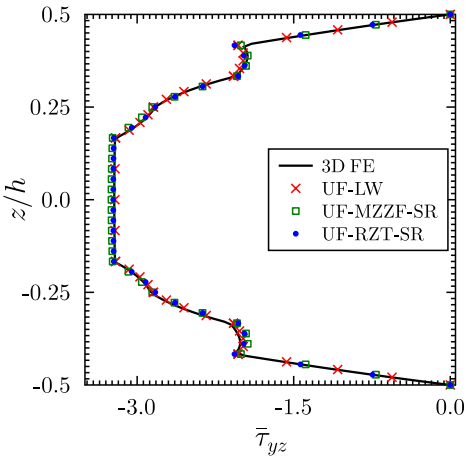

(d) VS Lam D: $\bar{\tau}_{yz}$ at $y = L/4$

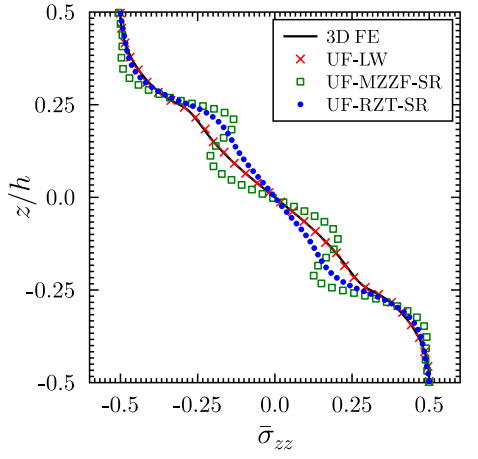

(e) VS Lam C: $\bar{\sigma}_{zz}$ at $y = L/2$

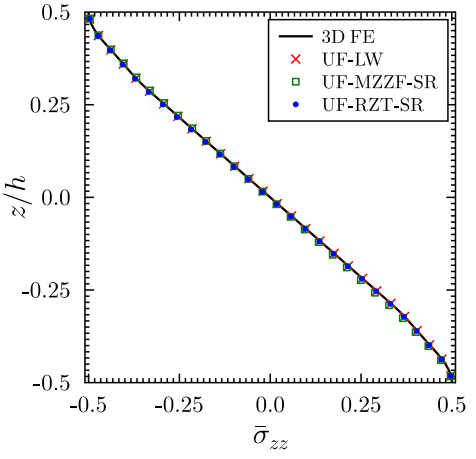

(f) VS Lam D: $\bar{\sigma}_{zz}$ at $y = L/2$

Figure 7.2: Through-thickness distribution of the normalized axial, transverse shear and transverse normal stresses variable-stiffness laminates C and D.

Table 7.2: Comparison of number of beam elements (Y), Serendipity Lagrange (SL) cross-section elements (Z), expansion order (N), DOFs (n) and computational complexities ($\mathcal{O}$) associated with each model.

Model	Y **B4**	Z **SL**N	**DOFs** n	**Time*** $\sim\mathcal{O}(n^2)$	**Space*** $\sim\mathcal{O}(nb^{**})$	Y **B4**	Z **SL**N	**DOFs** n	**Time** $\sim\mathcal{O}(n^2)$	**Space** $\sim\mathcal{O}(nb)$
	CS Lam A					**CS Lam B**				
UF-LW	30 B4	5 SL5	24,843	10^8	10^7	30 B4	7 SL5	34,125	10^9	10^7
UF-MZZF	30 B4	1 SL5	6,825	10^7	10^6	30 B4	1 SL5	6,825	10^7	10^6
UF-RZT	30 B4	1 SL5	6,825	10^7	10^6	30 B4	1 SL5	6,825	10^7	10^6
	VS Lam C					**VS Lam D**				
3D FE [11]	-	-	580,800	10^{11}	10^7	-	-	580,800	10^{11}	10^7
UF-LW	40 B4	8 SL4	36,663	10^9	10^7	40 B4	9 SL4	41,019	10^9	10^7
UF-MZZF	50 B4	1 SL5	10,721	10^8	10^6	40 B4	1 SL5	8,591	10^7	10^6
UF-RZT	50 B4	1 SL5	10,721	10^8	10^6	40 B4	1 SL5	8,591	10^7	10^6
	VS Lam E					**VS Lam F**				
3D FE [11]	-	-	580,800	10^{11}	10^7	-	-	580,800	10^{11}	10^7
UF-LW	40 B4	5 SL4	23,595	10^8	10^7	40 B4	9 SL4	41,019	10^9	10^7
UF-MZZF	50 B4	1 SL5	10,721	10^8	10^6	70 B4	1 SL6	19,412	10^8	10^6
UF-RZT	50 B4	1 SL5	10,721	10^8	10^6	70 B4	1 SL6	19,412	10^8	10^6

*Time and space complexities associated with a pre-conditioner conjugate gradient algorithm (iterative solver) (refer Section 5.4).
$^{**}b$ denotes the bandwidth of a matrix.

(DOFs) and algebraic system complexities, for each case are compared. The recovered stress distributions are shown as UF-MZZF-SR and UF-RZT-SR in the plots. Clearly, for CS laminate A, both ESL models, UF-MZZF and UF-RZT, predict the stress response accurately. However, the UF-RZT model outperforms the UF-MZZF model in capturing the extreme case of transverse orthotropy in CS laminate B. This stress distribution arises due to the low transverse shear stiffness of the inner layer which makes it insufficient to support the peak transverse shear stress of the adjacent outer layer, and thus, a stress reversal in stiffer layers occurs.

For VS laminates C-F, Figures 7.2 and 7.3 show through-thickness plots of in-plane normal stress $\bar{\sigma}_{yy}$ at the mid-span of the beam, transverse shear stress $\bar{\tau}_{yz}$ at the quarter-span of the beam and transverse normal stress $\bar{\sigma}_{zz}$ at the mid-span of the beam. From these plots, it is evident that the stress distribution obtained using the LW approach is in excellent agreement with the 3D FE solution. The axial normal $\bar{\sigma}_{yy}$ and transverse shear $\bar{\tau}_{yz}$ stress distribution obtained using the ESL model (UF-MZZF) correlates well with 3D FE for VS laminates C, D and E, whereas for

the arbitrary sandwich beam, VS laminate F, significant differences are observed (Figures 7.3(b) and 7.3(d)). These differences show the inability of MZZF in capturing the zig-zag effect accurately for highly heterogeneous sandwich beams. In contrast, the UF-RZT model predicts the stress response accurately for all variable-stiffness laminates considered herein and results are in close agreement with 3D FE solutions. However, from the transverse normal stress $\bar{\sigma}_{zz}$ plots, it seems that both ZZ models are unable to capture the thickness stretching effect for VS laminates C, E and F. The reason for this disparity is the presence of an absolute value in the function used to describe the fibre orientation (equation (6.1)), which leads to a discontinuity in fibre angle slope and curvature. This discontinuity, in turn, results in a continuous but non-differentiable distribution of transverse shear stress $\bar{\tau}_{yz}$ at the mid-span. Thus, the UF-MZZF and the UF-RZT models predict an incorrect $\bar{\sigma}_{zz}$ distribution as it is recovered from Cauchy's equilibrium equation, described in Section 7.1.4. On the other hand, the UF-LW model is able to predict the transverse stress results accurately as these are computed directly from the underlying constitutive equations. For VS laminate D, since all layers have fibre orientation angle (T_0) value at the mid-span with either 0° or 90°, the transverse shear stress distribution is continuous and differentiable, and therefore, the transverse normal stress correlates well for all models as shown in Figure 7.2(f). More insights on these intricacies in modelling variable-stiffness laminates were discussed in the previous chapter.

To check the applicability of proposed models (UF-MZZF and UF-RZT) at locations along the beam other than the fibre angle singularity (mid-span in the present case), through-thickness distributions of $\bar{\sigma}_{yy}$, $\bar{\tau}_{yz}$ and $\bar{\sigma}_{zz}$ are plotted at $y = 0.1L$ and $0.2L$, for laminates VS C, VS E and VS F, in Figures 7.4 to 7.6. It can be clearly seen that the results obtained using the UF-RZT model is in excellent agreement with the UF-LW model for all VS laminates, even near the boundary. The UF-MZZF model is accurate for VS laminates C and E, but fails to capture the zig-zag effect and a reversal in transverse shear stress profile intensified by the clamped support condition in VS sandwich laminate F. Furthermore, it is to be noted that this is the first time that RZT is used within a hierarchical displacement-based model to analyze variable-stiffness beams. Previously, Groh and Weaver [11] used the RZT ZZ function within the Hellinger-Reissner mixed formulation implemented in Differential Quadrature Method (DQM) to model variable-stiffness beams. It was observed that due to the dependence of the RZT ZZ function on transverse shear rigidities, the ZZ effect can vanish in some areas of the beam. Local areas with negligible ZZ effect lead to numerical instabilities in the model due to local singularities in the axial variation of laminate compliance terms. Since DQM computes derivatives based on all functional values within the domain, local singularities caused numerical instabilities in the model. This is not the case with the present Serendipity Lagrange finite element model because, in contrast to the work by Groh & Weaver, the mathematical domain is decomposed into smaller subdomains with local support (finite elements) rather than one domain with global support. Moreover, the UF-SLE ESL approach is computationally more efficient than the 3D FE and the UF-LW model,

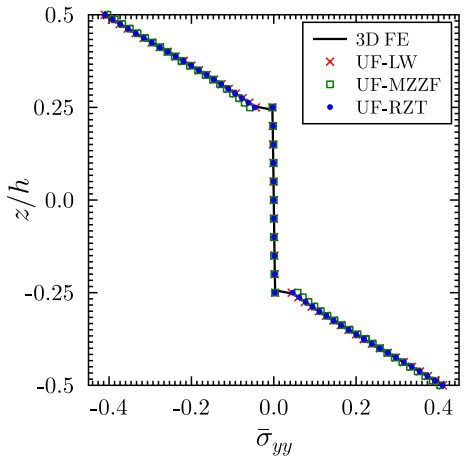

(a) VS Lam E: $\bar{\sigma}_{yy}$ at $y = L/2$

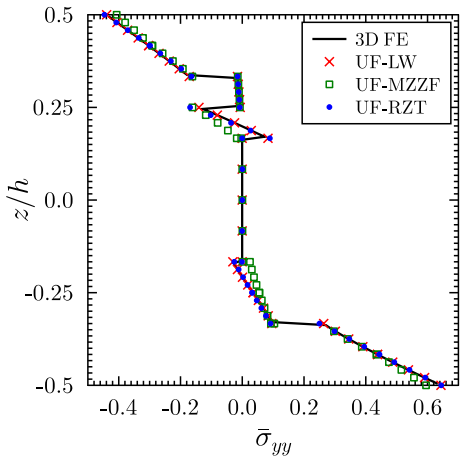

(b) VS Lam F: $\bar{\sigma}_{yy}$ at $y = L/2$

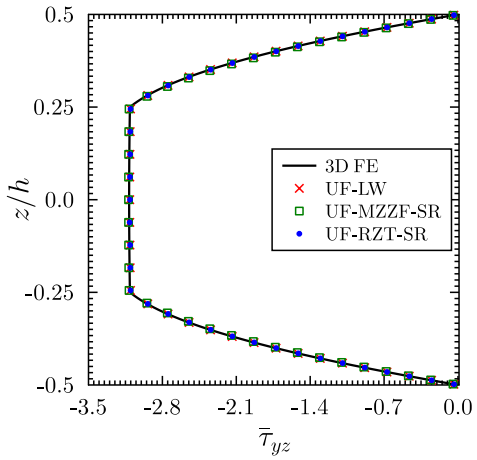

(c) VS Lam E: $\bar{\tau}_{yz}$ at $y = L/4$

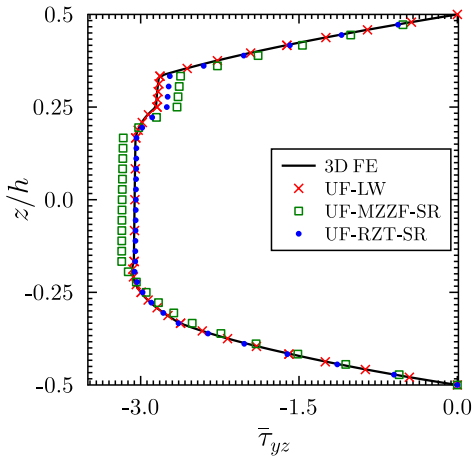

(d) VS Lam F: $\bar{\tau}_{yz}$ at $y = L/4$

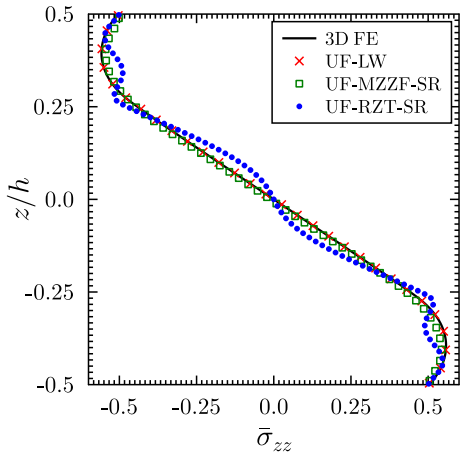

(e) VS Lam E: $\bar{\sigma}_{zz}$ at $y = L/2$

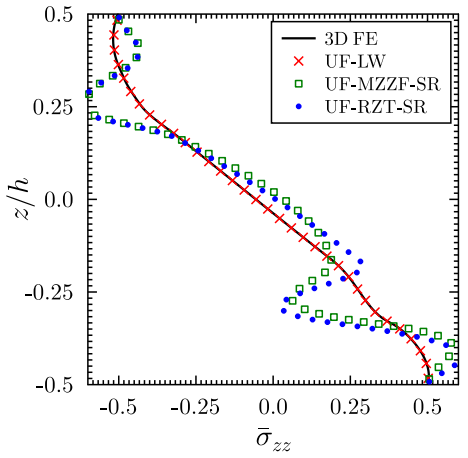

(f) VS Lam F: $\bar{\sigma}_{zz}$ at $y = L/2$

Figure 7.3: Through-thickness distribution of the normalized axial, transverse shear and transverse normal stresses variable-stiffness laminates E and F.

as shown in Table 7.2. However, the UF-LW model can be a viable alternative in cases where 3D FE analysis is required due to the presence of very localised stress gradients or layer-wise boundary conditions.

7.3 Conclusions

In previous chapters, the displacement-based Unified Formulation model, based on the hierarchical Serendipity Lagrange Expansion finite element (UF-SLE), was used to derive a Layer-Wise model for constant- and variable-stiffness beams. In this chapter, to reduce the computational expense, an Equivalent Single Layer (ESL) approach is implemented within the UF-SLE framework. To account for the ZZ effect, Murakami's Zig-Zag Function (MZZF) and Refined Zig-Zag Theory (RZT) functions are used to model constant- and variable-stiffness laminated and sandwich beams. The continuous distribution of transverse stresses across the layers is obtained *a posteriori* by integrating the in-plane stresses in Cauchy's 3D indefinite equilibrium equations. The UF-MZZF model is shown to be insufficient in capturing the stress response accurately for highly heterogeneous sandwich beams. On the other hand, the UF-RZT model predicts the three-dimensional (3D) stress response accurately for all cases considered herein, and is shown to be more computationally efficient than the UF-SLE layer-wise model (UF-LW) and the 3D finite element (FE) model. Thus, the combination of accuracy and computational expense makes this approach an attractive basis for industrial design tools. However, the UF-LW model is still preferred over the UF-RZT model in the presence of localised stress gradients or mathematical singularities in the constitutive relations, which can be observed for variable-stiffness composites.

An ESL approach predicts global structural response accurately and with appropriate zig-zag function, the approach can be used for capturing accurate stress fields, as shown in this chapter. However, in case of thick composites, where transverse stresses are significantly high and can cause delamination failure, layer-wise models become important. Moreover, predicting geometric nonlinear behaviour with an ESL approach would result in an inaccurate prediction of the overall structural response if transverse stresses are significant. For instance, modelling a multi-MW wind turbine blade, which is hugely long, and undergoes large deflection. The global response (nonlinear deflection) of the blade structure can be easily captured by an ESL model, however, the root of the blade is thick and it is a failure prone site. Therefore, capturing transverse stresses accurately near the blade root is of fundamental importance while designing the wind turbine structure. However, as shown in this chapter, accurate transverse stresses can be recovered from Cauchy's 3D equilibrium equations, but repeating this process for each iteration in a nonlinear analysis in the overall structure is cumbersome and expensive. For this reason, in the next chapter, the layer-wise form of the UF-SLE model is extended to account for geometric nonlinearilty in composite structures.

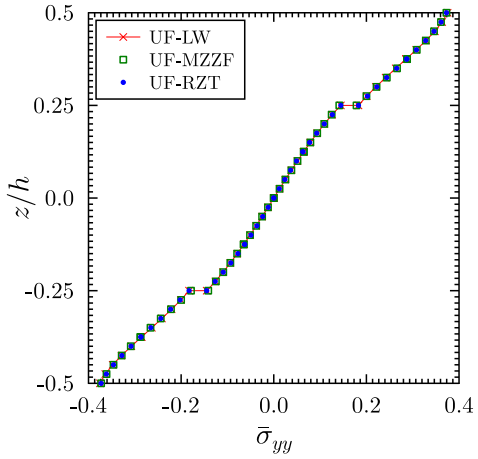

(a) VS Lam C: $\bar{\sigma}_{yy}$ at $y = 0.1L$

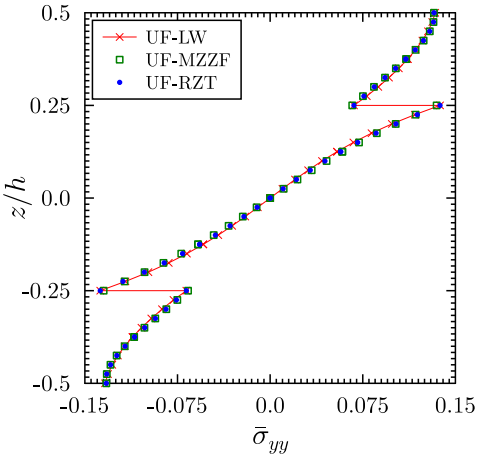

(b) VS Lam C: $\bar{\sigma}_{yy}$ at $y = 0.2L$

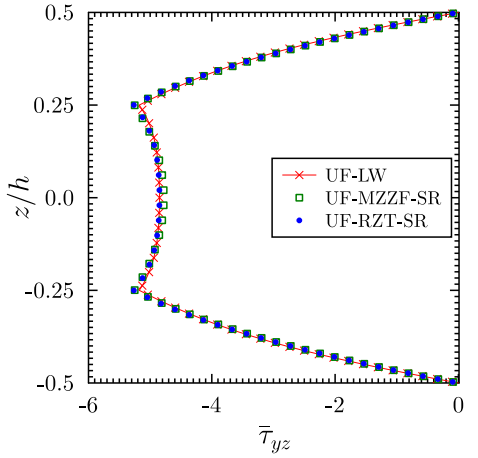

(c) VS Lam C: $\bar{\tau}_{yz}$ at $y = 0.1L$

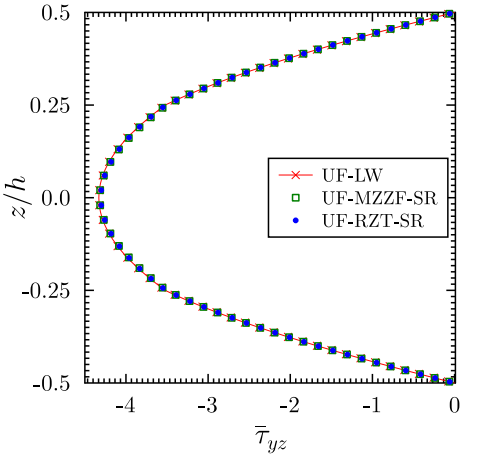

(d) VS Lam C: $\bar{\tau}_{yz}$ at $y = 0.2L$

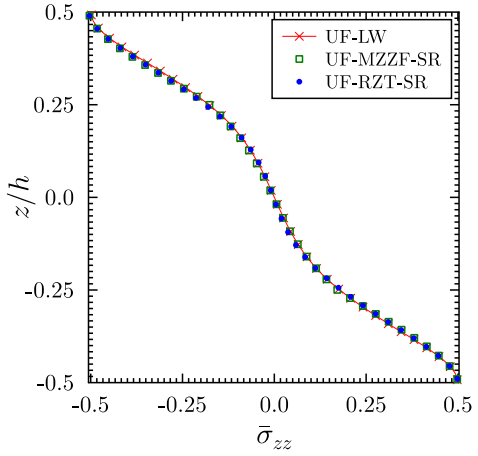

(e) VS Lam C: $\bar{\sigma}_{zz}$ at $y = 0.1L$

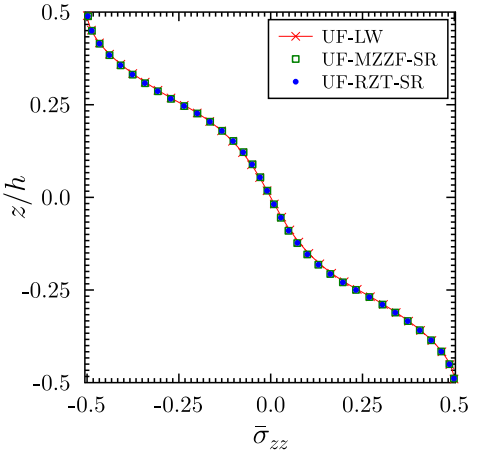

(f) VS Lam C: $\bar{\sigma}_{zz}$ at $y = 0.2L$

Figure 7.4: Through-thickness distribution of the normalized axial and transverse stresses, at 10% and 20% of the beam length from the clamped end, for variable-stiffness laminate C.

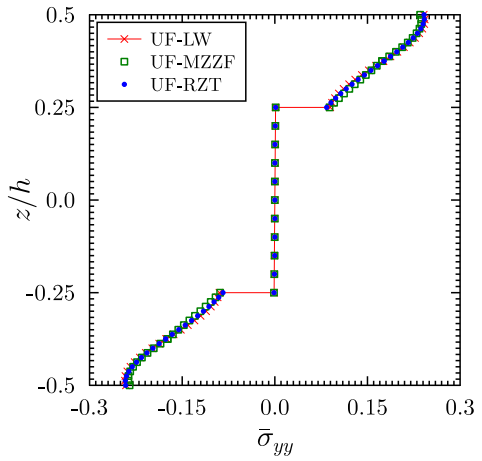

(a) VS Lam E: $\bar{\sigma}_{yy}$ at $y = 0.1L$

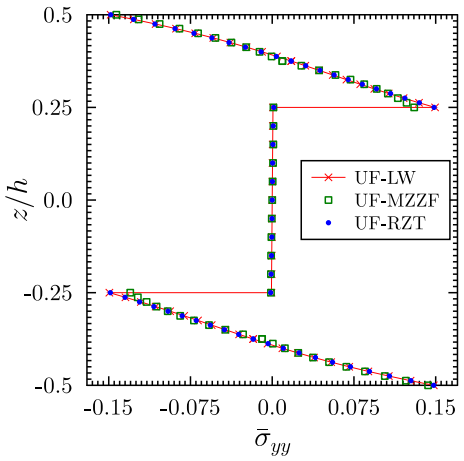

(b) VS Lam E: $\bar{\sigma}_{yy}$ at $y = 0.2L$

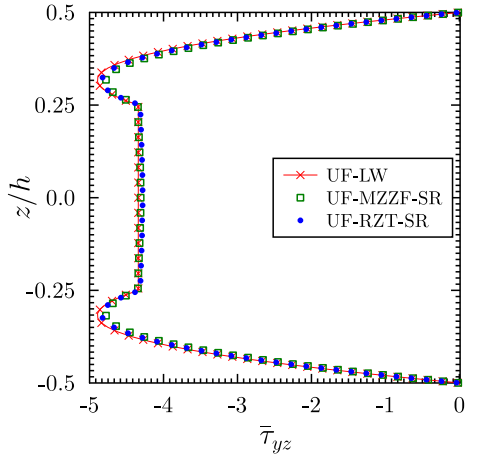

(c) VS Lam E: $\bar{\tau}_{yz}$ at $y = 0.1L$

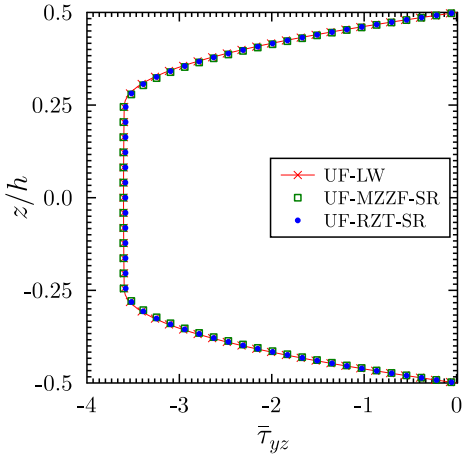

(d) VS Lam E: $\bar{\tau}_{yz}$ at $y = 0.2L$

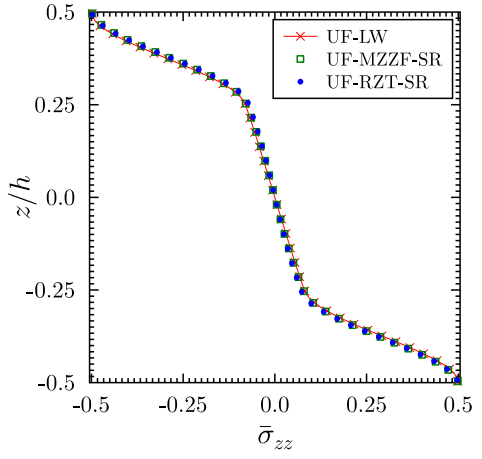

(e) VS Lam E: $\bar{\sigma}_{zz}$ at $y = 0.1L$

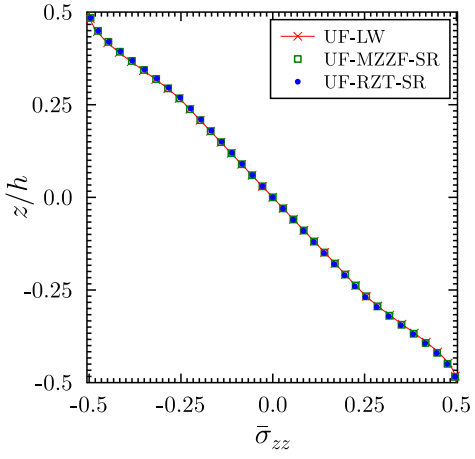

(f) VS Lam E: $\bar{\sigma}_{zz}$ at $y = 0.2L$

Figure 7.5: Through-thickness distribution of the normalized axial and transverse stresses, at 10% and 20% of the beam length from the clamped end, for variable-stiffness laminate E.

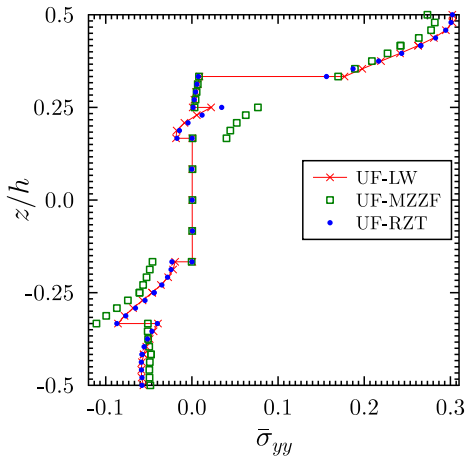

(a) VS Lam F: $\bar{\sigma}_{yy}$ at $y = 0.1L$

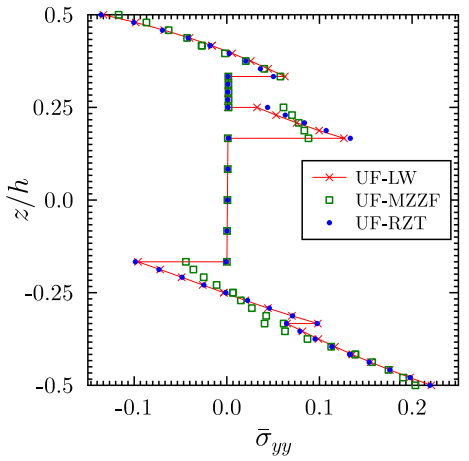

(b) VS Lam F: $\bar{\sigma}_{yy}$ at $y = 0.2L$

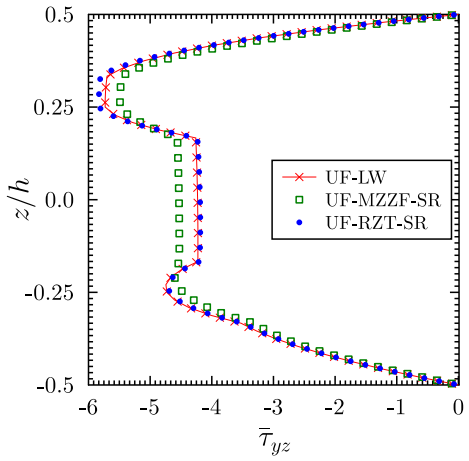

(c) VS Lam F: $\bar{\tau}_{yz}$ at $y = 0.1L$

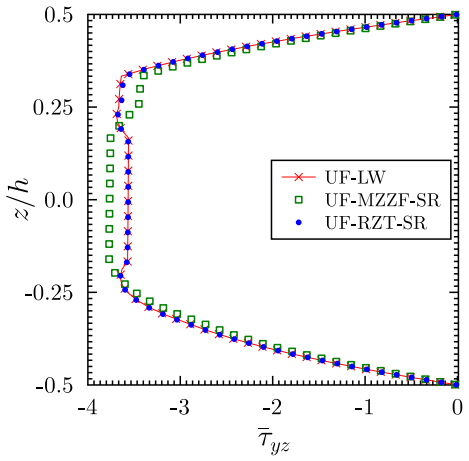

(d) VS Lam F: $\bar{\tau}_{yz}$ at $y = 0.2L$

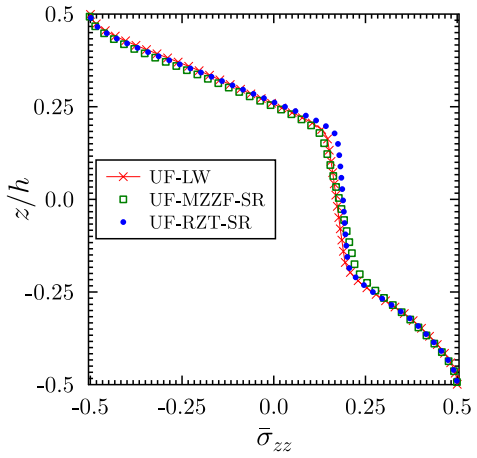

(e) VS Lam F: $\bar{\sigma}_{zz}$ at $y = 0.1L$

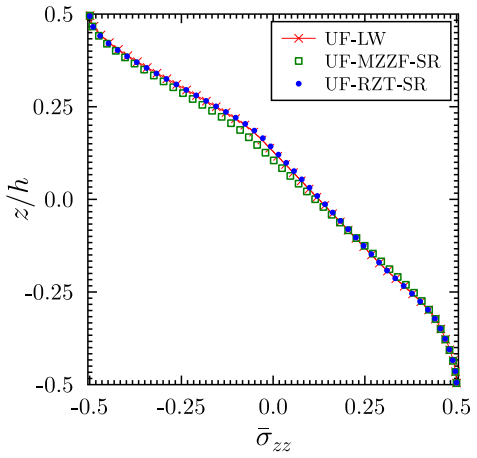

(f) VS Lam F: $\bar{\sigma}_{zz}$ at $y = 0.2L$

Figure 7.6: Through-thickness distribution of the normalized axial and transverse stresses, at 10% and 20% of the beam length from the clamped end, for variable-stiffness laminate F.

CHAPTER 8

Geometrically Nonlinear Serendipity Lagrange Expansions-based Unified Formulation Model

Composite structures are extensively used in many industries, where they are subjected to a variety of loads and may undergo large deformations. Reliable utilisation of such structures requires prior knowledge of their failure response. In order to predict failure loads and modes, accurate, yet computationally efficient, evaluation of three-dimensional (3D) stress fields becomes important. In this chapter, we extend the modelling approach, based on the Unified Formulation as discussed in previous chapters, to account for geometric nonlinearity in laminated composites and predict 3D stress fields for subsequent failure analysis. The approach builds upon the hierarchical Serendipity Lagrange finite elements and is able to capture high-order shear deformation, as well as local cross-sectional warping. A total Lagrangian approach is adopted and the classic Newton-Raphson method is employed to solve the nonlinear governing equations. A key novelty of the proposed formulation is its completeness and its applicability to fully anisotropic structures. In other words, using the Green-Lagrange strain components within the Unified Formulation framework, the explicit form of the tangent stiffness matrix is derived including general stiffness properties as discussed in Section 8.2. This new model is benchmarked against 3D finite element solution, as well as other formulations available in the literature, by means of static analyses of highly nonlinear, isotropic and laminated composite beam-like structures, presented in Sections 8.2.1 and 8.2.2. Significant computational efficiency gains over 3D finite elements are observed for similar levels of accuracy. Furthermore, in Section 8.2.3, to show the enhanced capabilities of the present formulation, the postbuckling response of a composite stiffened panel is compared with experimental results from the literature. The 3D stress fields computed in the postbuckling regime are used to detect failure of the stiffened panel. The corresponding failure mode, as obtained by the new model, is shown to match with the

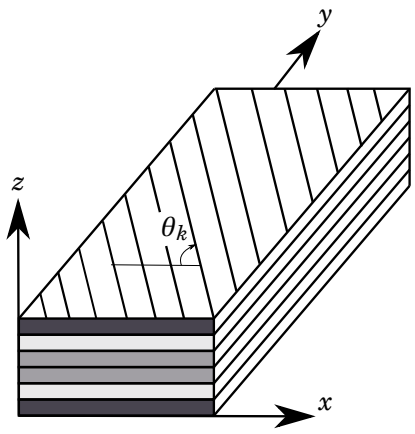

Figure 8.1: Reference system for a laminated beam.

experiment.

8.1 Numerical Formulation

8.1.1 Preliminaries

Consider a laminated beam of length L and rectangular cross-section of width b and thickness h, composed of N_l layers. The material properties and the thickness of each layer may be entirely different. The beam is referred to a Cartesian coordinate system (x,y,z), where the y-direction is defined to be along the principal beam axis, while the z-axis is in the transverse stacking direction as shown in Figure 8.1. Let θ denote the fibre orientation and the subscript k be used to refer to the k^{th} layer. For points in the structure's volume, the three-dimensional displacement field is given as

$$\boldsymbol{U}(x,y,z) = \{u \quad v \quad w\}^{\top}, \tag{8.1}$$

and the displacement gradient vector $\boldsymbol{\Phi}$ can be written as

$$\boldsymbol{\Phi} = \left\{u_{,x} \quad u_{,y} \quad u_{,z} \quad v_{,x} \quad v_{,y} \quad v_{,z} \quad w_{,x} \quad w_{,y} \quad w_{,z}\right\}^{\top}, \tag{8.2}$$

where a subscript preceded by a comma denotes differentiation with respect to the corresponding spatial coordinate.

To account for large deformations, the Green-Lagrange strain vector $\boldsymbol{E}$ is considered, which is

given by

$$
\begin{aligned}
E_{xx} &= u_{,x} + \frac{1}{2}\left(u_{,x}^2 + v_{,x}^2 + w_{,x}^2\right), \\
E_{yy} &= v_{,y} + \frac{1}{2}\left(u_{,y}^2 + v_{,y}^2 + w_{,y}^2\right), \\
E_{zz} &= w_{,z} + \frac{1}{2}\left(u_{,z}^2 + v_{,z}^2 + w_{,z}^2\right), \\
E_{yz} &= v_{,z} + w_{,y} + \left(u_{,y}u_{,z} + v_{,y}v_{,z} + w_{,y}w_{,z}\right), \\
E_{xz} &= u_{,z} + w_{,x} + \left(u_{,x}u_{,z} + v_{,x}v_{,z} + w_{,x}w_{,z}\right), \\
E_{xy} &= u_{,y} + v_{,x} + \left(u_{,x}u_{,y} + v_{,x}v_{,y} + w_{,x}w_{,y}\right).
\end{aligned}
\tag{8.3}
$$

Equation (8.3) can be written in matrix form as

$$
\boldsymbol{E} = \left[\boldsymbol{H} + \frac{1}{2}\boldsymbol{A}\right]\boldsymbol{\Phi}, \tag{8.4}
$$

and the virtual variation of the Green-Lagrange strain vector [205] is given by

$$
\delta\boldsymbol{E} = \delta\left\{\left[\boldsymbol{H} + \frac{1}{2}\boldsymbol{A}\right]\boldsymbol{\Phi}\right\} = [\boldsymbol{H} + \boldsymbol{A}]\delta\boldsymbol{\Phi}, \tag{8.5}
$$

where

$$
\boldsymbol{E} = \begin{Bmatrix} E_{xx} & E_{yy} & E_{zz} & E_{yz} & E_{xz} & E_{xy} \end{Bmatrix}^{\top},
$$

$$
\boldsymbol{H} = \begin{bmatrix}
1 & 0 & 0 & 0 & 0 & 0 & 0 & 0 & 0 \\
0 & 0 & 0 & 0 & 1 & 0 & 0 & 0 & 0 \\
0 & 0 & 0 & 0 & 0 & 0 & 0 & 0 & 1 \\
0 & 0 & 0 & 0 & 0 & 1 & 0 & 1 & 0 \\
0 & 0 & 1 & 0 & 0 & 0 & 1 & 0 & 0 \\
0 & 1 & 0 & 1 & 0 & 0 & 0 & 0 & 0
\end{bmatrix},
$$

$$
\boldsymbol{A} = \begin{bmatrix}
u_{,x} & 0 & 0 & v_{,x} & 0 & 0 & w_{,x} & 0 & 0 \\
0 & u_{,y} & 0 & 0 & v_{,y} & 0 & 0 & w_{,y} & 0 \\
0 & 0 & u_{,z} & 0 & 0 & v_{,z} & 0 & 0 & w_{,z} \\
0 & u_{,z} & u_{,y} & 0 & v_{,z} & v_{,y} & 0 & w_{,z} & w_{,y} \\
u_{,z} & 0 & u_{,x} & v_{,z} & 0 & v_{,x} & w_{,z} & 0 & w_{,x} \\
u_{,y} & u_{,x} & 0 & v_{,y} & v_{,x} & 0 & w_{,y} & w_{,x} & 0
\end{bmatrix}.
$$

The material is assumed to undergo deformation within the linear elastic range and, therefore, Hooke's law provides the constitutive relation at layer level:

$$
\boldsymbol{S} = \bar{\boldsymbol{C}}\boldsymbol{E}, \tag{8.6}
$$

where $\boldsymbol{S} = \{S_{xx} \quad S_{yy} \quad S_{zz} \quad S_{yz} \quad S_{xz} \quad S_{xy}\}^\top$ is the second Piola-Kirchhoff stress tensor and $\bar{\boldsymbol{C}}$ is the transformed material stiffness matrix expressed in the global Cartesian coordinate system,

$$\bar{\boldsymbol{C}} = \begin{bmatrix} \bar{C}_{11} & \bar{C}_{12} & \bar{C}_{13} & \bar{C}_{14} & \bar{C}_{15} & \bar{C}_{16} \\ & \bar{C}_{22} & \bar{C}_{23} & \bar{C}_{24} & \bar{C}_{25} & \bar{C}_{26} \\ & & \bar{C}_{33} & \bar{C}_{34} & \bar{C}_{35} & \bar{C}_{36} \\ & & & \bar{C}_{44} & \bar{C}_{45} & \bar{C}_{46} \\ & Symmetric & & & \bar{C}_{55} & \bar{C}_{56} \\ & & & & & \bar{C}_{66} \end{bmatrix}, \tag{8.7}$$

where the coefficients $\bar{C}_{ij}$ relate to the elastic coefficients in material coordinates, C_{ij}, via the transformation matrix $\boldsymbol{Q}$, whose elements are obtained from the direction cosines of the material coordinate system projected onto the global x, y, z coordinate directions. Specifically,

$$\bar{\boldsymbol{C}} = \boldsymbol{Q}\boldsymbol{C}\boldsymbol{Q}^\top. \tag{8.8}$$

The matrix $\boldsymbol{Q}$ can be found in Section 5.4 of [206].

8.1.2 Serendipity Lagrange-based nonlinear Finite Element Model

Our model employs the Unified Formulation framework, as discussed in previous chapters, where a 3D structure is discretised with a finite number of transverse planes running along the principal axis of the structure. In this setting, the longitudinal axis of the structure is discretised with N_e-noded, 1D finite elements, so that the displacement field can be approximated element-wise by means of local shape functions, $N_i(y)$. In addition, the transverse, or cross-sectional deformations, are approximated using hierarchical Serendipity Lagrange expansion (SLE) functions, $F_\tau(x,z)$ (refer Section 3.4.4), such that

$$\boldsymbol{U}(x,y,z) = \sum_{i=1}^{N_\text{e}} \sum_{\tau=1}^{m} N_i(y) F_\tau(x,z) \boldsymbol{U}_{i\tau}. \tag{8.9}$$

where m is the number of terms depending on the order of SL expansion, and $\boldsymbol{U}_{i\tau}$ are generalised three-dimensional displacement vectors.

Adopting this expansion model, cross-sections are discretised using four-noded Lagrange sub-domains (SLE nodes) and the layer-wise form of the UF-SLE model is adopted. By substituting equation (8.9) in equation (8.2), the displacement gradient vector can be written as

$$\boldsymbol{\Phi} = \boldsymbol{G}_{i\tau} \boldsymbol{U}_{i\tau} \tag{8.10}$$

where

$$\boldsymbol{G}_{i\tau} = \begin{bmatrix} N_i F_{\tau,x} & 0 & 0 \\ N_{i,y} F_\tau & 0 & 0 \\ N_i F_{\tau,z} & 0 & 0 \\ 0 & N_i F_{\tau,x} & 0 \\ 0 & N_{i,y} F_\tau & 0 \\ 0 & N_i F_{\tau,z} & 0 \\ 0 & 0 & N_i F_{\tau,x} \\ 0 & 0 & N_{i,y} F_\tau \\ 0 & 0 & N_i F_{\tau,z} \end{bmatrix}, \quad \boldsymbol{U}_{i\tau} = \begin{Bmatrix} u_{i\tau} \\ v_{i\tau} \\ w_{i\tau} \end{Bmatrix}.$$

In the previous expression and throughout remainder of the chapter, the Einstein summation convention is implied over repeated indices.

Elastic equilibrium is enforced via the Principle of Virtual Displacements, by equating the internal and external virtual work, δW_{int} and δW_{ext}. By definition, the internal work is the work done by the internal stresses over the corresponding internal strains and is equivalent to the elastic strain energy. Noting that $W_{\text{int}} = \sum_{\text{e}} W_{\text{int}}^{\text{e}}$, where $W_{\text{int}}^{\text{e}}$ represents the strain energy per element and V^{e} be the volume of the generic element in an undeformed state,

$$\delta W_{\text{int}}^{\text{e}} = \int_{V^{\text{e}}} \delta \boldsymbol{E}^{\top} \boldsymbol{S} \, dV. \tag{8.11}$$

In the notation of the Unified Formulation (refer equations (3.7) and (3.11)), the internal work can be re-written as

$$\delta W_{\text{int}}^{\text{e}} = \delta \boldsymbol{U}_{js}^{\top} \boldsymbol{K}_{\text{s}}^{\tau sij} \boldsymbol{U}_{i\tau}, \tag{8.12}$$

where the term $\boldsymbol{K}_{\text{s}}^{\tau sij}$ is referred to as the *Fundamental Nuclei* of the secant stiffness matrix. Its explicit form for an orthotropic lamina can be found in [147]. Fundamental nuclei are assembled into a global stiffness matrix following the standard finite element procedure. In the present work, we employ the full Newton-Raphson method to solve the nonlinear governing equations. The main disadvantage of using the secant stiffness matrix as in equation (8.12) would be its low convergence rate. Moreover, the secant matrix is not uniquely defined and is generally non-symmetric [147]. Therefore, in the following section, we derive the tangent stiffness matrix, as a more suitable alternative for the Newton-Raphson iterative solver employed herein.

8.1.3 Fundamental Nucleus of the Tangent Stiffness Matrix

In the present work, a classical Newton iteration method [207] is employed to solve the nonlinear system, which requires formulation of the tangent stiffness matrix. The fundamental nucleus of the tangent stiffness matrix is obtained from the linearisation of the virtual variation of the strain energy [147] as follows

$$d(\delta W_{\text{int}}^{\text{e}}) = \int_{V^{\text{e}}} d(\delta \boldsymbol{E}^{\top} \boldsymbol{S}) \, dV = \int_{V^{\text{e}}} \delta \boldsymbol{E}^{\top} d\boldsymbol{S} \, dV + \int_{V^{\text{e}}} d(\delta \boldsymbol{E}^{\top}) \boldsymbol{S} \, dV. \tag{8.13}$$

The first term requires the linearisation of the constitutive relation (equation (8.6)), which, under the assumption of constant material stiffness and following equation (8.5), can be recast as

$$\int_{V^{\mathrm{e}}} \delta \boldsymbol{E}^{\top} d\boldsymbol{S}\, dV = \int_{V^{\mathrm{e}}} \left(\delta \boldsymbol{\Phi}^{\top} \left\{ [\boldsymbol{H} + \boldsymbol{A}]^{\top} \bar{\boldsymbol{C}} [\boldsymbol{H} + \boldsymbol{A}] \right\} d\boldsymbol{\Phi} \right) dV. \tag{8.14}$$

The second term requires the linearisation of the virtual variation of the Green-Lagrange strain vector, which, after manipulation [205], can be written in the following form:

$$\int_{V^{\mathrm{e}}} d(\delta \boldsymbol{E}^{\top}) \boldsymbol{S}\, dV = \int_{V^{\mathrm{e}}} \delta \boldsymbol{\Phi}^{\top} \hat{\boldsymbol{S}} d\boldsymbol{\Phi}\, dV, \tag{8.15}$$

where

$$\hat{\boldsymbol{S}} = \begin{bmatrix} S_{xx} & S_{xy} & S_{xz} & 0 & 0 & 0 & 0 & 0 & 0 \\ S_{xy} & S_{yy} & S_{yz} & 0 & 0 & 0 & 0 & 0 & 0 \\ S_{xz} & S_{yz} & S_{zz} & 0 & 0 & 0 & 0 & 0 & 0 \\ 0 & 0 & 0 & S_{xx} & S_{xy} & S_{xz} & 0 & 0 & 0 \\ 0 & 0 & 0 & S_{xy} & S_{yy} & S_{yz} & 0 & 0 & 0 \\ 0 & 0 & 0 & S_{xz} & S_{yz} & S_{zz} & 0 & 0 & 0 \\ 0 & 0 & 0 & 0 & 0 & 0 & S_{xx} & S_{xy} & S_{xz} \\ 0 & 0 & 0 & 0 & 0 & 0 & S_{xy} & S_{yy} & S_{yz} \\ 0 & 0 & 0 & 0 & 0 & 0 & S_{xz} & S_{yz} & S_{zz} \end{bmatrix}.$$

Substituting equations (8.10), (8.14) and (8.15) into equation (8.13), the linearised version of the virtual variation of the strain energy is written as

$$\begin{aligned} d(\delta W_{\mathrm{int}}^{\mathrm{e}}) &= \delta \boldsymbol{U}_{js}^{\top} \left(\int_{V^{\mathrm{e}}} \boldsymbol{G}_{js}^{\top} \left\{ [\boldsymbol{H}^{\top} + \boldsymbol{A}^{\top}] \bar{\boldsymbol{C}} [\boldsymbol{H} + \boldsymbol{A}] + \hat{\boldsymbol{S}} \right\} \boldsymbol{G}_{i\tau}\, dV \right) d\boldsymbol{U}_{i\tau}, \\ &= \delta \boldsymbol{U}_{js}^{\top} \left(\boldsymbol{K}_{\mathrm{ll}}^{\tau sij} + \boldsymbol{K}_{\mathrm{lnl}}^{\tau sij} + \boldsymbol{K}_{\mathrm{nll}}^{\tau sij} + \boldsymbol{K}_{\mathrm{nlnl}}^{\tau sij} + \boldsymbol{K}_{\sigma}^{\tau sij} \right) d\boldsymbol{U}_{i\tau}, \\ &= \delta \boldsymbol{U}_{js}^{\top} \boldsymbol{K}_{\mathrm{T}}^{\tau sij}\, d\boldsymbol{U}_{i\tau}, \end{aligned} \tag{8.16}$$

where $\boldsymbol{K}_{\mathrm{T}}^{\tau sij}$ is the fundamental nucleus of the tangent stiffness matrix, which, in turn, is composed of a linear term, $\boldsymbol{K}_{\mathrm{ll}}^{\tau sij}$, the nonlinear terms, $\boldsymbol{K}_{\mathrm{lnl}}^{\tau sij}$, $\boldsymbol{K}_{\mathrm{nll}}^{\tau sij}$ and $\boldsymbol{K}_{\mathrm{nlnl}}^{\tau sij}$, and the geometric stiffness term, $\boldsymbol{K}_{\sigma}^{\tau sij}$, where these are defined as follows:

$$\begin{aligned} \boldsymbol{K}_{\mathrm{ll}}^{\tau sij} &= \int_{V^{\mathrm{e}}} \boldsymbol{G}_{js}^{\top} \boldsymbol{H}^{\top} \bar{\boldsymbol{C}} \boldsymbol{H} \boldsymbol{G}_{i\tau}\, dV, \\ \boldsymbol{K}_{\mathrm{lnl}}^{\tau sij} &= \int_{V^{\mathrm{e}}} \boldsymbol{G}_{js}^{\top} \boldsymbol{H}^{\top} \bar{\boldsymbol{C}} \boldsymbol{A} \boldsymbol{G}_{i\tau}\, dV, \\ \boldsymbol{K}_{\mathrm{nll}}^{\tau sij} &= \int_{V^{\mathrm{e}}} \boldsymbol{G}_{js}^{\top} \boldsymbol{A}^{\top} \bar{\boldsymbol{C}} \boldsymbol{H} \boldsymbol{G}_{i\tau}\, dV, \\ \boldsymbol{K}_{\mathrm{nlnl}}^{\tau sij} &= \int_{V^{\mathrm{e}}} \boldsymbol{G}_{js}^{\top} \boldsymbol{A}^{\top} \bar{\boldsymbol{C}} \boldsymbol{A} \boldsymbol{G}_{i\tau}\, dV, \\ \boldsymbol{K}_{\sigma}^{\tau sij} &= \int_{V^{\mathrm{e}}} \boldsymbol{G}_{js}^{\top} \hat{\boldsymbol{S}} \boldsymbol{G}_{i\tau}\, dV. \end{aligned} \tag{8.17}$$

These matrices are of size 3×3 for given i, j, τ, s and can be computed for each $\tau, s = 1, \ldots, m$, and $i, j = 1, \ldots, N_{\mathrm{e}}$, in order to obtain the elemental tangent stiffness matrix for beam models of

any order. Once the elemental tangent stiffness matrix is obtained, it is assembled into a global stiffness matrix following the standard finite element procedure.

The geometrically nonlinear stiffness terms, accounting for fully anisotropic material properties, are presented for the first time in the Unified Formulation framework. Therefore, for the sake of completeness, giving the explicit form of all nine components of the tangent stiffness matrix, for each of the nucleus sub-matrices, is important. However, each term in the fundamental nucleus involves summing a large number of expressions. Writing these long expressions is cumbersome and it also increases the chance of introducing a typing error while programming. For instance, each $\boldsymbol{K}_{\mathrm{ll}}^{\tau sij}$ term requires summation of 9 expressions as follows:

$$\begin{aligned}\boldsymbol{K}_{\mathrm{ll}}^{\tau sij}(1,1) = &\int_V \bar{C}_{11} F_{\tau,x} F_{s,x} N_i N_j dV + \int_V \bar{C}_{16} F_{\tau,x} F_s N_i N_{j,y} dV + \int_V \bar{C}_{15} F_{\tau,x} F_{s,z} N_i N_j dV \\ &+ \int_V \bar{C}_{16} F_\tau F_{s,x} N_{i,y} N_j dV + \int_V \bar{C}_{66} F_\tau F_s N_{i,y} N_{j,y} dV + \int_V \bar{C}_{56} F_\tau F_{s,z} N_{i,y} N_j dV \\ &+ \int_V \bar{C}_{15} F_{\tau,z} F_{s,x} N_i N_j dV + \int_V \bar{C}_{56} F_{\tau,z} F_s N_i N_{j,y} dV + \int_V \bar{C}_{55} F_{\tau,z} F_{s,z} N_i N_j dV .\end{aligned} \tag{8.18}$$

Similarly, $\boldsymbol{K}_{\mathrm{lnl}}^{\tau sij}$ and $\boldsymbol{K}_{\mathrm{nll}}^{\tau sij}$ terms require 27 expressions each, while $\boldsymbol{K}_{\mathrm{nlnl}}^{\tau sij}$ terms require 81 expressions. Furthermore, these matrices are of size 3×3 and non-symmetric, which increases the above count by a multiple of 9.

To overcome this complication, we devised an algorithmic and simplified way of writing the expressions in a concise form using Einstein's summation notation over repeated indices:

$$\begin{aligned}
\boldsymbol{K}_{\mathrm{ll}}^{\tau sij}(\alpha,\beta) &= < \bar{C}_{\alpha b \beta a} (N_i F_\tau)_{,a} (N_j F_s)_{,b} >, \\
\boldsymbol{K}_{\mathrm{lnl}}^{\tau sij}(\alpha,\beta) &= < \bar{C}_{\alpha b a c} (N_i F_\tau)_{,a} (N_j F_s)_{,b} (N_l F_p)_{,c} > \boldsymbol{U}_{lp}(\beta), \\
\boldsymbol{K}_{\mathrm{nll}}^{\tau sij}(\alpha,\beta) &= < \bar{C}_{\beta a b c} (N_i F_\tau)_{,a} (N_j F_s)_{,b} (N_m F_q)_{,c} > \boldsymbol{U}_{mq}(\alpha), \\
\boldsymbol{K}_{\mathrm{nlnl}}^{\tau sij}(\alpha,\beta) &= < \bar{C}_{acbd} (N_i F_\tau)_{,a} (N_j F_s)_{,b} (N_l F_p)_{,c} (N_m F_q)_{,d} > \boldsymbol{U}_{lp}(\beta) \boldsymbol{U}_{mq}(\alpha), \\
\boldsymbol{K}_{\sigma}^{\tau sij}(\alpha,\beta) &= \begin{cases} \boldsymbol{k}_{\sigma}^{\tau sij}(1,1) + \boldsymbol{k}_{\sigma}^{\tau sij}(2,2) + \boldsymbol{k}_{\sigma}^{\tau sij}(3,3) & \text{for} \quad \alpha = \beta \\ 0 & \text{for} \quad \alpha \neq \beta \end{cases},
\end{aligned} \tag{8.19}$$

with

$$\begin{aligned}\boldsymbol{k}_{\sigma}^{\tau sij}(\alpha,\alpha) = &< \bar{C}_{\alpha a b} (N_i F_\tau)_{,a} (N_j F_s)_{,b} (N_l F_p)_{,c} > \boldsymbol{U}_{lp}(\alpha) \\ &+ \frac{1}{2} < \bar{C}_{abcd} (N_i F_\tau)_{,a} (N_j F_s)_{,b} (N_l F_p)_{,c} (N_m F_q)_{,d} > \boldsymbol{U}_{lp}(\alpha) \boldsymbol{U}_{mq}(\alpha),\end{aligned} \tag{8.20}$$

where $\alpha,\beta = 1,2,3$, are row and column indices; $a,b,c,d = 1,2,3$, unless preceded by a comma denoting differentiation, in which case $a,b,c,d = x,y,z$; $<(.)>$ denotes $\int_V (.) dV$, which is evaluated numerically by employing Gaussian Quadrature; and where $\bar{\boldsymbol{C}}$ is expressed as a fourth-order

tensor (cf. equation (8.7)), as

$$\bar{\boldsymbol{C}} = \begin{bmatrix} \bar{C}_{1111} & \bar{C}_{1122} & \bar{C}_{1133} & \bar{C}_{1123} & \bar{C}_{1113} & \bar{C}_{1112} \\ & \bar{C}_{2222} & \bar{C}_{2233} & \bar{C}_{2223} & \bar{C}_{2213} & \bar{C}_{2212} \\ & & \bar{C}_{3333} & \bar{C}_{3323} & \bar{C}_{3313} & \bar{C}_{3312} \\ & & & \bar{C}_{2323} & \bar{C}_{2313} & \bar{C}_{2312} \\ & symmetric & & & \bar{C}_{1313} & \bar{C}_{1312} \\ & & & & & \bar{C}_{1212} \end{bmatrix}. \tag{8.21}$$

This concise way not only reduces the task, but also speeds up the computation process by natural vectorisation of the loop. Finally, it is to be noted that the expressions are independent of the type of expansion function used in the cross-section.

8.1.4 Corotational Cauchy Stress

The Cauchy stress tensor $\boldsymbol{\sigma}$ is derived from the Second-Piola stress tensor $\boldsymbol{S}$ using the deformation gradient $\boldsymbol{F}$. Specifically,

$$\boldsymbol{\sigma} = \frac{1}{\det \boldsymbol{F}} \boldsymbol{F}\boldsymbol{S}\boldsymbol{F}^{\top}, \tag{8.22}$$

where

$$\boldsymbol{F} = \begin{bmatrix} 1+u_{,x} & u_{,y} & u_{,z} \\ v_{,x} & 1+v_{,y} & v_{,z} \\ w_{,x} & w_{,y} & 1+w_{,z} \end{bmatrix}. \tag{8.23}$$

The Cauchy stress tensor is referenced in the global coordinate system, which does not have a clear physical meaning in case of large deformations. Therefore, corotational Cauchy stresses are computed on the deformed configuration using the rotation tensor, $\boldsymbol{R}$:

$$\hat{\boldsymbol{\sigma}} = \boldsymbol{R}^{\top} \boldsymbol{\sigma} \boldsymbol{R}. \tag{8.24}$$

The rotation tensor $\boldsymbol{R}$ is obtained by polar decomposition of the deformation gradient [208].

8.2 Numerical Results

In this section, to demonstrate the capabilities of the proposed geometrically nonlinear Unified Formulation, based on Serendipity Lagrange expansions (UF-SLE), various benchmark problems are addressed. The first example presents the large deflection analysis of an isotropic cantilever beam in bending. In the second, highly flexible, laminated composite plate strips are considered and their nonlinear responses are compared with 3D FE solutions and other numerical results available in the literature. In both cases, attention is focused on highlighting the ability of the UF-SLE model to account for complex nonlinear 3D stress states. In the third example, the postbuckling response of a single-stringer panel under axial compression is compared with experimental results from the literature. The 3D stress analysis capabilities of the present model are exploited for predicting the onset of failure in the panel.

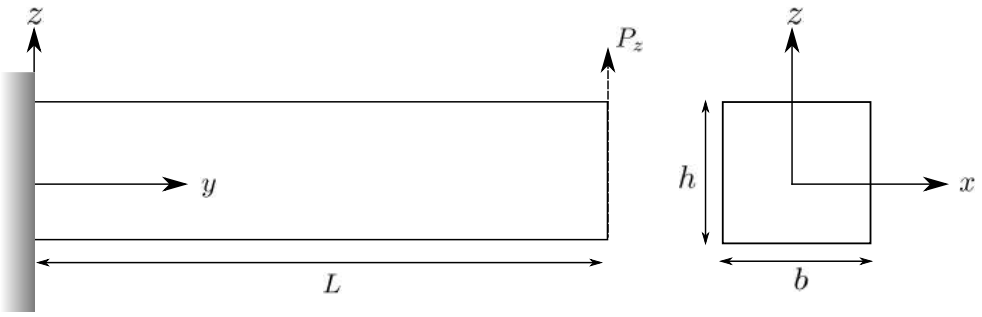

Figure 8.2: Square cross-section cantilever beam with applied tip load.

8.2.1 Isotropic Beam

Consider a clamped-free, square cross-section beam of length $L = 1$ m, height and width $h = b = 0.05$ m, subjected to a bending load, P_z, applied at the free end ($y = L$), as shown in Figure 8.2. The Young's modulus, E, and Poisson's ratio, ν, of the constituent material, which is isotropic, are 2.9 GPa and 0.33, respectively. The non-dimensional quantities

$$\bar{u}_z = \frac{u_z}{L}, \qquad \bar{u}_y = \frac{u_y}{L}, \qquad \bar{P} = \frac{P_z L^2}{EI}, \tag{8.25}$$

are defined as metrics to benchmark the results, where u_z indicates vertical deflection, u_y indicates axial deflection and I is the second moment of area of the square cross-section.

In the present UF-SLE model, the beam structure is discretised using 20 B4 (four-noded cubic Lagrange) elements along its length and 1 SL5 (fifth-order Serendipity Lagrange) element in the cross-section. A 3D FE analysis, performed with commercial finite element software ANSYS, is used as a reference for validation, where the beam is discretised using 10,000 `SOLID186` (3D 20-noded) elements to yield converged results. With the proposed model convergence is achieved with 4,209 degrees of freedom (DOFs), whereas in case of ANSYS, 139,623 DOFs are required. Figure 8.3 shows the normalised load-deflection curve, where the vertical and axial deflection components, $\bar{u}_z$ and $\bar{u}_y$, are measured at the centre of the tip of the beam. In addition to the 3D FE solution, an exact analytical solution given by Bisshopp and Drucker [5], and experimental results obtained by Kemper [6], are used to validate the UF-SLE model. From the plots, it is evident that the nonlinear equilibrium curve obtained using the UF-SLE model is in excellent agreement with the 3D FE solution. The curves slightly differ with the analytical solution, but a better correlation is observed with the experimental results.

Furthermore, to show the capability of the model in capturing stresses accurately, the through-thickness distribution of the axial normal, $\hat{\sigma}_{yy}$, and transverse shear, $\hat{\tau}_{yz}$, stresses, at two different load steps ($\bar{P}/2$ and $\bar{P}$), are shown in Figure 8.4. The stress results obtained are compared with the 3D FE solution. The nonlinear UF-SLE model, which employs the three-dimensional Green-Lagrange strain/displacement relation within a total Lagrangian approach, is able to replicate the 3D FE model with fewer of DOFs.

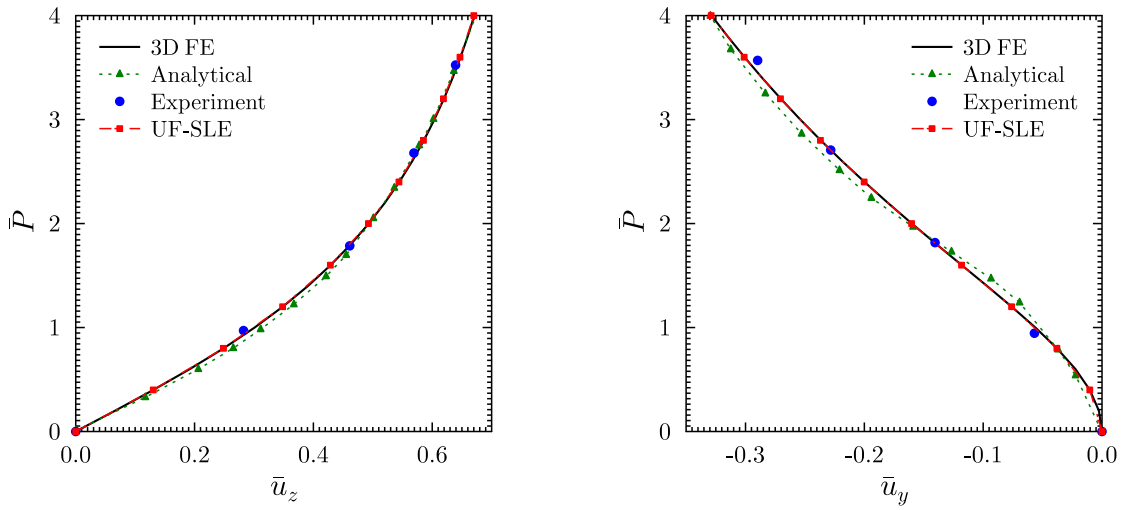

(a) $\hat{\sigma}_{yy}$ at $(0, L/2, z)$ (b) $\hat{\tau}_{yz}$ at $(0, L/2, z)$

Figure 8.3: Load-deflection curve at the tip centre of a square cross-section isotropic beam. Analytical and experimental results are taken from [5] and [6], respectively.

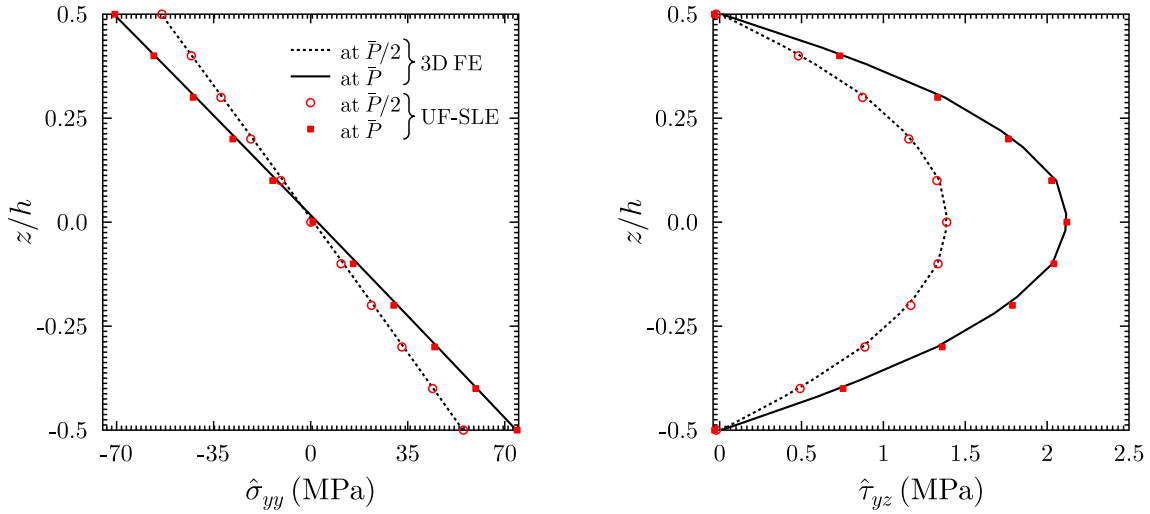

(a) $\hat{\sigma}_{yy}$ at $(0, L/2, z)$ (b) $\hat{\tau}_{yz}$ at $(0, L/2, z)$

Figure 8.4: Through-thickness distribution of the axial normal and transverse shear stresses at beam's mid-span for two load steps, $\bar{P}/2$ and $\bar{P}$.

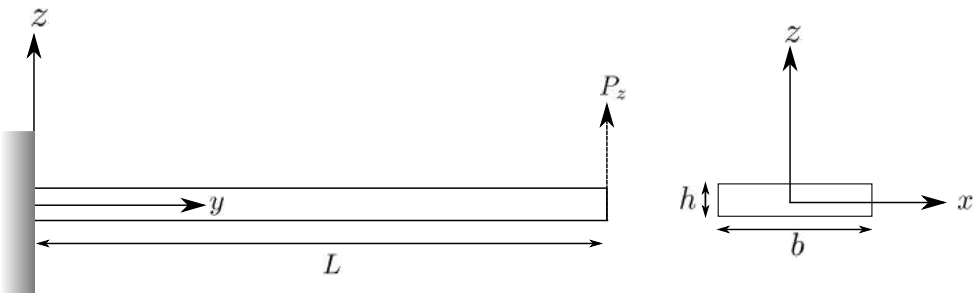

Figure 8.5: Thin plate strip subjected to a bending load

8.2.2 Thin Composite Plate Strip

In this section, a multi-layered composite plate strip is considered, as shown in Figure 8.5. The length, width and thickness of the strip are $L = 10$ m, $b = 1$ m and $h = 0.1$ m, respectively. The plate strip is clamped at the end $y = 0$ and is subjected to a bending load, $P_z = 5\ N$, applied uniformly across the section at the end $y = L$. The material properties of the orthotropic laminae, considered herein are:

$E_x = 0.3$ MPa	$E_y = 1$ MPa	$E_z = 0.3$ MPa
$G_{yz} = 0.15$ MPa	$G_{xz} = 0.12$ MPa	$G_{xy} = 0.15$ MPa
$\nu_{yz} = 0.25$	$\nu_{xz} = 0.25$	$\nu_{xy} = 0.075$.

Four different layups are used: [0/90/0], [90/0/90], [-45/45/-45/45], [30/-60/-60/30]. In order to decide the number of beam and cross-section elements employed in the UF-SLE model, a mesh convergence analysis was performed. For converged deflection and normal stress responses, 40 B4 elements along the y-direction and 1 SL5 (fifth-order expansion) element per layer in the cross-section proved sufficient. However, higher fidelity is required for nonlinear transverse shear stresses and, therefore, 3 SL8 (eighth order expansion) elements per layer were required for the cross-section. For the sake of brevity, only converged results are presented here.

The nonlinear load-deflection curve (P_z vs u_z) at the plate's tip centre $(0, L, 0)$, for the different lamination schemes, is plotted in Figure 8.6. The present results are compared with those obtained by performing a 3D FE analysis in ANSYS and also with the reference solution given by Payette & Reddy [7] using a seven-parameter, spectral/hp shell finite element. As expected, the stacking sequence [90/0/90] is the most flexible while [0/90/0] is the most stiff, out of all of the stacking sequences analysed herein.

From the load-deflection curve (Figure 8.6), it is evident that the examples considered in this section behave nonlinearly. Solving large-deflection problems can be cumbersome, especially if accurate stress fields are to be measured. In order to test the suitability of the UF-SLE model for predicting the nonlinear stress response accurately, the predicted distributions of axial normal stress, $\hat{\sigma}_{yy}$, and transverse shear stress, $\hat{\tau}_{yz}$, are compared with 3D FE solutions. Figures 8.7

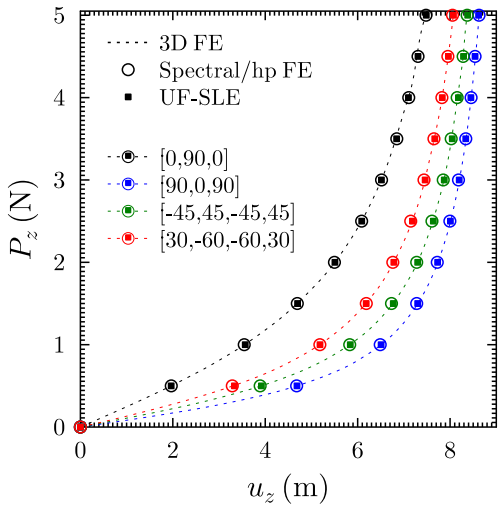

Figure 8.6: Load-deflection curve at the tip centre $(0, L, 0)$ of laminated plate strips. Spectral/hp FE results are taken from [7].

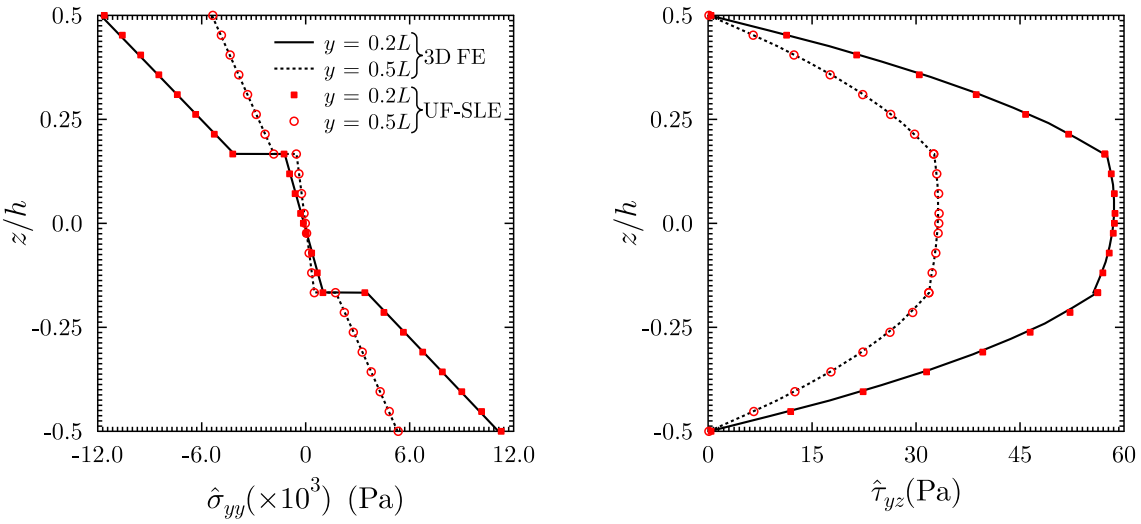

(a) $\hat{\sigma}_{yy}$ at $(0, L/5, z)$ and $(0, L/2, z)$

(b) $\hat{\tau}_{yz}$ at $(0, L/5, z)$ and $(0, L/2, z)$

Figure 8.7: Through-thickness distribution of the axial normal and transverse shear stresses at $y = 0.2L$ and $0.5L$, measured from the clamped end, for composite plate strip with layup [0/90/0].

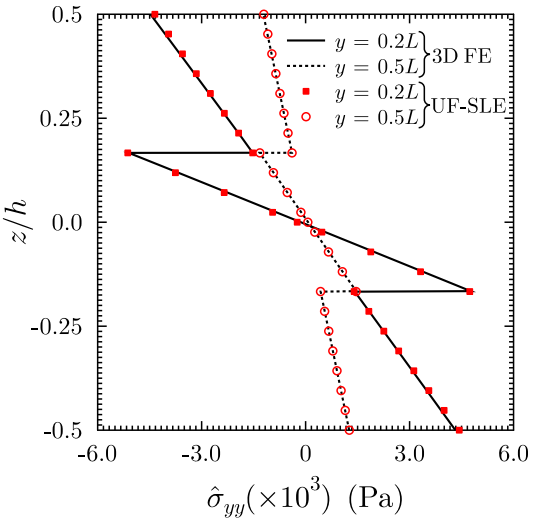

(a) $\hat{\sigma}_{yy}$ at $(0, L/5, z)$ and $(0, L/2, z)$

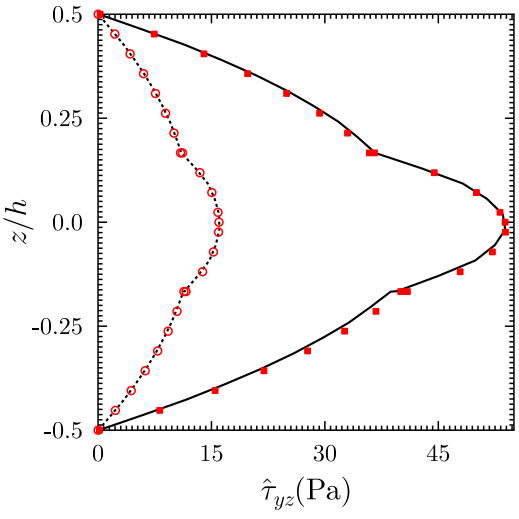

(b) $\hat{\tau}_{yz}$ at $(0, L/5, z)$ and $(0, L/2, z)$

Figure 8.8: Through-thickness distribution of the axial normal and transverse shear stresses at $y = 0.2L$ and $0.5L$, measured from the clamped end, for composite plate strip with layup [90/0/90].

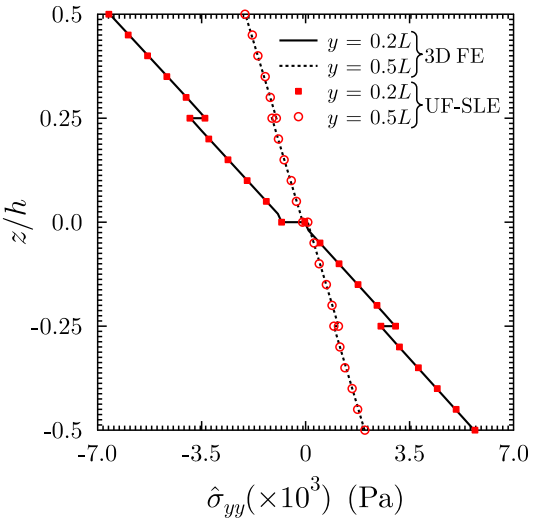

(a) $\hat{\sigma}_{yy}$ at $(0, L/5, z)$ and $(0, L/2, z)$

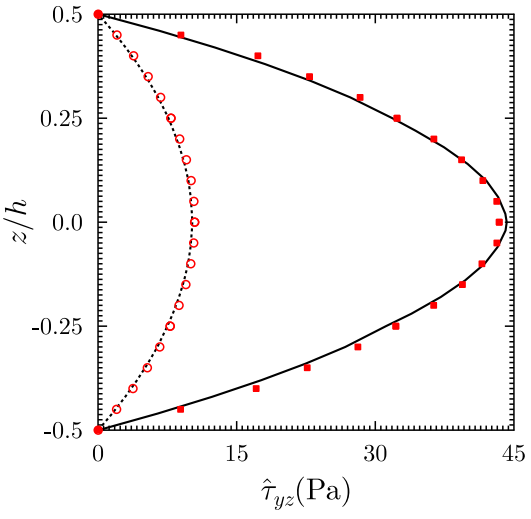

(b) $\hat{\tau}_{yz}$ at $(0, L/5, z)$ and $(0, L/2, z)$

Figure 8.9: Through-thickness distribution of the axial normal and transverse shear stresses at $y = 0.2L$ and $0.5L$, measured from the clamped end, for composite plate strip with layup [-45/45/-45/45].

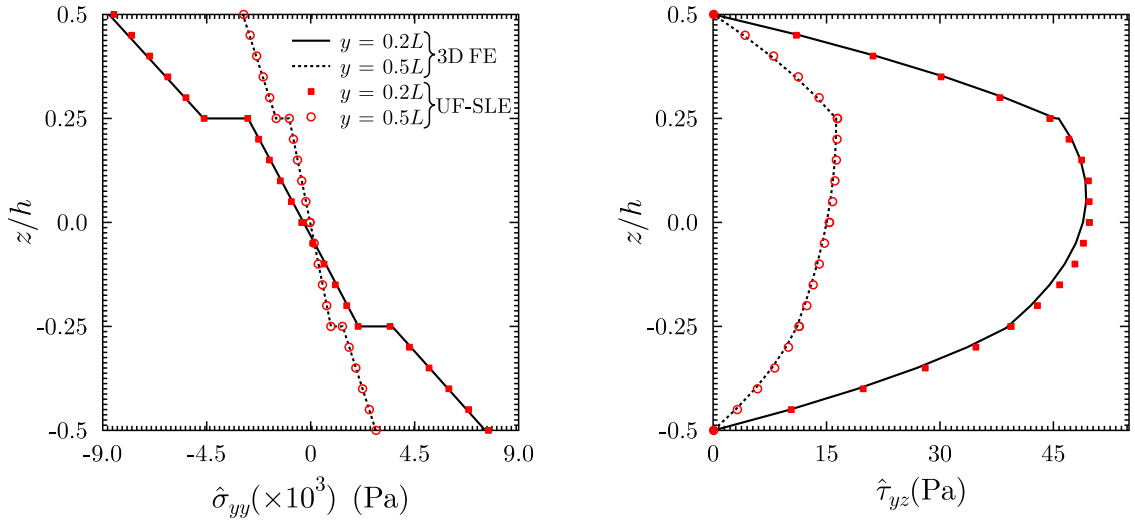

(a) $\hat{\sigma}_{yy}$ at $(0, L/5, z)$ and $(0, L/2, z)$

(b) $\hat{\tau}_{yz}$ at $(0, L/5, z)$ and $(0, L/2, z)$

Figure 8.10: Through-thickness distribution of the axial normal and transverse shear stresses at $y = 0.2L$ and $0.5L$, measured from the clamped end, for composite plate strip with layup [30/-60/-60/30].

to 8.10 show an excellent agreement between the two models, where the through-thickness stress distribution, computed at two different locations along the structure's length ($y = 0.2L$ and $0.5L$), are plotted for all the layups considered herein. The benefit of using the UF-SLE model is the ability to tune its fidelity by changing the order of expansion, as opposite to remeshing. As mentioned previously, to obtain the stress response of Figures 8.7 to 8.10, an eighth order expansion model is employed. This high-order model is computationally expensive (with ~0.15 million DOFs), but it is still preferable to the ANSYS solution, which requires 102,000 20-noded brick elements and ~1.3 million DOFs.

8.2.3 Composite Stiffened Panel

In this section, the proposed geometrically nonlinear UF-SLE model is employed for predicting the onset of failure in a single-stringer composite panel subjected to compression. This example is adapted from the work done by Bisagni *et al.* [8, 132, 209], where experimental tests were conducted on single-stringer compression (SSC) specimens and a shell-based FE model with damage capabilities was developed to predict the panel's postbuckling response, and the damage evolution from initiation to collapse. In the present study, the UF-SLE model is assessed by evaluating its performance in predicting the postbuckling response of the SSC specimen. Moreover, the model's capability to evaluate 3D stress fields accurately is exploited for predicting damage initiation.

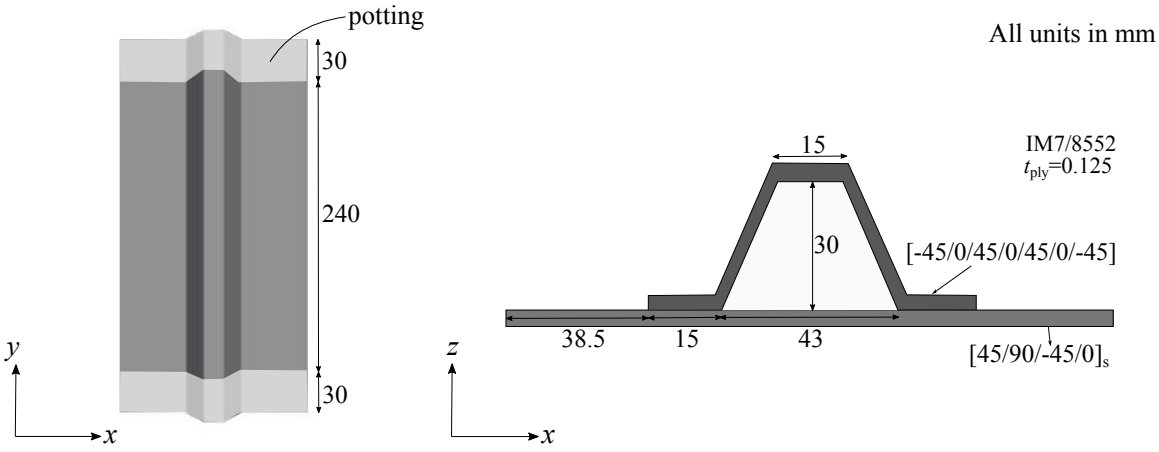

Figure 8.11: Single-stringer composite stiffened panel: configuration and dimensions.

Table 8.1: Mechanical properties of the IM7/8552 graphite-epoxy composite [1].

E_x	E_y	E_z	G_{yz}	G_{xz}	G_{xy}	ν_{yz}	ν_{xz}	ν_{xy}
(GPa)								
9.08	150	9.08	5.6	2.8	5.6	0.32	0.5	0.019

Table 8.2: Material strength values (in MPa) of the IM7/8552 composite [1].

Intralaminar							Interlaminar	
ST_{11}	SC_{11}	ST_{22}	SC_{22}	SS_{12}	SS_{13}	SS_{23}	ST_{33}	SS_{33}
2560	1590	73	185	90	90	57	63	90

The geometrical configuration and dimensions of the single-stringer hat specimen are shown in Figure 8.11. Both the skin and the stringer are made from IM7/8552 graphite-epoxy material, with mechanical properties and strength values as shown in Tables 8.1 and 8.2, respectively. The skin consists of an 8-ply quasi-isotropic laminate with a stacking sequence of $[45/90/-45/0]_s$, resulting in the total thickness of 1 mm. The stringer comprises of 7 plies with symmetric stacking sequence $[-45/0/45/0/45/0/-45]$, which results in a total thickness of 0.875 mm. The displacement constraints imposed at the two ends of the SSC specimen, using potting (by means of two 30 mm long tabs cast), ensure a uniform distribution of the load during the experiment [8]. To mimic this condition in the UF-SLE model, all the nodes within the potting region (refer to Figure 8.11) are fixed at one end (between $y = 0$ and $y = 30$ mm) and are allowed to move only in the longitudinal direction at the opposite end (between $y = 270$ mm and $y = 300$ mm). The specimen is subjected to a uniformly distributed compressive load $P = 41$ kN, applied to the end $y = 300$ mm.

To obtain the nonlinear static response of the SSC specimen, in the UF-SLE model, the

cross-section is discretised with 195 SL5 (fifth-order expansion) elements, while 10 B4 elements are employed in the longitudinal direction. This discretisation and cross-sectional expansion results in a total of 234,825 DOFs, which guaranty convergence. Figure 8.12 shows the load-displacement curve obtained with the UF-SLE model, which agrees well with the shell-based FE solution. The structural response is also compared with the experimental results. It can be seen that the experimental load-displacement curve exhibits softer behaviour than the numerical predictions. As discussed in [8], one possible reason for this behaviour could be the nonlinearity of the compression modulus E_y, which is not taken into account in either numerical model. Another reason for this discrepancy could be the difference between the specimen's actual and predicted stiffness values, as the compressive stiffness and strength of carbon composites are notoriously difficult to measure and length-scale dependent.

For further comparison and verification of the present modelling approach, Figure 8.13 shows the out-of-plane displacement response at different load levels. Up to an applied load of 2 kN (Point A), the structure exhibits a quasi-linear response with a single-wave out-of-plane deformation of the skin. The first buckling load (Point B) corresponds to a three half-wave mode and affects the skin only. The buckling load is predicted to be 7.8 kN by the UF-SLE model and 7.5 kN by the shell model (see [8]). Progressing with the UF-SLE model to the load level of 24.5 kN (Point C), shallow buckles become visible on the two webs of the stringer. This load corresponds to stringer buckling. Similar out-of plane deformation with the shell FE model is observed at 23.5 kN. Upon further loading, at 39.5 kN, the out-of-plane displacements are maximum. This load triggers failure initiation. Figure 8.13(e) shows the comparison of the predicted and measured deformation shapes immediately before collapse. It is observed that the number of half-waves in both the skin and the stringer, as predicted by the UF-SLE model, correlates well with the experimental observation and the shell FE solution.

Figure 8.14(a) and 8.14(b) show the crippling and delamination modes of failure in the test specimen. The crippling of the stringer is characterised by a fracture that travels across the stringer width. Different modes of crippling of the stringer were obtained for different specimens. Figure 8.14(a) shows a specimen in which the fracture is oriented at 45° in the crown and in the webs, and at 90° in the flanges. Whereas, the specimen shown in Figure 8.14(b) exhibits a fracture at approximately the mid-length of the specimen that runs across the stringer at a 90° angle. In most of the specimens, fibre pullouts were identified at various locations along the stringer and no fibre damage was recorded in the skin. The second major failure observed is skin/stringer separation. The delaminated surfaces remain within the interface between skin and stiffener and crack jumping is not apparent. In order to predict the damage initiation load and mode, the 3D stress fields obtained by the UF-SLE model, at various load levels in the post-buckling regime, are plugged in the Hashin 3D failure criteria [210] for the prediction of ply failure, and in the mixed mode quadratic criteria [211] to determine the onset of delamination. The failure indices are calculated using the stress state in the material coordinate system (1,2,3) by:

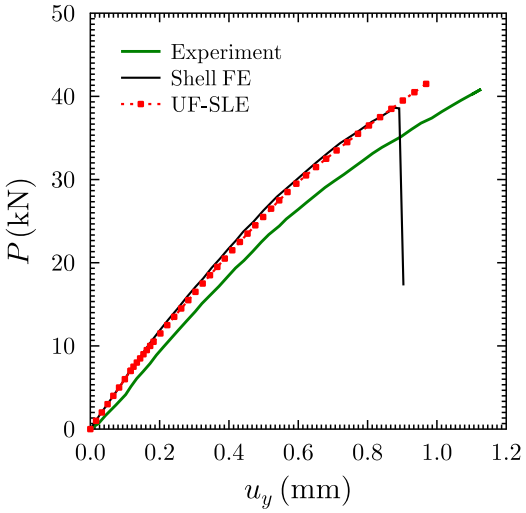

Figure 8.12: Load-displacement curve for the single-stringer composite panel subjected to compression. Experiment and Shell FE results are taken from [8].

1. Fibre Tension for $\sigma_{11} \geq 0$:

$$\left(\frac{\sigma_{11}}{ST_{11}}\right)^2 + \left(\frac{\sigma_{12}^2 + \sigma_{13}^2}{SS_{12}^2}\right) \geq 1, \tag{8.26}$$

2. Fibre Compression for $\sigma_{11} < 0$:

$$\left(\frac{\sigma_{11}}{SC_{11}}\right)^2 \geq 1, \tag{8.27}$$

3. Matrix Tension for $\sigma_{22} + \sigma_{33} \geq 0$:

$$\left(\frac{\sigma_{22} + \sigma_{33}}{ST_{22}}\right)^2 + \left(\frac{\sigma_{23}^2 - \sigma_{22}\sigma_{33}}{SS_{23}^2}\right) + \left(\frac{\sigma_{12}^2 + \sigma_{13}^2}{SS_{12}^2}\right) \geq 1, \tag{8.28}$$

4. Matrix Compression for $\sigma_{22} + \sigma_{33} < 0$:

$$\left[\left(\frac{SC_{22}}{2SS_{23}}\right)^2 - 1\right]\left(\frac{\sigma_{22} + \sigma_{33}}{SC_{22}}\right) + \left(\frac{\sigma_{22} + \sigma_{33}}{2SS_{23}}\right)^2 + \left(\frac{\sigma_{23}^2 - \sigma_{22}\sigma_{33}}{SS_{23}^2}\right) + \left(\frac{\sigma_{12}^2 + \sigma_{13}^2}{SS_{12}^2}\right) \geq 1, \tag{8.29}$$

5. Delamination for $\sigma_{33} \geq 0$:

$$\left(\frac{\sigma_{33}}{ST_{33}}\right)^2 + \left(\frac{\sigma_{23}}{SS_{33}}\right)^2 + \left(\frac{\sigma_{13}}{SS_{33}}\right)^2 \geq 1, \tag{8.30}$$

where ST, SC and SS denotes tensile strength, compressive strength and shear strength of the material, σ_{ij} terms denote the components of the stress tensor in the material coordinate system, and subscripts 1, 2 and 3 represents the fibre direction, the in-plane direction orthogonal to fibres, and the direction normal to the layer plane, respectively.

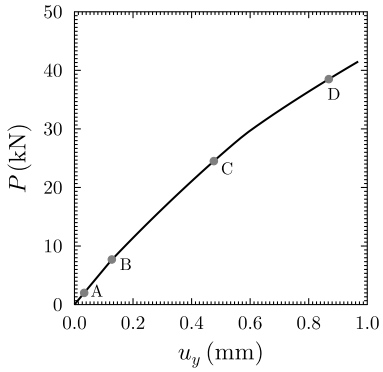

(a) Load-axial displacement curve predicted by the UF-SLE model

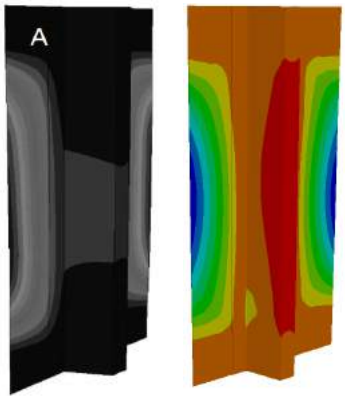

(b) Response predicted at 2 kN. Shell FE (left) and UF-SLE (right)

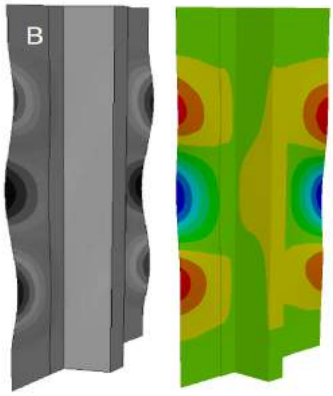

(c) Skin buckling: 7.5 kN (Shell FE, left) and 7.8 kN (UF-SLE, right)

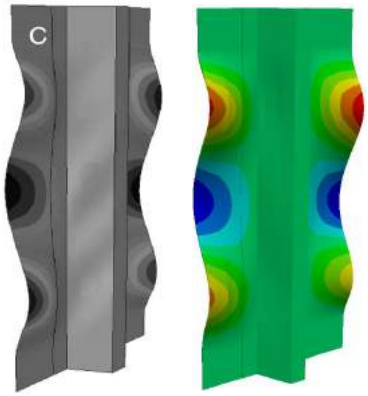

(d) Stringer buckling: 23.5 kN (Shell FE, left) and 24.5 kN (UF-SLE, right)

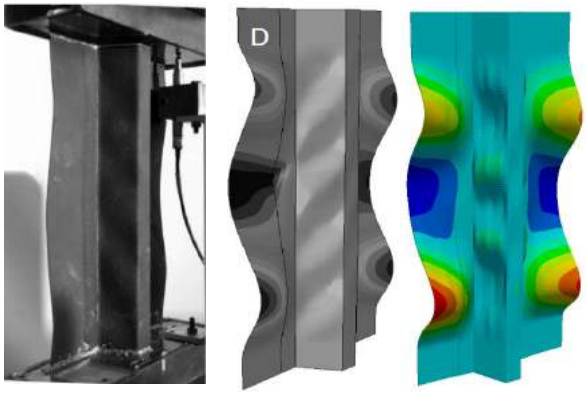

(e) Before collapse: 41 kN (Experiment, left), 39 kN (Shell FE, centre) and 39.5 kN (UF-SLE, right)

Figure 8.13: Out of plane displacement response predicted by the UF-SLE model at different load levels compared to those obtained by the Shell FE model and Experiment [8].

The intralaminar damage of the fibre and the matrix is evaluated in terms of failure indices using equations (8.26) to (8.29). It is observed that at a load level of 36 kN, transverse tension and in-plane shear cause matrix cracking at different locations along the stringer. Although, transverse matrix cracking is considered as the benign mode of failure, that corresponds to a small reduction in the overall stiffness of the structure which can affect the evolution of damage. However, the present model does not account for any degradation in the material stiffness property, and is used herein for first-ply failure analysis. With a further increase in applied load, the areas with matrix damage become more extensive and starts to extend into the skin. At a load level of 39.5 kN, fibre damage initiation is observed and fractures are predicted at the corners between the stringer webs and the corresponding flanges, as shown in Figure 8.14(c). Also, the matrix damage contour is shown in Figure 8.14(d) which is highly diffused. These failure contour plots indicate fibre-matrix debonding at discrete locations along the stringer, which can further cause fibre pullouts in these regions as was observed in the experiment.

The transverse stress fields obtained by the UF-SLE model are used for predicting the onset of delamination using Eq. (8.30). Figure 8.14(e) shows the delamination index contour obtained at the applied load of 39.5 kN. From the contour plot, the skin and the stringer separation (red fringe) is likely to initiate from: (i) two different locations along the length, at the stringer flange and skin interface, present on either side of the stringer; and (ii) from the the mid-length in the region around the stringer web and flange junction. This delamination prediction by the present model is in close agreement with experiments. Although, with current capabilities and using 3D stress fields, it is difficult to predict the crippling fracture of the specimen as its accurate prediction requires progressive failure models.

To conclude it is important to remark on the computational efficiency of the UF-SLE model compared to the reference shell FE model, which can be estimated by comparing the degrees of freedom required for convergence. The approximate number of DOFs required by the shell model is 710,000, which is three times more than that required by the present model. Moreover, unlike shell elements, Serendipity Lagrange elements are capable of predicting 3D stress fields. In contrast, obtaining 3D stress fields using a FE model require brick elements, and solving such high-fidelity model is cumbersome and expensive. Thus, the proposed model offers significant computational benefit, over shell FE model, together with solid-like FE capabilities.

8.3 Conclusions

Previous chapters highlighted the ability of the Unified Formulation, based on Serendipity Lagrange expansions (UF-SLE), to capture localised three-dimensional (3D) stress fields accurately, in isotropic, constant- and variable-stiffness, laminated composite and sandwich structures. The hierarchical nature of the Serendipity Lagrange expansions allows the fidelity of the model to be tuned, such that low-fidelity and high-fidelity models can be used concurrently to assess

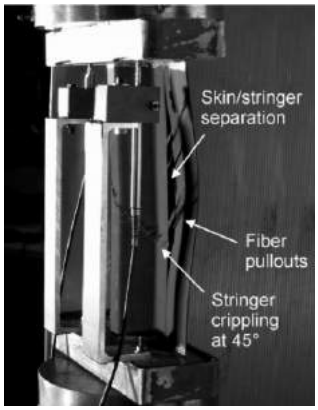

(a) Experimental failure mode

(b) Experimental collapse mode

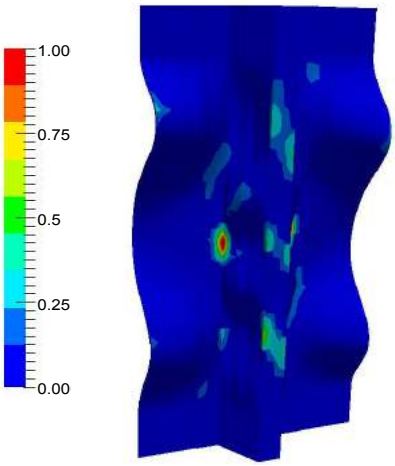

(c) Fibre damage

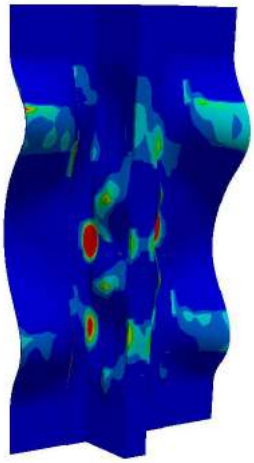

(d) Matrix damage

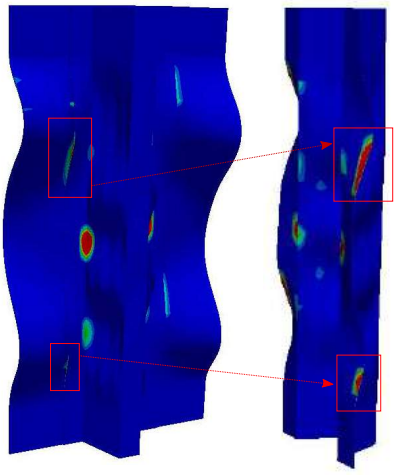

(e) Onset of delamination

Figure 8.14: Experimental [8] and predicted numerical failure modes of a single-stringer composite panel.

global response and 3D stresses. In this chapter, geometric nonlinear modelling capabilites are incorporated within the UF-SLE model and then employed for the large deflection analysis of isotropic and laminated composite structures. The nonlinear governing equations and the finite element approximation are formulated using the principle of virtual work. All classical material stiffness terms are considered in the formulation, thereby making it complete and suitable for analysing fully anisotropic structures. The explicit form of the tangent stiffness matrix, in terms of the fundamental nuclei, is provided in a clear concise notation and the benefit of writing these expressions in such a way is discussed. These expressions are general, meaning they can be adapted, as they are independent of the expansion function used in the cross-section, within the Unified Formulation framework. The nonlinear structural response obtained by the UF-SLE model is shown to match experimental data, shell and solid Finite Element (FE) solutions and numerical results available in the literature. The nonlinear 3D stress fields, evaluated using the present model, are used for predicting damage initiation in a stiffened composite structure subjected to compression. The results indicate a good correlation with experimental data in terms of load-displacement response in the pre- and post-buckling range. The model also offers insight on the intralaminar failure mechanisms and correctly predicts the initiation of the separation of the skin from the stringer as obtained experimentally. Finally, the proposed model offers computational benefits over conventional FE models, while maintaining similar levels of accuracy. This study provides confidence in using advanced damage modelling capabilities within the present formulation, and together with its efficiency and accurate stress predicting capability, can be a useful tool for structural analysis.

CHAPTER 9

MODELLING NON-PRISMATIC AND CURVED BEAM-LIKE STRUCTURES

Modelling tapered and curved, 3D beam-like structures can be complex, especially if large deformations are expected. The nonlinear 3D finite element method is commonly used, although the approach is computationally expensive. In this chapter, we extend the modelling approach based on the Unified Formulation, described in the previous chapters, to account for non-prismatic and curved beam-like structures. In the classical Unified Formulation, the kinematic description of a beam structure builds upon two shape functions, one representing its axis and other its cross-section. This approach accurately predicts 3D displacement and stress fields and is computationally efficient compared with 3D FE methods. However, its modelling capabilities are limited to prismatic structures. As a novelty, we propose to use a separate set of functions to exactly describe the structural geometry in addition to its kinematic description. As a result, the 3D Jacobian or the local curvilinear basis vectors, obtained from the geometry description, are used within the classical Unified Formulation to represent non-prismatic and curved beam structures as described in Section 9.1. The proposed model is benchmarked against commercial 3D FE analysis, as well as analytical models available in the literature, by means of linear static analyses of tapered isotropic and sandwich structures presented in Sections 9.2.1 and 9.2.2. Significant computational efficiency gains over 3D finite elements are observed for similar levels of accuracy. Furthermore, to show the enhanced capabilities of the present formulation, in Section 9.2.3, geometric non-linear behaviour of corrugated structures under tensile loading is presented. The results obtained by the present model are shown to match well with experimental data.

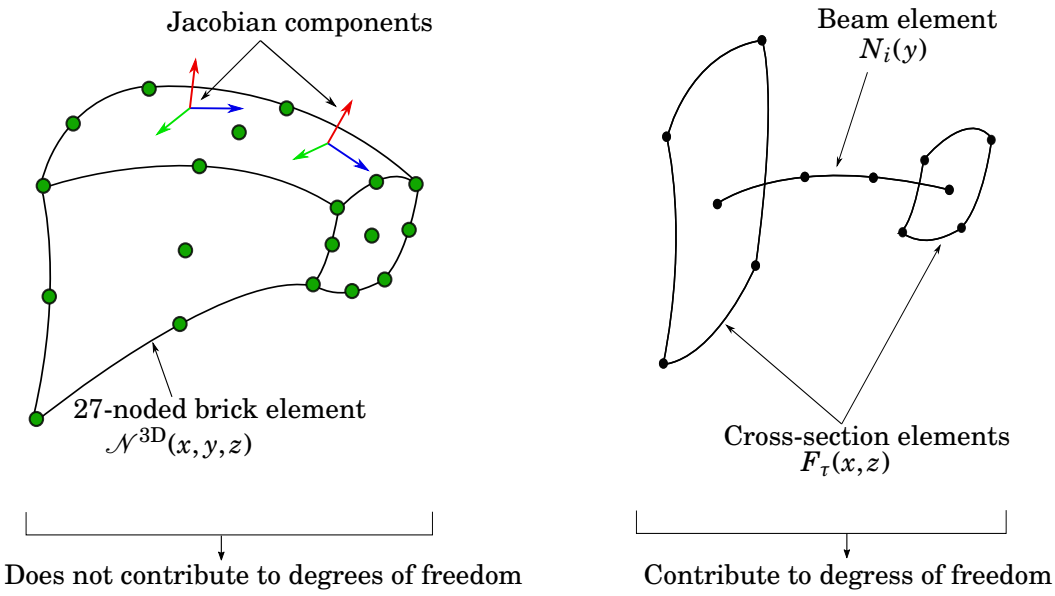

(a) 3D geometry description

(b) Displacement field approximation

Figure 9.1: Geometric and kinematic description used for modelling non-prismatic beam-like structures.

9.1 3D Mapping via Jacobian Transformation

When dealing with complex geometries the correct geometrical description is of fundamental importance. As discussed in Section 8.1.2, the Unified Formulation employs two shape functions, $F_\tau(x,z)$ and $N_i(y)$, to describe the structure's kinematics as given by equation (8.9). The cross-section expansion functions, F_τ, are defined on the master element in $\Xi^{2D} = \{(\alpha,\beta) \in \mathbb{R}^2 : -1 \leq \alpha \leq 1, -1 \leq \beta \leq 1\}$, while the shape functions along the beam axis, N_i, are defined in $\Xi^{1D} = \{(\eta) \in \mathbb{R} : -1 \leq \eta \leq 1\}$. These functions are then mapped onto (x,y,z), *i.e.* the position in global coordinates using the Jacobian of transformation and their derivatives are given by

$$\begin{Bmatrix} N_i F_{\tau,x} \\ N_{i,y} F_\tau \\ N_i F_{\tau,z} \end{Bmatrix} = \underbrace{\begin{bmatrix} x_{,\alpha} & y_{,\alpha} & z_{,\alpha} \\ x_{,\eta} & y_{,\eta} & z_{,\eta} \\ x_{,\beta} & y_{,\beta} & z_{,\beta} \end{bmatrix}^{-1}}_{\boldsymbol{J}^{3D}} \begin{Bmatrix} N_i F_{\tau,\alpha} \\ N_{i,\eta} F_\tau \\ N_i F_{\tau,\beta} \end{Bmatrix}, \tag{9.1}$$

where $\boldsymbol{J}^{3D}$ is a 3×3 Jacobian matrix, which accounts for the geometry description and its components $(x_{,\alpha}, y_{,\alpha}, z_{,\alpha})$, $(x_{,\eta}, y_{,\eta}, z_{,\eta})$ and $(x_{,\beta}, y_{,\beta}, z_{,\beta})$ represent local curvilinear basis vectors, *i.e.* tangent, axial and normal directions, at any point in the structure.

The components of the Jacobian matrix are calculated using derivatives of shape functions with respect to the local coordinates α, η, β and global coordinates of element nodes. Following the classical Unified Formulation, if shape functions $F_\tau(\alpha,\beta)$ and $N_i(\eta)$ are used to describe the

geometry, then the components of $\boldsymbol{J}^{3D}$ are evaluated as

$$\begin{aligned} x_{,\alpha} &= F_{\tau,\alpha} x_\tau, \qquad y_{,\alpha} = N_{i,\alpha} y_i, \qquad z_{,\alpha} = F_{\tau,\alpha} z_\tau, \\ x_{,\eta} &= F_{\tau,\eta} x_\tau, \qquad y_{,\eta} = N_{i,\eta} y_i, \qquad z_{,\eta} = F_{\tau,\eta} z_\tau, \\ x_{,\beta} &= F_{\tau,\beta} x_\tau, \qquad y_{,\alpha} = N_{i,\beta} y_i, \qquad z_{,\beta} = F_{\tau,\beta} z_\tau. \end{aligned} \tag{9.2}$$

Clearly, the components $y_{,\alpha}$, $y_{,\beta}$, $x_{,\eta}$ and $z_{,\eta}$ of the Jacobian matrix becomes zero. As a result, only prismatic structures can be modelled. This procedure of evaluating the Jacobian matrix is followed in all the research published using the Unified Formulation [44, 52, 140, 146–149, 176–181, 212–214], and 2D and 1D integrals, over the cross-section and along the beam, are performed separately by employing 2D and 1D Jacobians given by

$$\boldsymbol{J}^{2D} = \begin{bmatrix} x_{,\alpha} & z_{,\alpha} \\ x_{,\beta} & z_{,\beta} \end{bmatrix} \qquad \text{and} \qquad \boldsymbol{J}^{1D} = \begin{bmatrix} y_{,\eta} \end{bmatrix}. \tag{9.3}$$

To overcome the above limitation and to model general solid-like structures (*e.g.* non-prismatic or curved beams), we propose to use an additional set of functions for geometry description. These could be CAD basis functions, such as B-splines or Non-Uniform Rational B-Splines (NURBS), that guarantee an exact geometric representation or could be a higher-order Lagrange functions that approximately describes the geometry. On the other hand, the Unified Formulation functions (F_τ and N_i) are used, in the usual manner, for approximating displacement fields. To demonstrate the validity of the proposed technique, in the present work, we use 27-noded brick elements, with 3D Lagrange shape functions, $\mathcal{N}^{3D}(x,y,z)$, to describe the geometry and to evaluate local curvilinear basis vectors (or Jacobian matrix components) at each point in the structure, as shown in Figure 9.1. Following the above procedure, the components of $\boldsymbol{J}^{3D}$ are evaluated as

$$\begin{aligned} x_{,\alpha} &= \mathcal{N}^{3D}_{,\alpha} x_\tau, \qquad y_{,\alpha} = \mathcal{N}^{3D}_{,\alpha} y_i, \qquad z_{,\alpha} = \mathcal{N}^{3D}_{,\alpha} z_\tau, \\ x_{,\eta} &= \mathcal{N}^{3D}_{,\eta} x_\tau, \qquad y_{,\eta} = \mathcal{N}^{3D}_{,\eta} y_i, \qquad z_{,\eta} = \mathcal{N}^{3D}_{,\eta} z_\tau, \\ x_{,\beta} &= \mathcal{N}^{3D}_{,\beta} x_\tau, \qquad y_{,\alpha} = \mathcal{N}^{3D}_{,\beta} y_i, \qquad z_{,\beta} = \mathcal{N}^{3D}_{,\beta} z_\tau. \end{aligned} \tag{9.4}$$

Furthermore, it is important to note that, the proposed methodology requires integration, along the beam axis and over the cross-section, to be performed simultaneously. For instance, the first component of the fundamental nucleus of the tangent stiffness matrix (for a geometrically linear model) is given as follows [176]:

$$\begin{aligned} \boldsymbol{K}_T^{\tau s ij}(1,1) = &\int_V \bar{C}_{11} F_{\tau,x} F_{s,x} N_i N_j dV + \int_V \bar{C}_{16} F_{\tau,x} F_s N_i N_{j,y} dV + \int_V \bar{C}_{15} F_{\tau,x} F_{s,z} N_i N_j dV \\ &+ \int_V \bar{C}_{16} F_\tau F_{s,x} N_{i,y} N_j dV + \int_V \bar{C}_{66} F_\tau F_s N_{i,y} N_{j,y} dV + \int_V \bar{C}_{56} F_\tau F_{s,z} N_{i,y} N_j dV \\ &+ \int_V \bar{C}_{15} F_{\tau,z} F_{s,x} N_i N_j dV + \int_V \bar{C}_{56} F_{\tau,z} F_s N_i N_{j,y} dV + \int_V \bar{C}_{55} F_{\tau,z} F_{s,z} N_i N_j dV. \end{aligned} \tag{9.5}$$

The integrals are evaluated numerically by employing Gaussian Quadrature. The first term of Eq.(9.5) can be evaluated as

$$\begin{aligned}\int_V \bar{C}_{11} F_{\tau,x} F_{s,x} N_i N_j dV &= \int_{-1}^{1}\int_{-1}^{1}\int_{-1}^{1} \bar{C}_{11}\big(N_i F_{\tau,x}\big)\big(N_j F_{s,x}\big)|\boldsymbol{J}^{3D}|d\alpha\, d\eta\, d\beta \\ &= \sum_{l=1}^{l_{gp}}\sum_{k=1}^{k_{gp}}\sum_{m=1}^{m_{gp}} \bar{C}_{11}(\alpha_l,\eta_k,\beta_m)\big(N_i(\eta_k)F_{\tau,x}(\alpha_l,\beta_m)\big)\big(N_j(\eta_k)F_{s,x}(\alpha_l,\beta_m)\big)|\boldsymbol{J}^{3D}|w_l w_k w_m,\end{aligned} \tag{9.6}$$

where w_l, w_k and w_m are the weights related to the Gauss points α_l, η_k and β_m while l_{gp}, k_{gp} and m_{gp} are the number of Gauss points used; $\bar{C}_{11}(\alpha_l,\eta_k,\beta_m)$ is the material constant evaluated at a specific Gauss point; $|\boldsymbol{J}^{3D}|$ is the determinant of the Jacobian matrix.

In contrast, the traditional Unified Formulation approach splits the beam and the cross-sectional integration as follows:

$$\begin{aligned}\int_V \bar{C}_{11} F_{\tau,x} F_{s,x} N_i N_j dV &= \bar{C}_{11}\int_{-1}^{1}\int_{-1}^{1} F_{\tau,x}F_{s,x}|\boldsymbol{J}^{2D}|d\alpha\, d\beta \int_{-1}^{1} N_i N_j |\boldsymbol{J}^{1D}|d\eta \\ &= \bar{C}_{11}\sum_{l=1}^{l_{gp}}\sum_{m=1}^{m_{gp}} F_{\tau,x}(\alpha_l,\beta_m)F_{s,x}(\alpha_l,\beta_m)|\boldsymbol{J}^{2D}|w_l w_m \sum_{k=1}^{k_{gp}} N_i(\eta_k)N_j(\eta_k)|\boldsymbol{J}^{1D}|w_k.\end{aligned} \tag{9.7}$$

Clearly, following Eq. (9.6), increases the stiffness matrix computational cost compared to the approach followed in Eq. (9.7), as the number of loops required for evaluating the integral increases from $(l_{gp}\times m_{gp}+k_{gp})$ to $(l_{gp}\times k_{gp}\times m_{gp})$. Nevertheless, performing the beam and the cross-sectional integration simultaneously and considering the 3D Jacobian matrix enhances the Unified Formulation modeling capabilities.

9.2 Numerical Results

In this section, the proposed UF-SLE model, with separate geometric and kinematic description, is assessed by means of static analyses of various non-prismatic and curved structures. The first example presents a linear static analysis of a tapered I-beam structure. In the second part, a tapered sandwich beam-like structure is considered and the effect of increasing taper angle on the 3D stress distribution is studied. In the third example, three corrugated structures of different corrugation amplitudes are considered and nonlinear force-displacement and stress responses obtained are compared with numerical and experimental results.

9.2.1 Tapered I-beam

The first assessment deals with the linear static analysis of a tapered I-beam structure, as shown in Figure 9.2, with dimensions given as follows

length, $L = 10,000$mm,	flange width, $b_f = 250$mm,	flange height, $h_f = 16$mm,
web width, $b_w = 6$mm,	web height, $h_w(0) = 900$mm,	web height, $h_w(L) = 100$mm.

The Young's modulus, E, and Poisson's ratio, ν, of the constituent material are 210 GPa and 0.3, respectively. The forces and moments acting on the beam ends are

$$V(0) = 100\text{kN}, \qquad M(0) = 700\text{kNm}.$$
$$V(L) = 100\text{kN}, \qquad M(L) = 300\text{kNm}.$$

The example is adapted from [9], which employs a planar non-prismatic beam model [156] with enhanced stress recovery, based on a rigorous generalisation of the Jourawsky theory. Solving this problem with the UF-SLE model requires two sets of input mesh. The first set consists of 27-noded brick elements that are used to discretise the tapered I-beam. Using this data and employing 3D Lagrange shape functions, the local curvilinear basis vectors (or 3D Jacobian) are computed at any desired point in the structure. The number of elements used to discretise the structure are not important, as long as they are sufficient to represent the geometry exactly. Moreover, these elements do not contribute to the structure's degrees of freedom (DOFs) or, in other words, to the computational cost. The second set has the Unified Formulation mesh data, *i.e.* cross-sectional discretisation and 1D beam elements. The tapered I-beam, considered herein, is discretised using 20 B4 (four-noded cubic Lagrange) elements along its length and 25 SL4 (fourth-order Serendipity Lagrange) elements in the cross-section (with 5 elements along the width and 2 elements through thickness in the flanges; and 5 elements along the height in the web). This discretisation and cross-sectional expansion results in a total of 42,273 DOFs, which guarantees convergence. A 3D FE analysis, performed with commercial finite element software ANSYS, is used as a reference for verification of the proposed UF-SLE model. We adopted a structured mesh of 400 × 3 × 20 for the flanges and a structured mesh of 400 × 50 × 4 for the web, resulting in the global count of 64,000 `SOLID186` (3D 20-noded) elements with 1,038,687 DOFs. Furthermore, for both models, UF-SLE and 3D FE, at the beam ends, the shear forces result from a uniform surface vertical shear stress over the web and the bending moment results from a uniform surface traction/compression over the flanges. Although, the applied forces satisfy equilibrium, just to avoid rigid body motion, we suppress u_x and u_z at $(0,0,\pm(h_f + h_w/2))$ and u_y at $(0,0,0)$.

Figures 9.3 to 9.5 show the through-thickness distribution of the axial normal, σ_{yy}, transverse shear, τ_{yz}, and von-Mises stress, σ_{eq}, measured in global coordinates, at several locations along the beam length. From the loading condition, it is observed that the bending moment is negative in the left hand part of the domain, vanishes at $y = 7000$ mm and becomes positive in the right hand part of the domain. This effect can be observed by looking at the through-thickness distribution of σ_{yy} between $y = 3000$ mm to $y = 9000$ mm, as shown in Figure 9.3. Moreover, the through-thickness distribution of τ_{yz} and σ_{eq} induced by the continuous variation of the beam height, different from that occurring in prismatic beams, is well captured by the proposed UF-SLE model. Furthermore, the results obtained are in an excellent agreement with 3D solutions. Overall comparison with the analytical solution proposed by [9] is good with slight discrepancies in shear and von-Mises stresses observed, particularly near the web-flange junction. The analytical

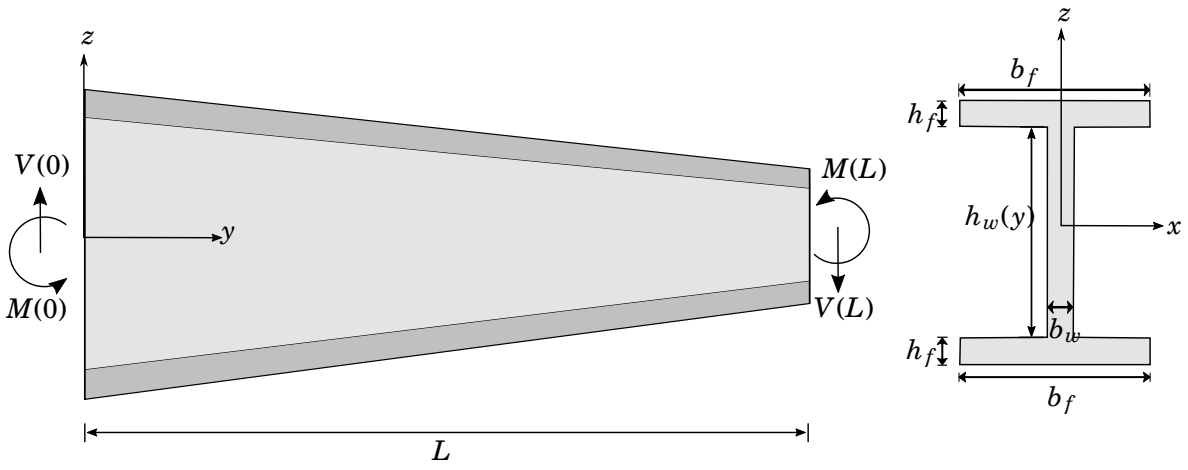

Figure 9.2: Tapered I-section beam: dimensions and load definition.

method assumes the plane stress condition. Moreover, it is derived from Jourawsky's theory and is unable to predict the response accurately in the vicinity of geometric discontinuity.

9.2.2 Tapered Sandwich Beam-like 3D Structure

In this section, a tapered sandwich beam-like structure of length, $L = 1000$ mm and width, $b = 300$ mm, is considered as shown in Figure 9.6. The beam is fixed at the end $y = 0$ and is subjected to a bending load, P_z, applied uniformly across the section at the end $y = L$. The facings of the sandwich composite are made of IM7/8552 graphite-epoxy material of thickness $h_f = 10$ mm, whose properties in the principal material coordinates are shown in Table 8.1. The core is assumed to be made of PVC foam with isotropic properties, Young's modulus, $E = 100$ MPa and shear modulus, $G = 38.5$ MPa. The core thickness, $h_c(0) = 300$ mm, varies linearly along the beam length depending on the taper angle, ϕ.

The finite element analysis is performed using the proposed UF-SLE model. The beam is discretised with 20 B4 elements along its length, with node distribution following Chebyshev biased mesh, as described in Section 3.3. This distribution in the longitudinal direction accurately captures the boundary layer effect, induced by the clamped support. The initial cross-section (at $y = 0$) is discretised with 3 SL5 (fifth-order Serendipity Lagrange) elements (with one element each for outer facings and one for the core). This discretisation and order of expansion results in 10,431 DOFs. In addition, 27-noded brick elements are used to describe the 3D tapered geometry and to evaluate local curvilinear basis vectors required during the analysis. Four different sandwich structures, with taper angle $\phi = 0^\circ, 3^\circ, 5^\circ$ and 8°, are analysed by employing the proposed approach. For model verification, the reference solution, for each case, is obtained by performing 3D FE analysis in ANSYS. The 3D FE model is meshed with 25,600 `SOLID186`

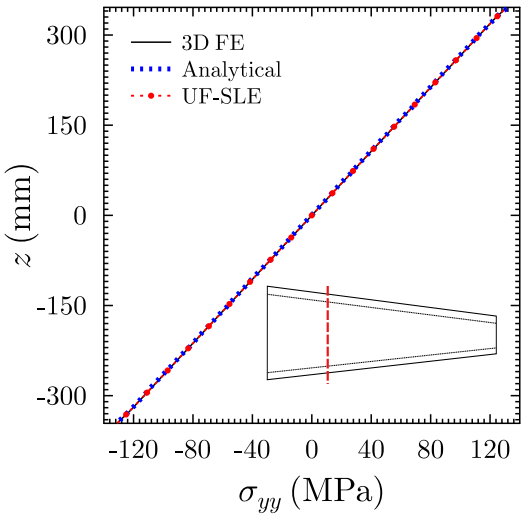

(a) σ_{yy} at $(0, 3000, z)$

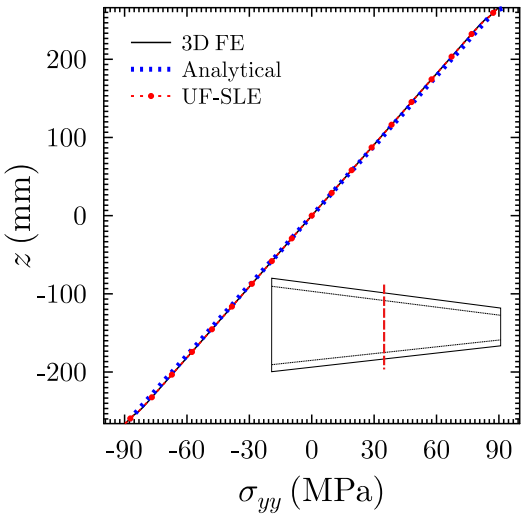

(b) σ_{yy} at $(0, 5000, z)$

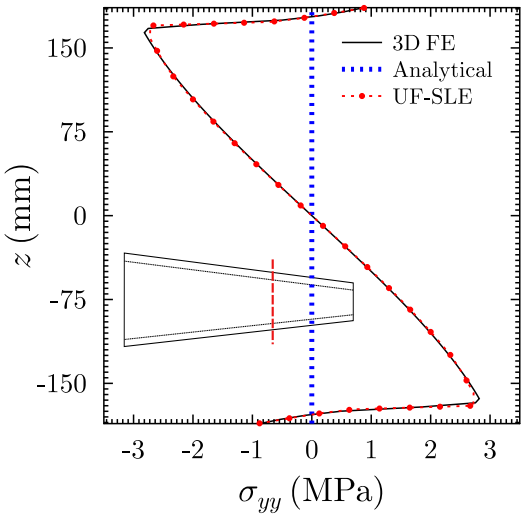

(c) σ_{yy} at $(0, 7000, z)$

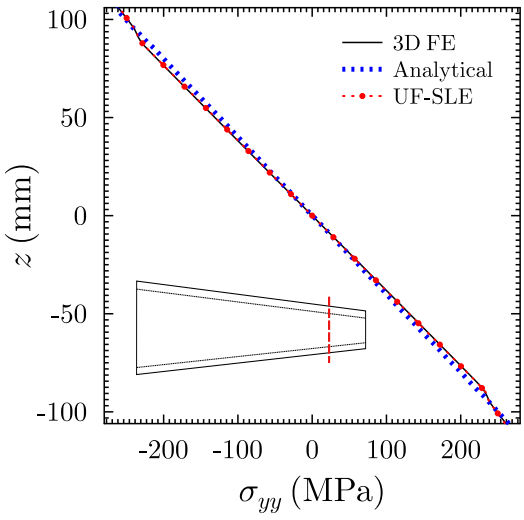

(d) σ_{yy} at $(0, 9000, z)$

Figure 9.3: Through-thickness variation of axial normal stress evaluated at various locations along the length of the tapered I-section beam. Analytical results are taken from [9].

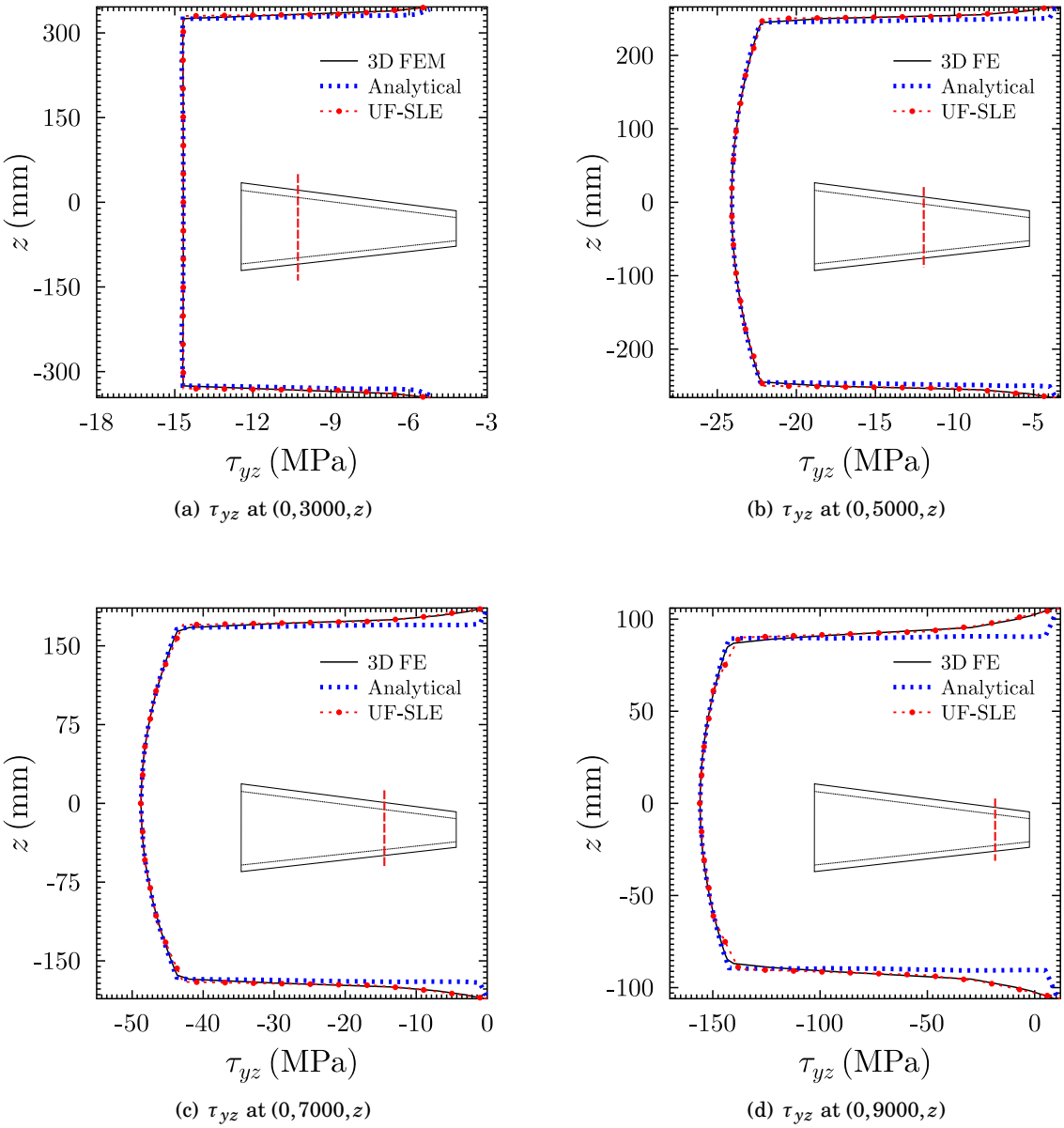

(a) τ_{yz} at $(0, 3000, z)$

(b) τ_{yz} at $(0, 5000, z)$

(c) τ_{yz} at $(0, 7000, z)$

(d) τ_{yz} at $(0, 9000, z)$

Figure 9.4: Through-thickness variation of transverse shear stress evaluated at various locations along the length of the tapered I-section beam. Analytical results are taken from [9].

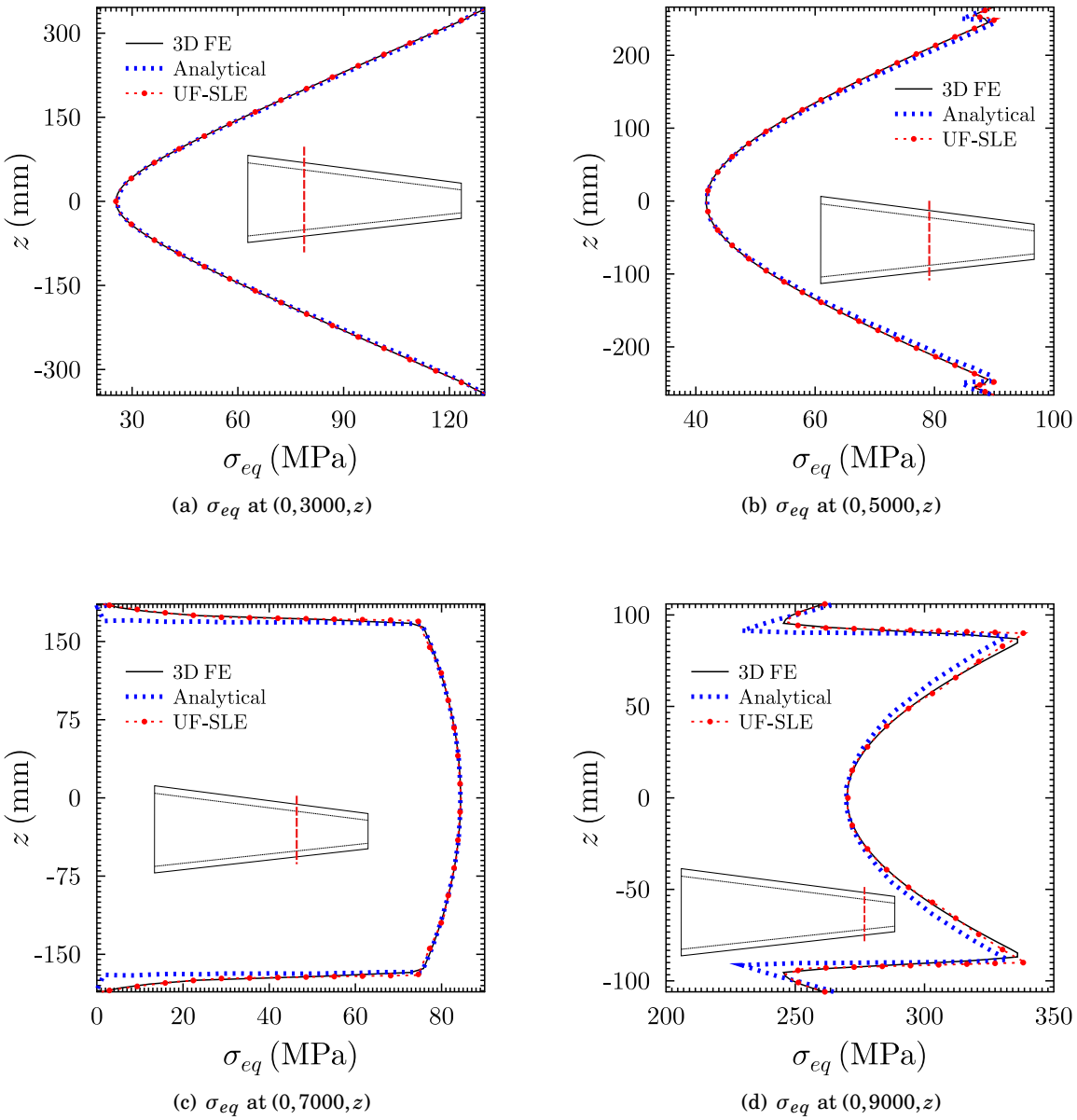

(a) σ_{eq} at $(0, 3000, z)$

(b) σ_{eq} at $(0, 5000, z)$

(c) σ_{eq} at $(0, 7000, z)$

(d) σ_{eq} at $(0, 9000, z)$

Figure 9.5: Through-thickness variation of von-Mises stress evaluated at various locations along the length of the tapered I-section beam. Analytical results are taken from [9].

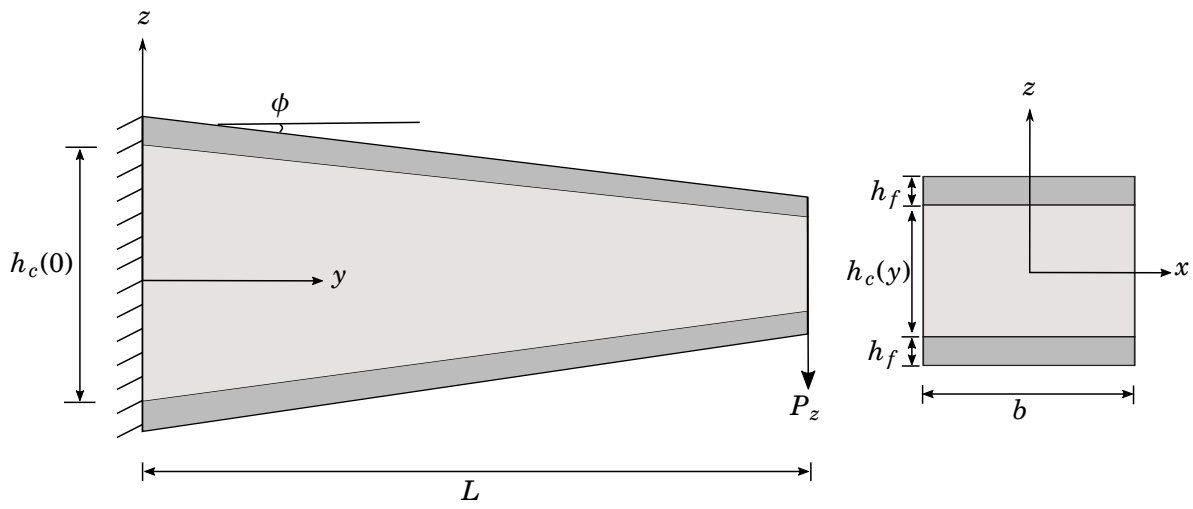

Figure 9.6: Tapered sandwich beam: dimensions and load definition.

elements (100 elements along the length, 15 elements across the width and 16 elements through the thickness, with 10 in the core and 3 in each face sheet), resulting in 339,099 DOFs.

All the stresses are presented in the local x-s-n coordinate system and are non-dimensionalised as follows:

$$\bar{\sigma}_{ss} = \frac{\sigma_{ss} b h_0^2}{P_z L}, \qquad \bar{\tau}_{ns} = \frac{\tau_{ns} b h_0}{P_z}, \qquad \bar{\sigma}_{nn} = \frac{\sigma_{nn} b h_0}{P_z}, \tag{9.8}$$

where h_0 is the total thickness at $y = 0$, σ_{ss} is the extensional stress, τ_{ns} is the transverse shear stress and σ_{nn} is the peeling stress.

Figure 9.7 depicts the axial variation of the normalised extensional stress, $\bar{\sigma}_{ss}$, on the top-most surface of the top facing for taper angles $\phi = 0°, 3°, 5°$ and $8°$. The axial distribution of the normalised transverse shear stress, τ_{ns}, and the normalised peeling stress, σ_{nn}, at the interface between the top facing and the core is plotted in Figures 9.8 and 9.9, respectively. Results obtained are in excellent agreement with 3D FE solutions, even in the vicinity of the clamped support. With an increase in the taper angle, the extensional stress increases and redistributes along the length. For $\phi = 8°$, the stress at the top surface remains nearly uniform, except near the right end where it exhibits a large gradient. The increase in the extensional stress with increasing taper angle is also shown by Figure 9.10(a), where the through-thickness stress variation is plotted at the mid-span of the structure.

Large interlaminar stresses cause free-edge delamination and subsequent delamination growth along the length in laminated fibre-reinforced composites. Experiments have shown that transverse stresses can cause failure of a tapered sandwich member, such as debonding of the facings from the core [215, 216]. Therefore, in order to design tapered sandwich structures, it is important to compute the stresses at the interface between the core and the facing. Figures 9.8

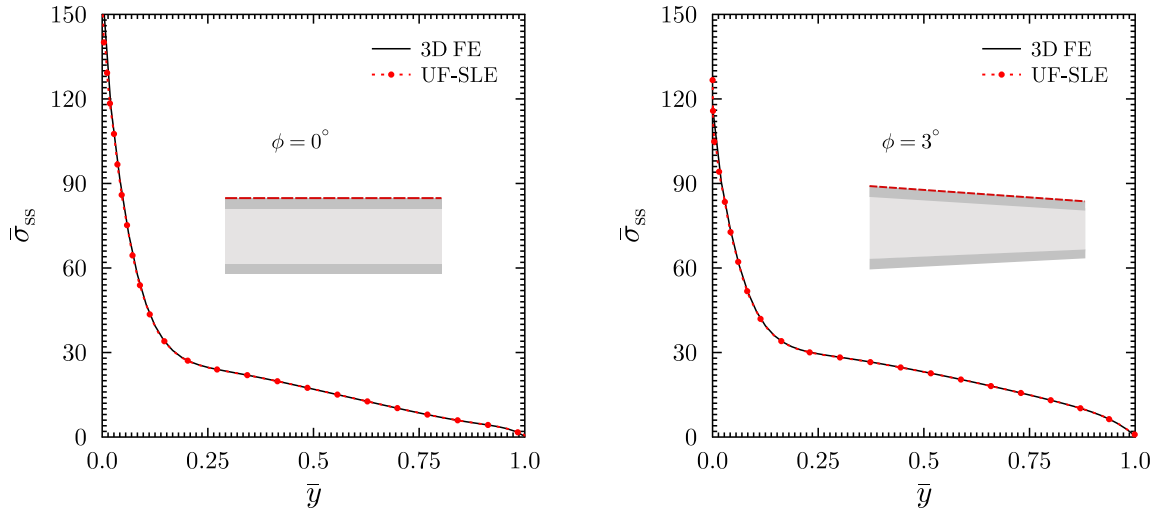

(a) $\bar{\sigma}_{ss}$ vs $\bar{y}$ for $\phi = 0°$

(b) $\bar{\sigma}_{ss}$ vs $\bar{y}$ for $\phi = 3°$

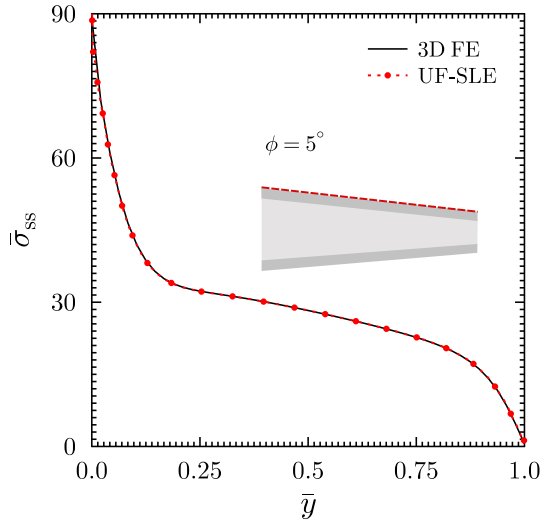

(c) $\bar{\sigma}_{ss}$ vs $\bar{y}$ for $\phi = 5°$

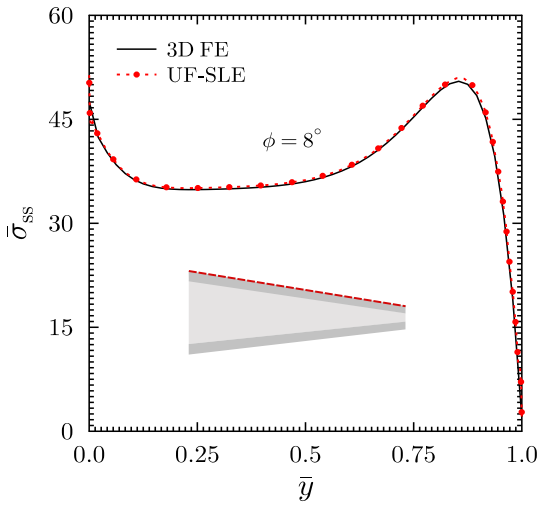

(d) $\bar{\sigma}_{ss}$ vs $\bar{y}$ for $\phi = 8°$

Figure 9.7: Axial variation of normalised extensional or longitudinal stress at the top surface of the tapered sandwich beam for various taper angles.

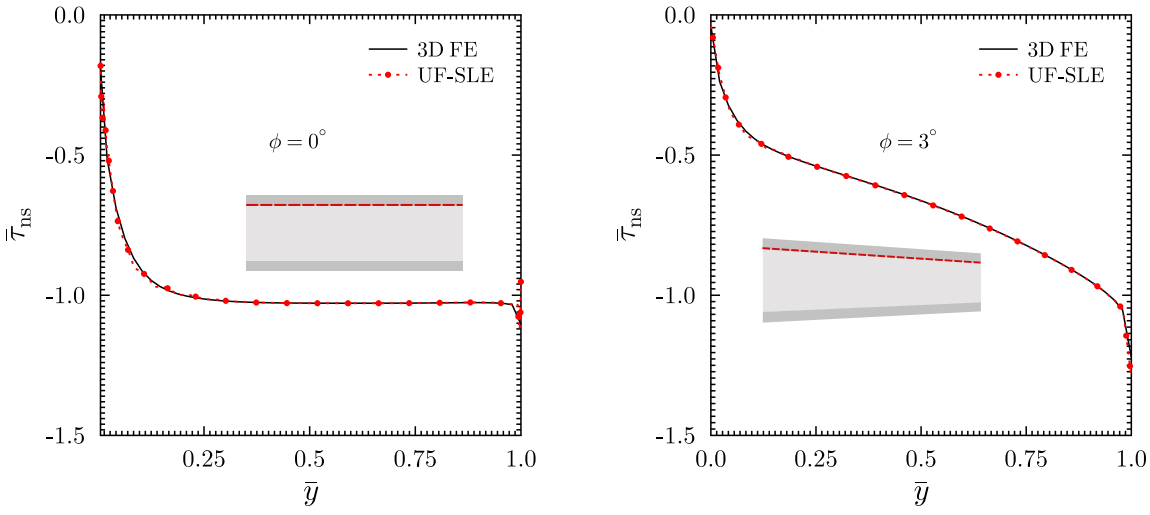

(a) $\bar{\tau}_{ns}$ vs $\bar{y}$ for $\phi = 0°$

(b) $\bar{\tau}_{ns}$ vs $\bar{y}$ for $\phi = 3°$

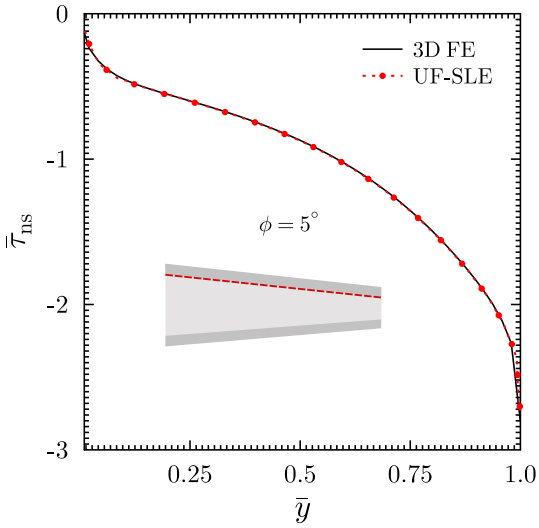

(c) $\bar{\tau}_{ns}$ vs $\bar{y}$ for $\phi = 5°$

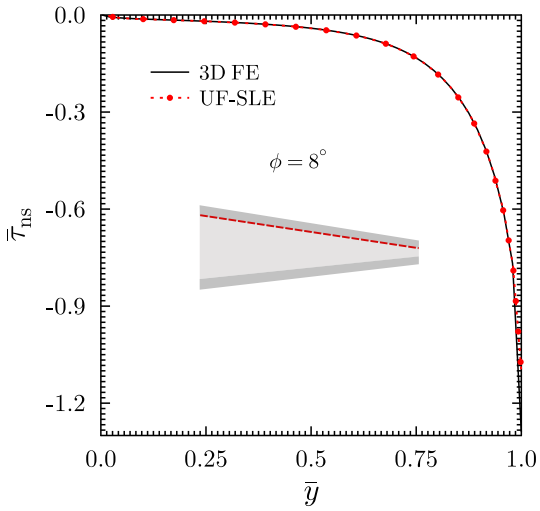

(d) $\bar{\tau}_{ns}$ vs $\bar{y}$ for $\phi = 8°$

Figure 9.8: Axial variation of normalised transverse shear stress between the core and the top facing of the tapered sandwich beam for various taper angles.

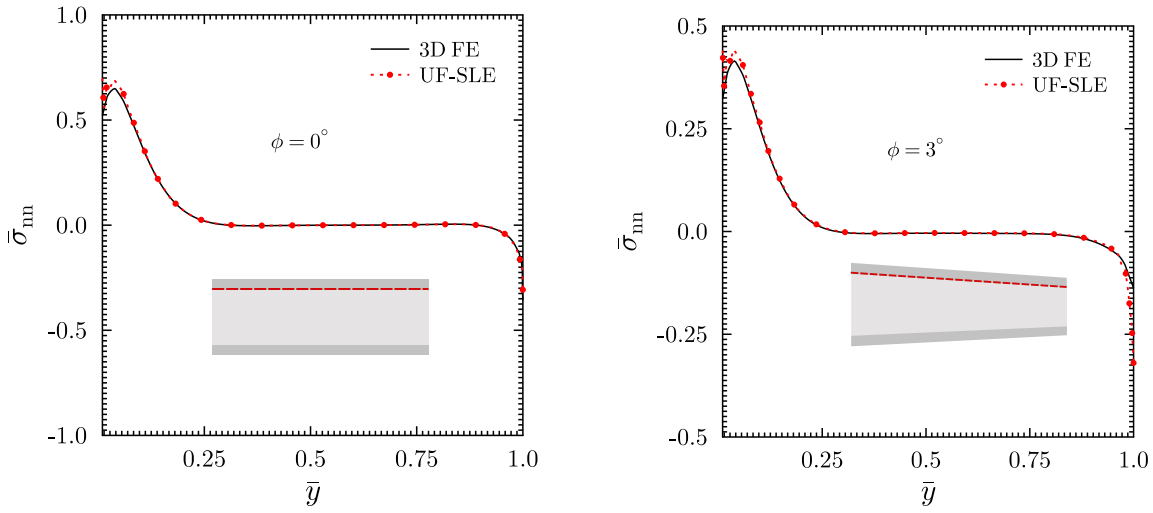

(a) $\bar{\sigma}_{nn}$ vs $\bar{y}$ for $\phi = 0°$

(b) $\bar{\sigma}_{nn}$ vs $\bar{y}$ for $\phi = 3°$

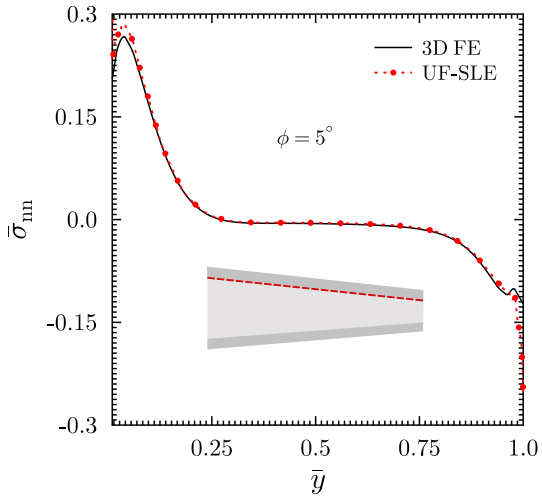

(c) $\bar{\sigma}_{nn}$ vs $\bar{y}$ for $\phi = 5°$

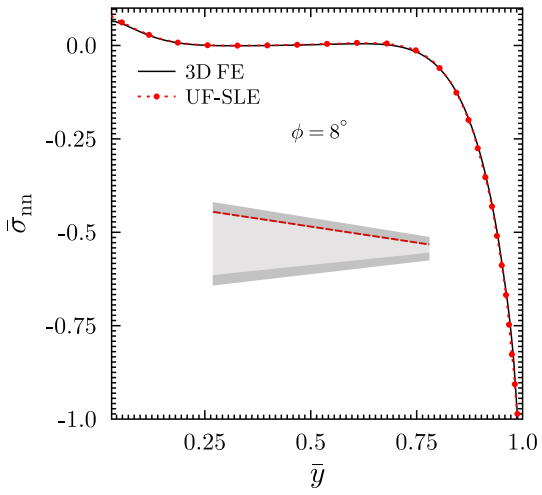

(d) $\bar{\sigma}_{nn}$ vs $\bar{y}$ for $\phi = 8°$

Figure 9.9: Axial variation of normalised peeling stress between the core and the top facing of the tapered sandwich beam for various taper angles.

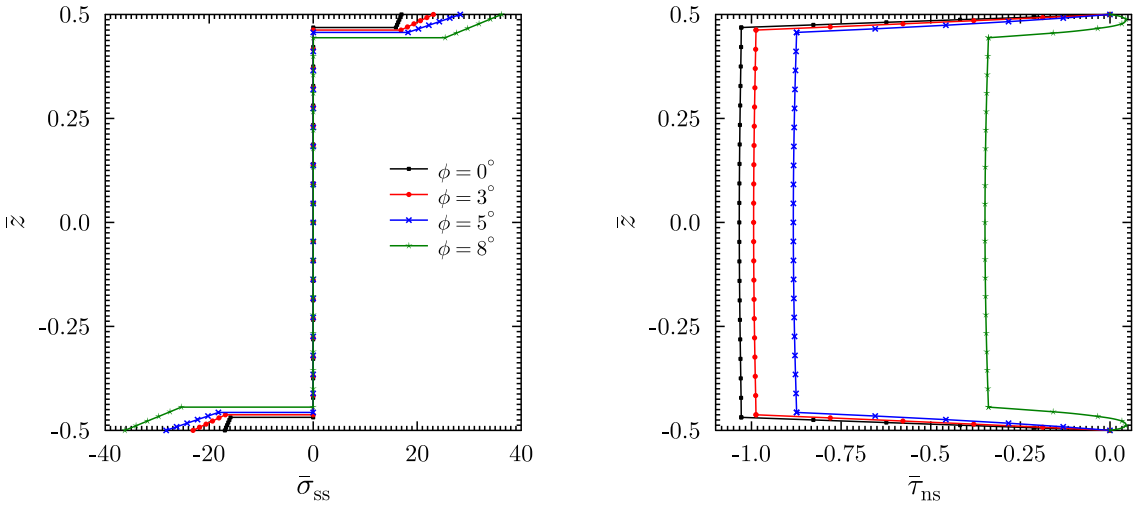

(a) $\bar{\sigma}_{ss}$ at $(0, L/2, \bar{z})$

(b) $\bar{\tau}_{ns}$ at $(0, L/2, \bar{z})$

Figure 9.10: Through-thickness distribution of normalised extensional and normalised transverse shear stress at the mid-span of the tapered sandwich beam for various taper angles obtained by the UF-SLE model.

and 9.9 clearly show that with an increase in the taper angle, the core thickness at the right end decreases and the transverse shear stress increases. For the prismatic sandwich beam, the transverse shear stress is constant along the length, and redistributes such that it concentrates towards the right end. Interestingly, the transverse shear stresses at the mid-span of the beam structure decreases as the taper angle increases, as shown in the Figure 9.10(b). Moreover, due to the increased participation of the facings in resisting transverse shear force, the interlaminar peeling stress increases monotonically with an increasing taper angle. Clearly, for large taper angles, higher transverse stresses cause delamination to initiate at the interface between the core and facing at the right edge that then leads to debonding of the facings [215]. The overall 3D stress response in the tapered sandwich structures is well predicted by the proposed UF-SLE model and is computationally efficient compared to the 3D FE model.

9.2.3 Corrugated Structures

In order to further exploit the capabilities of the UF-SLE model, the geometric non-linear behaviour of corrugated structures in tensile loading is investigated. This example is adapted from the work done by Thurnherr *et al.* [10]. The objective is to show the proposed model's capability in analysing such complex curved structures and describing their non-linear behaviour.

A corrugation pattern consisting of unit cells with two circular sections is now described. The elementary unit cell is shown in Figure 9.11, together with the definition of its parameters:

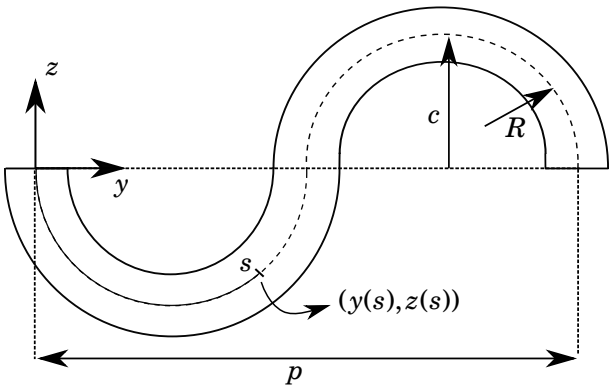

Figure 9.11: Corrugated structure: unit cell geometry definition.

radius of curvature R, amplitude c, periodic cell length p, arc-length parameter s and coordinates $(y(s), z(s))$ of a point on the mid-plane. The coordinates of any point on the mid-surface are given by the parametric equation [217, 218]:

$$\begin{aligned} y(s) &= R\left[\sin(\psi(s)) + (2+m)\sin(\psi_0)\right] \\ z(s) &= -mR\left[\cos(\psi(s)) - \cos(\psi_0)\right], \end{aligned} \tag{9.9}$$

where m switches the sign between the first and second unit cell. It is $+1$ for the first half and -1 for the second half. The radius of curvature R follows from the periodic length p and the corrugation amplitude c, and is given by

$$R = \frac{16c^2 + p^2}{32c}. \tag{9.10}$$

The opening angle ψ_0 is expressed with the hoop variable ψ and is given by

$$\psi_0 = \begin{cases} \arcsin\left(\frac{p}{4R}\right) & \text{if } c \leq \frac{p}{4} \\ \arccos\left(\frac{p}{4R}\right) + \frac{\pi}{2} & \text{if } c > \frac{p}{4}, \end{cases} \tag{9.11}$$

and

$$\psi(s) = \kappa s - (2-m)\psi_0. \tag{9.12}$$

Three different structures, referred as A, B and C, each consisting of four unit cells are studied. Dimensions for each case are shown in Figure 9.12. All configurations are clamped on both sides and axial displacement, u_y, is applied on one end. Thurnherr *et al.* [10] conducted the experimental study and the test samples were fabricated using a 3D printer as shown in Figure 9.13. All specimens were made from Polylactic acid (PLA). Due to the fabrication process the samples are printed layer by layer. This leads to anisotropic material behaviour where the direction parallel to the layers is the stiffest. However, under tensile loading the mechanical response is mainly governed by the stiffness in the axial direction. Therefore, the constituent material is assumed to be isotropic [10], with Young's modulus $E = 3.5$ GPa and Poisson's ratio $\nu = 0.346$.

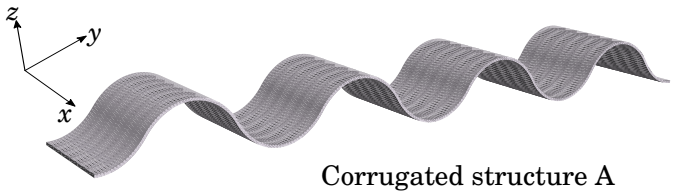

amplitude, $c = 5mm$
cell length, $p = 40.8mm$
width, $b = 25mm$
thickness, $t = 0.52mm$

Corrugated structure A

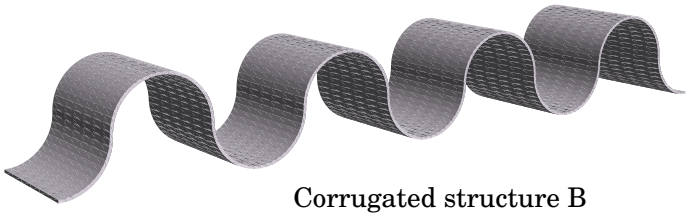

$c = 10mm$
$p = 41.15mm$
$b = 25mm$
$t = 0.55mm$

Corrugated structure B

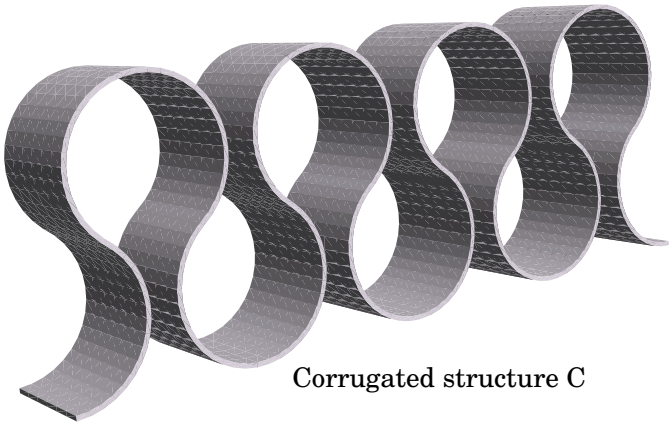

$c = 30mm$
$p = 42.2m$
$b = 25mm$
$t = 1.0mm$

Corrugated structure C

Figure 9.12: Corrugated structures modelled as curved beams.

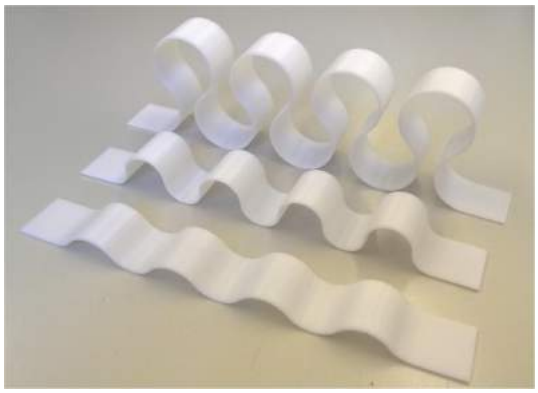

Figure 9.13: Corrugated structure: test samples [10]

The corrugated structures considered herein are analysed using the UF-SLE model. For the corrugated structure A, 3 SL3 (third-order expansion) elements are used in the cross-section and 50 B4 elements are employed along the longitudinal direction. The increase in the curvature demands that more beam elements along the longitudinal direction are used to capture the nonlinear deflection and stress response accurately. For corrugated structures B and C, 80 B4 and 150 B4 elements are employed. This discretisation across the section and in the longitudinal direction results in 12,684, 20,224 and 37,884 DOFs for configurations A, B and C, respectively. In order to verify the results obtained using the UF-SLE model, 3D FE analyses are performed in the commercial finite element code, ANSYS. The corrugated structures are discretised using 13,440 `SOLID186` (20-noded brick) elements (with 2 elements through the thickness, 320 elements along the corrugation pattern and 20 elements across the width), resulting in 229,959 DOFs.

Figure 9.14 shows the nonlinear force versus displacement curve for the three configurations, A, B and C, analysed herein. The force-displacement responses obtained from the UF-SLE model correlate well with 3D FE solutions. Furthermore, the two numerical models are validated against the experimental results as given in [10]. Overall, the numerical results obtained match well with experiments. Certain discrepancies could be due to the isotropic material assumption instead of accounting for layer-wise anisotropy. It is to be noted that, due to the thinness of the samples and the use of position support to clamp the samples in the tensile machine, a slight pre-stretching on both ends could have occurred [10]. Therefore, a pre-stretching correction of 2 mm, 2.6 mm and 8 mm is applied in the force-displacement curve of corrugated structure A, B and C, respectively, obtained from UF-SLE and 3D FE models.

From the force-displacement curves, it is shown that the corrugated structures considered are sufficiently compliable to be easily deformed under a tensile loading. Clearly, in the beginning the response is linear and is driven by the bending moment. However, as the structure deforms, its amplitude decreases and the axial stiffness increases. The slope changes drastically and the mechanical response is fully controlled by the axial force. Modelling this behaviour requires a geometrically nonlinear framework, and the proposed UF-SLE model is shown to capture this response accurately. Furthermore, the nonlinear stress predicting capability of the UF-SLE model is also tested. Figure 9.15 shows the 3D contour plot of the axial stress, σ_{yy}, for the three corrugated structures A, B and C obtained from 3D FE and UF-SLE models. It is shown that the overall stress obtained from both models is almost the same. Small differences in the maximum and minimum values are observed, which are mainly due to the clamped support conditions.

9.3 Conclusions

Previous chapters based on the classical Unified Formulation highlighted its ability in solving a wide range of structural mechanics problems in a computationally efficient manner. However, its modelling capabilities are limited to prismatic structures, and therefore, the formulation is not

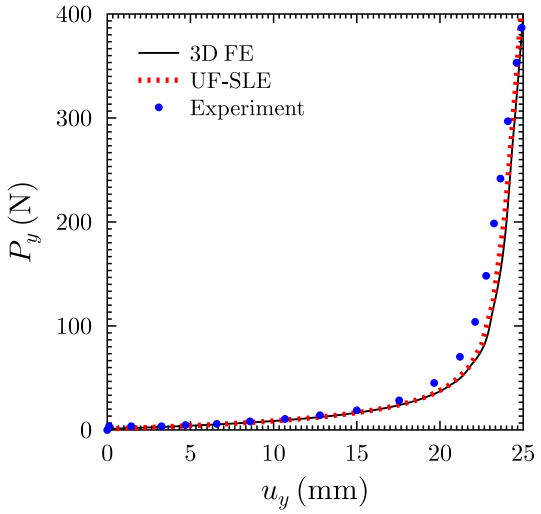

(a) Corrugated Structure A

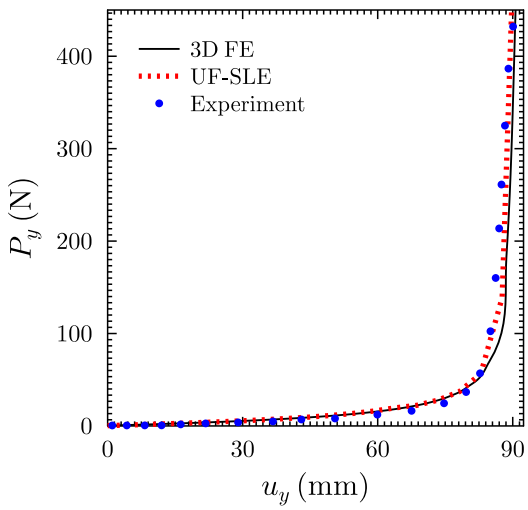

(b) Corrugated Structure B

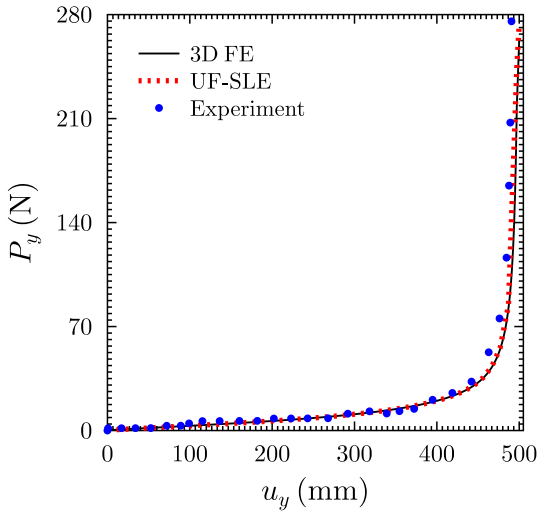

(c) Corrugated Structure C

Figure 9.14: Force vs axial displacement curve for the three corrugated structures A, B and C. Experimental results are taken from Thurnherr *et al.* [10].

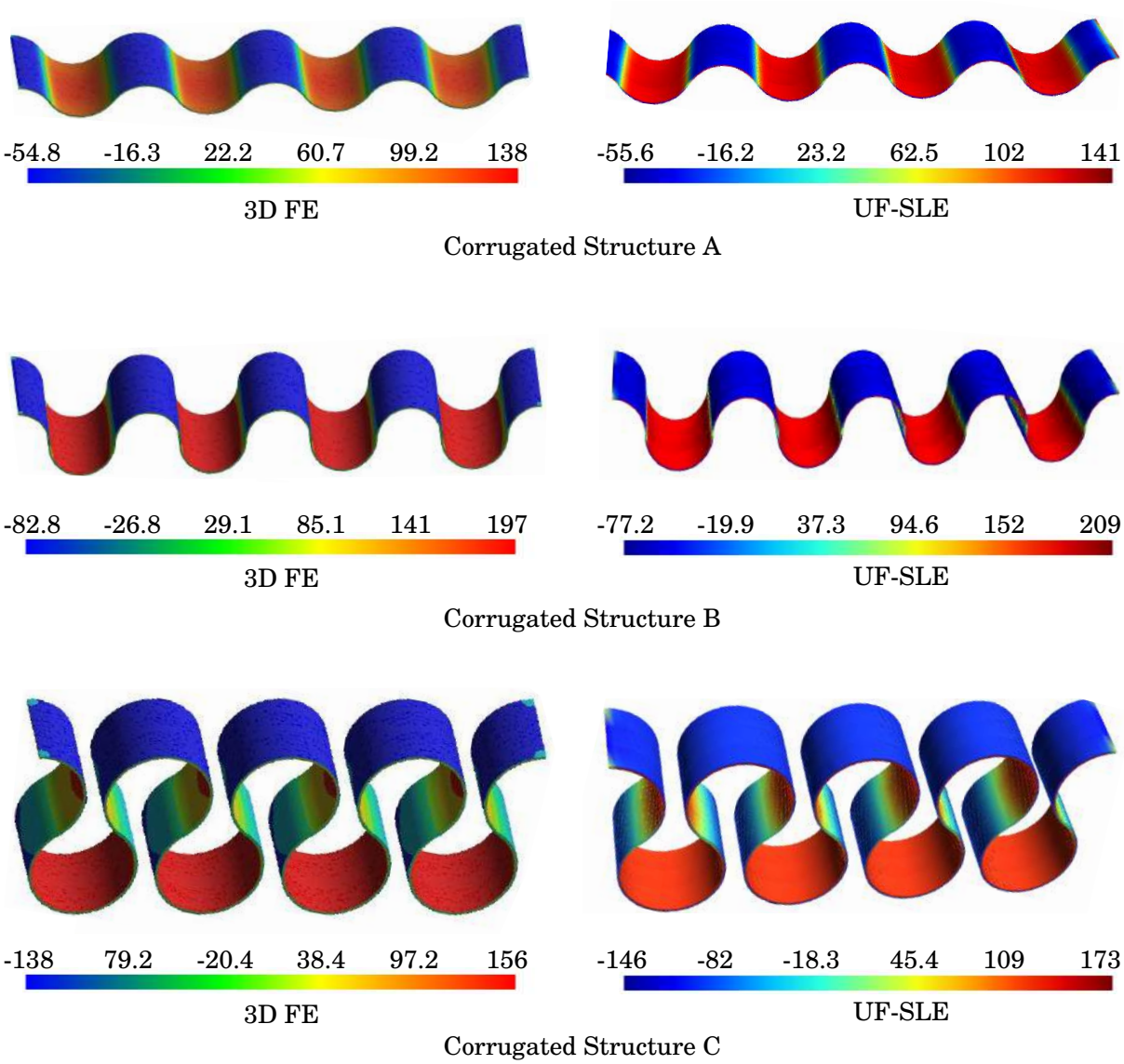

Figure 9.15: Contour plot of axial normal stress σ_{yy} (in Pa) for the three corrugated structures A, B and C.

suitable for analysing complex geometries used in many practical situations. To overcome this limitation and to enhance the capabilities of the Unified Formulation, separate set of functions are used to approximate the geometry and displacement fields. With this approach, the existing shortcomings of the classical Unified Formulation are solved and the model is able to represent both non-prismatic and curved structures. In this chapter, the UF-SLE is employed to model tapered I-beam, tapered sandwich and corrugated structures. The hierarchical nature of the Serendipity Lagrange expansions allows the fidelity of the model to be tuned, such that low-fidelity and high-fidelity models can be used concurrently to assess global response and 3D stresses. The 3D stress distribution obtained for the tapered I-beam and tapered sandwich structures indicate a good correlation with the 3D FE solutions. In addition, the proposed model offers computational benefits over FE models. Furthermore, the non-linear behaviour of corrugated structures under tensile loading is investigated and the static response obtained is shown to match with numerical and experimental results. This study provides us confidence to integrate any CAD tool (for exact geometry description) with the Unified Formulation framework, in order to increase its usability across various industries.

CHAPTER 10

CONCLUSIONS AND FUTURE WORK

This dissertation focused on the development of computationally-efficient, high-fidelity numerical model for predicting localised 3D stress fields in beam-like structures for industrial design applications. The numerical framework was based on Carrera's Unified Formulation that provides computationally efficient refined beam models through variable kinematic definitions. A particular novelty of this work was that non-classical effects in both straight-fibre and tow-steered laminates were investigated. Hence, the research aimed to develop a robust modelling framework for multilayered beam-like structures with so-called 3D heterogeneity, *i.e.* the material properties change discretely through the thickness due to the layered construction of the laminates, and also vary continuously in-plane as a result of curvilinear fibre paths. The capabilities of the 1D higher-order model to provide accurate 3D displacement and stress fields were extended to geometric non-linear problems pertaining to composite structures. The accurate 3D stress predicting capabilities of the numerical framework in a diversified set of structures makes it an attractive proposition for industrial design tools. Overall, the work presented herein can be summarised as follows.

The 1D Unified Formulation, presented in Chapter 3, relies on the displacement based version of the finite element method. The 1D Lagrange shape functions were used to approximate the kinematics along the beam while a different set of shape functions was employed to expand the beam's kinematics over its cross-section. Taylor- and Lagrange-based cross-sectional expansion models were widely employed within the Unified Formulation framework. However, certain limitations are associated with these expansion models as demonstrated in Chapter 4. To summarise, Taylor models make the system ill-conditioned and numerically unstable with an increase the order of expansion, while numerically stable Lagrange models can be highly cumbersome as remeshing is the only way for refining the kinematics. A new class of expansion model, based on

the Serendipity Lagrange functions, was developed in the Unified Formulation framework, with an aim to overcome the above mentioned limitations and to retain benefits offered by both the models (*i.e.* cross-sectional discretisation of the Lagrange model and the hierarchical approximations of the Taylor model). As a result, the proposed model was able to capture higher-order non-classical effects and 3D stress fields in localised regions with reduced model building and computational efforts. The Serendipity Lagrange expansion model also enabled a beam to be modelled with different cross-sections along its length, and maintained displacement and stress continuity at the interface, thereby allowing complex structures such as stiffened panels to be modelled. The UF-SLE model was shown to predict the structural response with greater computational efficiency than 3D finite element analyses for a similar levels of accuracy. To further reduce the computational expense, a variable kinematics approach was proposed which allowed different kinematic approximation over the cross-section at each beam node. With this approach, the accuracy of the solution in the region with strong local effects was improved and the need for a separate global/local analyses could be eliminated. However, the application of this approach requires prior knowledge of the structural response behaviour in order to decide the region where refinement is needed. For cases where the external stimuli leads to non-intuitive deformation fields, this method may not yield accurate results.

The application of the present UF-SLE model to the bending of multilayered, 3D heterogeneous beams was presented in Chapters 5, 6 and 7. Particular focus was placed on modelling a large set of different stacking sequences and material systems to test the full capability of the proposed model. In Chapters 5 and 6, the Layer-Wise (LW) form of the UF-SLE model was adopted while in Chapter 7, an Equivalent Single Layer (ESL) UF-SLE model was proposed and employed for modelling constant- and variable-stiffness, laminated and sandwich beams. The present formulation, which has displacements as degrees of freedom, does not ensure continuous transverse stresses across layer interfaces in both the formats (LW and ESL). To ensure the accurate capture of transverse stresses, a posteriori stress recovery step was employed. Recovering the transverse stresses from Cauchy's equilibrium equations creates a stronger condition than simply post-processing the stresses from the displacement unknowns in the kinematic and constitutive relations. The UF-SLE-LW model, however, in most cases, had sufficient fidelity to naturally satisfy the stress equilibrium equations and to accurately capture the transverse stresses from constitutive relations, whereas, for the UF-SLE-ESL model, transverse stress recovery was always performed. Furthermore, to account for the zig-zag effect in multilayered composites, two Zig-Zag (ZZ) functions, namely Murakami's ZZ function (MZZF) and the Refined ZZ theory function (RZT), were implemented with the ESL approach of the UF-SLE model. The MZZF assumed a periodic change of the displacement field slope at layer interfaces while the RZT accounted for layer-wise differences in transverse shear moduli, which are the properties that physically drive the ZZ effect. The UF-SLE-MZZF model was shown to be insufficient in capturing the stress response accurately for highly heterogeneous sandwich beams. On the other

hand, the UF-SLE-RZT model predicted the 3D stress response accurately for all laminates considered, and was shown to offer significant computational gains over the UF-SLE-LW model and the 3D finite element model. However, in the presence of layer-wise boundary conditions, localised stress gradients or singularities, the layer-wise models were shown to be preferable over equivalent single layer models. The hierarchical nature of the Serendipity Lagrange expansions allows LW and ESL theories to be implemented along with tuning the fidelity of the model, such that low-fidelity and high-fidelity models can be used concurrently to assess global response and localised 3D stresses. Thus, with the present model, global and local responses can be concurrently assessed using ESL and LW theories, in addition to tuning the fidelity of the model by varying the order of expansion function.

Another important finding from this research was the presence of mathematical singularity within the domain of a continuous fibre distribution, which led to localised stress concentrations in the transverse stresses. This singularity arose from an absolute value in the function used to describe fibre orientation along VAT laminates. This condition was overlooked by researchers when modelling VAT composites. For instance, in the case of the HR3-MZZF model [11], a Differential Quadrature method (DQM) was employed to model the beam structure using a single continuous domain. This modelling technique yielded inaccurate transverse shear stress distributions at the beam's mid-span where the singularity, and hence a mathematical boundary, is present. This inaccuracy in the transverse shear stress calculation was further amplified in the computation of the transverse normal stress. In contrast, the present approach used a finite element discretisation along the beam direction, and therefore, separated the domain at the point of mathematical singularity. This approach must be implemented in the DQM-based HR model using an element-based domain decomposition such as the differential quadrature-based finite element method.

The UF-SLE layer-wise model was further extended to incorporate geometric nonlinearity as presented in Chapter 8. A total Lagrangian approach was adopted and the classic Newton-Raphson method was employed to solve the nonlinear governing equations. A key novelty of the proposed nonlinear formulation was its completeness and its applicability to fully anisotropic structures, *i.e.* using the Green-Lagrange strain components within the Unified Formulation framework, the explicit form of the tangent stiffness matrix was derived including general stiffness properties. The explicit form of the tangent stiffness matrix, in terms of the fundamental nuclei, was provided in a clear concise notation which not only reduces the coding task, but also speeds up the computation process by natural vectorisation of the loop. Moreover, the expressions are independent of the type of expansion function used in the cross-section, *i.e.* the explicit form of the tangent stiffness matrix could be used as it is for other nonlinear Unified Formulation models. The nonlinear structural response obtained by the UF-SLE model for laminated composite structures was shown to match with experimental and numerical results from the literature. The results obtained for the stiffened composite structure indicated a good correlation with

experimental data in terms of load-displacement response in the pre- and post-buckling range. The model also offered insight on the intralaminar failure mechanisms and correctly predicted the initiation of the separation of the skin from the stringer as obtained experimentally for the stiffened composite panel. For correctly predicting the damage initiation, accurate 3D layer-wise stresses were required in the post-buckling regime. The proposed UF-SLE layer-wise model was able to predict it accurately. Predicting a similar response using an equivalent single layer model would have resulted in an expensive solution, as it would require stress recovery step for computing transverse stresses in the overall structure for each nonlinear iteration.

Finally, the methodology proposed in Chapter 9 has opened the door, for the Unified Formulation based models, to an enlarged design space. The classical 1D Unified Formulation, presented in Chapter 3, could only model prismatic beam-like structures. For any numerical framework to be suitable for industrial design applications, it must be capable of modelling a variety of complex structures. Having said that, the capabilities of the classical 1D Unified Formulation were enhanced by describing the structure's geometry and kinematics using a separate set of shape functions to model non-prismatic and curved beam-like structures. Using different set of shape functions for geometric and kinematic description enables a broad class of structure to be modelled regardless of the geometrical complexity of the cross-section. Any function that guarantee an exact geometric representation could be employed for evaluating the 3D Jacobian matrix or the local curvilinear basis vectors at each point in the structure. For instance, one could easily integrate a CAD tool and use CAD basis functions, such as B-splines or Non-Uniform Rational B-Splines (NURBS) for describing the geometry. The Unified Formulation functions (along the beam and across the section) were used in the usual manner for approximating displacement fields. The linear and nonlinear, displacement and 3D stress responses obtained, by the implementing the proposed methodology, for tapered I-beam, tapered sandwich beam and corrugated structures were shown to match with numerical and experimental results.

Future Work

The numerical modelling framework proposed in this thesis shall be considered as a basis for subsequent extensions and applications. Potential avenues for future work, along with suggestions for improvement of the developed model, are summarised as follows:

1. **Damage Propagation**: The proposed model is shown to be computationally efficient compared to 3D finite element model whilst capable of capturing three-dimensional stress fields accurately. In Chapter 8, the computed stress fields are used to predict the damage onset. The developed numerical framework could be potentially employed with an advanced progressive failure model for predicting damage propagation in laminated composites. Moreover, with the current model capabilities, as described in Chapter 8, complex structures used in industrial applications can be accounted.

2. **Hierarchical Beam Element**: Despite the excellent potential of the UF-SLE model for analysis of laminated composites, observation showed that the achieved computational efficiency of the approach significantly scales with the mesh density along the beam axis. For example, with a four-node beam element (B4), a high mesh density along the beam is often required to obtain good convergence of the system solution, particularly for variable-angle tow laminates. In the author's recent collaboration [212], hierarchical 1D finite elements are developed and applied to constant-stiffness (straight-fibre) laminated composites. The approach is shown to enhance the computational efficiency of the model. However, its applicability and performance for variable-stiffness laminates still needs to be explored. Furthermore, the hierarchical elements together with the equivalent single layer zig-zag model could potentially be one the most efficient numerical models.

3. **Adaptive Refinement**: In the proposed UF-SLE model, a variable kinematic description can be used at each beam node as described in Sections 3.6 and 4.4. This technique effectively captures localised regions of the structure. However, it could be ineffective in case of non-intuitive structural response. Furthermore, in the current implementation, the order of expansion is decided by performing several iterations until the convergence is achieved. One way to overcome the aforementioned limitations could be to integrate a suitable adaptive refinement technique with the UF-SLE model. This approach would make the proposed model more robust and suitable for applications that require global-local framework.

4. **Mixed-Variational UF-SLE Model**: The displacement-based UF-SLE model requires post-processing steps for accurate transverse stress predictions. The transverse stress components are recovered, from the Cauchy's 3D equilibrium equations, at desired locations. Recovering these stresses for the entire structure is time consuming. Moreover, in case of a nonlinear analysis, computation of 3D stress fields are required at each iteration for the entire structure, which may not be feasible. To overcome this drawback, an alternative approach could be to generalise the UF-SLE model and incorporate mixed-variational statements, such as Reissner's Mixed-Variational Theory (RMVT).

5. **Modelling Ply Drops**: The proposed numerical framework can model non-prismatic structures. The current implementation, however, requires further development to account for tapered laminated structures, which are formed by dropping off some of the plies at discrete positions over the laminate. Methods to model resin pockets that surrounds the dropped plies require developing wedge elements within the UF framework.

APPENDIX A

GENERALISED HOOKE'S LAW

The linear constitutive model for infinitesimal deformation is referred to as the generalised Hooke's law. According to the generalised Hooke's law, for an anisotropic material, the stress-strain relationship in the material coordinate system $(1,2,3)$ can be written as follows

$$\begin{Bmatrix} \sigma_1 \\ \sigma_2 \\ \sigma_3 \\ \tau_{23} \\ \tau_{13} \\ \tau_{12} \end{Bmatrix} = \begin{bmatrix} C_{11} & C_{12} & C_{13} & C_{14} & C_{15} & C_{16} \\ & C_{22} & C_{23} & C_{24} & C_{25} & C_{26} \\ & & C_{33} & C_{34} & C_{35} & C_{36} \\ & & & C_{44} & C_{45} & C_{46} \\ & Symmetric & & & C_{55} & C_{56} \\ & & & & & C_{66} \end{bmatrix} \begin{Bmatrix} \varepsilon_1 \\ \varepsilon_2 \\ \varepsilon_3 \\ \gamma_{23} \\ \gamma_{13} \\ \gamma_{12} \end{Bmatrix}. \tag{A.1}$$

For an orthotropic material, three mutually orthogonal planes of material symmetry exist and the stress-strain relation takes the form

$$\begin{Bmatrix} \sigma_1 \\ \sigma_2 \\ \sigma_3 \\ \tau_{23} \\ \tau_{13} \\ \tau_{12} \end{Bmatrix} = \begin{bmatrix} C_{11} & C_{12} & C_{13} & 0 & 0 & 0 \\ & C_{22} & C_{23} & 0 & 0 & 0 \\ & & C_{33} & 0 & 0 & 0 \\ & & & C_{44} & 0 & 0 \\ & Symmetric & & & C_{55} & 0 \\ & & & & & C_{66} \end{bmatrix} \begin{Bmatrix} \varepsilon_1 \\ \varepsilon_2 \\ \varepsilon_3 \\ \gamma_{23} \\ \gamma_{13} \\ \gamma_{12} \end{Bmatrix}. \tag{A.2}$$

The coefficients C_{ij} are expressed in terms of the engineering constants, E_i, G_{ij} and ν_{ij} as

$$
\begin{aligned}
&C_{11} = \frac{(1-\nu_{23}\nu_{32})E_1}{\Delta},\ C_{22} = \frac{(1-\nu_{13}\nu_{31})E_2}{\Delta},\ C_{33} = \frac{(1-\nu_{12}\nu_{21})E_3}{\Delta}\\
&C_{12} = \frac{(\nu_{12}+\nu_{13}\nu_{32})E_2}{\Delta} = \frac{(\nu_{21}+\nu_{23}\nu_{31})E_1}{\Delta},\\
&C_{13} = \frac{(\nu_{13}+\nu_{12}\nu_{23})E_3}{\Delta} = \frac{(\nu_{31}+\nu_{32}\nu_{21})E_1}{\Delta},\\
&C_{23} = \frac{(\nu_{23}+\nu_{21}\nu_{13})E_3}{\Delta} = \frac{(\nu_{32}+\nu_{31}\nu_{12})E_2}{\Delta},\\
&C_{44} = G_{44},\ C_{55} = G_{55},\ C_{66} = G_{66}\\
&\Delta = (1-\nu_{12}\nu_{21}-\nu_{23}\nu_{32}-\nu_{13}\nu_{31}-2\nu_{21}\nu_{13}\nu_{32}).
\end{aligned}
$$

In an isotropic material, there exist no preferred directions and every plane is a plane of symmetry. Thus, for isotropic materials we have

$$E_1 = E_2 = E_3,\ G_{12} = G_{13} = G_{23},\ \nu_{12} = \nu_{13} = \nu_{23}.$$

For any of the above linearly elastic material, the stress-strain relationship, in the global (x,y,z) coordinate system can be written as

$$
\begin{Bmatrix} \sigma_{xx} \\ \sigma_{yy} \\ \sigma_{zz} \\ \tau_{yz} \\ \tau_{xz} \\ \tau_{xy} \end{Bmatrix} =
\begin{bmatrix}
\bar{C}_{11} & \bar{C}_{12} & \bar{C}_{13} & \bar{C}_{14} & \bar{C}_{15} & \bar{C}_{16} \\
 & \bar{C}_{22} & \bar{C}_{23} & \bar{C}_{24} & \bar{C}_{25} & \bar{C}_{26} \\
 & & \bar{C}_{33} & \bar{C}_{34} & \bar{C}_{35} & \bar{C}_{36} \\
 & & & \bar{C}_{44} & \bar{C}_{45} & \bar{C}_{46} \\
 & Symmetric & & & \bar{C}_{55} & \bar{C}_{56} \\
 & & & & & \bar{C}_{66}
\end{bmatrix}
\begin{Bmatrix} \varepsilon_{xx} \\ \varepsilon_{yy} \\ \varepsilon_{zz} \\ \gamma_{yz} \\ \gamma_{xz} \\ \gamma_{xy} \end{Bmatrix}. \tag{A.3}
$$

where the coefficients $\bar{C}_{ij}$ relate to the elastic coefficients in material coordinates, C_{ij}, via the transformation matrix $\boldsymbol{Q}$, whose elements are obtained from the direction cosines of the material coordinate system projected onto the global x, y, z coordinate directions. Specifically,

$$\bar{\boldsymbol{C}} = \boldsymbol{Q}\boldsymbol{C}\boldsymbol{Q}^{\top}. \tag{A.4}$$

The matrix $\boldsymbol{Q}$ are not included here for sake of brevity, but can be found in Section 5.4 of [206].

APPENDIX B

FUNDAMENTAL NUCLEUS OF THE STIFFNESS MATRIX

The fundamental nucleus $\boldsymbol{K}^{\tau si j}$ is a (3×3) matrix and the explicit expression for its components is given as follows

$$
\begin{aligned}
K_{xx}^{\tau si j} =& \bar{C}(6,6)\int_A F_\tau F_s dx dz \int_l N_{i,y} N_{j,y} dy + \bar{C}(5,5)\int_A F_{\tau,z} F_{s,z} dx dz \int_l N_i N_j dy \\
&+\bar{C}(5,6)\int_A F_\tau F_{s,z} dx dz \int_l N_{i,y} N_j dy + \bar{C}(5,6)\int_A F_{\tau,z} F_s dx dz \int_l N_i N_{j,y} dy \\
&+\bar{C}(1,5)\int_A F_{\tau,z} F_{s,x} dx dz \int_l N_i N_j dy + \bar{C}(1,5)\int_A F_{\tau,x} F_{s,z} dx dz \int_l N_i N_j dy \\
&+\bar{C}(1,6)\int_A F_\tau F_{s,x} dx dz \int_l N_{i,y} N_j dy + \bar{C}(1,6)\int_A F_{\tau,x} F_s dx dz \int_l N_i N_{j,y} dy \\
&+\bar{C}(1,1)\int_A F_{\tau,x} F_{s,x} dx dz \int_l N_i N_j dy,
\end{aligned}
\tag{B.1}
$$

$$
\begin{aligned}
K_{xy}^{\tau si j} =& \bar{C}(4,6)\int_A F_{\tau,z} F_s dx dz \int_l N_i N_{j,y} dy + \bar{C}(6,6)\int_A F_{\tau,x} F_s dx dz \int_l N_i N_{j,y} dy \\
&+\bar{C}(2,5)\int_A F_\tau F_{s,z} dx dz \int_l N_{i,y} N_j dy + \bar{C}(1,2)\int_A F_\tau F_{s,x} dx dz \int_l N_{i,y} N_j dy \\
&+\bar{C}(4,5)\int_A F_{\tau,z} F_{s,z} dx dz \int_l N_i N_j dy + \bar{C}(1,4)\int_A F_{\tau,z} F_{s,x} dx dz \int_l N_i N_j dy \\
&+\bar{C}(5,6)\int_A F_{\tau,x} F_{s,z} dx dz \int_l N_i N_j dy + \bar{C}(2,6)\int_A F_\tau F_s dx dz \int_l N_{i,y} N_{j,y} dy \\
&+\bar{C}(1,6)\int_A F_{\tau,x} F_{s,x} dx dz \int_l N_i N_j dy,
\end{aligned}
\tag{B.2}
$$

$$
\begin{aligned}
K_{xz}^{\tau sij} =& \bar{C}(4,6)\int_A F_\tau F_s dx dz \int_l N_{i,y} N_{j,y} dy + \bar{C}(3,6)\int_A F_{\tau,z} F_s dx dz \int_l N_i N_{j,y} dy \\
&+\bar{C}(5,6)\int_A F_{\tau,x} F_s dx dz \int_l N_i N_{j,y} dy + \bar{C}(4,5)\int_A F_\tau F_{s,z} dx dz \int_l N_{i,y} N_j dy \\
&+\bar{C}(1,4)\int_A F_\tau F_{s,x} dx dz \int_l N_{i,y} N_j dy + \bar{C}(3,5)\int_A F_{\tau,z} F_{s,z} dx dz \int_l N_i N_j dy \\
&+\bar{C}(1,3)\int_A F_{\tau,z} F_{s,x} dx dz \int_l N_i N_j dy + \bar{C}(5,5)\int_A F_{\tau,x} F_{s,z} dx dz \int_l N_i N_j dy \\
&+\bar{C}(1,5)\int_A F_{\tau,x} F_{s,x} dx dz \int_l N_i N_j dy,
\end{aligned} \tag{B.3}
$$

$$
\begin{aligned}
K_{yx}^{\tau sij} =& \bar{C}(2,5)\int_A F_{\tau,z} F_s dx dz \int_l N_i N_{j,y} dy + \bar{C}(1,2)\int_A F_{\tau,x} F_s dx dz \int_l N_i N_{j,y} dy \\
&+\bar{C}(4,6)\int_A F_\tau F_{s,z} dx dz \int_l N_{i,y} N_j dy + \bar{C}(6,6)\int_A F_\tau F_{s,x} dx dz \int_l N_{i,y} N_j dy \\
&+\bar{C}(4,5)\int_A F_{\tau,z} F_{s,z} dx dz \int_l N_i N_j dy + \bar{C}(5,6)\int_A F_{\tau,z} F_{s,x} dx dz \int_l N_i N_j dy \\
&+\bar{C}(1,4)\int_A F_{\tau,x} F_{s,z} dx dz \int_l N_i N_j dy + \bar{C}(2,6)\int_A F_\tau F_s dx dz \int_l N_{i,y} N_{j,y} dy \\
&+\bar{C}(1,6)\int_A F_{\tau,x} F_{s,x} dx dz \int_l N_i N_j dy,
\end{aligned} \tag{B.4}
$$

$$
\begin{aligned}
K_{yy}^{\tau sij} =& \bar{C}(2,2)\int_A F_\tau F_s dx dz \int_l N_{i,y} N_{j,y} dy + \bar{C}(2,4)\int_A F_{\tau,z} F_s dx dz \int_l N_i N_{j,y} dy \\
&+\bar{C}(2,4)\int_A F_\tau F_{s,z} dx dz \int_l N_{i,y} N_j dy + \bar{C}(4,4)\int_A F_{\tau,z} F_{s,z} dx dz \int_l N_i N_j dy \\
&+\bar{C}(4,6)\int_A F_{\tau,z} F_{s,x} dx dz \int_l N_i N_j dy + \bar{C}(4,6)\int_A F_{\tau,x} F_{s,z} dx dz \int_l N_i N_j dy \\
&+\bar{C}(6,6)\int_A F_{\tau,x} F_{s,x} dx dz \int_l N_i N_j dy + \bar{C}(2,6)\int_A F_{\tau,x} F_s dx dz \int_l N_i N_{j,y} dy \\
&+\bar{C}(2,6)\int_A F_\tau F_{s,x} dx dz \int_l N_{i,y} N_j dy,
\end{aligned} \tag{B.5}
$$

$$
\begin{aligned}
K_{yz}^{\tau sij} =& \bar{C}(2,4)\int_A F_\tau F_s dx dz \int_l N_{i,y} N_{j,y} dy + \bar{C}(2,3)\int_A F_{\tau,z} F_s dx dz \int_l N_i N_{j,y} dy \\
&+\bar{C}(2,5)\int_A F_{\tau,x} F_s dx dz \int_l N_i N_{j,y} dy + \bar{C}(4,4)\int_A F_\tau F_{s,z} dx dz \int_l N_{i,y} N_j dy \\
&+\bar{C}(4,6)\int_A F_\tau F_{s,x} dx dz \int_l N_{i,y} N_j dy + \bar{C}(3,4)\int_A F_{\tau,z} F_{s,z} dx dz \int_l N_i N_j dy \\
&+\bar{C}(3,6)\int_A F_{\tau,z} F_{s,x} dx dz \int_l N_i N_j dy + \bar{C}(4,5)\int_A F_{\tau,x} F_{s,z} dx dz \int_l N_i N_j dy \\
&+\bar{C}(5,6)\int_A F_{\tau,x} F_{s,x} dx dz \int_l N_i N_j dy,
\end{aligned} \tag{B.6}
$$

$$
\begin{aligned}
K_{zx}^{\tau sij} =& \bar{C}(4,6)\int_A F_\tau F_s dxdz \int_l N_{i,y} N_{j,y} dy + \bar{C}(4,5)\int_A F_{\tau,z} F_s dxdz \int_l N_i N_{j,y} dy \\
&+\bar{C}(1,4)\int_A F_{\tau,x} F_s dxdz \int_l N_i N_{j,y} dy + \bar{C}(3,6)\int_A F_\tau F_{s,z} dxdz \int_l N_{i,y} N_j dy \\
&+\bar{C}(5,6)\int_A F_\tau F_{s,x} dxdz \int_l N_{i,y} N_j dy + \bar{C}(3,5)\int_A F_{\tau,z} F_{s,z} dxdz \int_l N_i N_j dy \\
&+\bar{C}(5,5)\int_A F_{\tau,z} F_{s,x} dxdz \int_l N_i N_j dy + \bar{C}(1,3)\int_A F_{\tau,x} F_{s,z} dxdz \int_l N_i N_j dy \\
&+\bar{C}(1,5)\int_A F_{\tau,x} F_{s,x} dxdz \int_l N_i N_j dy,
\end{aligned} \tag{B.7}
$$

$$
\begin{aligned}
K_{zy}^{\tau sij} =& \bar{C}(2,4)\int_A F_\tau F_s dxdz \int_l N_{i,y} N_{j,y} dy + \bar{C}(4,4)\int_A F_{\tau,z} F_s dxdz \int_l N_i N_{j,y} dy \\
&+\bar{C}(4,6)\int_A F_{\tau,x} F_s dxdz \int_l N_i N_{j,y} dy + \bar{C}(2,3)\int_A F_\tau F_{s,z} dxdz \int_l N_{i,y} N_j dy \\
&+\bar{C}(2,5)\int_A F_\tau F_{s,x} dxdz \int_l N_{i,y} N_j dy + \bar{C}(3,4)\int_A F_{\tau,z} F_{s,z} dxdz \int_l N_i N_j dy \\
&+\bar{C}(4,5)\int_A F_{\tau,z} F_{s,x} dxdz \int_l N_i N_j dy + \bar{C}(3,6)\int_A F_{\tau,x} F_{s,z} dxdz \int_l N_i N_j dy \\
&+\bar{C}(5,6)\int_A F_{\tau,x} F_{s,x} dxdz \int_l N_i N_j dy,
\end{aligned} \tag{B.8}
$$

$$
\begin{aligned}
K_{zz}^{\tau sij} =& \bar{C}(4,4)\int_A F_\tau F_s dxdz \int_l N_{i,y} N_{j,y} dy + \bar{C}(3,4)\int_A F_{\tau,z} F_s dxdz \int_l N_i N_{j,y} dy \\
&+\bar{C}(4,4)\int_A F_{\tau,x} F_s dxdz \int_l N_i N_{j,y} dy + \bar{C}(3,4)\int_A F_\tau F_{s,z} dxdz \int_l N_{i,y} N_j dy \\
&+\bar{C}(4,5)\int_A F_\tau F_{s,x} dxdz \int_l N_{i,y} N_j dy + \bar{C}(3,3)\int_A F_{\tau,z} F_{s,z} dxdz \int_l N_i N_j dy \\
&+\bar{C}(3,5)\int_A F_{\tau,z} F_{s,x} dxdz \int_l N_i N_j dy + \bar{C}(3,5)\int_A F_{\tau,x} F_{s,z} dxdz \int_l N_i N_j dy \\
&+\bar{C}(5,5)\int_A F_{\tau,x} F_{s,x} dxdz \int_l N_i N_j dy,
\end{aligned} \tag{B.9}
$$

The remainder of this appendix supplements Chapter 7. The explicit form for matrices, $\boldsymbol{K}^{\tau\varphi ij}$, $\boldsymbol{K}^{\phi sij}$ and $\boldsymbol{K}^{\phi\varphi ij}$, as required by ESL-ZZ models, are given as follows

$$
\begin{aligned}
K_{xx}^{\tau\varphi ij} =& \int_V \bar{C}_{66} F_\tau \varphi_x^R N_{i,y} N_{j,y} dV + \int_V \bar{C}_{55} F_{\tau,z} \varphi_{x,z}^R N_i N_j dV + \int_V \bar{C}_{56} F_\tau \varphi_{x,z}^R N_{i,y} N_j dV \\
&+ \int_V \bar{C}_{56} F_{\tau,z} \varphi_x^R N_i N_{j,y} dV + \int_V \bar{C}_{15} F_{\tau,z} \varphi_{x,x}^R N_i N_j dV + \int_V \bar{C}_{15} F_{\tau,x} \varphi_{x,z}^R N_i N_j dV \\
&+ \int_V \bar{C}_{16} F_\tau \varphi_{x,x}^R N_{i,y} N_j dV + \int_V \bar{C}_{16} F_{\tau,x} \varphi_x^R N_i N_{j,y} dV + \int_V \bar{C}_{11} F_{\tau,x} \varphi_{x,x}^R N_i N_j dV \\
&+ \int_V \bar{C}_{16} F_{\tau,x} \varphi_{x,y}^R N_i N_j dV + \int_V \bar{C}_{56} F_{\tau,z} \varphi_{x,y}^R N_i N_j dV + \int_V \bar{C}_{66} F_\tau \varphi_{x,y}^R N_{i,y} N_j dV,
\end{aligned} \tag{B.10}
$$

$$
\begin{aligned}
K_{xy}^{\tau\varphi ij} = &\int_V \bar{C}_{26} F_\tau \varphi_y^R N_{i,y} N_{j,y} dV + \int_V \bar{C}_{45} F_{\tau,z} \varphi_{y,z}^R N_i N_j dV + \int_V \bar{C}_{25} F_\tau \varphi_{y,z}^R N_{i,y} N_j dV \\
&+ \int_V \bar{C}_{46} F_{\tau,z} \varphi_y^R N_i N_{j,y} dV + \int_V \bar{C}_{14} F_{\tau,z} \varphi_{y,x}^R N_i N_j dV + \int_V \bar{C}_{56} F_{\tau,x} \varphi_{y,z}^R N_i N_j dV \\
&+ \int_V \bar{C}_{12} F_\tau \varphi_{y,x}^R N_{i,y} N_j dV + \int_V \bar{C}_{66} F_{\tau,x} \varphi_y^R N_i N_{j,y} dV + \int_V \bar{C}_{16} F_{\tau,x} \varphi_{y,x}^R N_i N_j dV \\
&+ \int_V \bar{C}_{66} F_{\tau,x} \varphi_{y,y}^R N_i N_j dV + \int_V \bar{C}_{46} F_{\tau,z} \varphi_{y,y}^R N_i N_j dV + \int_V \bar{C}_{26} F_\tau \varphi_{y,y}^R N_{i,y} N_j dV,
\end{aligned} \tag{B.11}
$$

$$
\begin{aligned}
K_{yx}^{\tau\varphi ij} = &\int_V \bar{C}_{26} F_\tau \varphi_x^R N_{i,y} N_{j,y} dV + \int_V \bar{C}_{45} F_{\tau,z} \varphi_{x,z}^R N_i N_j dV + \int_V \bar{C}_{46} F_\tau \varphi_{x,z}^R N_{i,y} N_j dV \\
&+ \int_V \bar{C}_{25} F_{\tau,z} \varphi_x^R N_i N_{j,y} dV + \int_V \bar{C}_{56} F_{\tau,z} \varphi_{x,x}^R N_i N_j dV + \int_V \bar{C}_{14} F_{\tau,x} \varphi_{x,z}^R N_i N_j dV \\
&+ \int_V \bar{C}_{66} F_\tau \varphi_{x,x}^R N_{i,y} N_j dV + \int_V \bar{C}_{12} F_{\tau,x} \varphi_x^R N_i N_{j,y} dV + \int_V \bar{C}_{16} F_{\tau,x} \varphi_{x,x}^R N_i N_j dV \\
&+ \int_V \bar{C}_{12} F_{\tau,x} \varphi_{x,y}^R N_i N_j dV + \int_V \bar{C}_{25} F_{\tau,z} \varphi_{x,y}^R N_i N_j dV + \int_V \bar{C}_{26} F_\tau \varphi_{x,y}^R N_{i,y} N_j dV,
\end{aligned} \tag{B.12}
$$

$$
\begin{aligned}
K_{yy}^{\tau\varphi ij} = &\int_V \bar{C}_{22} F_\tau \varphi_y^R N_{i,y} N_{j,y} dV + \int_V \bar{C}_{44} F_{\tau,z} \varphi_{y,z}^R N_i N_j dV + \int_V \bar{C}_{24} F_\tau \varphi_{y,z}^R N_{i,y} N_j dV \\
&+ \int_V \bar{C}_{24} F_{\tau,z} \varphi_y^R N_i N_{j,y} dV + \int_V \bar{C}_{46} F_{\tau,z} \varphi_{y,x}^R N_i N_j dV + \int_V \bar{C}_{46} F_{\tau,x} \varphi_{y,z}^R N_i N_j dV \\
&+ \int_V \bar{C}_{26} F_\tau \varphi_{y,x}^R N_{i,y} N_j dV + \int_V \bar{C}_{26} F_{\tau,x} \varphi_y^R N_i N_{j,y} dV + \int_V \bar{C}_{66} F_{\tau,x} \varphi_{y,x}^R N_i N_j dV \\
&+ \int_V \bar{C}_{26} F_{\tau,x} \varphi_{y,y}^R N_i N_j dV + \int_V \bar{C}_{24} F_{\tau,z} \varphi_{y,y}^R N_i N_j dV + \int_V \bar{C}_{22} F_\tau \varphi_{y,y}^R N_{i,y} N_j dV,
\end{aligned} \tag{B.13}
$$

$$
\begin{aligned}
K_{zx}^{\tau\varphi ij} = &\int_V \bar{C}_{46} F_\tau \varphi_x^R N_{i,y} N_{j,y} dV + \int_V \bar{C}_{35} F_{\tau,z} \varphi_{x,z}^R N_i N_j dV + \int_V \bar{C}_{36} F_\tau \varphi_{x,z}^R N_{i,y} N_j dV \\
&+ \int_V \bar{C}_{45} F_{\tau,z} \varphi_x^R N_i N_{j,y} dV + \int_V \bar{C}_{55} F_{\tau,z} \varphi_{x,x}^R N_i N_j dV + \int_V \bar{C}_{13} F_{\tau,x} \varphi_{x,z}^R N_i N_j dV \\
&+ \int_V \bar{C}_{56} F_\tau \varphi_{x,x}^R N_{i,y} N_j dV + \int_V \bar{C}_{14} F_{\tau,x} \varphi_x^R N_i N_{j,y} dV + \int_V \bar{C}_{15} F_{\tau,x} \varphi_{x,x}^R N_i N_j dV \\
&+ \int_V \bar{C}_{14} F_{\tau,x} \varphi_{x,y}^R N_i N_j dV + \int_V \bar{C}_{45} F_{\tau,z} \varphi_{x,y}^R N_i N_j dV + \int_V \bar{C}_{46} F_\tau \varphi_{x,y}^R N_{i,y} N_j dV,
\end{aligned} \tag{B.14}
$$

$$
\begin{aligned}
K_{zy}^{\tau\varphi ij} = &\int_V \bar{C}_{24} F_\tau \varphi_y^R N_{i,y} N_{j,y} dV + \int_V \bar{C}_{34} F_{\tau,z} \varphi_{y,z}^R N_i N_j dV + \int_V \bar{C}_{23} F_\tau \varphi_{y,z}^R N_{i,y} N_j dV \\
&+ \int_V \bar{C}_{44} F_{\tau,z} \varphi_y^R N_i N_{j,y} dV + \int_V \bar{C}_{45} F_{\tau,z} \varphi_{y,x}^R N_i N_j dV + \int_V \bar{C}_{36} F_{\tau,x} \varphi_{y,z}^R N_i N_j dV \\
&+ \int_V \bar{C}_{25} F_\tau \varphi_{y,x}^R N_{i,y} N_j dV + \int_V \bar{C}_{46} F_{\tau,x} \varphi_y^R N_i N_{j,y} dV + \int_V \bar{C}_{56} F_{\tau,x} \varphi_{y,x}^R N_i N_j dV \\
&+ \int_V \bar{C}_{46} F_{\tau,x} \varphi_{y,y}^R N_i N_j dV + \int_V \bar{C}_{44} F_{\tau,z} \varphi_{y,y}^R N_i N_j dV + \int_V \bar{C}_{24} F_\tau \varphi_{y,y}^R N_{i,y} N_j dV,
\end{aligned} \tag{B.15}
$$

$$
\begin{aligned}
K_{xx}^{\phi sij} = &\int_V \bar{C}_{66}\,\phi_x^R F_s N_{i,y} N_{j,y} dV + \int_V \bar{C}_{55}\,\phi_{x,z}^R F_{s,z} N_i N_j dV + \int_V \bar{C}_{56}\,\phi_x^R F_{s,z} N_{i,y} N_j dV \\
&+ \int_V \bar{C}_{56}\,\phi_{x,z}^R F_s N_i N_{j,y} dV + \int_V \bar{C}_{15}\,\phi_{x,z}^R F_{s,x} N_i N_j dV + \int_V \bar{C}_{15}\,\phi_{x,x}^R F_{s,z} N_i N_j dV \\
&+ \int_V \bar{C}_{16}\,\phi_x^R F_{s,x} N_{i,y} N_j dV + \int_V \bar{C}_{16}\,\phi_{x,x}^R F_s N_i N_{j,y} dV + \int_V \bar{C}_{11}\,\phi_{x,x}^R F_{s,x} N_i N_j dV \\
&+ \int_V \bar{C}_{16}\,\phi_{x,y}^R F_{s,x} N_i N_j dV + \int_V \bar{C}_{56}\,\phi_{x,y}^R F_{s,z} N_i N_j dV + \int_V \bar{C}_{66}\,\phi_{x,y}^R F_s N_i N_{j,y} dV,
\end{aligned}
\tag{B.16}
$$

$$
\begin{aligned}
K_{xy}^{\phi sij} = &\int_V \bar{C}_{26}\,\phi_x^R F_s N_{i,y} N_{j,y} dV + \int_V \bar{C}_{45}\,\phi_{x,z}^R F_{s,z} N_i N_j dV + \int_V \bar{C}_{25}\,\phi_x^R F_{s,z} N_{i,y} N_j dV \\
&+ \int_V \bar{C}_{46}\,\phi_{x,z}^R F_s N_i N_{j,y} dV + \int_V \bar{C}_{14}\,\phi_{x,z}^R F_{s,x} N_i N_j dV + \int_V \bar{C}_{56}\,\phi_{x,x}^R F_{s,z} N_i N_j dV \\
&+ \int_V \bar{C}_{12}\,\phi_x^R F_{s,x} N_{i,y} N_j dV + \int_V \bar{C}_{66}\,\phi_{x,x}^R F_s N_i N_{j,y} dV + \int_V \bar{C}_{16}\,\phi_{x,x}^R F_{s,x} N_i N_j dV \\
&+ \int_V \bar{C}_{12}\,\phi_{x,y}^R F_{s,x} N_i N_j dV + \int_V \bar{C}_{25}\,\phi_{x,y}^R F_{s,z} N_i N_j dV + \int_V \bar{C}_{26}\,\phi_{x,y}^R F_s N_i N_{j,y} dV,
\end{aligned}
\tag{B.17}
$$

$$
\begin{aligned}
K_{xz}^{\phi sij} = &\int_V \bar{C}_{46}\,\phi_x^R F_s N_{i,y} N_{j,y} dV + \int_V \bar{C}_{35}\,\phi_{x,z}^R F_{s,z} N_i N_j dV + \int_V \bar{C}_{45}\,\phi_x^R F_{s,z} N_{i,y} N_j dV \\
&+ \int_V \bar{C}_{36}\,\phi_{x,z}^R F_s N_i N_{j,y} dV + \int_V \bar{C}_{13}\,\phi_{x,z}^R F_{s,x} N_i N_j dV + \int_V \bar{C}_{55}\,\phi_{x,x}^R F_{s,z} N_i N_j dV \\
&+ \int_V \bar{C}_{14}\,\phi_x^R F_{s,x} N_{i,y} N_j dV + \int_V \bar{C}_{56}\,\phi_{x,x}^R F_s N_i N_{j,y} dV + \int_V \bar{C}_{15}\,\phi_{x,x}^R F_{s,x} N_i N_j dV \\
&+ \int_V \bar{C}_{14}\,\phi_{x,y}^R F_{s,x} N_i N_j dV + \int_V \bar{C}_{45}\,\phi_{x,y}^R F_{s,z} N_i N_j dV + \int_V \bar{C}_{46}\,\phi_{x,y}^R F_s N_i N_{j,y} dV,
\end{aligned}
\tag{B.18}
$$

$$
\begin{aligned}
K_{yx}^{\phi sij} = &\int_V \bar{C}_{26}\,\phi_y^R F_s N_{i,y} N_{j,y} dV + \int_V \bar{C}_{45}\,\phi_{y,z}^R F_{s,z} N_i N_j dV + \int_V \bar{C}_{46}\,\phi_y^R F_{s,z} N_{i,y} N_j dV \\
&+ \int_V \bar{C}_{25}\,\phi_{y,z}^R F_s N_i N_{j,y} dV + \int_V \bar{C}_{56}\,\phi_{y,z}^R F_{s,x} N_i N_j dV + \int_V \bar{C}_{14}\,\phi_{y,x}^R F_{s,z} N_i N_j dV \\
&+ \int_V \bar{C}_{66}\,\phi_y^R F_{s,x} N_{i,y} N_j dV + \int_V \bar{C}_{12}\,\phi_{y,x}^R F_s N_i N_{j,y} dV + \int_V \bar{C}_{16}\,\phi_{y,x}^R F_{s,x} N_i N_j dV \\
&+ \int_V \bar{C}_{66}\,\phi_{y,y}^R F_{s,x} N_i N_j dV + \int_V \bar{C}_{46}\,\phi_{y,y}^R F_{s,z} N_i N_j dV + \int_V \bar{C}_{26}\,\phi_{y,y}^R F_s N_i N_{j,y} dV,
\end{aligned}
\tag{B.19}
$$

$$
\begin{aligned}
K_{yy}^{\phi sij} = &\int_V \bar{C}_{22}\,\phi_y^R F_s N_{i,y} N_{j,y} dV + \int_V \bar{C}_{44}\,\phi_{y,z}^R F_{s,z} N_i N_j dV + \int_V \bar{C}_{24}\,\phi_y^R F_{s,z} N_{i,y} N_j dV \\
&+ \int_V \bar{C}_{24}\,\phi_{y,z}^R F_s N_i N_{j,y} dV + \int_V \bar{C}_{46}\,\phi_{y,z}^R F_{s,x} N_i N_j dV + \int_V \bar{C}_{46}\,\phi_{y,x}^R F_{s,z} N_i N_j dV \\
&+ \int_V \bar{C}_{26}\,\phi_y^R F_{s,x} N_{i,y} N_j dV + \int_V \bar{C}_{26}\,\phi_{y,x}^R F_s N_i N_{j,y} dV + \int_V \bar{C}_{66}\,\phi_{y,x}^R F_{s,x} N_i N_j dV \\
&+ \int_V \bar{C}_{26}\,\phi_{y,y}^R F_{s,x} N_i N_j dV + \int_V \bar{C}_{24}\,\phi_{y,y}^R F_{s,z} N_i N_j dV + \int_V \bar{C}_{22}\,\phi_{y,y}^R F_s N_i N_{j,y} dV,
\end{aligned}
\tag{B.20}
$$

$$
\begin{aligned}
K_{yz}^{\phi s i j} = &\int_V \bar{C}_{24}\, \phi_y^R F_s N_{i,y} N_{j,y} dV + \int_V \bar{C}_{34}\, \phi_{y,z}^R F_{s,z} N_i N_j dV + \int_V \bar{C}_{44}\, \phi_y^R F_{s,z} N_{i,y} N_j dV \\
&+ \int_V \bar{C}_{23}\, \phi_{y,z}^R F_s N_i N_{j,y} dV + \int_V \bar{C}_{36}\, \phi_{y,z}^R F_{s,x} N_i N_j dV + \int_V \bar{C}_{45}\, \phi_{y,x}^R F_{s,z} N_i N_j dV \\
&+ \int_V \bar{C}_{46}\, \phi_y^R F_{s,x} N_{i,y} N_j dV + \int_V \bar{C}_{25}\, \phi_{y,x}^R F_s N_i N_{j,y} dV + \int_V \bar{C}_{56}\, \phi_{y,x}^R F_{s,x} N_i N_j dV \\
&+ \int_V \bar{C}_{46}\, \phi_{y,y}^R F_{s,x} N_i N_j dV + \int_V \bar{C}_{44}\, \phi_{y,y}^R F_{s,z} N_i N_j dV + \int_V \bar{C}_{24}\, \phi_{y,y}^R F_s N_i N_{j,y} dV,
\end{aligned}
\tag{B.21}
$$

$$
\begin{aligned}
K_{xx}^{\phi\varphi i j} = &\int_V \bar{C}_{66}\, \phi_x^R \varphi_x^R N_{i,y} N_{j,y} dV + \int_V \bar{C}_{55}\, \phi_{x,z}^R \varphi_{x,z}^R N_i N_j dV + \int_V \bar{C}_{56}\, \phi_x^R \varphi_{x,z}^R N_{i,y} N_j dV \\
&+ \int_V \bar{C}_{56}\, \phi_{x,z}^R \varphi_x^R N_i N_{j,y} dV + \int_V \bar{C}_{15}\, \phi_{x,z}^R \varphi_{x,x}^R N_i N_j dV + \int_V \bar{C}_{15}\, \phi_{x,x}^R \varphi_{x,z}^R N_i N_j dV \\
&+ \int_V \bar{C}_{16}\, \phi_x^R \varphi_{x,x}^R N_{i,y} N_j dV + \int_V \bar{C}_{16}\, \phi_{x,x}^R \varphi_x^R N_i N_{j,y} dV + \int_V \bar{C}_{11}\, \phi_{x,x}^R \varphi_{x,x}^R N_i N_j dV \\
&+ \int_V \bar{C}_{16}\, \phi_{x,x}^R \varphi_{x,y}^R N_i N_j dV + \int_V \bar{C}_{16}\, \phi_{x,y}^R \varphi_{x,x}^R N_i N_j dV + \int_V \bar{C}_{56}\, \phi_{x,y}^R \varphi_{x,z}^R N_i N_j dV \\
&+ \int_V \bar{C}_{56}\, \phi_{x,z}^R \varphi_{x,y}^R N_i N_j dV + \int_V \bar{C}_{66}\, \phi_{x,y}^R \varphi_{x,y}^R N_i N_j dV + \int_V \bar{C}_{66}\, \phi_x^R \varphi_{x,y}^R N_{i,y} N_j dV \\
&+ \int_V \bar{C}_{66}\, \phi_{x,y}^R \varphi_x^R N_i N_{j,y} dV,
\end{aligned}
\tag{B.22}
$$

$$
\begin{aligned}
K_{xy}^{\phi\varphi i j} = &\int_V \bar{C}_{26}\, \phi_x^R \varphi_y^R N_{i,y} N_{j,y} dV + \int_V \bar{C}_{45}\, \phi_{x,z}^R \varphi_{y,z}^R N_i N_j dV + \int_V \bar{C}_{25}\, \phi_x^R \varphi_{y,z}^R N_{i,y} N_j dV \\
&+ \int_V \bar{C}_{46}\, \phi_{x,z}^R \varphi_y^R N_i N_{j,y} dV + \int_V \bar{C}_{14}\, \phi_{x,z}^R \varphi_{y,x}^R N_i N_j dV + \int_V \bar{C}_{56}\, \phi_{x,x}^R \varphi_{y,z}^R N_i N_j dV \\
&+ \int_V \bar{C}_{12}\, \phi_x^R \varphi_{y,x}^R N_{i,y} N_j dV + \int_V \bar{C}_{66}\, \phi_{x,x}^R \varphi_y^R N_i N_{j,y} dV + \int_V \bar{C}_{16}\, \phi_{x,x}^R \varphi_{y,x}^R N_i N_j dV \\
&+ \int_V \bar{C}_{66}\, \phi_{x,x}^R \varphi_{y,y}^R N_i N_j dV + \int_V \bar{C}_{12}\, \phi_{x,y}^R \varphi_{y,x}^R N_i N_j dV + \int_V \bar{C}_{25}\, \phi_{x,y}^R \varphi_{y,z}^R N_i N_j dV \\
&+ \int_V \bar{C}_{46}\, \phi_{x,z}^R \varphi_{y,y}^R N_i N_j dV + \int_V \bar{C}_{26}\, \phi_{x,y}^R \varphi_{y,y}^R N_i N_j dV + \int_V \bar{C}_{26}\, \phi_x^R \varphi_{y,y}^R N_{i,y} N_j dV \\
&+ \int_V \bar{C}_{26}\, \phi_{x,y}^R \varphi_y^R N_i N_{j,y} dV,
\end{aligned}
\tag{B.23}
$$

$$
\begin{aligned}
K_{yx}^{\phi\varphi i j} = &\int_V \bar{C}_{26}\, \phi_y^R \varphi_x^R N_{i,y} N_{j,y} dV + \int_V \bar{C}_{45}\, \phi_{y,z}^R \varphi_{x,z}^R N_i N_j dV + \int_V \bar{C}_{46}\, \phi_y^R \varphi_{x,z}^R N_{i,y} N_j dV \\
&+ \int_V \bar{C}_{25}\, \phi_{y,z}^R \varphi_x^R N_i N_{j,y} dV + \int_V \bar{C}_{56}\, \phi_{y,z}^R \varphi_{x,x}^R N_i N_j dV + \int_V \bar{C}_{14}\, \phi_{y,x}^R \varphi_{x,z}^R N_i N_j dV \\
&+ \int_V \bar{C}_{66}\, \phi_y^R \varphi_{x,x}^R N_{i,y} N_j dV + \int_V \bar{C}_{12}\, \phi_{y,x}^R \varphi_x^R N_i N_{j,y} dV + \int_V \bar{C}_{16}\, \phi_{y,x}^R \varphi_{x,x}^R N_i N_j dV \\
&+ \int_V \bar{C}_{12}\, \phi_{y,x}^R \varphi_{x,y}^R N_i N_j dV + \int_V \bar{C}_{66}\, \phi_{y,y}^R \varphi_{x,x}^R N_i N_j dV + \int_V \bar{C}_{46}\, \phi_{y,y}^R \varphi_{x,z}^R N_i N_j dV \\
&+ \int_V \bar{C}_{25}\, \phi_{y,z}^R \varphi_{x,y}^R N_i N_j dV + \int_V \bar{C}_{26}\, \phi_{y,y}^R \varphi_{x,y}^R N_i N_j dV + \int_V \bar{C}_{26}\, \phi_y^R \varphi_{x,y}^R N_{i,y} N_j dV \\
&+ \int_V \bar{C}_{26}\, \phi_{y,y}^R \varphi_x^R N_i N_{j,y} dV,
\end{aligned}
\tag{B.24}
$$

$$
\begin{aligned}
K_{yy}^{\phi\varphi i j} = & \int_V \bar{C}_{22}\, \phi_y^R \varphi_y^R N_{i,y} N_{j,y} dV + \int_V \bar{C}_{44}\, \phi_{y,z}^R \varphi_{y,z}^R N_i N_j dV + \int_V \bar{C}_{24}\, \phi_y^R \varphi_{y,z}^R N_{i,y} N_j dV \\
& + \int_V \bar{C}_{24}\, \phi_{y,z}^R \varphi_y^R N_i N_{j,y} dV + \int_V \bar{C}_{46}\, \phi_{y,z}^R \varphi_{y,x}^R N_i N_j dV + \int_V \bar{C}_{46}\, \phi_{y,x}^R \varphi_{y,z}^R N_i N_j dV \\
& + \int_V \bar{C}_{26}\, \phi_y^R \varphi_{y,x}^R N_{i,y} N_j dV + \int_V \bar{C}_{26}\, \phi_{y,x}^R \varphi_y^R N_i N_{j,y} dV + \int_V \bar{C}_{66}\, \phi_{y,x}^R \varphi_{y,x}^R N_i N_j dV \\
& + \int_V \bar{C}_{26}\, \phi_{y,x}^R \varphi_{y,y}^R N_i N_j dV + \int_V \bar{C}_{26}\, \phi_{y,y}^R \varphi_{y,x}^R N_i N_j dV + \int_V \bar{C}_{24}\, \phi_{y,y}^R \varphi_{y,z}^R N_i N_j dV \\
& + \int_V \bar{C}_{24}\, \phi_{y,z}^R \varphi_{y,y}^R N_i N_j dV + \int_V \bar{C}_{22}\, \phi_{y,y}^R \varphi_{y,y}^R N_i N_j dV + \int_V \bar{C}_{22}\, \phi_y^R \varphi_{y,y}^R N_{i,y} N_j dV \\
& + \int_V \bar{C}_{22}\, \phi_{y,y}^R \varphi_y^R N_i N_{j,y} dV,
\end{aligned}
\tag{B.25}
$$

where $\bar{C}_{ij}$ are the material stiffness coefficients as described in Appendix A and intergrals are calculated using Gaussian quadrature. The above expressions (equations (B.10)–(B.25)) are applicable for the UF-RZT model. The stiffness matrix for the UF-MZZF model can be calculated by replacing ϕ_x^R and ϕ_y^R by ϕ^M and its variation φ_x^R and φ_y^R by φ^M.

APPENDIX C

SERENDIPITY LAGRANGE EXPANSION SHAPE FUNCTIONS

The explicit form of the Serendipity Lagrange expansion shape functions for the first five orders are given as follows

Order One:

$$F_1^{(\mathrm{I})} = \frac{1}{4}(1-\alpha)(1-\beta), \qquad F_2^{(\mathrm{I})} = \frac{1}{4}(1+\alpha)(1-\beta)$$
$$F_3^{(\mathrm{I})} = \frac{1}{4}(1+\alpha)(1+\beta), \qquad F_4^{(\mathrm{I})} = \frac{1}{4}(1-\alpha)(1+\beta).$$

Order Two:

$$F_5^{(\mathrm{IIA})} = \frac{1}{2}(1-\beta)(\alpha^2-1), \qquad F_6^{(\mathrm{IIA})} = \frac{1}{2}(1+\alpha)(\beta^2-1)$$
$$F_7^{(\mathrm{IIB})} = \frac{1}{2}(1+\beta)(\alpha^2-1), \qquad F_8^{(\mathrm{IIB})} = \frac{1}{2}(1-\alpha)(\beta^2-1).$$

Order Three:

$$F_9^{(\mathrm{IIA})} = \frac{1}{2}(1-\beta)(\alpha^3-\alpha), \qquad F_{10}^{(\mathrm{IIA})} = \frac{1}{2}(1+\alpha)(\beta^3-\beta)$$
$$F_{11}^{(\mathrm{IIB})} = \frac{1}{2}(1+\beta)(-\alpha^3+\alpha), \qquad F_{12}^{(\mathrm{IIB})} = \frac{1}{2}(1-\alpha)(-\beta^3+\beta).$$

Order Four:

$$F_{13}^{(\mathrm{IIA})} = \frac{1}{2}(1-\beta)(\alpha^4-\frac{10}{9}\alpha^2+\frac{1}{9}), \qquad F_{14}^{(\mathrm{IIA})} = \frac{1}{2}(1+\alpha)(\beta^4-\frac{10}{9}\beta^2+\frac{1}{9})$$
$$F_{15}^{(\mathrm{IIB})} = \frac{1}{2}(1+\beta)(\alpha^4-\frac{10}{9}\alpha^2+\frac{1}{9}), \qquad F_{16}^{(\mathrm{IIB})} = \frac{1}{2}(1-\alpha)(\beta^4-\frac{10}{9}\beta^2+\frac{1}{9})$$
$$F_{17}^{(\mathrm{III})} = (\alpha^2-1)(\beta^2-1).$$

Order Five:

$$F_{18}^{(\mathrm{IIA})} = \frac{1}{2}(1-\beta)(\alpha^5 - \frac{5}{4}\alpha^3 + \frac{1}{4}\alpha), \qquad F_{19}^{(\mathrm{IIA})} = \frac{1}{2}(1+\alpha)(\beta^5 - \frac{5}{4}\beta^3 + \frac{1}{4}\beta)$$

$$F_{20}^{(\mathrm{IIB})} = \frac{1}{2}(1+\beta)(-\alpha^5 + \frac{5}{4}\alpha^3 - \frac{1}{4}\alpha), \qquad F_{21}^{(\mathrm{IIB})} = \frac{1}{2}(1-\alpha)(-\beta^5 + \frac{5}{4}\beta^3 - \frac{1}{4}\beta)$$

$$F_{22}^{(\mathrm{III})} = (\alpha^2 - 1)(\beta^3 - \beta), \qquad F_{23}^{(\mathrm{III})} = (\beta^2 - 1)(\alpha^3 - \alpha).$$

APPENDIX D

HOOKE'S LAW FOR MODELLING PLANE STRAIN CONDITION

To mimic the plane-strain condition, required for Sections 5.2, 5.3 and 6.2, where strains in the x-direction are considered to be negligible, $\varepsilon_{xx} = \gamma_{xz} = \gamma_{xy} = 0$, the stress-strain stiffness relationship for a lamina becomes

$$\begin{Bmatrix} \sigma_{xx} \\ \sigma_{yy} \\ \sigma_{zz} \\ \tau_{yz} \\ \tau_{xz} \\ \tau_{xy} \end{Bmatrix} = \begin{bmatrix} \bar{C}_{11} & \bar{C}_{12} & \bar{C}_{13} & \bar{C}_{14} & \bar{C}_{15} & \bar{C}_{16} \\ \bar{C}_{21} & \bar{C}_{22} & \bar{C}_{23} & \bar{C}_{24} & \bar{C}_{25} & \bar{C}_{26} \\ \bar{C}_{31} & \bar{C}_{32} & \bar{C}_{33} & \bar{C}_{34} & \bar{C}_{35} & \bar{C}_{36} \\ \bar{C}_{41} & \bar{C}_{42} & \bar{C}_{43} & \bar{C}_{44} & \bar{C}_{45} & \bar{C}_{46} \\ \bar{C}_{51} & \bar{C}_{52} & \bar{C}_{53} & \bar{C}_{54} & \bar{C}_{55} & \bar{C}_{56} \\ \bar{C}_{61} & \bar{C}_{62} & \bar{C}_{63} & \bar{C}_{64} & \bar{C}_{65} & \bar{C}_{66} \end{bmatrix} \begin{Bmatrix} 0 \\ \varepsilon_{yy} \\ \varepsilon_{zz} \\ \gamma_{yz} \\ 0 \\ 0 \end{Bmatrix}. \tag{D.1}$$

The three zero strain entries in the strain vector indicate that their associated columns in the stiffness matrix (*i.e.* columns 1, 5, and 6) can be ignored. If the rows associated with the stress components with x-subscripts are also ignored, then, the stiffness matrix reduces to a simple 3×3 matrix, as given by

$$\begin{Bmatrix} \sigma_{yy} \\ \sigma_{zz} \\ \tau_{yz} \end{Bmatrix} = \begin{bmatrix} \bar{C}_{22} & \bar{C}_{23} & \bar{C}_{24} \\ \bar{C}_{32} & \bar{C}_{33} & \bar{C}_{34} \\ \bar{C}_{42} & \bar{C}_{43} & \bar{C}_{44} \end{bmatrix} \begin{Bmatrix} \varepsilon_{yy} \\ \varepsilon_{zz} \\ \gamma_{yz} \end{Bmatrix}. \tag{D.2}$$

In order to model the plane-strain behavior within the Unified Formulation framework, we use the following material stiffness matrix

$$\begin{Bmatrix} \sigma_{xx} \\ \sigma_{yy} \\ \sigma_{zz} \\ \tau_{yz} \\ \tau_{xz} \\ \tau_{xy} \end{Bmatrix} = \begin{bmatrix} \bar{C}_{11} & 0 & 0 & 0 & 0 & 0 \\ 0 & \bar{C}_{22} & \bar{C}_{23} & \bar{C}_{24} & 0 & 0 \\ 0 & \bar{C}_{32} & \bar{C}_{33} & \bar{C}_{34} & 0 & 0 \\ 0 & \bar{C}_{42} & \bar{C}_{43} & \bar{C}_{44} & 0 & 0 \\ 0 & 0 & 0 & 0 & \bar{C}_{55} & 0 \\ 0 & 0 & 0 & 0 & 0 & \bar{C}_{66} \end{bmatrix} \begin{Bmatrix} \varepsilon_{xx} \\ \varepsilon_{yy} \\ \varepsilon_{zz} \\ \gamma_{yz} \\ \gamma_{xz} \\ \gamma_{xy} \end{Bmatrix}. \tag{D.3}$$

BIBLIOGRAPHY

[1] C. C. Chamis, F. Abdi, M. Garg, L. Minnetyan, H. Baid, D. Huang, J. Housner, F. Talagani, Micromechanics-based progressive failure analysis prediction for WWFE-III composite coupon test cases, Journal of Composite Materials 47 (2013) 2695–2712.

[2] V. Mihai, S. Baetu, Comparative analysis of the bending theories for isotropic plates: Case study, Bulletin of the Polytechnic Institute of Jassy, CONSTRUCTIONS. ARCHITECTURE Section LXIII 3 (2013) 133–145.

[3] E. Carrera, M. Cinefra, M. Petrolo, E. Zappino, Finite Element Analysis of Structures through Unified Formulation, John Wiley & Sons Ltd., West Sussex, United Kingdom, 2014.

[4] B. Szabó, I. Babuška, Introduction to Finite Element Analysis: Formulation, Verification and Validation, Wiley, 2011.

[5] K. E. Bisshopp, D. C. Drucker, Large deflection of cantilever beams, Quarterly of Applied Mathematics 3 (1945) 272–275.

[6] J. D. Kemper, Large deflections of tapered cantilever beams, International Journal of Mechanical Sciences 10 (6) (1968) 469 – 478.

[7] G. S. Payette, J. N. Reddy, A seven-parameter spectral/hp finite element formulation for isotropic, laminated composite and functionally graded shell structures, Computer Methods in Applied Mechanics and Engineering 278 (2014) 664 – 704.

[8] C. Bisagni, R. Vescovini, C. G. Dávila, Single-stringer compression specimen for the assessment of damage tolerance of postbuckled structures, Journal of Aircraft 48 (2011) 495–502.

[9] G. Balduzzi, G. Hochreiner, J. Füssl, Stress recovery from one dimensional models for tapered bi-symmetric thin-walled I beams: Deficiencies in modern engineering tools and procedures, Thin-Walled Structures journal 119 (2017) 934–945.

[10] C. Thurnherr, L. Ruppen, G. Kress, P. Ermanni, Non-linear stiffness response of corrugated laminates in tensile loading, Composite Structures 157 (2016) 244–255.

[11] R. M. J. Groh, Non-classical effects in straight-fibre and tow-steered composite beams and plates, PhD thesis, Department of Aerospace Engineering,University of Bristol, 2015.

[12] G. Everstine, A. Pipkin, Stress channelling in transversely isotropic elastic composites, Zeitung fuer angewandte Mathematik und Physik (ZAMP) 22 (1971) 825 – 834.

[13] L. Euler, De curvis elasticis, Bousquet, Geneva, 1744.

[14] S. P. Timoshenko, On the corrections for shear of the differential equation for transverse vibration of prismatic bars, The London, Edinburgh, and Dublin Philosophical Magazine and Journal of Science 41:245 (1921) 744–746.

[15] S. P. Timoshenko, On the transverse vibrations of bars of uniform cross-section, The London, Edinburgh, and Dublin Philosophical Magazine and Journal of Science 43:253 (1922) 125–131.

[16] D. Mucichescu, Bounds for stiffness of prismatic beams, Journal of Structural Engineering 110 (1984) 1410–1414.

[17] S. P. Timoshenko, J. N. Goodier, Theory of elasticity, New York: McGraw-Hill, 1970.

[18] G. R. Cowper, The Shear Coefficient in Timoshenko's Beam Theory, Journal of Applied Mechanics 33.2 (1966) 335–340.

[19] I. S. Sokolnikoff, Mathematical Theory of Elasticity, New York: McGraw-Hill, 1956.

[20] A. V. K. Murty, On the shear deformation theory for dynamic analysis of beams, Journal of Sound and Vibration 101 (1985) 1–12.

[21] F. F. Pai, M. J. Schulz, Shear correction factors and an energy consistent beam theory, International Journal of Solids and Structures 36 (1999) 1523–1540.

[22] I. Mechab, A. Tounsi, M. A. Benatta, E. A. Bedia, Deformation of short composite beam using refined theories, Journal of Mathematical Analysis and Applications 346 (2008) 468–479.

[23] F. Gruttmann, R. Sauer, W. Wagner, Shear stresses in prismatic beams with arbitrary cross-sections, International Journal for Numerical Methods in Engineering 45 (1999) 865–889.

[24] F. Gruttmann, W. Wagner, Shear correction factors in Timoshenko's beam theory for arbitrary shaped cross-sections, Computational Mechanics 27 (2001) 199–207.

[25] W. Wagner, F. Gruttmann, A displacement method for the analysis of flexural shear stresses in thin-walled isotropic composite beams, Computers & Structures 80 (2002) 199–207.

[26] J. Prescott, Elastic waves and vibrations in thin rods, Philosophical Magazine 33 (1942) 703 – 754.

[27] G. Kennedy, J. Hansen, J. Mart, A Timoshenko beam theory with pressure corrections for layered orthotropic beams, International Journal of Solids and Structures 48 (2011) 2373 – 2382.

[28] R. M. J. Groh, P. M. Weaver, Static inconsistencies in certain axiomatic higher-order shear deformation theories for beams, plates and shells, Composite Structures 120 (2015) 231 – 245.

[29] K. Washizu, Variational methods in elasticity and plasticity, Elsevier Science and Technology, Oxford, New York, 1968.

[30] M. Levinson, A new rectangular beam theory, Journal of Sound and Vibration 74 (1981) 81–87.

[31] J. N. Reddy, A refined nonlinear theory of plates with transverse shear deformation, International Journal of Solids and Structures 20 (1983) 881–896.

[32] de Saint-Venant A., Mèmoire sur la flexion des prismes, Journal de Mathèmatiques pures et appliquès 1 (1856) 89–189.

[33] P. Ladevèze, J. Simmonds, De nouveaux concepts en théorie des poutres pour des charges et des géométries quelconques, Comptes Rendus de l'Académie des Sciences 332 (1996) 445–462.

[34] P. Ladevèze, J. Simmonds, New concepts for linear beam theory with arbitrary geometry and loading, European Journal of Mechanics, A/Solids 17 (3) (1998) 377–402.

[35] Iesan, On Saint-Venant's problem, Archive for Rational Mechanics and Analysis 91 (1986) 363–373.

[36] S. B. Dong, J. B. Kosmatka, H. C. Lin, On Saint-Venant's problem for an inhomogeneous, anisotropic cylinder-Part I: Methodology for Saint-Venant solutions, Journal of Applied Mechanics 68 (2001) 376–381.

[37] J. B. Kosmatka, H. C. Lin, S. B. Dong, On Saint-Venant's problem for an inhomogeneous, anisotropic cylinder-Part II: Cross-sectional properties, Journal of Applied Mechanics 68 (2001) 382–391.

[38] V. Berdichevsky, Equations of the theory of anisotropic inhomogeneous rods, Doklady Akademii Nauk 228 (1976) 558–561.

[39] V. L. Berdichevsky, E. Armanios, A. Badir, Theory of anisotropic thin-walled closed-cross-section beams, Composites Engineering 2.5-7 (1992) 411–432.

[40] W. Yu, V. V. Volovoi, D. H. Hodges, X. Hong, Validation of the Variational Asymptotic Beam Sectional Analysis, AIAA Journal 40(10) (2002) 2105–2112.

[41] W. Yu, D. H. Hodges, J. C. Ho, Variational asymptotic beam sectional analysis - An updated version, International Journal of Engineering Science 59 (2012) 40–64.

[42] E. Carrera, Theories and finite elements for multilayered, anisotropic, composite plates and shells, Archives of Computational Methods in Engineering 9 (2002) 87–140.

[43] N. Silvestre, D. Camotim, First-order generalised beam theory for arbitrary orthotropic materials, Thin Walled Structures 40.9 (2002) 791–820.

[44] E. Carrera, G. Giunta, Refined beam theories based on a unified formulation, International Journal of Applied Mechanics 02 (2010) 117–143.

[45] E. Carrera, G. Giunta, M. Petrolo, A Modern and Compact Way to Formulate Classical and Advanced Beam Theories, Saxe-Coburg Publications, United Kingdom, 2010.

[46] E. Carrera, A class of two-dimensional theories for anisotropic multilayered plates analysis, Acc. Sc. Torino 19-20 (1995) 1–39.

[47] E. Carrera, M. Filippi, E. Zappino, Laminated beam analysis by polynomial, trigonometric, exponential and zig-zag theories, European Journal of Mechanics, A/Solids 41 (2013) 58–69.

[48] M. Filippi, A. Pagani, M. Petrolo, G. Colonna, E. Carrera, Static and free vibration analysis of laminated beams by refined theory based on Chebyshev polynomials, Composite Structures 132 (2015) 1248–1259.

[49] A. Pagani, A. G. de Miguel, M. Petrolo, E. Carrera, Analysis of laminated beams via Unified Formulation and Legendre polynomial expansions, Composite Structures 156 (2016) 78–92.

[50] L. Demasi, ∞^3 hierarchy plate theories for thick and thin composite plates: The generalized unified formulation, Composite Structures 84 (2008) 256–270.

[51] L. Demasi, Invariant finite element model for composite structures: The generalized unified formulation, AIAA Journal 48 (2010) 1602–1619.

[52] E. Carrera, E. Zappino, Carrera Unified Formulation for Free-Vibration Analysis of Aircraft Structures, AIAA Journal 54 (2016) 280 – 292.

[53] S. Brischetto, E. Carrera, L. Demasi, Improved bending analysis of sandwich plates using zig-zag functions, Composite Structures 89 (2009) 408 – 415.

[54] M. D. Sciuva, A refinement of the transverse shear deformation theory for multilayered orthotropic plates, L'aerotecnica missile e spazio 62 (1984) 84–92.

[55] R. M. Jones, Mechanics of Composite Materials, Taylor & Francis Ltd., London, UK, 1998.

[56] R. D. Mindlin, Influence of rotary inertia and shear on flexural motion of isotropic elastic plates, Journal of Applied Mechanics 18 (1951) 31–38.

[57] J. M. Whitney, N. J. Pagano, Shear deformation in heterogeneous anisotropic plates, Journal of Applied Mechanics 37 (1970) 1031–1036.

[58] J. N. Reddy, A simple higher order theory for laminated composites, Journal of Applied Mechanics 51 (1984) 745–752.

[59] K. Lo, R. Christensen, E. Wu, A high-order theory of plate deformation, Journal of Applied Mechanics 44 (4) (1977) 669–676.

[60] P. Seide, An improved approximate theory for the bending of laminated plates, Mechanics Today 5 (1980) 451–466.

[61] S. Srinivas, Refined analysis of laminated composites, Journal of Sound and Vibration 30 (1973) 495–507.

[62] A. Nosier, R. K. Kapania, J. N. Reddy, Free vibration analysis of laminated plates using a layer-wise theory, American Institute of Aeronautics and Astronautics 31 (1993) 2335–2346.

[63] G. W. Swift, R. A. Heller, Layered beam analysis, Journal of the Engineering Mechanics Division 100 (1974) 267 – 282.

[64] J. N. Reddy, D. Robbins, Theories and computational models for composite laminates, Applied Mechanics Review 47 (1994) 147–169.

[65] M. D. Sciuva, U. Icardi, Discrete-layer models for multilayered shells accounting for interlayer continuity, Meccanica 28 (1993) 281–291.

[66] D. Owen, Z. Li, A refined analysis of laminated plates by finite element displacement methods—I. Fundamentals and static analysis, Computers and Structures 26 (1987) 907–914.

[67] A. J. M. Ferreira, Analysis of composite plates using a layerwise theory and multiquadrics discretization, Mechanics of Advanced Materials and Structures 12 (2005) 99–112.

[68] A. J. M. Ferreira, C. M. C. Roque, R. M. N. Jorge, E. J. Kansa, Static deformations and vibration analysis of composite and sandwich plates using a layerwise theory and multiquadrics discretizations, Engineering Analysis with Boundary Elements 29 (2005) 1104–1114.

[69] T. S. Plagianakos, D. A. Saravanos, Higher-order layerwise laminate theory for the prediction of interlaminar shear stresses in thick composite and sandwich composite plates, Composite Structures 87 (2009) 23–35.

[70] M. Cetkovic, Thermal buckling of laminated composite plates using layerwise displacement model, Composite Structures 142 (2016) 238–253.

[71] F. Tornabene, N. Fantuzzi, M. Bacciocchi, E. Viola, Accurate inter-laminar recovery for plates and doubly-curved shells with variable radii of curvature using layer-wise theories, Composite Structures 124 (2015) 368 – 393.

[72] F. Tornabene, General higher-order layer-wise theory for free vibrations of doubly-curved laminated composite shells and panels, Mechanics of Advanced Materials and Structures 23 (2016) 1046 – 1067.

[73] K. M. Liew, Z. Z. Pan, L. W. Zhang, An overview of layerwise theories for composite laminates and structures: Development ,numerical implementation and application, Composite Structures 216 (2019) 240–259.

[74] O. O. Ochoa, J. N. Reddy, Finite Element Analysis of Composite Laminates, Kluwer, Dordrecht, The Netherlands, 1992.

[75] M. V. V. Murthy, An improved transverse shear deformation theory for laminated anisotropic plates, NASA Technical Paper 1903 (1981) 1–37.

[76] G. M. Kulikov, S. V. Plotnikova, Equivalent Single-Layer and Layerwise Shell Theories and Rigid-Body Motions — Part II: Computational Aspects, Mechanics of Advanced Materials and Structures 12 (2005) 331–340.

[77] M. R. T. Arrudaa, M. S. Castro, A. J. M. Ferreira, M. Garrido, J. Gonilha, J. R. Correia, Analysis of composite layered beams using Carrera unified formulation with Legendre approximation, Composites Part B: Engineering 137 (2018) 39–50.

[78] E. Carrera, Historical review of Zig-Zag theories for multilayered plates and shells, Applied Mechanics Reviews 56(3) (2003) 287–308.

[79] S. G. Lekhnitskii, Strength calculation of composite beams, Vestn. Inzh. Tekh., 1935.

[80] J. G. Ren, A new theory of laminated plates, Composites Science and Technology 26 (1986) 225–239.

[81] S. A. Ambartsumyan, Theory of anisotropic plates: strength, stability, vibration, Technomic Publishing Company, 1970.

[82] E. Carrera, Developments, ideas and evaluations based upon reissner's mixed variational theorem in the modeling of multilayered plates and shells, Composite Structures 37 (1997) 373–383.

[83] E. Carrera, On the use of the murakami's zig-zag function in the modeling of layered plates and shells, Computers and Structures 82 (2004) 541 – 554.

[84] L. Demasi, Refined multilayered plate elements based on murakami zig-zag function, Composite Structures 70 (2005) 308 – 316.

[85] M. Ganapathi, B. P. Patel, D. S. Pawargi, Dynamic analysis of laminated cross-ply composite non-circular thick cylindrical shells using higher-order theory, International Journal of Solids and Structures 39 (2002) 5945 – 5962.

[86] M. Gherlone, On the use of zigzag functions in equivalent single layer theories for laminated composite and sandwich beams: A comparative study and some observations on external weak layers, Journal of Applied Mechanics 80 (2013) JAM–12–1229.

[87] A. Tessler, M. di Sciuva, M. Gherlone, Refinement of Timoshenko beam theory for composite and sandwich beams using zigzag kinematics, National Aeronautics and Space Administration 215086.

[88] A. Tessler, M. di Sciuva, M. Gherlone, A refined zigzag beam theory for composite and sandwich beams, Journal of Composite Materials 43 (2009) 1051–1081.

[89] R. M. J. Groh, P. M. Weaver, On displacement-based and mixed-variational equivalent single layer theories for modelling highly heterogeneous laminated beams, International Journal of Solids and Structures 59 (2015) 147–170.

[90] R. M. J. Groh, A. Tessler, Computationally efficient beam elements for accurate stresses in sandwich laminates and laminated composites with delaminations, Computer Methods in Applied Mechanics and Engineering 320 (2017) 369–395.

[91] J. Whiteny, Stress analysis of thick laminated composite and sandwich plates, Journal of Composite Materials 6 (1972) 426–440.

[92] E. Carrera, A priori vs. a posteriori evaluation of transverse stresses in multilayered orthotropic plates, Composite Structures 48 (2000) 245–260.

[93] H. Stolarski, T. Belytschko, On the equivalence of mode decomposition and mixed finite elements based on the hellinger-reissner principle. part i: Theory, Computer Methods in Applied Mechanics and Engineering 58 (1986) 249–263.

[94] E. Reissner, On a certain mixed variational theorem and a proposed application, International Journal for Numerical Methods in Engineering 20(7) (1984) 1366–1368.

[95] E. Reissner, On a mixed variational theorem and on a shear deformable plate theory, International Journal for Numerical Methods in Engineering 23 (1986) 193–198.

[96] Z. Gürdal, R. Olmedo, In-plane response of laminates with spatially varying fiber orientations: variable stiffness concept, AIAA Journal 31(4) (1993) 751 – 758.

[97] P. Ribeiro, H. Akhavan, A. Teter, J. Warmiński, A review on the mechanical behaviour of curvilinear fibre composite laminated panels, Journal of Composite Materials 48 (2014) 2761 – 2777.

[98] L. Bittrich, A. Spickenheuer, J. H. S. Almeida, S. Müller, L. Kroll, G. Heinrich, Optimizing Variable-Axial Fiber-Reinforced Composite Laminates: The Direct Fiber Path Optimization Concept, Mathematical Problems in Engineering 2019 (2019) 1 – 12.

[99] A. A. G. Cooper, Trajectorial fiber reinforcement of composite structures, PhD thesis, Department of Mechanical and Aerospace Engineering, Washington University, 1972.

[100] H. Ghiasi, K. Fayazbakhsh, D. Pasini, L. Lessard, Optimum stacking sequence design of composite materials Part II: Variable stiffness design, Composite Structures 93 (2010) 1 – 13.

[101] M. Rouhi, H. Ghayoor, S. V. Hoa, M. Hojjati, P. M. Weaver, Stiffness tailoring of elliptical composite cylinders for axial buckling performance, Composite Structures 150 (2016) 115 – 123.

[102] M. W. Hyer, H. Lee, The use of curvilinear fiber format to improve buckling resistance of composite plates with central circular holes, Composite Structures 18 (1991) 239 – 261.

[103] S. Setoodeh, M. M. Abdalla, S. T. IJsselmuiden, Z. Gürdal, Design of variable-stiffness composite panels for maximum buckling load, Composite Structures 87 (2009) 109 – 117.

[104] M. W. Hyer, R. F. Charette, Use of curvilinear fiber format in composite structure design, AIAA Journal 29 (1991) 1011 – 1015.

[105] C. S. Lopes, Z. Gürdal, P. P. Camanhoc, Tailoring for strength of composite steered-fibre panels with cutouts, Composites, Part A: Applied Science and Manufacturing 41 (2010) 1760 – 1767.

[106] Z. Gürdal, B. Tatting, C. Wu, Variable stiffness composite panels: Effects of stiffness variation on the in-plane and buckling response, Composites, Part A: Applied Science and Manufacturing 39 (2008) 911 – 922.

[107] Z. Wu, P. M. Weaver, G. Raju, B. C. Kim, Buckling Analysis and Optimisation of Variable Angle Tow Composite Plates, Thin-Walled Structures 60 (2012) 163 – 172.

[108] Z. Wu, G. Raju, P. M. Weaver, Framework for the buckling optimization of variable angle tow composite plates, AIAA Journal 53 (2015) 1 – 17.

[109] G. Raju, S. White, Z. Wu, Optimal postbuckling design of variable angle tow composites using lamination parameters, In Proceedings of the 56th AIAA/ASME/ASCE/AHS/ASC Structures, Structural Dynamics and Materials Conference, Kissimmee, Florida, USA.

[110] P. Hao, C. Liu, X. Yuan, B. Wang, G. Li, T. Zhu, F. Niu, Buckling optimization of variable-stiffness composite panels based on flow field function, Composite Structures 181 (2017) 240 – 255.

[111] Z. Stodieck, J. E. Cooper, P. M. Weaver, P. Kealy, Improved aeroelastic tailoring using tow-steered composites, Composite Structures 106 (2013) 703–715.

[112] B. H. Coburn, Z. Wu, P. M. Weaver, Buckling analysis of stiffened variable angle tow panels, Composite Structures 111 (2014) 259 – 270.

[113] S. Scott, M. Capuzzi, D. Langston, E. Bossanyi, G. McCann, P. M. Weaver, A. Pirrera, Effects of aeroelastic tailoring on performance characteristics of wind turbine systems, Renewable Energy 114 (2017) 887–903.

[114] M. M. Abdalla, S. Setoodeh, Z. Gürdal, Design of variable stiffness composite panels for maximum fundamental frequency using lamination parameters, Composite Structures 81 (2007) 283 – 291.

[115] A. W. Blom, S. Setoodeh, J. M. A. M. Hol, Z. Gürdal, Design of variable-stiffness conical shells for maximum fundamental eigen frequency, Composite Structures 86 (2008) 870 – 878.

[116] H. Akhavan, P. Ribeiro, Natural modes of vibration of variable stiffness composite laminates with curvilinear fibers, Composite Structures 93 (2011) 3040 – 3047.

[117] P. Ribeiro, Non-linear free periodic vibrations of variable stiffness composite laminated plates, Nonlinear Dynamics 70 (2012) 1535 – 1548.

[118] Z. Wu, P. M. Weaver, G. Raju, Postbuckling optimisation of variable angle tow composite plates, Composite Structures 103 (2013) 34 – 42.

[119] Z. Xin, Y. Duan, W. Xu, T. Zhang, B. Wang, Review of the mechanical performance of variable stiffness design fiber-reinforced composites, Science and Engineering of Composite Materials 25(3) (2016) 425 – 437.

[120] R. M. J. Groh, P. M. Weaver, Deleterious localized stress fields: the effects of boundaries and stiffness tailoring in anisotropic laminated plates, Proceedings of the Royal Society A, Mathematical, Physical and Engineering Sciences 472 (2194) (2016) 1 – 22.

[121] A. H. Akbarzadeh, M. A. Nik, D. Pasini, The role of shear deformation in laminated plates with curvilinear fiber paths and embedded defects, Composite Structures 118 (2014) 217 – 227.

[122] H. Akhavan, P. Ribeiro, Non-linear vibrations of variable stiffness composite laminated plates, Composite Structures 94 (2012) 2424 – 2432.

[123] H. Akhavan, P. Ribeiro, M. F. S. F. de Moura, Large deflection and stresses in variable stiffness composite laminates with curvilinear fibre, International Journal of Mechanical Sciences 73 (2013) 14 – 26.

[124] J. Díaz, C. Fagiano, M. M. Abdalla, Z. Gürdal, S. Hernández, A study of interlaminar stresses in variable stiffness plates, Composite Structures 94 (2012) 1192 – 1199.

[125] A. Soriano, J. Díaz, Failure analysis of variable stiffness composite plates using continuum damage mechanics models, Composite Structures 184 (2018) 1071 – 1080.

[126] L. Demasi, G. Biagini, F. Vannucci, E. Santarpia, R. Cavallaro, Equivalent single layer, zigzag, and layer wise theories for variable angle tow composites based on the generalized unified formulation, Composite Structures 177 (2017) 54 – 79.

[127] L. Demasi, Hierarchy plate theories for thick and thin composite plates: The generalized unified formulation, Composite Structures 84 (2008) 256–270.

[128] F. Tornabene, N. Fantuzzi, M. Bacciocchi, E. Viola, Higher-order theories for the free vibrations of doubly-curved laminated panels with curvilinear reinforcing fibers by means of a local version of the gdq method, Composites Part B: Engineering 81 (2015) 196 – 230.

[129] F. Tornabene, M. Bacciocchi, Effect of Curvilinear Reinforcing Fibers on the Linear Static Behavior of Soft-Core Sandwich Structures, Journal of Composites Science 2(14) (2018) 1 – 43.

[130] R. M. J. Groh, P. M. Weaver, A computationally efficient 2D model for inherently equilibrated 3D stress predictions in heterogeneous laminated plates. Part I: Model formulation, Composite Structures 156 (2016) 171–185.

[131] G. Raju, Z. Wu, B. C. Kim, P. M. Weaver, Prebuckling and buckling analysis of variable angle tow plates with general boundary conditions, Composite Structures 94 (2012) 2961 – 2970.

[132] R. Vescovini, C. G. Dávila, C. Bisagni, Failure analysis of composite multi-stringer panels using simplified models, Composites Part B: Engineering 45 (2013) 939–951.

[133] M. J. Hinton, P. D. Soden, Failure criteria for composite laminates, Composite Science and Technology 58 (1998) 1001–1010.

[134] J. N. Reddy, A. K. Pandey, A first-ply failure analysis of composite laminate, Composite Structures 25 (1987) 371–393.

[135] Y. S. N. Reddy, J. N. Reddy, Linear and non-linear failure analysis of composite laminates with transverse shear, Composite Science and Technology 44 (1992) 227–255.

[136] Y. S. N. Reddy, J. N. Reddy, Three-dimensional finite element progressive failure analysis of composite laminates under axial extension, Journal of Composite Technology 15 (1993) 73–87.

[137] P. Maimí, P. P. Camanho, J. A. Mayugo, C. G. Dávila, A continuum damage model for composite laminates: Part I – Constitutive model, Mechanics of Materials 39 (2007) 897–908.

[138] G. Catalanotti, P. P. Camanho, A. T. Marques, Three-dimensional failure criteria for fiber-reinforced laminates, Composite Structures 95 (2013) 63–79.

[139] M. Meng, H. R. Le, M. J. Rizvi, S. M. Grove, 3d FEA modelling of laminated composites in bending and their failure mechanisms, Composite Structures 119 (2015) 693–708.

[140] A. G. de Miguel, I. Kaleel, M. H. Nagaraj, A. Pagani, M. Petrolo, E. Carrera, Accurate evaluation of failure indices of composite layered structures via various fe models, Composites Science and Technology 167 (2018) 174–189.

[141] N. S. Putcha, J. N. Reddy, A refined mixed shear flexible finite element for the nonlinear analysis of laminated plates, Computers and Structures 22 (1986) 529–538.

[142] E. J. Barbero, J. N. Reddy, Nonlinear analysis of composite laminates using a generalized laminated plate theory, AIAA Journal 28 (1990) 1987–1994.

[143] K. Lee, S. W. Lee, A postprocessing approach to determine transverse stresses in geometrically nonlinear composite and sandwich structures, Journal of Composite Material 37 (2003) 2207–2224.

[144] Y. X. Zhang, K. S. Kim, A simple displacement-based 3-node triangular element for linear and geometrically nonlinear analysis of laminated composite plates, Computational Methods in Applied Mechanics 194 (2005) 4607–4632.

[145] Y. X. Zhang, C. H. Yang, Recent developments in finite element analysis for laminated composite plates, Composite Structures 88 (2009) 147–157.

[146] A. Pagani, E. Carrera, Large-deflection and post-buckling analyses of laminated composite beams by Carrera Unified Formulation, Composite Structures 170 (2017) 40 – 52.

[147] A. Pagani, E. Carrera, Unified formulation of geometrically nonlinear refined beam theories, Mechanics of Advanced Materials and Structures 25 (1) (2018) 15 – 31.

[148] Y. Hui, G. D. Pietro, G. Giunta, S. Belouettar, H. Hu, E. Carrera, A. Pagani, Geometrically nonlinear analysis of beam structures via hierarchical one-dimensional finite elements, Mathematical Problems in Engineering 2018 (2018) 1–22.

[149] S. Minera, M. Patni, E. Carrera, M. Petrolo, P. M. Weaver, A. Pirrera, Three-dimensional stress analysis for beam-like structures using serendipity lagrange shape functions, International Journal of Solids and Structures 141-142 (2018) 279 – 296.

[150] B. Kim, A. Oliver, J. Vyse, Bending Stresses of Steel Web Tapered Tee Section Cantilevers, Journal of Civil Engineering and Architecture 7 (11) (2013) 1329–1342.

[151] A. Beltempo, G. Balduzzi, G. Alfano, F. Auricchio, Analytical derivation of a general 2D non-prismatic beam model based on the Hellinger-Reissner principle, Engineering Structures 101 (2015) 88–98.

[152] G. Balduzzi, M. Aminbaghai, E. Sacco, J. Füssl, J. Eberhardsteiner, F. Auricchio, Non-prismatic beams: a simple and effective Timoshenko-like model, International Journal of Solids and Structures 90 (2016) 236–250.

[153] V. Mercuri, G. Balduzzi, D. Asprone, F. Auricchio, 2D non-prismatic beam model for stiffness matrix evaluation, In Proceedings of the Word Conference on Timber Engineering.

[154] D. H. Hodges, A. Rajagopal, J. C. Ho, W. Yu, Stress and strain recovery for the in-plane deformation of an isotropic tapered strip-beam, Journal of Mechanics of Materials and Structures 5 (2010) 963–975.

[155] T. H. Trinh, B. S. Gan, Development of consistent shape functions for linearly solid tapered Timoshenko beam, Journal of Structural and Construction Engineering 80 (2015) 1103–1111.

[156] G. Balduzzi, M. Aminbaghai, E. Sacco, J. Füssl, Planar Timoshenko-like model for multi-layer non-prismatic beams, International Journal of Mechanics and Materials in Design 14 (2018) 51–70.

[157] A. P. Gupta, K. P. Sharma, Bending of a Sandwich Annular Plate of Variable Thickness, Indian Journal of Pure and Applied Mathematics 13 (1982) 1313–1321.

[158] N. Paydar, C. Libove, Stress Analysis of Sandwich Plates of Variable Thickness, Journal of Applied Mechanics 55 (1988) 419–424.

[159] C. Libove, C. H. Lu, Beamlike Bending of Variable-thickness Sandwich Plates, AIA Journal 12 (1989) 1617–1618.

[160] C. H. Lu, Bending of Anisotropic Sandwich Beams with Variable Thickness, Journal of Thermoplastic Composite Materials 7 (1994) 364–374.

[161] D. Peled, Y. Frostig, High-order Bending of Sandwich Beams with Variable Flexible Core and Nonparallel Skins, ASCE Journal of Engineering Mechanics 120 (1994) 1255–1269.

[162] S. V. Hoa, B. L. Du, T. Vu-Khanh, Interlaminar stresses in tapered laminates, Polymer Composites 9 (1988) 337–344.

[163] J. S. Jeon, C. S. Hong, Bending of tapered anisotropic sandwich plates with arbitrary edge conditions, AIAA Journal 30 (1992) 1762–1769.

[164] Q. Ai, P. M. Weaver, Simplified analytical model for tapered sandwich beams using variable stiffness materials, Journal of Sandwich Structures and Materials 19 (2017) 3–25.

[165] T. Belytschko, L. W. Glaum, Applications of higher order corotational stretch theories to nonlinear finite element analysis, Computers & Structures 10 (1-2) (1979) 175–182.

[166] L. W. Glaum, Direct Iteration and Perturbation Methods for the Analysis of Nonlinear Structures, Ph.D. thesis, University of Illinois at Chicago (1976).

[167] K. S. Surana, R. M. Sorem, Geometrically non-linear formulation for three dimensional curved beam elements with large rotations, International Journal for Numerical Methods in Engineering 28 (1) (1989) 43–73.

[168] A. Ibrahimbegović, On finite element implementation of geometrically nonlinear reissner's beam theory: three-dimensional curved beam elements, Computer methods in applied mechanics and engineering 122 (1-2) (1995) 11–26.

[169] A. Ibrahimbegović, F. Frey, Finite element analysis of linear and non-linear planar deformations of elastic initially curved beams, International journal for numerical methods in engineering 36 (19) (1993) 3239–3258.

[170] E. Petrov, M. Géradin, Finite element theory for curved and twisted beams based on exact solutions for three-dimensional solids part 1: Beam concept and geometrically exact nonlinear formulation, Computer methods in applied mechanics and engineering 165 (1-4) (1998) 43–92.

[171] A. M. Yu, J. W. Yang, G. H. Nie, X. G. Yang, An improved model for naturally curved and twisted composite beams with closed thin-walled sections, Composite Structures 93 (9) (2011) 2322–2329.

[172] C. N. Chen, DQEM analysis of in-plane vibration of curved beam structures, Advances in Engineering Software 36 (6) (2005) 412–424.

[173] G. Karami, P. Malekzadeh, In-plane free vibration analysis of circular arches with varying cross-sections using differential quadrature method, Journal of Sound and Vibration 274 (2004) 777–799.

[174] M. A. D. Rosa, C. Franciosi, Exact and approximate analysis of circular arches using DQM, International Journal of Solids and Structures 37 (2000) 1103–1117.

[175] S. Ghuku, K. N. Saha, A review on stress and deformation analysis of curved beams under large deflection, International Journal of Engineering and Technology 11 (2017) 13–39.

[176] M. Patni, S. Minera, C. Bisagni, P. M. Weaver, A. Pirrera, Geometrically nonlinear finite element model for predicting failure in composite structures, Composite Structures 225 (2019) 111068.

[177] M. Patni, S. Minera, R. M. J. Groh, A. Pirrera, P. M. Weaver, Three-dimensional stress analysis for laminated composite and sandwich structures, Composites Part B: Engineering 155 (2018) 299–328.

[178] M. Patni, S. Minera, R. M. J. Groh, A. Pirrera, P. M. Weaver, On the accuracy of localised 3D stress fields in tow-steered laminated composite structures, Composite Structures 225 (2019) 111034.

[179] I. Kaleel, M. Petrolo, A. M. Waas, E. Carrera, Micromechanical progressive failure analysis of fiber-reinforced composite using refined beam models, Journal of Applied Mechanics,s 85 (2018) 1–8.

[180] A. Pagani, Y. Yan, E. Carrera, Exact solutions for free vibration analysis of laminated, box and sandwich beams by refined layer-wise theory, Composites Part B: Engineering 131 (2017) 62 – 75.

[181] E. Carrera, A. Pagani, J. R. Banerjee, Linearized buckling analysis of isotropic and composite beam-columns by Carrera Unified Formulation and dynamic stiffness method, Mechanics of Advanced Materials and Structures 23 (2016) 1092–1103.

[182] E. Zappino, A. Viglietti, E. Carrera, Analysis of tapered composite structures using a refined beam theory, Composite Structures 183 (2018) 42–52.

[183] E. Zappino, A. Viglietti, E. Carrera, The analysis of tapered structures using a component-wise approach based on refined one-dimensional models, Aerospace Science and Technology 65 (2017) 141–156.

[184] G. D. Pietro, A. G. de Miguel, E. Carrera, G. Giunta, S. Belouettar, A. Pagani, Strong and weak form solutions of curved beams via Carrera's unified formulation, Mechanics of Advanced Materials and Structures (2018) 1–13.

[185] E. Kreyszig, Advanced Engineering Mathematics, Wiley, 2011.

[186] E. Carrera, M. Petrolo, Refined One-Dimensional Formulations for Laminated Structure Analysis, AIAA Journal 50 (1) (2012) 176–189.

[187] J. Boyd, R. Petschek, The relationships between chebyshev, legendre and jacobi polynomials: The generic superiority of chebyshev polynomials and three important exceptions., J. Sci. Comput 59 (1) (2014) 1–27.

[188] T. J. Rivlin, W. M. Wayne, An optimal property of chebyshev expansions, Journal of Approximation Theory 2 (1969) 312 – 317.

[189] G. B. Arfken, H. J. Weber, F. E. Harris, Mathematical Methods for Physicists, 2013.

[190] A. Pagani, A. G. de Miguel, E. Carrera, Cross-sectional mapping for refined beam elements with applications to shell-like structures, Computational Mechanics 59 (6) (2017) 1031–1048.

[191] E. Carrera, E. Zappino, G. Li, Finite element models with node-dependent kinematics for the analysis of composite beam structures, Composites Part B: Engineering 132 (2018) 35–48.

[192] J. M. Gere, B. J. Goodno, Mechanics of Materials, Cengage Learning, Inc, Stamford CT, USA, 2011.

[193] N. J. Pagano, Exact solutions for composite laminates in cylindrical bending, Journal of Composite Materials 3(3) (1969) 398–411.

[194] J. N. Reddy, Mechanics of Laminated Composite Plates and Shells. Theory and Analysis, CRC Press, 2004.

[195] J. R. Shewchuk, Comparing direct and iterative equation solvers in a large structural analysis software system, Computing Systems in Engineering 2 (1991) 397–408.

[196] J. R. Shewchuk, An introduction to the conjugate gradient method without the agonizing pain, Report-School of Computer Science Carnegie Mellon University.

[197] J. Thorson, Gaussian elimination on a banded matrix, SEP-Report 20 (1979) 143–154.

[198] P. Danziger, Big o notation, Source:http://www.scs.ryerson.ca/ mth110/Handouts/PD/bigO.pdf.

[199] E. Carrera, A. G. de Miguel, A. Pagani, Hierarchical theories of structures based on Legendre polynomial expansions with finite element applications, International Journal of Mechanical Sciences 120 (2017) 286–300.

[200] R. M. J. Groh, P. M. Weaver, S. White, G. Raju, Z. Wu, A 2D equivalent single-layer formulation for the effect of transverse shear on laminated plates with curvilinear fibres, Composite Structures 100 (2013) 464–478.

[201] H. Murakami, Laminated composite plate theory with improved in-plane responses, Journal of Applied Mechanics 53 (1986) 661 – 666.

[202] A. Tessler, Refined zigzag theory for homogeneous, laminated composite, and sandwich beams derived from Reissner's mixed variational principle, Advances in the Mechanics of Composite and Sandwich Structures 50 (10) (2015) 2621–2648.

[203] F. Tornabene, N. Fantuzzi, F. Ubertini, E. Viola, Strong formulation finite element method based on differential quadrature: A survey, Applied Mechanics Reviews 67 (2015) 020801.

[204] L. Demasi, G. Biagini, F. Vannucci, E. Santarpia, R. Cavallaro, Equivalent single layer, zigzag, and layer wise theories for variable angle tow composites based on the generalized unified formulation, Composite Structures 177 (2017) 54 – 79.

[205] M. A. Crisfield, J. J. Remmers, C. V. Verhoosel, et al., Nonlinear finite element analysis of solids and structures, John Wiley & Sons, 2012.

[206] K. J. Bathe, Finite Element Procedures, Prentice-Hall, Inc., USA, 1996.

[207] J. N. Reddy, An Introduction to Nonlinear Finite Element Analysis, Second Edition, Oxford University Press, UK, 2015.

[208] A. Hoger, D. E. Carlson, Determination of the stretch and rotation in the polar decomposition of the deformation gradient, Quarterly of Applied Mathematics 42 (1984) 113 – 117.

[209] C. Bisagni, C. G. Dávila, Experimental investigation of the postbuckling response and collapse of a single-stringer specimen, Composite Structures 108 (2014) 493–503.

[210] Z. Hashin, Failure criteria for unidirectional fiber composites, Journal of Applied Mechanics 47 (1980) 329–334.

[211] J. C. Brewer, P. A. Lagace, Quadratic stress criterion for initiation of delamination, Journal of Composite Materials 22 (1988) 1141–1155.

[212] S. O. Ojo, M. Patni, P. M. Weaver, Comparison of Weak and Strong Formulations for the 3D stress predictions of composite beam structures, International Journal of Solids and Structures 178-179 (2019) 145–166.

[213] M. Patni, S. Minera, R. M. J. Groh, A. Pirrera, P. M. Weaver, Efficient 3D Stress Capture of Variable-Stiffness and Sandwich Beam Structures, AIAA Journal 57(9) (2019) 4042–4056.

[214] M. Patni, S. Minera, A. Pirrera, P. M. Weaver, A computationally efficient model for three-dimensional stress analysis of stiffened curved panels, In Proceedings of the International Conference on Composite Materials and Structures (ICCMS), Hyderabad, India (2017) 1–11.

[215] H. Zhao, Stress Analysis of Tapered Sandwich Panels with Isotropic or Laminated Composite Facings, Electronic Theses and Dissertations, 309, 2002.

[216] S. K. Kuczma, A. J. Vizzini, Failure of Sandwich to Laminate Tapered Composite Structures, AIAA Journal 37 (1999) 227–231.

[217] C. Thurnherr, New analysis methods for corrugated laminates, Ph.D. thesis, ETH Zurich (2017).

[218] C. Thurnherr, L. Ruppen, S. Brändli, C. M. Franceschi, G. Kress, P. Ermanni, Stiffness analysis of corrugated laminates under large deformation, Composite Structures 160 (2017) 457–467.